LBL-29257

Lawrence Berkeley Laboratory
UNIVERSITY OF CALIFORNIA

EARTH SCIENCES DIVISION

Acoustic Emission in a Fluid Saturated Heterogeneous Porous Layer with Application to Hydraulic Fracture

J.T. Nelson
(Ph.D. Thesis)

November 1988

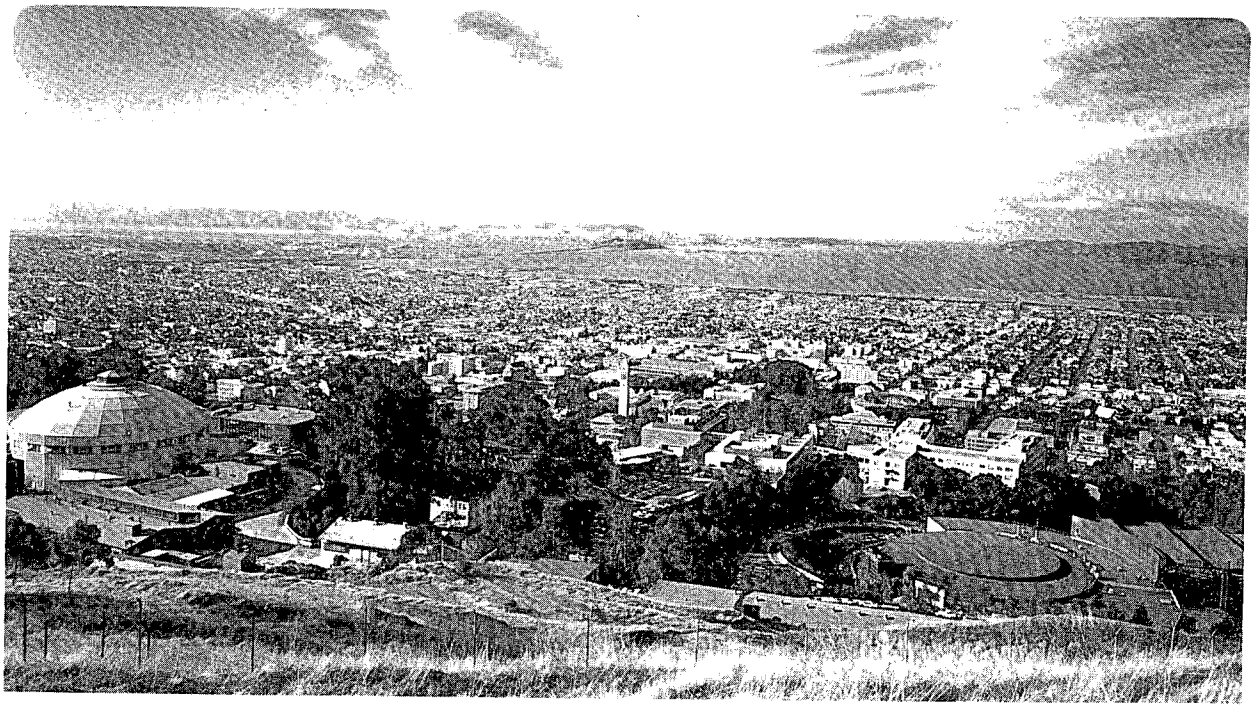

Prepared for the U.S. Department of Energy under Contract Number DE-AC03-76SF00098.

DISCLAIMER

LBL--29257

DE91 000223

Acoustic Emission in a Fluid Saturated Heterogeneous Porous Layer with Application to Hydraulic Fracture

James Tuman Nelson

(Ph.D. Thesis)

Department of Mechanical Engineering
University of California

and

Earth Sciences Division
Lawrence Berkeley Laboratory
University of California
Berkeley, California 94720

November 1988

This work was supported by the U.S. Department of Energy under Contract No. DE-AC03-76SF00098.

Acoustic Emission in a Fluid Saturated Heterogeneous Porous Layer with Application to Hydraulic Fracture

James Tuman Nelson

Abstract

A theoretical model for acoustic emission in a vertically heterogeneous porous layer bounded by semi-infinite solid regions is developed using linearized equations of motion for a fluid/solid mixture and a reflectivity method. Green's functions are derived for both point loads and moments. Numerically integrated propagators represent solutions for intermediate heterogeneous layers in the porous region. These are substituted into a global matrix for solution by Gaussian elimination and back-substitution.

Fluid partial stress and seismic responses to dislocations associated with fracturing of a layer of rock with a hydraulicly conductive fracture network are computed with the model. A constitutive model is developed for representing the fractured rock layer as a porous material, using commonly accepted relationships for moduli. Derivations of density, tortuosity, and sinuosity are provided.

The main results of the model application are the prediction of a substantial fluid partial stress response related to a second mode wave for the porous material. The response is observable for relatively large distances, on the order of several tens of meters. The visco-dynamic transition frequency associated with parabolic versus planar fluid velocity distributions across micro-crack apertures is in the low audio or seismic range, in contrast to materials with small pore size, such as porous rocks, for which the transition frequency is ultrasonic.

Seismic responses are predicted for receiver locations both in the layer and in the outlying solid regions. In the porous region, the seismic response includes both shear and dilatational wave arrivals and a second-mode arrival. The second-mode arrival is not observable outside of the layer because of its low velocity relative to the dilatational and shear wave propagation velocities of the solid region.

Structural dislocations and fluid volume supply are represented by linear combinations of moment tensors for the solid and fluid phase. Fluid flow is included as an independent parameter in the moment tensor representation for dislocation of the porous material. Reverse fluid flow into the void left by a dilatational fracturing process has a substantial effect on the character of the fluid partial stress and seismic responses.

Michael M. Carroll

Dissertation Committee Chair

To my mother,

Zos Tuman Nelson

and in memory of my father,

James Calvin Nelson

Acknowledgement

Dr. Michael Carroll served as dissertation committee chairman, and provided encouragement and guidance during my course work and research. Dr. Carroll initially suggested applying Biot's theory to a variable porosity representation of hydraulic fractures. I shall always remember with pleasure our lunchtime discussions concerning various problems in mechanics. Dr. Lane Johnson of the Department of Geology and Geophysics, served on my committee and provided insight and valuable observations regarding the use of the reflectivity method. His direction was invaluable for numerical calculation of the response functions presented here. Dr. Shimon Cohen's informative observations and teachings regarding mathematical physics and numerical analysis have been invaluable.

My research was conducted at the Center for Computational Seismology, of the Earth Sciences Division at Lawrence Berkeley Laboratory. Dr. Thomas McEvilly of the Earth Sciences Division, and Dr. Ernest Majer of the Center for Computational Seismology provided a place to work, support, and great amounts of computer time. Dr. Robert Zimmerman and Dr. John Kemeny of the Earth Sciences Division provided insight regarding the effect of cracks on the moduli of rock. Phil Cummins, Don Vasco, Dave Tralli, Michael Leonard, Jonathan Scheiner, John Peterson, and Dan O'Connell, provided useful subroutines, good humor, and moral support.

Many thanks to my professors at the Department of Mechanical Engineering. These include, but are not limited to, Dr. Paul Naghdi, chairman of my qualifying committee and advisor, Dr. David Bogy, member of my dissertation committee, Dr. George Johnson, Dr. Chieh Hsu, and Dr. C. D. Mote, Jr.

My mother instilled in me the value of a college education, and provided me with the necessary support during my undergraduate years. My uncle and mathematician, Dr. David A. Page, gave me an early childhood appreciation of mathematics and physics, which appreciation has stayed with me to this day. I still remember our circle in the sand.

My fellow workers and colleagues in the field of acoustics have provided me with inspiration and purpose. These include Dr. George Paul Wilson, Dr. Tor Kihlman, and Dr. Hugh Saurenman, and many others.

Finally, my wife Bari, and my children, Erika, Vanessa, and Ryan, bore the burden of my absence during countless evenings. To them I owe the greatest debt.

Table of Contents

Dedication i
Acknowledgment ii
Table of Contents iii
Chapter 1: Introduction 1
1.1 Acoustic Emission in Fluid Saturated Porous Media 1
1.2 Relevance to Hydraulic Fracture Monitoring 3
1.3 Hydraulic Fracture Pressure Transient and Seismic Modeling 4
1.4 Fracture Networks and Continuum Representations 7
Chapter 2: Continuum Model for Fractured Media 10
2.1 Continuum Approximation 10
2.2 Micro-Mechanical and Macro-Mechanical Descriptions 12
2.3 Porosity 13
2.4 Biot's Equations of Motion 13
2.5 Displacement and Velocity Fields 15
2.6 Densities 16
2.7 Induced Mass 17
2.8 Moduli 21
2.8.1 Hydrostatic Test 21
2.8.2 Jacketed Test 22
2.8.3 Reconciliation with Equations of Biot and Willis 23
2.8.4 Discussion 23
2.9 Estimation of Elastic Moduli for Dry Fractured Rock 24
2.9.1 Self-Consistent Approximations 24
2.9.2 Bruner's Formulae 26
2.10 Crack Density Estimation 28
2.10.1 Minimum Porosity and Crack Density for Conduction 30
2.11 Dissipation 31
2.12 Crack Apertures 33
2.13 Summary 34
Chapter 3: Boundary Value Problem and Solution 36
3.1 Representation Theorem 37
3.2 Displacement-Stress Representation for the Porous Region 39
3.2.1 Cylindrical Harmonic Expansion 39
3.2.2 Propagator Matrices 40
3.2.3 General Solution 43
3.2.4 Hybrid Multiple Layer Solution Method 44

3.3 Representation for Semi-Infinite Solid Regions 45
3.3.1 Radiation Conditions 47
3.3.2 Displacement-Stress Representation for the Solid Region 49
3.4 Boundary Conditions 50
3.5 Hankel Inversion and Fourier Summation 51
3.5.1 Displacement Components and Fluid Partial Stress 52
3.5.2 Point Load Representation 52
3.5.3 Point Load Green's Functions 55
3.5.4 Gradients of the Green's Functions 57
Chapter 4: Numerical Procedures 64
4.1 Integration of the Displacement-Stress Equations 64
4.2 Solution of the Boundary Value Problem 67
4.2.1 Inhomogeneous Terms for Stress Discontinuities 70
4.2.2 Inhomogeneous Terms for Derivative Evaluations 73
4.2.3 Summary 74
4.2.4 Discussion 75
4.3 Hankel Inversion Procedures 76
4.3.1 Constant Q Velocity Dispersion 76
4.3.2 Integration Contour 78
4.4 Computers 80
4.5 Verification 81
Chapter 5: Application to Hydraulic Fracture 83
5.1 Input Parameters 83
5.1.1 Porosity Profile 84
5.1.2 Total Aperture and Fracture Conductivity 85
5.1.3 Crack Density Parameter 89
5.1.4 Characteristic Velocity Profiles 89
5.1.5 Loss Factor Profile 94
5.2 Fundamental Response Functions 98
5.2.1 Center Plane Responses 103
5.2.2 Solid Region Responses 105
5.2.3 Responses Along the Upper Boundary 106
5.3 Responses to Isotropic Dilatational Sources 107
5.3.1 Responses Along Center Plane 109
5.3.2 Responses Along Upper Boundary 117
5.3.3 Responses In Solid Region 122
5.4 Responses to Fracturing Events 127
5.4.1 Responses to Dilatational Failures 127
5.4.1.1 Center Plane Responses 129
5.4.1.2 Upper Boundary Responses 137
5.4.1.3 Discussion 142

5.4.2 Responses to Deviatoric Failures 142
5.4.2.1 Center Plane Responses to $r-\theta$ Shear Failures 142
5.4.2.2 Center Plane Responses to $\theta-z$ Shear Failures 147
5.4.2.3 Center Plane Responses to $z-r$ Shear Failures 152
5.4.2.4 Upper Boundary Responses 152
5.5 Discussion 160
Chapter 6: Summary Discussion and Conclusion 163
6.1 Reflectivity Model 163
6.2 Constitutive Model 164
6.3 Hydraulic Fractures 165
6.4 Suggestions for Research 167
6.5 Conclusion 169
References 170
Appendix A: Representation Theorems and Reciprocity Relations 176
A1 Generalization of Betti's Reciprocal Theorem 176
A2 Reciprocity 178
A3 Representation Theorem 183
A4 Moment Tensor Source Representation 184
A5 Moment Representation Based on Scattering Theory 186
A6 Representation Theorem for Point Displacement Discontinuities 190
A7 Fracture vs. Fluid Dilatation 192
Appendix B: Displacement-Stress Representation for Poroelastic Materials 195
B1 Fundamental Equations 195
B2 Expansion in Orthogonal Vector Functions 201
B3 Matrix Representation 207
B4 Propagator Representation 210
Appendix C: Center Plane Displacement and Fluid Stress Responses 212
Appendix D: Solid Region Displacement Responses 237
Appendix E: Upper Boundary Displacement Responses 255

Chapter 1: Introduction

Biot's equations of motion are applied to a densely fractured fluid-saturated heterogeneous layer bounded by semi-infinite solid regions to calculate seismic displacement and fluid partial stress responses to point loads and symmetric moments. Sources are located on the vertical axis of a cylindrical coordinate system, with receivers at the center of the fracture layer and in the competent elastic regions. A displacement stress representation for the porous matrix and an extension of a reflectivity method for synthesizing the seismic response of vertically heterogeneous elastic isotropic media are used for solving the boundary value problem. Spectral responses are obtained at each receiver location by Hankel transform inversion and Fourier summation of displacement stress components, from which temporal waveforms are computed via the fast Fourier transform. The solutions thus obtained are complete Green's function for both point loads and symmetric moments.

The principal motivation for and application of the model is the synthesis of seismic and fluid pressure waves caused by acoustic emissions in a densely fractured saturated rock layer. The model is intended to provide a basis for interpreting seismic and fluid partial stress responses during hydraulic fracturing, and aid development of hydraulic fracture monitoring techniques. With minimal or no adjustment, the model can be used for studying acoustic emissions from fault zones, which may be indicators of incipient fault rupture. Another example is the propagation of ground vibration in vertically heterogeneous soils from subsurface sources, requiring a straight forward adjustment of the boundary conditions to include a free surface. There are practical limitations of the model related to the acoustic wave, or second mode, phase velocity, which will preclude its use for some materials where pore dimensions are very small.

1.1 Acoustic Emission in Fluid Saturated Porous Media

The general subject of this dissertation concerns the response of a fluid-saturated porous layer to point loads and moments. There is limited literature on this subject, though there are a number of notable contributions regarding Green's functions for unbounded homogeneous media. Some of the pertinent literature are mentioned below.

Burridge and Vargas (1979), use Laplace transform procedures to compute Green's functions for infinite homogeneous fluid saturated porous materials in the time domain. Four scalar potentials are used, and solutions for large time are obtained by saddle point analysis. A dilatational wave is found

to propagate at the P-wave velocity of the solid, obtained by constraining the fluid to move with the solid. The P-wave exhibits a Gaussian shaped velocity dispersion, evidently related to high frequency energy dissipation at a rate proportional to the square of frequency. A shear wave is obtained, with similar velocity dispersion. Finally, a long term diffusion wave is obtained. In a related paper, Minzoni and Vargas (1981), discuss the propagation of precursors to the arrival of the main content of the fast P-wave, indicating that the Gaussian velocity profile is actually on a pedestal with finite arrival time. Thus, the principle of causality is not violated. The precursors are of very low amplitude.

Norris (1985) obtained spectral, or time harmonic, representations of Green's functions for point loads in isotropic homogeneous infinite media and discusses reciprocity relations and scattering from inclusions. Temporal responses are obtained for the case of zero fluid viscosity, in which case the coupled dilatational waves and the shear wave propagate as delta-function pulses. In the presence of viscosity, asymptotic approximations indicate that the fast dilatational wave and the shear wave exhibit Gaussian shaped dispersion, and the slow wave is purely diffusive, as with the solutions by Burridge and Vargas. Norris' approach is used to develop the representation theorem used here.

Bonnet (1987) takes issue with the methods of Norris, and employs thermodynamic analogies to develop basic singular solutions for poro-elastic materials, using fluid divergence rather than displacement as the fundamental field quantity describing fluid motion. Use of the divergence allows specification of fluid volume source terms directly, rather than requiring differentiation of point load Green's functions with respect to position to develop fluid volume source representations. In fact, Bonnet indicates that Norris' approach is inadequate to represent fluid volume sources, because the fluid is incapable of supporting a point load. The use of a point load applied to the fluid is a mathematical convenience, however, and at finite frequency the response functions are well defined.

Boutin, Bonnet, and Bard, (1987), compute Green's functions for infinite and stratified poroelastic media, using the thermo-dynamic analogy discussed by Bonnet, (1987). Boundary element procedures are employed to compute responses to dipole and fluid volume supplies in a poroelastic layer over a uniform half-space. This work comes closest to the work described here, regarding the Green's functions for dislocation and fluid volume sources in a porous layer.

Bowen and Lockett (1983) compute Green's functions for a point load acting on the surface of a poroelastic inviscid fluid saturated layer resting on an impervious rigid surface. The results of the analysis indicate the need for including inertial effects to compute resonance displacements at certain

frequencies. Procedures are described for computing the response functions. The analysis is limited to uniaxial displacements and compression.

Dereciewicz discusses, in a series of papers, the effects of boundaries on wave propagation in fluid-saturated porous media. (See Dereciewicz, 1964, for a list of references.) Yamamoto (1983), employs a propagator matrix representation to study propagation of waves through continuous vertically heterogeneous porous materials of constant porosity. The approach used by Yamamoto is very similar to the approach used here, though load and moment sources are not considered. Berryman, et al, 1983, evidently use a propagator matrix representation to study pulse propagation in fluid-saturated homogeneous layers, though this reference was not obtained for review.

1.2 Relevance to Hydraulic Fracture Monitoring

Hydraulic fracturing is a method for enhancing petroleum and geothermal reservoir production and developing hazardous waste repositories. Monitoring of hydraulic fracture growth, azimuth and other properties is an important part of any hydraulic fracture project. Perhaps the most promising mapping technique is real-time down-hole monitoring of acoustic emissions, or micro-seismicity, because the wavelengths and frequencies are of appropriate scale and standard seismic inversion techniques are available to locate sources and determine associated seismic moments. Seismic monitoring is most economically performed with sensors in the primary borehole used for fluid injection; costs for drilling to depths on the order of several thousand feet preclude auxiliary boreholes strictly for monitoring purposes on a practical basis. Unfortunately, primary borehole monitoring may be frustrated by tube waves propagating along the fluid-filled borehole. Tube waves are bound-state, or trapped, modes consisting of an acoustic wave in the borehole fluid coupled with an elastic wave in the surrounding solid material, and may obscure elastic wave arrivals, adding to the "noise" of the monitoring system.

The source of these tube waves is not clearly identified. Wave conversion at the borehole of incident P and S waves due to borehole heterogeneity may be responsible. A more interesting explanation is that acoustic energy travels from sources through the fracture fluid in the fracture zone and enters the fluid-filled borehole. The ensuing pressure drop at the fracture mouth would induce a fluid volume extraction from the borehole and be a particularly efficient source.

If fluid pressure transients related to acoustic waves in the fracture fluid are sufficiently strong to cause tube wave noise during fracturing or after shut-in, (neglecting the noise due to reciprocating

fluid pumps) then perhaps they may be useful for providing information about the fracture directly. Specifically, the spectral ratios of the fluid pressure and exterior seismic responses may yield information on the fracture or micro-fracture apertures. Comparison of arrival times between fluid pressure and seismic responses may yield information on the tortuousity of the fracture matrix and bulk stiffness parameters. A knowledge of fracture permeability, crack apertures, and tortuousities may allow estimating the effective porosity of the fracture matrix, or the fracture volume. A model of wave propagation in fluid saturated fracture networks is thus valuable.

1.3 Hydraulic Fracture Pressure Transient and Seismic Modeling

There are evidently no prior models of fluid-phase acoustic wave transmission through a hydraulicly fractured rock layer with fracture network modeled as a porous material. Diffusive flow models do exist for calculating fluid pressure transients at the well head due to pumping and shut-in, but these are not suitable for studying high-frequency acoustic wave transmission and attenuation of fluid and seismic waves.

Effective models have been developed for modeling waves generated in discrete fluid-filled cracks. Chouet and Julien (1985) developed a finite difference model of the dynamic expansion of a fluid-filled crack, describing the nature of fluid pressure and elastic wave responses to an incremental expansion of a fracture. The work was later extended to three dimensions for a finite size fracture (Chouet, 1986). Both of the models include a fluid layer confined between two semi-infinite isotropic elastic regions. The method of characteristics is employed to model fluid acoustic pressure responses in the fluid layer. Both of these models indicate that significant "acoustic" pressures are generated and propagated within the fluid layer as a result of fracture extension. Chouet's models are perhaps the most realistic for dynamically modeling hydraulic fractures as discrete fluid layers, and could conceivably be extended to a network of fractures.

Ferrazzini and Aki (1987) analyze the wave propagation modes associated with a fluid layer sandwiched between two semi-infinite elastic regions using a two-dimensional plane-strain representation. They identify a fundamental symmetric mode of propagation with phase and group velocities approaching the acoustic velocity in the limit of short wavelength and zero velocity in the long wavelength limit. The fluid is assumed inviscid, so that the decrease in propagation velocity with increasing wavelength is not a diffusion effect, but a result of the inability of the semi-infinite regions

to provide reactions against the fluid pressure at long wavelength; there is no solid "connection" between the two semi-infinite regions. Thus, a model of an infinite fluid layer confined between two semi-infinite regions is not particularly realistic, a problem which Chouet's 3-D model of a finite fracture overcomes. The phase velocities computed by Ferrazzini and Aki are compared directly with Chouet's results for a 2-D finite length fracture, with good agreement. A particular result of the Ferrazzini model comparison is that the finite dimension of the fracture has a significant influence on the phase velocity of the "fundamental" mode. Evidently, the phase velocity of the fundamental mode for the infinite layer model exceeds the phase velocities obtained by Chouet's model for various crack stiffness parameters.

Ferrazzini and Aki indicate that the low velocity symmetric mode may be a source of volcanic tremor. As an example, a magmatic fluid-filled crack of length 1 km and thickness 0.5 m will exhibit a fundamental period of oscillation of 10 sec, 10 times the period obtained based on the acoustic velocity of the fluid alone.

The computer model "SALE" (Amsden, et al, 1980) was employed prior to development of the model presented here, for preliminary study of the propagation of a pressure wave in a thin fluid layer due to a pressure drop at the tip of a fracture. The model was of limited use for modeling attenuation with distance due to the low rates of attenuation found for fracture apertures on the order of a millimeter. Secondly, realistic source parameters could not be input to the model, and the boundaries of the fluid layer were rigid. Chouet's model mentioned above is considerably more realistic, though cannot be used for modeling the geometry of the wave front associated with the pressure wave, a minor difficulty.

Biot (1956b) described the attenuation of acoustic pressure waves in a viscous fluid sandwiched between two rigid boundaries in his now classic discussion of the "friction" between a viscous fluid and porous matrix. Later, Biot (1962) generalized fluid-matrix relaxation effects with a "viscodynamic" operator. These models predict a transition from low frequency behavior of the fluid layer characterized by a parabolic velocity profile to high frequency behavior characterized by a nearly planar wave front or velocity profile, and a 45 degree phase shift between average fluid pressure and displacement. For fluid layers with apertures on the order of millimeters down to perhaps a hundred microns, the transition frequency falls between 1 Hz and 1 Khz, well within the range of frequencies normally covered by a fracture monitoring network. Thus, Biot's (1956) theory of high frequency

effects of viscosity and transition frequencies for porous materials is particularly well suited to densely fractured rock with large crack apertures.

The problem of waves propagating within a viscous-fluid-saturated thin layer sandwiched between two semi-infinite elastic media was also considered by this author prior to the current model development, using potentials. As with the results obtained with "SALE", low rates of attenuation of fluid pressure waves were obtained, suggesting that there should be significant acoustic energy at the fracture mouth. The model is essentially equivalent to the model used by Ferrazzini and Aki, except that viscosity is included. The results of these investigations were not published, though Biot (1956) summarized the main results regarding attenuation with distance for the case of rigid boundaries.

Narasimhan (1987) considers a hydraulic fracture as a single fluid-filled fracture with characteristic permeability and conductivity in a homogeneous elastic medium. Fracture initiation and propagation are included. The approach is based on diffusive flow in a finite single fracture characterized by a fracture permeability. The work follows a theoretical analysis by Palen and Narasimhan (1981). Again, this latter work is concerned with diffusive flow of the fracture fluid over long time periods relative to seismic events.

Mahrer and Mauk (1987) modeled the seismic response of a finite length fluid layer bounded by two weakened elastic regions, or low velocity zones, using a two-dimensional plane-strain representation. The low velocity zone is bounded in both directions. The numerical solution was by finite difference techniques, very similar in scope to Chouet's finite difference model of a fluid filled two-dimensional crack, except that fluid motion is neglected. Most of the wave energy is confined to the weakened region, with very little escaping to the "outside". The authors indicate that monitoring points may best be located within the fracture zone to maximize the amount of information which may be obtained.

A feature of the model by Mahrer and Mauk is that fundamental "organ-pipe" modes are identified with a Rayleigh wave for the un-altered elastic regions surrounding the LVZ. Chouet's model, which includes fluid motion, indicates the presence of an acoustic mode, corresponding to a fluid pressure pulse propagating down the fracture. Thus the two models consider two entirely different types of waves.

1.4 Fracture Networks and Continuum Representations

The above models all represent the fracture as a single discrete fluid layer contained between two solid regions. Though this represents conventional wisdom, evidence is provided in the literature suggesting that such a simple idealization may not be appropriate in all cases. The best example is offered by Green and Baria (1987) who report that during stimulation of a hot dry rock geothermal well at 2 to 2.6 kilometer depth, numerous acoustic emission events were recorded and mapped. These data indicate that the region of seismicity induced by fracturing extended over a cylindrical vertical tubular structure measuring 70 meters by 70 meters by about 200 meters. Cross-hole survey data indicate that the region of joint dilation corresponds to the region of seismicity. With regard to the cross hole survey data, the authors further state: "The attenuation of high frequencies in the region of microseismicity suggests that the reservoir is composed of a complex zone of cracks rather than a single large fracture." (Mahrer, et al, 1987, p. 131) The authors further identify fluid storage in dilated joints as responsible for attenuation.

Palmer, et al, (unpublished manuscript) compare well bore pressures measured during hydraulic fracturing at the Multiwell Experiment Project (MWX) with numerical models which substantially underpredict the well bore pressure. Order-of-magnitude increases of rock moduli and/or fracture toughness are required to simulate the well bore pressure data. One of the possible causes discussed and discounted by the authors is that the fracture consists of a network of fractures, either parallel planar fractures or a branched network. The authors indicate that approximately 100 parallel fracture strands would be required to simulate the observed pressure data, or a very large number of branches. Palmer, et al, further indicate that although micro-seismic data suggest that the fracture zone is larger than predicted by a planar discrete fracture model, these micro-seismic events are caused by structural transformation of the crack layer surrounding the fracture and shear slippage along micro-cracks, or combined shear-tensile failures, not necessarily occasioned by fluid penetration. Palmer, et al conclude that the toughness of the fracture is much larger than indicated by laboratory measurements, and that the size discrepancy between seismic data and model predictions is due to shear slippage in joints or natural fractures ahead of the main fracture, producing a densely cracked layer around the main fracture.

Hull, et al, (1987) investigate the use of continuum representations to simulate discrete fracture networks associated with geothermal systems. These authors suggest that the spatial distribution of

pressures are reasonably well represented by a continuum, but that tracer and heat transport, related to fluid flow distribution, are not. The authors point out that a significant portion of the total porosity may not be conductive, drawing a distinction between "active" porosity and "total" porosity, where fluid flow is dependent on the "active" porosity. Effective modeling of fluid flow in geothermal fracture networks is best achieved by use of the active porosity.

Long and Witherspoon (1985) study the permeability of discrete fracture networks. Directional permeabilities are determined and compared with results obtained for an ideal porous material. The conclusion is that as fracture lengths increase, the degree of interconnection and permeability of the fracture system increases. Fracture systems with short but dense fractures behave less like porous media than do systems with longer but less dense fractures.

The application of continuum representations of fluid conduction to fracture networks in rock is questionable, and depends on whether or not sufficiently high fracture or crack densities exist. The crack density is a measure of the ratio of the volume represented by the cube of the crack radius to the volume per crack, which is in turn directly related to the effective bond occupation probability employed in percolation theory (Long and Witherspoon, 1985). For some types of rock a single or a few discrete fractures may comprise the fracture network, while for others, the fracture network may consist of numerous interconnected fissures with fluid conductivity approximating that of a continuum.

Weber and Bakker (1981) provide a compendium of fracture and vuggy porosities for various reservoir rocks, an area of intense interest to oil producers. Fracture porosities, distinct from vuggy porosities, may range from a fraction of a percent to as high as 8 percent. Examples include fractured cherts from the Santa Maria area of California, (5 to 8%), and fractured tuffs and igneous rocks found in Germany and Russia (2 to 8%). Crack apertures found in these systems are as large as several millimeters. At the low end are porosities on the order of 0.01 % to .1 %, represented by monoclines and low-dip anticlines, with crack apertures on the order of 10 to 100 microns. Thus, the validity of Biot's theory for modeling fluid pressure and seismic waves in fractured rock will depend on the type of rock and fracturing involved.

Biot's (1956) theory of wave propagation in porous media has certain desirable features for modeling seismic displacements and fluid stresses in densely fractured rock with large crack apertures and high fluid conductivity. Fracture networks are usually described with parameters such as permeability, porosity, fracture density, etc. These descriptors are contained in the Biot theory, and are fundamental

to the concept of a porous material. The micro-fracture apertures contributing to fluid flow are sufficiently large such that the transition frequency between low frequency parabolic flow and high frequency fluid-solid relaxation falls well below or within the seismic or low audio frequency range. This may be contrasted with conventional porous materials, such as unfractured or finely fractured rock, for which the transition occurs at much higher frequencies.

Biot's (1956) theory is exploited here as much as possible within the framework of standard geophysical theoretical techniques to provide a tool for interpreting acoustic emission events in densely fractured rock layers with high fluid conductivity.

Chapter 2: Continuum Model For Fractured Media

A continuum model is discussed for application of Biot's equations of motion to saturated fractured rock. The discussion begins with a comment regarding the validity of using a continuum representation for fluid motion in fracture networks. Definitions are given regarding the macromechanical quantities appearing in Biot's equations, and the micromechanical quantities associated with the constituents. Kinematical arguments based on volume averaging are given for estimating the mass coupling parameter between solid and fluid constituent velocities. Bruner's (1976) formulae for the modulus of elasticity and Poisson ratio of materials containing fractures are used to estimate moduli for the dry fractured rock matrix. These moduli are combined with the relations given by Biot and Willis (1957) to determine the moduli appearing in Biot's equations. The "tortuosity" and "sinuosity" parameters describing the effect of geometry on inertial coupling and friction between the fluid and solid constituents are included. Fundamental limitations are placed on the crack density parameter to support fluid conduction, limiting the porosity to a small but finite value depending on crack aspect ratio.

2.1 Continuum Approximation

Long and Whitherspoon (1985) performed numerical studies of fracture networks to determine those characteristics statistically consistent with continuum approximations for porous materials. An important parameter is the "effective bond occupation probability," ζ, (Engelman, et al, 1983) given by:

$$\zeta = \pi \lambda_A \bar{l}^2 \tag{2.1}$$

where λ_A is the number of fractures per unit area for two dimensional problems, and $\bar{l}$ is the mean fracture length. A critical value ζ^* exists such that if $\zeta > \zeta^*$, the material will become more permeable as the area of the material is increased. Conversely, for $\zeta < \zeta^*$, the material will become less permeable with increasing area.

The results of Long and Witherspoon suggest that for a two-dimension geometry and length-density value of $\bar{l}\lambda_A = .288$, (with dimension L^{-1}), the critical bond occupation probability, ζ^*, is approximately 8, above which the continuum approximation appears to be acceptable for modeling diffusive flow. Thus, if the fracture network is made up of sufficiently long fractures, the permeability of the fracture network approaches that of a continuum for a sufficiently large region, and is approximately isotropic provided that there is no preferred orientation for the fractures. For fractures with preferred orientation, the permeability will have tensor character.

Long and Witherspoon describe the departure of numerically computed permeabilities for fracture network models from continuous media permeabilities by a "normalized mean square error," or NMSE. The NMSE describes the "least squares fit" of the norm of a second rank tensor to the measured or numerically derived permeabilities of a fracture network over all possible angles. Again, for sufficiently large fractures, the apparent density of the fractures increases, promoting permeability, and for sufficiently large volumes, the NMSE approaches zero, corresponding to a continuum. The work of Long, et al, (1985) suggest that for an effective bond occupation probability, ζ, of 8 , the NMSE is roughly about 0.3.

A physical interpretation of the effective bond occupation probability for two dimensional problems may be obtained by requiring that the mean fracture length, $\bar{l}$, be greater than the diameter, d, of the area per fracture (distinct from the actual fracture area) given by the inverse of the area fracture density (λ_A). In this case,

$$\pi \lambda_A \bar{l}^2 > 4 \tag{2.2}$$

a result within a factor of two of that suggested for ζ by the work of Long and Witherspoon. The above requirement is thus a practical rule of thumb for determining the minimum value of ζ necessary for the fractured zone to support fluid conduction.

The above rule of thumb will be generalized to three dimensions by requiring that the fracture mean diameter exceed the diameter of the spherical volume per fracture, as a minimum. In this case, if n is the number of fractures per unit volume, and $\bar{l}$ is again the mean fracture diameter, then

$$\zeta = \pi n \bar{l}^3 > 6 \tag{2.3}$$

As will be discussed below, ζ is directly related to the crack density parameter employed in studies of fracture mechanics, and also to the ratio of porosity to crack aspect ratio. Thus, lower limits will be placed on these descriptors, below which fluid conduction will be considered nonexistent.

The fracture network is assumed to be isotropic to allow a "first cut" at modeling seismic and fluid pressure responses. Although anisotropy may be significant, the fundamental character of the responses should be obtained.

2.2 Micromechanical and Macromechanical Descriptions

The macromechanical quantities used in Biot's theory are volume averages of the corresponding micromechanical quantities of the constituents. Thus, the micromechanical description of the porous matrix includes the pore or crack geometry, flow geometry, intrinsic moduli for the solid portion of the porous matrix, and so forth. Definitions are presented below to clarify the relationships between these two descriptions.

The volumes occupied by the fluid and solid constituents are given by:

$$V_f = \int_R H_f(\mathbf{x}')dv' \tag{2.4a}$$

$$V_s = \int_R H_s(\mathbf{x}')dv' \tag{2.4b}$$

$$V = \int_R \left[H_s(\mathbf{x}') + H_f(\mathbf{x}')\right]dv' = \int_R dv' \tag{2.4c}$$

where R is the region of integration occupied by the mixture of solid and fluid constituents, and $H_f(\mathbf{x})$ and $H_s(\mathbf{x})$ are sampling functions such that if R_s and R_f are disjoint regions occupied by the solid and fluid constituents, respectively:

$$H_f(\mathbf{x}) = 1, H_s(\mathbf{x}) = 0, \mathbf{x} \varepsilon R_f \tag{2.5a}$$

$$H_f(\mathbf{x}) = 0, H_s(\mathbf{x}) = 1, \mathbf{x} \varepsilon R_s \tag{2.5b}$$

Thus, V_s is the volume occupied by the solid material, V_f is the volume occupied by the fluid material, and V is the volume occupied by the combined solid and fluid constituents in the region of integration, R.

Macroscopic quantities are described as volume averages of micromechanical quantities. For example, a field quantity ϕ assigned to the fluid component may be computed from its corresponding micromechanical field quantity ϕ^f by

$$\phi(\mathbf{x}) = \frac{1}{V_f}\int_R \phi^f(\mathbf{x}')H_f(\mathbf{x}')dv' = \langle \phi^f(\mathbf{x}) \rangle_f \tag{2.6}$$

$$\mathbf{x}' \varepsilon R$$

The subscripted brackets denote the average over the region occupied by the respective individual

constituent. Examples include fluid and solid displacements. However, partial stresses associated with the fluid or solid parts of the mixture are obtained by using the above formula and multiplying the result by the ratio of the respective constituent volume to the total volume.

The region, R, is large enough such that the medium can be considered as a continuum, though small enough to assign a quantity to the macroscopic field variable at the position, **x**. For example, the region R may be a ball of radius r centered at **x**. Values of ϕ at adjacent points are computed with similar integrals over regions which may overlap. Similar techniques are used by Drew (1971).

2.3 Porosity

The porosity, β, is the ratio of pore volume to total volume, or, equivalently, for a fluid saturated condition, the ratio of fluid volume to total volume:

$$\beta = \frac{V_f}{V} \tag{2.7a}$$

The ratio of porous solid volume to total volume is $1-\beta$:

$$(1-\beta) = \frac{V_s}{V} \tag{2.7b}$$

The porosity varies with position **x**, but not with time, consistent with the use of linearized constitutive relations for the porous material. Chemical reactions producing variations in porosity are excluded.

Finally, a realistic fracture network will contain numerous dead ends and not necessarily be well represented by a regularly jointed medium. In this case, the effective porosity will be different from the actual porosity. For the purposes of modeling, the effective porosity will be assumed identical to the actual porosity, so that all the fluid participates in the wavemotion.

2.4 Biot's Equations of Motion

Biot's (1956) time transformed equations of motion for fluid-saturated poro-elastic isotropic materials, augmented with body force terms, are:

$$-\omega^2\left[\rho_{11}u_i(\mathbf{x},\omega)+\rho_{12}U_i(\mathbf{x},\omega)\right] = \tag{2.8a}$$

$$\sigma_{ij,j}(\mathbf{x},\omega) + i\,\omega b(\mathbf{x},\omega)\left[U_i(\mathbf{x},\omega) - u_i(\mathbf{x},\omega)\right] + f_i(\mathbf{x},\omega)$$

$$-\omega^2\left[\rho_{21}u_i(\mathbf{x},\omega) + \rho_{22}U_i(\mathbf{x},\omega)\right] = \tag{2.8b}$$

$$s_{,i}(\mathbf{x},\omega) - i\,\omega b(\mathbf{x},\omega)\left[U_i(\mathbf{x},\omega) - u_i(\mathbf{x},\omega)\right] + F_i(\mathbf{x},\omega)$$

The following constitutive assumptions determine the partial stresses:

$$\sigma_{ij}(\mathbf{x},\omega) = \left[A(\mathbf{x})\delta_{ij}\delta_{kl} + N(\mathbf{x})(\delta_{ik}\delta_{jl} + \delta_{il}\delta_{jk})\right]u_{k,l}(\mathbf{x},\omega) + Q(\mathbf{x})\delta_{ij}U_{i,j}(\mathbf{x},\omega) \tag{2.9a}$$

$$s(\mathbf{x},\omega) = Q(\mathbf{x},\omega)u_{k,k}(\mathbf{x},\omega) + R(\mathbf{x},\omega)U_{k,k}(\mathbf{x},\omega) \tag{2.9b}$$

The notation used above are defined as follows:

δ_{ij} is the Kronecker delta,

$\rho_{\alpha\beta}$ are mass density parameters,

A, N, Q, and R are position dependent moduli for the porous solid and fluid constituents,

σ_{ij} are the partial stresses associated with the porous solid,

s is the isotropic partial stress associated with the fluid,

b is a friction coefficient describing the dissipative forces produced by relative motion between the fluid and solid constituents,

f_i is the body force per unit volume acting on the porous solid

F_i is the body force per unit volume acting on the porous fluid

u_i is the macromechanical displacement field of the porous solid

U_i is the macromechanical displacement field of the porous fluid

ω is the angular frequency

x is the position coordinate

Implicit in the above formulation is the Fourier transform with respect to time:

$$\hat{f}(\omega) = \int_{-\infty}^{+\infty} f(t) e^{-i\omega t} dt \tag{2.10}$$

Thus, the time derivative operator, $\frac{\partial}{\partial t}$, is replaced by $i\omega$ in going from the temporal to the spectral domain. The sign convention for the argument of the exponent is chosen to remain consistent with Biot's formulations for the frequency dependent effects of fluid motion through a porous matrix, and is opposite to the current popular convention in seismology.

Biot's equations determine the coupled acceleration of matrix and fluid constituents as sums of divergences of partial stresses, friction resulting from fluid flow relative to the matrix, and assigned body forces. The constitutive relations given for the partial stresses are isotropic, but the moduli may vary with position. Specifically, the moduli will be functions of vertical coordinate, z.

The partial tractions, t_i, associated with the partial stresses, σ_{ij}, are the average tractions applied to the solid portion of the porous matrix over an element of total area:

$$t_i(\mathbf{x}) = \frac{1}{A} \int_{R'} \hat{t}_i(\mathbf{x}') H_s(\mathbf{x}') da' \tag{2.11a}$$

Similarly, the partial traction, T_i, associated with the fluid stress, s, is the average traction due to the fluid's micromechanical stress, or negative of pore pressure, over the same macroscopic area element.

$$T_i(\mathbf{x}) = \frac{1}{A} \int_{R'} \hat{T}_i(\mathbf{x}') H_f(\mathbf{x}') da' \tag{2.11b}$$

The sum of the partial tractions is equal to the total traction applied to the element of area. The definitions of the partial tractions (and thus partial stresses) are thus different from those used for defining the displacement fields, in that the integrals are normalized by the total area (or volume) of integration, rather than that associated with the particular constituent.

2.5 Displacement and Velocity Fields

The displacement fields appearing in Biot's equations for the porous solid and fluid constituents are defined as averages of the corresponding micromechanical displacement fields of the solid and fluid

constituents over their respective regions of occupation. The sampling functions are used to define the region of integration for the mixture, a region which consists of disjoint regions occupied by the solid and fluid constituents. Thus, for the displacement field of the porous matrix:

$$u_i(\mathbf{x}) = \frac{1}{V_s}\int_R u_i^s(\mathbf{x}')H_s(\mathbf{x}')dv' = \langle u_i^s \rangle_s \tag{2.12a}$$

and for the fluid displacement:

$$U_i(\mathbf{x}) = \frac{1}{V_f}\int_R u_i^f(\mathbf{x}')H_f(\mathbf{x}')dv' = \langle u_i^f \rangle_f \tag{2.12b}$$

where u_i^s and u_i^f are the micromechanical displacement fields of the solid and fluid parts, respectively. The integral over the region R is divided by the fractional volume occupied by the particular constituent, rather than by the volume of the region R. Thus, the displacements are averages over the respective constituent regions.

Similarly, the macromechanical velocity fields v_i and V_i for the solid and fluid constituents, respectively, are defined with respect to the micromechanical velocity fields v_i^s and v_i^f by the same averaging operation:

$$v_i(\mathbf{x}) = \frac{1}{V_s}\int_R v_i^s(\mathbf{x}')H_s(\mathbf{x}')dv' = \langle v_i^s \rangle_s \tag{2.13a}$$

$$V_i(\mathbf{x}) = \frac{1}{V_f}\int_R v_i^f(\mathbf{x}')H_f(\mathbf{x}')dv' = \langle v_i^f \rangle_f \tag{2.13b}$$

2.6 Densities

The density parameters appearing in Biot's equations are related as:

$$\rho_{11}(\mathbf{x}) + \rho_{12}(\mathbf{x}) = \rho_1(\mathbf{x}) \tag{2.14a}$$

$$\rho_{12}(\mathbf{x}) + \rho_{22}(\mathbf{x}) = \rho_2(\mathbf{x}) \tag{2.14b}$$

$$\rho_1(\mathbf{x}) + \rho_2(\mathbf{x}) = \rho(\mathbf{x}) \tag{2.14c}$$

where

ρ_1 is the macroscopic density of the porous matrix

ρ_2 is the macroscopic density of the porous fluid

ρ is the density of the combined porous solid and fluid mixture.

The average density, ρ_1, is related to the density of the solid portion of the porous matrix, ρ_s, by

$$\rho_1 = (1-\beta)\rho_s \tag{2.15a}$$

and the average density ρ_2 is related to the fluid density, ρ_f, by:

$$\rho_2 = \beta\rho_f \tag{2.15b}$$

2.7 Induced Mass

The density ρ_{12}, is the "induced mass" resulting from inertial coupling between the porous solid and fluid average accelerations. The induced mass is the result of the deviation from rectilinear motion of the micromechanical fluid flow through the porous solid, and has been the subject of much discussion and experimental study by Plona and Johnson (1984) and Berryman (1981) The induced mass is one of the more fascinating features of the Biot theory from the standpoint of mixture theory.

Given the porosity, the densities ρ_1 and ρ_2 are determined. If the induced mass ρ_{12} can be estimated, the remaining densities ρ_{11} and ρ_{22} are then determined. Therefore, a procedure is given below for estimating the induced mass for a fracture network, or any pore geometry, purely from kinematical considerations, though the procedure will not be used here for quantitative calculations.

The total kinetic energy of the region R of volume V in the macromechanical description is (Biot, 1956):

$$T = \frac{V}{2}\left[\rho_{11} v_i v_i + 2\rho_{12}(v_i V_i) + \rho_{22} V_i V_i\right] \tag{2.16}$$

Again, R is small enough such that the macromechanical field quantities are reasonably constant in R. In the micromechanical description, the kinetic energy is

$$T = \frac{1}{2}\int_R \left[\rho_s v_i^s v_i^s H_s(\mathbf{x}') + \rho_f v_i^f v_i^f H_f(\mathbf{x}')\right] dv' \tag{2.17}$$

Assuming that the densities of the fluid and solid constituents are approximately constant over their

respective solid and fluid regions, consistent with the linear approximations inherent in the Biot theory, the kinetic energy becomes:

$$T = \frac{1}{2}\rho_s \int_R v_i^s v_i^s H_s \, dv' + \frac{1}{2}\rho_f \int_R v_i^f v_i^f H_f \, dv' \tag{2.18}$$

$$= \frac{\rho_s}{2} V_s \langle v_i^s v_i^s \rangle_s + \frac{\rho_f}{2} V_f \langle v_i^f v_i^f \rangle_f$$

Equating the micromechanical and macromechanical expressions for the kinetic energy, and using the definition of porosity:

$$\rho_{11} v_i v_i + 2\rho_{12} v_i V_i + \rho_{22} V_i V_i = (1-\beta)\rho_s \langle v_i^s v_i^s \rangle_s + \beta\rho_f \langle v_i^f v_i^f \rangle_f \tag{2.19}$$

Because $\rho_{11} = (1-\beta)\rho_s - \rho_{12}$ and $\rho_{22} = \beta\rho_f - \rho_{12}$, the above relations may be rearranged to obtain an expression for the induced mass:

$$\rho_{12} = -\frac{(1-\beta)\rho_s \left[\langle v_i^s v_i^s \rangle_s - v_i v_i \right] + \beta\rho_f \left[\langle v_i^f v_i^f \rangle_f - V_i V_i \right]}{(V_i - v_i)(V_i - v_i)} \tag{2.20}$$

Thus, the induced mass is given by the differences between the mean square velocities and the squares of the corresponding macromechanical velocities, weighted by the constituent densities. Since $0 \le \beta \le 1$, the induced mass is always negative, as noted by Biot (1956).

Defining velocity defects Δv_i^s and Δv_i^f by

$$\Delta v_i^s = v_i^s - v_i \tag{2.21a}$$

$$\Delta v_i^f = v_i^f - V_i \tag{2.21b}$$

the above expression for the induced mass can be rearranged and expressed as:

$$\rho_{12} = -\frac{(1-\beta)\rho_s \langle \Delta v_i^s \Delta v_i^s \rangle_s + \beta\rho_f \langle \Delta v_i^f \Delta v_i^f \rangle_f}{(V_i - v_i)(V_i - v_i)} \tag{2.22}$$

The induced mass is determined by the deviations of the micromechanical velocity fields averaged over their respective regions R_s and R_f, together with the relative macromechanical velocities.

As an alternative, by rearranging the previous relation, (2.21), for the induced mass, the following may be obtained:

$$\rho_{12} = -(1-\beta)\rho_s \left\{ \frac{<(v_i^s - V_i)(v_i^s - V_i)>_s}{(V_i - v_i)(V_i - v_i)} - 1 \right\} - \beta\rho_f \left\{ \frac{<(v_i^f - v_i)(v_i^f - v_i)>_f}{(V_i - v_i)(V_i - v_i)} - 1 \right\} \tag{2.23}$$

If tortuosities α_s and α_f are now introduced:

$$\alpha_s = \frac{<(v_i^s - V_i)(v_i^s - V_i)>_s}{(V_i - v_i)(V_i - v_i)} \tag{2.24a}$$

$$\alpha_f = \frac{<(v_i^f - v_i)(v_i^f - v_i)>_f}{(V_i - v_i)(V_i - v_i)} \tag{2.24b}$$

the induced mass can be expressed concisely as:

$$\rho_{12} = -(1-\beta)\rho_s(\alpha_s - 1) - \beta\rho_f(\alpha_f - 1) \tag{2.25}$$

The tortuosity for the solid is the mean square deviation of the micromechanical velocity field of the solid from the fluid mean velocity field, normalized by the square of the relative velocity between fluid and solid constituents. Similarly, the tortuosity for the fluid phase is the mean square deviation of the micromechanical fluid velocity field from the mean velocity field of the solid, again normalized by the square of the macromechanical relative velocity field.

For rigid porous solids, a simplification may be obtained because the micromechanical velocity field will be equivalent to the macromechanical velocity field. Then, the solid region tortuosity will be unity, giving:

$$\rho_{12} \approx -\beta\rho_f(\alpha_f - 1) \tag{2.26}$$

Equation (2.26) is equivalent to that described by Plona and Johnson (1984) with respect to the tortuosity, α. The tortuosity, α_f, shall henceforth be identified with the tortuosity, α, found in the literature.

Plona (1980) has demonstrated the existence of the induced mass for glass beads immersed in fluid, and both Plona and Johnson discuss relations between tortuosity and porosity for porous materials such as soils or rocks characterized by spheroidal grains. For these materials, the tortuosities are on the order of unity.

Equation (2.24b) is a recipe for the induced mass or tortuosity, given the micromechanical velocity field of the fluid and assuming that the micromechanical velocity field of the solid is constant over the region of integration. Determining the micromechanical velocity field of fluid flow in fractures would

require detailed fluid flow analyses. For example, the fracture networks modeled by Long and Witherspoon may exhibit high tortuosities for relatively low apparent fracture densities or short fracture lengths. If the velocity field can be calculated for a given net average fluid flow, then the tortuosity can be determined for modeling purposes.

An expression mentioned by Plona and Johnson (1984), evidently due to Berryman (1980), for the tortuosity as a function of porosity for isolated spherical solid particles (a canonical porous material) is:

$$\alpha = \frac{1}{2}(\beta^{-1}+1) \tag{2.27}$$

For very low porosities on the order of 3%, the estimated tortuosity is about 17.

If the micromechanical fluid velocity is approximately equal to the average velocity, V, multiplied by the ratio of the tortuous path length, l, between two points to the straight line distance, L, between the points, then the tortuosity is simply:

$$\alpha = \frac{l^2}{L^2} \tag{2.28}$$

The tortuosity is thus closely related to the square of the relative path length. For regularly jointed rocks such as considered by Morland (1974), the tortuosity may be relatively low. For a regularly jointed square fracture network in two dimensions with distance between opposite vertices of 1, the tortuous relative path length is 1.4, and the tortuosity factor for fluid flow between opposite vertices is thus 2, regardless of porosity. Thus, the above expression for tortuosity appearing in the literature for conventional porous materials is not appropriate for fracture networks. Rather, tortuosity should be based on mean square path length differences, or, more precisely, by mean-square velocity distributions.

The tortuosity should have a significant effect on the arrival time of the acoustic "slow" wave predicted by Biot's theory. Conversely, the fluid tortuosity might be estimated acoustically by comparing arrival times between fast and slow dilatational waves. As pointed out by Johnson (1984), the tortuosity might also be determined by electrical means, since the resistivity of the fracture network is directly related to the length of the path followed by the electrical current.

2.8 Moduli

A number of constitutive coefficients for the partial stresses must be determined. Universal relations exist (Biot and Willis, 1957) between the various moduli which reduce the number of assumptions required to define the constitutive coefficients. Equivalent relations will be used to estimate the moduli, given values for the bulk stiffness of the fractured rock under dry conditions and the shear stiffness, represented by formulae developed by Bruner (1976) and evaluated by Zimmerman (1985).

Following the procedures of Biot and Willis (1957) relations are developed below between these moduli.

2.8.1 Hydrostatic Test

If a fluid saturated porous material is immersed in a fluid and then pressurized, the micromechanical stress within the solid portions of the matrix will be hydrostatic and equivalent to the negative of the pore pressure, in turn equivalent to the hydrostatic pressure of the fluid. Under this condition, the constitutive relations for the partial stresses give:

$$\sigma_{kk} = (3A + 2N)u_{k,k} + 3QU_{k,k} \tag{2.29a}$$

$$s = Qu_{k,k} + RU_{k,k} \tag{2.29b}$$

The trace of the partial stress for the porous matrix is equivalent to the trace of the micromechanical stress of the solid portion of the porous matrix, averaged over the region R containing the combined fluid and solid materials:

$$\sigma = -3(1-\beta)p \tag{2.30}$$

Similarly, the partial stress for the fluid constituent is equivalent to the negative of the pore pressure, averaged over the fluid regions:

$$s = -\beta p \tag{2.31}$$

Under hydro-static compression, the pore geometry will shrink but will not distort, nor will the porosity be changed. Thus, the volumetric strains of the solid and fluid constituents are given by:

$$u_{k,k} = -\frac{p}{K_s} \tag{2.32a}$$

$$U_{k,k} = -\frac{p}{K_f} \tag{2.32b}$$

where K_s and K_f are the micromechanical bulk moduli for the solid and fluid materials, respectively. These relations can be derived by considering volume integrals over a region R and assuming that the pore geometry is unchanged under hydrostatic pressure.

As pointed out by Biot and Willis (1957), the relation between pore pressure, p, and dilatation of the fluid, given by the second of the above relations, will be "strictly valid only for materials such that the pore volume and the bulk volume remain in constant ratio." Biot and Willis further provide procedures for the case when the above does not hold. For this study, the special case of constancy of ratio between pore volume and bulk volume shall be assumed.

Combining the above relations, obtain:

$$(1-\beta)=\frac{3A+2N}{3K_s}+\frac{Q}{K_f} \tag{2.33a}$$

$$\beta=\frac{Q}{K_s}+\frac{R}{K_f} \tag{2.33b}$$

2.8.2 Jacketed Test

If the sample undergoes a jacketed test, where the porous solid is subjected to an isotropic stress but the pore pressure is relieved by draining, then the matrix bulk modulus for the "drained" or "dry" condition may be determined. Thus, during a jacketed test:

$$\sigma_{kk}=(3A+2N)u_{k,k}+3QU_{k,k} \tag{2.34a}$$

$$0=Qu_{k,k}+RU_{k,k} \tag{2.34b}$$

Using the second of these relations in the first,

$$\sigma_{kk}=\left[3A+2N-3\frac{Q^2}{R}\right]u_{k,k} \tag{2.35}$$

from which the bulk modulus for the fractured rock with zero pore pressure is deduced as

$$B=\frac{3A+2N}{3}-\frac{Q^2}{R} \tag{2.36}$$

This relation was also obtained by Biot and Willis (1957). If the bulk modulus, K_s, for the drained condition and the shear modulus, N, can be measured or estimated, then the above equations determine A, Q, and R:

$$A = K_s \frac{\left[\frac{1-\beta}{K_s} - \frac{\beta}{K_f}\right] B - (1-\beta)^2}{\frac{B}{K_s} - \beta\frac{K_s}{K_f} - (1-\beta)} - \frac{2}{3}N \tag{2.37a}$$

$$R = -K_s \frac{\beta^2}{\frac{B}{K_s} - \beta\frac{K_s}{K_f} - (1-\beta)} \tag{2.37b}$$

$$Q = K_s \frac{\beta\left[\frac{B}{K_s} - (1-\beta)\right]}{\frac{B}{K_s} - \beta\frac{K_s}{K_f} - (1-\beta)} \tag{2.37c}$$

2.8.3 Reconciliation with Equations of Biot and Willis

Equations (2.37a) through (2.37c) are equivalent to those of Biot and Willis (1957), given in terms of the coefficient of fluid content, γ, and the coefficient of unjacketed compressibility, δ. In the development given above, subject to the restriction of constant porosity under hydro-static compression obtained during an unjacketed compressibility test, the coefficient of unjacketed compressibility is equal to the bulk modulus of the solid material making up the porous matrix:

$$\delta = \frac{1}{K_s} \tag{2.38}$$

The coefficient of fluid content is given by

$$\gamma = \beta(K_f - K_s) \tag{2.39}$$

These equations reconcile the above relations for the moduli (2.37a,2.37b,2.37c) with the Biot-Willis relations.

2.8.4 Discussion

Berryman (1981) stated that during the jacketed test, the pore fluid remains both unstressed and unstrained. This cannot be true since during such a test, the pore volume will change, thus displacing the fluid, producing a volumetric strain of the macromechanical fluid. During the jacketed test, the micromechanical fluid dilatation is zero because the pore pressure is zero, but considerable average straining of the fluid will have occurred due to displacement of the fluid by the solid. Berryman

introduces the above concept as a new result to be compared with the results of Biot and Willis (1957). Korringa (1981), in an analysis of Berryman's work, points out that the correct equations derived by Biot and Willis, one of which was derived by Gassman (1951) have "withstood thirty years of scrutiny." Berryman (1981b) acknowledges the error.

In another case, Lovera (1987) observes that the pore pressure should always equal the normal component of the total stress traction at a boundary. If this were true, the jacketed compressibility test would not work. Therefore, Lovera's assumption is invalid. Lovera develops boundary conditions between porous and solid materials, boundary conditions which are at odds with those used here and with those derived by Deresiewicz (1964) in a series of articles on the subject

2.9 Estimation of Elastic Moduli for Dry Fractured Rock

The problem of identifying Biot's coefficients for the fractured region is reduced to determining the moduli for the fractured rock under drained conditions. A number of models have been developed for predicting moduli as a function of crack density and geometry. They are primarily intended for application to materials with relatively low crack density and crack radii and thus to relatively small reductions of shear and bulk stiffnesses. Extending the constitutive models for micro-fractured rock characterized by crack radii on the order of a millimeter or less to high fluid conductivity or hydraulicly fractured rock with crack radii on the order of a fraction or more of a meter is at best a rough approximation. The micro-crack models, though, yield the proper qualitative parametric dependence of stiffnesses and permeability on fracture density and size, and form the basis of the development given here.

2.9.1 Self-Consistent Approximations

O'Connel and Budiansky (1974,1977) use a self-consistent approximation to estimate the modulus of elasticity for rock containing thin fractures. The formulae given by O'Connel and Budiansky for moduli of drained elastic cracked solids with crack density, ε, for the limiting case of zero frequency, are:

$$\frac{\tilde{K}}{K} = 1 - \frac{16}{9}\left[\frac{1-\nu^2}{1-2\nu}\right]\varepsilon \tag{2.40a}$$

$$\frac{\tilde{G}}{G} = 1 - \frac{32}{45}\frac{(1-\nu)(5-\nu)}{(2-\nu)}\varepsilon \tag{2.40b}$$

$$\tilde{\nu} = \nu - \frac{16}{45}\frac{(1-\tilde{\nu}^2)(10\nu - 3\nu\tilde{\nu} - \tilde{\nu})}{(2-\tilde{\nu})} \tag{2.40c}$$

where K, G, and ν are the bulk modulus, shear modulus, and Poisson ratio for the uncracked solid, and $\tilde{K}$, $\tilde{G}$, and $\tilde{\nu}$ are the corresponding parameters for the the cracked solid. The crack density, ε, is given by

$$\varepsilon = (2n/\pi)\langle A^2/P \rangle \tag{2.41}$$

where A is the crack area, P is the perimeter of the cracks, and n is the number of cracks per unit volume. The brackets denote an average quantity. Thus, the crack density, ε, is actually dimensionless. For circular cracks, the crack density reduces to

$$\varepsilon = n\langle a^3 \rangle \tag{2.42}$$

where a is the crack radius.

The authors further discuss two high frequency effects. One of these is the case where the fluid is too stiff or the frequency is too high for the fluid to be able to squeeze out of or into the crack, resulting in the "saturated isolated" case. At still higher frequencies, the effect of fluid viscosity is so strong as to make the fluid behave as a solid, thus adhering the surfaces of the crack together, so that the shear modulus for the cracked solid approaches that of the uncracked solid. Transition frequencies are proposed to describe the frequency ranges over which each of these conditions hold. The first of these transition frequencies is ω_1, for the transition from the "saturated isobaric" to the "saturated isolated" case, is:

$$\omega_1 = (K/\eta)(h_f/a)^3 \tag{2.43}$$

where $2h_f$ is the crack height, a the crack radius, and h_f/a the crack aspect ratio. The second transition frequency, ω_2, represents the transition from "saturated isolated" to rigid, as the frequency is increased above ω_2:

$$\omega_2 \approx (\frac{G}{\eta})(\frac{h_f}{a}) \tag{2.44}$$

The fact that the crack aspect ratio and not the crack height alone determines these transition frequencies is interesting. As shown by Biot (1956), the ratio of the square of crack aperture to fluid viscosity is the primary factor in determining viscous coupling of the fluid with the porous solid. The above relations evidently describe a phenomenon not represented by Biot's theory for friction between fluid and solid constituents. A theoretical analysis from the point of view of mixture theory and including

fluid shear might shed further light on the second of these transitions.

The above transition frequencies for water with viscosity $.001 N sec/m^2$, crack aspect ratio .001, and bulk and shear moduli for rock on the order of $3\times10^{10} N/m^2$ (quartz) are:

$$f_1 \approx 5\times10^3 Hz \tag{2.45a}$$

$$f_2 \approx 5\times10^9 Hz \tag{2.45b}$$

If the viscosity were 100 times that of water, corresponding to some of the "frac fluids" used for hydraulic fracturing, the above frequencies would be reduced by a factor of 100 to:

$$f_1 \approx 50 Hz \tag{2.46a}$$

$$f_2 \approx 5\times10^7 Hz \tag{2.46b}$$

However, if the crack aspect ratio is 0.01 instead of 0.001, the transition frequencies for water become:

$$f_1 \approx 5\times10^6 Hz \tag{2.47a}$$

$$f_2 \approx 5\times10^{10} Hz \tag{2.47b}$$

while for high-viscosity frac fluids the transition frequencies are:

$$f_1 \approx 5\times10^4 Hz \tag{2.48a}$$

$$f_2 \approx 5\times10^8 Hz \tag{2.48b}$$

Assuming that an appropriate crack aspect ratio, c/a, for fractured rock, is between 0.001 and 0.01, the above estimates of transition frequencies suggest that the static self-consistent estimates for bulk and shear moduli for the drained (but saturated) cracked solid are valid for frequencies up to at least 50 Hz for high viscosity "frac fluids" in very low aspect ratio fractures, and up to much higher frequencies for water. Thus, for simplicity, the high frequency effects of fluid shear are neglected in the present model.

2.9.2 Bruner's Formulae

Bruner (1976) introduces the following approximate formulae for calculating moduli for cracked media:

$$\frac{\bar{E}}{E} \approx e^{-16\epsilon/9} \tag{2.49a}$$

$$\frac{\bar{\nabla}}{\nu} \approx e^{-8\epsilon/5} \tag{2.49b}$$

where E, and $\bar{E}$ are the moduli of elasticity for the uncracked and cracked solid, respectively, and ν, and ∇ are the corresponding Poisson ratios.

Bruner proposed the above formulae as a modification to the work by O'Connel and Budiansky to remove certain difficulties. The first of these difficulties, to paraphrase Bruner, is that the shear modulus can become negative for sufficiently high crack density, and Poisson's ratio can exceed 1/2 for saturated cracks. Bruner makes the point that the work by O'Connel and Budiansky is based on linearized continuum theory, and cannot be expected to predict failure due to cracking, which amounts to a phase change. O'Connel and Budiansky (1976) are quick to raise counter arguments to Bruner's objections, saying that there are certain "unsatisfying" mathematical derivations in Bruner's development. Further, they point out that the self-consistent method is well established in the literature. One of the main objections raised by O'Connel and Budiansky to Bruner's theory is that the contribution of each crack to the overall strain energy changes in Bruner's model as more and more cracks are introduced to the system. They do not offer a clear argument against such a phenomenon, and the approach by Bruner appears to be at least as acceptable as that used by O'Connel and Budiansky.

O'Connel and Budiansky's theory predicts complete loss of shear stiffness for finite fracture densities, $\epsilon = na^3$, on the order of 1.4 for saturated cracks. As discussed below, the crack densities employed for modeling fluid conduction are in excess of .24, and range to as high as 2 or 3, substantially in excess of the density predicted for failure by O'Connel and Budiansky. The renormalization group theoretical approach of Madden (1983) also suggests cleavage of the rock material at finite fracture density. Although the fractured rock may fall apart due to extensive fractures if removed from confinement, it may yet be able to support shear *in-situ*. Bruner suggests that if a massively fractured body is subjected to compressive loading with small deviatoric stress, the body "...should remain coherent for arbitrarily large crack densities." (1976, p. 2573)

The formulae developed by Bruner predicts a finite shear stiffness for arbitrary crack densities, and, moreover, there is no violation of limiting constraints imposed on Poisson's ratio for the dry fractured material as fracture density goes to infinity. In practice, the actual shear stiffness in the presence of high fracture density may fall between the finite values represented by the work of Bruner and the

zero values obtained by O'Connel and Budiansky for sufficiently high crack densities.

Zimmerman (1985) has developed exact models for spherical pores and has verified Salganik's (1973) modified self-consistent method of which the above formulas given by Bruner are approximations. Zimmerman and King (1985) point out that direct verification of Bruner's formulae are probably not possible due to the difficulty in determining crack density. Zimmerman and King provide a comparison of theory with experimental data by relating changes in shear wave velocities to compression wave velocities reported by several experimenters, and conclude that the approximate relations provided by Bruner are reasonable.

From a modeling point of view, Bruner's formulae for modulus of elasticity and Poisson ratio are attractive because of their simplicity and because they will not result in a singular problem at finite fracture density when propagating shear and dilatational waves through a medium with varying crack density. In view of the work by Zimmerman and King, the equations proposed by Bruner are adopted here for modeling fractured rock materials of arbitrary crack density parameter.

2.10 Crack Density Estimation

The crack density, identical to that used by O'Connel and Budiansky (1974) for circular cracks, appearing in Bruner's formulae discussed above, is given by:

$$\varepsilon = n\langle a^3\rangle \tag{2.50}$$

$$\langle a^3\rangle = \int_0^{\infty} u^3 f(u)\,du \tag{2.51}$$

where n is the number of cracks per unit volume, u is the crack radius and $f(u)$ is a distribution function for the radius. To simplify the development, the distribution function is assumed to be given by a delta function:

$$f(u) = \delta(u - a_0(x)) \tag{2.52}$$

so that the mean cube crack radius at a given point will be given by:

$$\langle a^3\rangle = a_0^3 \tag{2.53}$$

Thus, the crack density parameter becomes:

$$\varepsilon = n a_0^3 \tag{2.54}$$

The volume of each "penny-shaped" crack is approximated by

$$v_0 = 2\pi a_0^2 h_f \tag{2.55}$$

where $2h_f$ is the mean crack aperture over the surface of the crack. If there are n cracks per unit volume, each with volume v_0, the total volume of cracks per unit volume, that is, the porosity, is:

$$\beta = n v_0 = n\, 2\pi a_0^2 h_f \tag{2.56}$$

Solving for the crack radius:

$$a_0^2 = \frac{\beta}{2n\pi h_f} \tag{2.57}$$

The crack density parameter can thus be expressed as the product of the porosity, β, and the inverse of the crack aspect ratio, $\frac{h_f}{a_0}$:

$$\varepsilon = \frac{\beta}{2\pi}\frac{a_0}{h_f} \tag{2.58}$$

Substituting into Bruner's (1976) approximate relations for the modified self-consistent formulae for Young's modulus and Poisson ratio:

$$\frac{\bar{E}}{E} \approx e^{-\beta\frac{8}{9\pi}\frac{a_0}{h_f}} \tag{2.59a}$$

$$\frac{\bar{\nu}}{\nu} \approx e^{-\beta\frac{4}{5\pi}\frac{a_0}{h_f}} \tag{2.59b}$$

Using the standard expressions for bulk and shear moduli for linear isotropic materials, the bulk and shear moduli for the drained porous solid are:

$$B = \frac{\bar{E}}{3(1-2\bar{\nu})} \tag{2.60a}$$

$$N = \frac{\bar{E}}{2(1+\bar{\nu})} \tag{2.60b}$$

These expressions are used in the above expressions for the Biot moduli A, Q, and R, where the high-frequency effects described by O'Connel and Budiansky are neglected.

2.10.1 Minimum Porosity and Crack Density for Conduction

A constraint is imposed on the porosity to maintain conditions for fluid conduction, discussed above in Section 2.1. For a three-dimensional space, require that the mean fracture diameter, $2a_0$, exceed the diameter of the spherical volume per fracture, $\frac{1}{n}$:

$$2a_0 > \left[\frac{6}{n\pi}\right]^{1/3} \tag{2.61}$$

Using the relation for fracture porosity, $\beta = 2\pi n a_0^2 h_f$, the following minimum fracture porosity must be maintained to have a chance for fluid conduction in the fracture network:

$$\beta > \frac{3}{2}\left[\frac{h_f}{a_0}\right] \tag{2.62}$$

The minimum value of β is governed by the crack aspect ratio. For an aspect ratio of .0033, the minimum porosity required for fluid conduction is about 0.005, or 0.5%. The above are order of magnitude estimates, and should not be interpreted as preferable to estimates of critical crack lengths for supporting fracture connectivity made by Long and Witherspoon (1985) or Engelman(1983). A rule of thumb is simply proposed for limiting the fracture porosity to a finite value within the fracture zone. Below this value, the material is considered solid.

Generalizing the two-dimensional effective bond occupation number discussed above, the three dimensional effective bond occupation, ζ, is given by:

$$\zeta = \pi n (2a_0)^3 \tag{2.63}$$

An alternative expression for ζ in terms of the porosity,β, is:

$$\zeta = 4\beta\left[\frac{h_f}{a_0}\right]^{-1} \tag{2.64}$$

Using the above inequality, the effective bond occupation number must satisfy the following, as noted at the beginning of this chapter.:

$$\zeta > 6 \tag{2.65}$$

The minimum crack density parameter is simply:

$$\varepsilon > \frac{3}{4\pi} \approx .24 \tag{2.66}$$

The ratio of the crack diameter to the diameter of the specific crack spherical volume:

$$\frac{\bar{l}}{d} = \left[\frac{2\beta a_0}{3h_f}\right]^{\frac{1}{3}} = \left[\frac{\beta}{\beta_{min}}\right] \tag{2.67}$$

Again, the assumption is that this ratio must be greater than one to obtain connectivity and thus support fluid conduction.

The value of $3/(4\pi) = .24$ for crack density parameter is relatively large compared to that used for modeling shear and bulk stiffness reductions due to cracks. In fact, the range of crack density parameter used here is generally in excess of that over which the perturbation approximations employed by Salganik(1973) are applied, though within the range considered by Bruner (1976). A crack density parameter as high as 1.5 to 2 will be considered, approaching the upper limit of the range considered by Bruner. The equations employed for estimating dry cracked solid material stiffnesses may not be accurate at such large crack densities. However, an estimate of shear stiffness reduction as a function of crack density parameter, or porosity, is required to proceed, and the equations developed by Bruner are convenient for this purpose; they predict severe reduction of shear stiffness for high crack density parameter, while maintaining a finite shear stiffness, convenient for modeling. Bruner's formulae are thus used here for extrapolation of moduli to large crack density parameter.

2.11 Dissipation

The next and final constitutive coefficient to be estimated is the friction coefficient, $b(\omega)$, appearing in Biot's (1956) equations. Biot (1956) presents a simple model of fluid friction for fluid flow between two rigid plates. In the low frequency regime, parabolic flow is recovered, while above a characteristic frequency, the velocity profile of the fluid becomes planar and the attenuation rate changes character. The fluid shear strain at the boundary of the fluid region increases with frequency, resulting in greater viscous forces at the boundary, and thus greater dissipation, as well as a $\pi/4$ phase shift of fluid pressure relative to fluid velocity. For water in fractures of the order of a millimeter in width, the transition frequency is actually on the order of 1 Hz, within or below the range of seismicity associated with hydraulic fracturing. The transitional effect should, therefore, be included in a

realistic model, especially as crack apertures are reduced or viscosity is increased.

Biot's expression for the friction coefficient in the limit of zero frequency is:

$$b = \frac{3\eta\beta\zeta}{h_f^2} \tag{2.68}$$

where η is the fluid viscosity, β the porosity, $2h_f$ the fracture aperture, and ζ the sinuosity.

Biot introduces the sinuosity, ζ, analogous to the tortuosity, α, to represent the effect of a sinuous fluid flow path in producing a higher rate of energy dissipation for a given fluid discharge velocity than would be the case if the fluid were flowing uniformly in parallel, planar fractures. The calculation of sinuosity might be determined by equating the energy dissipation per unit volume in the micromechanical description to the dissipation for the macromechanical description. The result should be similar to that obtained for the tortuosity, depending primarily on the deviation of flow from rectilinear motion. For the present purposes, the sinuosity is assumed equivalent to the tortuosity.

To account for the high-frequency effects of non-Poisseuille flow within the cracks, Biot introduces an adjustment to the above expression for the friction coefficient:

$$b(\omega) = 3\beta\zeta\frac{\eta}{h_f^2}F(\kappa_1) \tag{2.69}$$

$$F(\kappa_1) = \frac{1}{3}\frac{i^{\frac{1}{2}}\kappa_1\tanh(i^{\frac{1}{2}}\kappa_1)}{1-\frac{1}{i^{\frac{1}{2}}\kappa_1}\tanh(i^{\frac{1}{2}}\kappa_1)} \tag{2.70}$$

$$\kappa_1 = h_f\left[\frac{\omega\rho_f}{\eta}\right]^{\frac{1}{2}} \tag{2.71}$$

As Biot (1956) indicates, everything happens as though the static fluid viscosity is replaced by a dynamic fluid viscosity given by $\eta F(i^{\frac{1}{2}}\kappa_1)$.

The following limits apply:

$$F(i^{\frac{1}{2}}\kappa_1) \to 1 \; ; \; \omega \to 0 \tag{2.72a}$$

$$F(i^{\frac{1}{2}}\kappa_1) \to i^{\frac{1}{2}}\frac{\kappa_1}{3} \; ; \; \omega \to \infty \tag{2.72b}$$

The above expression may be simplified considerably:

$$b(\omega) = i\omega\beta\zeta_o\rho_f \frac{1}{\frac{\kappa}{\tanh(\kappa)} - 1} \tag{2.73}$$

$$\kappa = i^{\frac{1}{2}}\kappa_1 \tag{2.74}$$

In the time domain, the form of the relation between relative fluid flow and friction is a convolution of the relative velocity with a response function describing the relaxation effects associated with relative average motion between the constituents. The Fourier transform of the above visco-dynamic operator is evidently not expressible in closed form, requiring approximate analysis at finite frequency. In the frequency domain, the complex friction coefficient simply multiplies the relative fluid velocity, as described by Biot (1956). In later papers, Biot (1961) introduces a visco-dynamic operator and describes the form of the operator in either the temporal or spectral domain.

2.12 Crack Apertures

The crack aperture, $2h_f$, appears only in the expression for the friction coefficient as the ratio of the square of the aperture to viscosity, provided that the crack aspect ratio is constant. There are three cases to consider, all of which affect only the fluid friction coefficient for constant crack aspect ratio. In one case, the number of cracks decreases with increasing porosity. An intermediate case is one where the number of cracks per unit volume is independent of porosity, consistent with an assumption that only existing cracks are expanded as a result of the fracturing process. The third case is where the number of cracks per unit volume increases with increasing porosity. Again, for constant aspect ratio, the selection influences only the fluid friction term. Examples of these conditions follow.

Assume that the crack aperture is related to porosity by:

$$h_f = h_{f0}\left[\frac{\beta}{\beta_0}\right]^{\gamma} \tag{2.75}$$

If $\gamma > 1/3$, then the number of effective cracks per unit volume decreases with increasing porosity. In particular, for $\gamma = 1$, the number of cracks per unit volume varies as:

$$n = n_0 \left[\frac{\beta_0}{\beta} \right]^2 \tag{2.76}$$

The crack aperture decreases linearly with porosity while the number of cracks per unit volume increases as the inverse of the square of the porosity, consistent with a fracture process where as higher porosities are developed, individual cracks are lengthened and combined to form larger but fewer cracks. Another possible interpretation is that of the population of cracks, only a fraction are expanded during fracturing, and these dominate fluid flow, so that fewer cracks need be considered as porosity increases.

For $\gamma = 1/3$, the second case is obtained:

$$h_f = h_{f0} \left[\frac{\beta}{\beta_{max}} \right]^{1/3} \tag{2.77}$$

A constant number of cracks per unit volume are maintained, again provided the crack aspect ratio is constant:

$$n = n_0 \tag{2.78}$$

This condition corresponds with a hydraulic fracturing process which simply expands and lengthens all existing cracks.

For $\gamma < 1/3$, the third condition is obtained. A particular example is $\gamma = 0$, in which case the number of cracks per unit volume varies in direct proportion to the porosity, requiring the creation of cracks of radius a_0 and aperture h_{f0} as porosity is increased. This condition is less attractive than the above two, since some crack size increase is expected with increasing porosity.

Though crack aspect ratio is assumed constant throughout this discussion, variation of crack aspect ratio with porosity can also be considered. This will have implications regarding the moduli, however. The crack aspect ratio is held constant and crack apertures are assumed to very as a function of porosity for reasons of modeling expediency. Moreover, the first of the above cases will be used in demonstrating the model, since it includes a relatively high rate of attenuation of the slow dilatational wave due to fluid viscosity near the edge of the fracture zone, thus representing a worst case condition with respect to detection of the slow wave.

2.12 Summary

A complete set of constitutive parameters have been developed for applying Biot's equations of motion to a fluid-saturated fractured material, using well established relationships for porous materials, subject to the reasonableness of a continuum approximation for the fracture network. One of the most noteworthy results of the above discussion is that the transition frequency discussed by Biot with respect to the departure of wave motion from non-parabolic velocity profiles within individual cracks is in the low audio or seismic range. An implication of this is that Biot's theory regarding viscous losses is particularly well suited to the problem at hand. As will be shown, the loss factors and attenuation rates for acoustic wave transmission within the fracture network are relatively low, thus supporting efficient propagation of both fast and slow dilatational waves at frequencies associated with micro-seismicity.

Slow dilatational waves are ignored in usual models of diffusive fluid flow in fractured earth materials, where rate effects are determined by fracture permeability without regard to inertial terms. There should be much information contained in the fluid pressure high-frequency responses to acoustic emission events in high-conductivity fracture networks.

Chapter 3: Boundary Value Problem and Solution

Porous matrix displacements and fluid partial stress Green's functions and associated gradients for sources within the vertically heterogeneous porous layer are computed by a reflectivity method, producing near field responses and long term solutions. The reflectivity method is a standard and well developed tool for computing seismograms for vertically heterogeneous media (Aki and Richards, 1980). Extension of the method to a porous layer is straight forward.

The general solution procedure is described below, beginning with a representation theorem for moment sources in a linear heterogeneous fluid-saturated porous material embedded in a solid. The representation theorem is derived in Appendix A, and is restated here for a separable geometry in cylindrical coordinates. The displacements and stresses are first decomposed into spectral cylindrical harmonics, equivalent to application of Hankel transforms and Fourier decomposition of azimuthal dependence. The solutions for the porous layer are represented by numerically determined propagator matrices and displacement-stress, or motion-stress, vectors. Solutions for the solid regions are represented by displacement potentials. Because of azimuthal symmetry about the vertical axis, and the assumption of vertical heterogeneity in vertical coordinate, z, the problem is decomposed into vertically polarized pressure and shear waves (PSV) and transversely polarized shear waves (SH), analogous to elastic wave propagation in vertically heterogeneous media. Boundary conditions are applied to solutions for the displacement-stress components in the porous region and potential coefficients in the solid regions.

Two methods of solution were considered. The first is more efficient, using propagators from the plane of symmetry to the layer boundaries as fundamental solutions for the layer in satisfying the boundary conditions. Unfortunately, the approach suffers from numerical precision for evanescent waves, a well known difficulty with displacement-stress propagators (Chin, et al, 1984). The second approach employs propagators over a small number of inhomogeneous layers to avoid propagating over large distances, and solving a banded matrix representing the boundary conditions between the individual layers and the solid regions. The latter approach requires more computer time, but gives good results over large vertical distances.

Load representations for the porous matrix and fluid are presented and their respective solutions are incorporated into the cylindrical vector harmonic expansions of the displacement and stress fields.

The procedure is general for any porous material described by Biot's (1956) equations of motion, so the discussion will be with respect to a general porous material rather than be restricted to fractured rock.

3.1 Representation Theorem

A representation theorem is derived in Appendix A for a fluid-saturated porous material embedded in a solid region. The displacement response, $u_k^{\alpha}(\mathbf{x})$, to concentrated moments, acting at $\mathbf{x}_0$, or point loads at acting at $\mathbf{x}_1$ are:

$$u_k^{\alpha}(\mathbf{x}) = \frac{\partial G_{k;m}^{\alpha M}(\mathbf{x}|\mathbf{x}_0)}{\partial x_{0n}} M_{mn}^{M}(\mathbf{x}_0) + \frac{\partial G_{k;m}^{\alpha F}(\mathbf{x}|\mathbf{x}_0)}{\partial x_{0m}} M^{F}(\mathbf{x}_0) \tag{3.1}$$

$$+ G_{k;m}^{\alpha M}(\mathbf{x}|\mathbf{x}_1) f_m(\mathbf{x}_1) + G_{k;m}^{\alpha F}(\mathbf{x}|\mathbf{x}_1) F_m(\mathbf{x}_1)$$

The fluid partial stress is given by:

$$s(\mathbf{x}) = M_{mn}^{M}(\mathbf{x}_0) \frac{\partial s_{;m}^{M}(\mathbf{x}|\mathbf{x}_0)}{\partial x_{0n}} + M^{F}(\mathbf{x}_0) \frac{\partial s_{;m}^{F}(\mathbf{x}|\mathbf{x}_0)}{\partial x_{0m}} \tag{3.2}$$

$$+ s_{;m}^{M}(\mathbf{x}|\mathbf{x}_1) f_m(\mathbf{x}_1) + s_{;m}^{F}(\mathbf{x}|\mathbf{x}_1) F_m(\mathbf{x}_1)$$

The superscript, α, refers to the material for which the displacement is being computed. Thus, $\alpha=M$ refers to the porous matrix, $\alpha=F$ refers to the fluid component, and $\alpha=S$ refers to the solid. The moments acting on the matrix or fluid, respectively, are $M_{mn}^{M}(\mathbf{x}_0)$ and $M^{F}(\mathbf{x}_0)$. The point loads acting on the porous matrix and fluid are, respectively, $f_m(\mathbf{x}_1)$ and $F_m(\mathbf{x}_1)$. The fluid stress Green's functions are $s_{;m}^{\alpha}(\mathbf{x}|\mathbf{x}_0)$. The source and receiver locations are illustrated in Figure 3.1.

A discussion is given in Appendix A concerning various forms that the symmetric moment may take. The moment is the fundamental source representation for any type of passive acoustic emission phenomena considered as a point source in the absence of externally applied forces and torques. Unless otherwise indicated, the term "moment" refers to a symmetric moment tensor.

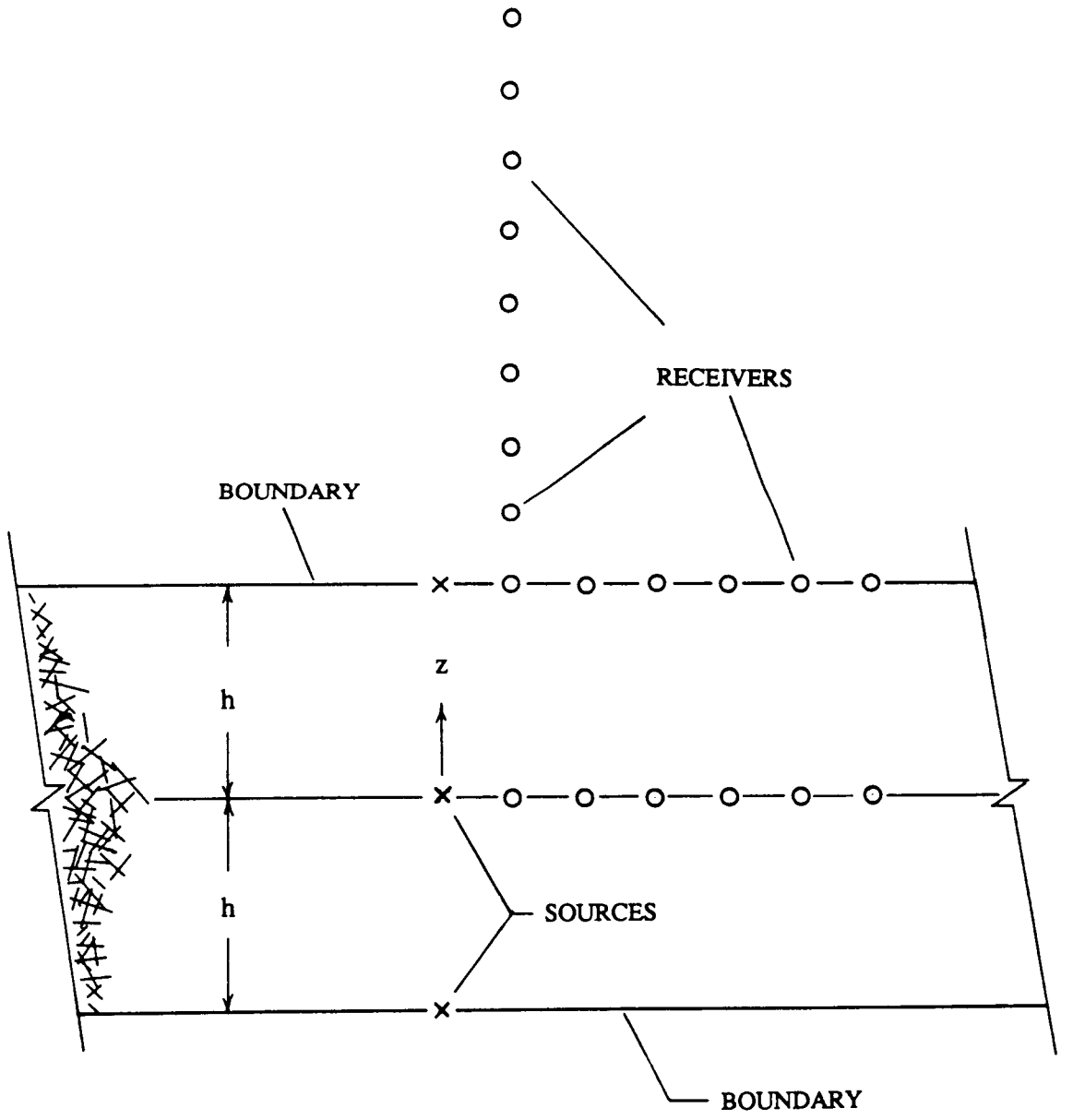

FIGURE 3.1 SOURCE AND RECEIVER LOCATIONS

3.2 Displacement-Stress Representation for the Porous Region

In Appendix B, a displacement-stress representation for a vertically heterogeneous porous layer is derived. Cylindrical harmonics and Fourier transforms with respect to time decompose Biot's (1956) equations of motion into ordinary differential equations in vertical coordinate, z. These representations are equivalent to a Hankel transform with respect to radial coordinate, r, Fourier decomposition of the azimuthal dependence, and Fourier transformation with respect to time. The result is a representation of displacements and stresses involving two sets of first-order ordinary differential equations in z; one for vertically polarized pressure and shear (PSV) waves and the other for horizontally polarized shear (SH) waves.

3.2.1 Cylindrical Harmonic Expansion

The displacements of the porous matrix and fluid are, respectively (Aki and Richards, 1980, p. 305):

$$\mathbf{u}(r,\theta,z,\omega)=\frac{1}{4\pi}\sum_{m=-\infty}^{m=+\infty}\int_0^{\infty}\Big[l_1(k,m,z,\omega)\mathbf{T}_k^m(r,\theta,\omega)+r_1(k,m,z,\omega)\mathbf{S}_k^m(r,\theta,\omega) \\ +r_2(k,m,z,\omega)\mathbf{R}_k^m(r,\theta,\omega)\Big]kdk \tag{3.3a}$$

$$U_z(r,\theta,z,\omega)\hat{z}=\frac{1}{4\pi}\sum_{m=-\infty}^{m=+\infty}\int_0^{\infty}s_1(k,m,z,\omega)\mathbf{R}_k^m(r,\theta,\omega)kdk \tag{3.3b}$$

The partial tractions associated with the porous matrix and fluid and acting on a horizontal plane perpendicular to the z-axis are, respectively:

$$\mathbf{T}(r,\theta,z,\omega)=\frac{1}{4\pi}\sum_{m=-\infty}^{m=+\infty}\int_0^{\infty}\Big[l_2(k,m,z,\omega)\mathbf{T}_k^m(r,\theta,\omega)+r_3(k,m,z,\omega)\mathbf{S}_k^m(r,\theta,\omega) \\ +r_4(k,m,z,\omega)\mathbf{R}_k^m(r,\theta,\omega)\Big]kdk \tag{3.4a}$$

$$\mathbf{S}(r,\theta,z,\omega)=s(r,\theta,z,\omega)\hat{z}=\frac{1}{4\pi}\sum_{m=-\infty}^{m=+\infty}\int_0^{\infty}s_2(k,m,z,\omega)\mathbf{R}_k^m(r,\theta,\omega)kdk \tag{3.4b}$$

The cylindrical vector harmonics appearing above are:

$$\mathbf{T}_k^m(r,\theta) = \frac{1}{kr}\frac{\partial Y_k^m(r,\theta)}{\partial \theta}\hat{\mathbf{r}} - \frac{1}{k}\frac{\partial Y_k^m(r,\theta)}{\partial r}\hat{\boldsymbol{\theta}} \tag{3.5a}$$

$$\mathbf{S}_k^m(r,\theta) = \frac{1}{k}\frac{\partial Y_k^m(r,\theta)}{\partial r}\hat{\mathbf{r}} + \frac{1}{kr}\frac{\partial Y_k^m(r,\theta)}{\partial \theta}\hat{\boldsymbol{\theta}} \tag{3.5b}$$

$$\mathbf{R}_k^m(r,\theta) = -Y_k^m(r,\theta)\hat{\mathbf{z}} \tag{3.5c}$$

where Y_k^m is the scalar cylindrical harmonic given by:

$$Y_k^m(r,\theta) = J_m(kr)e^{im\theta} \tag{3.6}$$

and $J_m(kr)$ are the Bessel functions of the first kind of order m with radial wavenumber k.

Only the vertical component of fluid displacement is needed because fluid partial shear stresses are not included, and transverse displacements of the fluid need not satisfy boundary conditions. Transverse displacements are determined, however, by the equations of motion at finite frequency. Similarly, only the normal fluid partial stress is represented, since fluid shear stresses are nonexistent in Biot's equations.

The fluid isotropic stress is thus conveniently represented by a vertical component of a displacement-stress vector, as is the normal partial stress associated with the porous matrix. Because the fluid partial stress is directly related to the divergence of the porous matrix and fluid displacements, propagation of fluid stress is equivalent to propagation of the coupled divergences of the matrix and fluid.

3.2.2 Propagator Matrices

The coefficients multiplying the cylindrical vector harmonics are components of the displacement-stress vectors for the PSV and SH problems:

$$\mathbf{v}^{PSV}(k,m,z,\omega)=\begin{Bmatrix} r_1 \\ r_2 \\ r_3 \\ r_4 \\ s_1 \\ s_2 \end{Bmatrix} \tag{3.7a}$$

$$\mathbf{v}^{SH}(k,m,z,\omega)=\begin{Bmatrix} l_1 \\ l_2 \end{Bmatrix} \tag{3.7b}$$

The displacement-stress vectors satisfy two sets of first order differential equations in z; one for the PSV problem, the other for the SH problem. In matrix form:

$$\frac{\partial \mathbf{v}(k,m,z,\omega)}{\partial z}=\mathbf{A}(k,z,\omega)\mathbf{v}(k,m,z,\omega) \tag{3.8}$$

The matrix, **A**, is of order 6 for the PSV problem and order 2 for the SH problem. The matrix elements are derived in Appendix B. For the PSV problem, the matrix $\mathbf{A}^{PSV}(z)$ is:

$$\mathbf{A}^{PSV}(z)= \tag{3.9a}$$

$$\begin{bmatrix}
0 & k & \frac{1}{N} & 0 & 0 & 0 \\
-\frac{(RA-Q^2)}{K^2}k & 0 & 0 & \frac{R}{K^2} & 0 & \frac{-Q}{K^2} \\
4Nk^2\frac{R(A+N)-Q^2}{K^2}-\frac{\omega^2}{\tilde{\rho}_{22}}\tilde{\rho}^2 & 0 & 0 & \frac{(RA-Q^2)}{K^2}k & 0 & \left[\frac{2NQ}{K^2}-\frac{\tilde{\rho}_{12}}{\tilde{\rho}_{22}}\right]k \\
0 & -\omega^2\tilde{\rho}_{11} & -k & 0 & -\omega^2\tilde{\rho}_{12} & 0 \\
\left[\frac{\tilde{\rho}_{12}}{\tilde{\rho}_{22}}-\frac{2NQ}{K^2}\right]k & 0 & 0 & -\frac{Q}{K^2} & 0 & \left[\frac{A+2N}{K^2}-\frac{k^2}{\omega^2\tilde{\rho}_{22}}\right] \\
0 & -\omega^2\tilde{\rho}_{12} & 0 & 0 & -\omega^2\tilde{\rho}_{22} & 0
\end{bmatrix}$$

The matrix $\mathbf{A}^{SH}(z)$ is:

$$\mathbf{A}^{SH}(z) = \begin{bmatrix} 0 & Nk^2 - \dfrac{\omega^2}{\tilde{\rho}_{22}}\tilde{\rho}^2 \\ \dfrac{1}{N} & 0 \end{bmatrix} \tag{3.9b}$$

In the above:

$$K^2 = R(A+2N) - Q^2 \tag{3.10}$$

and

$$\tilde{\rho}^2 = \tilde{\rho}_{11}\tilde{\rho}_{22} - \tilde{\rho}_{12}^2 \tag{3.11}$$

The moduli N, A, R, and Q, and the visco-dynamic "densities", $\tilde{\rho}_{\alpha\beta}$, are functions of vertical coordinate, z, and radian frequency, ω, and are discussed in Chapter 2, and Appendix B.

Propagators, $\mathbf{P}(z, z_0)$, map the displacement-stress vectors at z_0 to displacement-stress vectors at z. Thus:

$$\mathbf{v}(k, m, z, \omega) = \mathbf{P}(z, z_0)\mathbf{v}(k, m, z_0, \omega) \tag{3.12}$$

The propagators satisfy the same differential equations as do the displacement stress vectors:

$$\frac{\partial \mathbf{P}(k, z, \omega)}{\partial z} = \mathbf{A}(k, z, \omega)\mathbf{P}(k, z, \omega) \tag{3.13}$$

and satisfy the following relations:

$$\mathbf{P}(z_2, z_1)\mathbf{P}(z_1, z_0) = \mathbf{P}(z_2, z_0) \tag{3.14a}$$

$$\mathbf{P}(z, z_0)\mathbf{P}(z_0, z) = \mathbf{P}(z, z) = \mathbf{I} \tag{3.14b}$$

The propagators are computed by integrating the above differential equation from z_1 to z_2 with the unit matrix as an initial condition. For isotropic materials and azimuthally symmetric geometries, neither the propagator nor the matrix **A** depend on azimuthal harmonic mode number, m. The propagators are fundamental solutions for the porous layer, analogous to sine and cosine solutions for a homogeneous elastic layer. The solutions to the boundary value problem are thus obtained by solving a set of initial value problems in vertical coordinate, z.

3.2.3 General Solution

A general solution for the displacements and stresses within the porous region is a superposition of a solution to the homogeneous problem (source-free) with a particular integral resulting from a stress discontinuity at the source plane. In one approach, the source-free solutions are represented by the displacements and stresses at the central plane of symmetry. These are "propagated" to the layer edges where they are superposed with solutions representing displacement discontinuities (inhomogeneous terms) to satisfy boundary conditions. The general solution is thus:

$$\mathbf{v}(z) = \mathbf{v}_H(z) + \mathbf{v}_I(z) \tag{3.15}$$

The particular integral represents a wave incident on the boundary between the porous and solid regions. The reflected and transmitted waves are the "source-free" waves, represented by the solutions to the homogeneous differential equations for the respective porous and solid regions. By combining the particular integral, or incident wave, with the source-free solution, the boundary conditions between the porous and elastic regions can be satisfied.

The source-free displacement-stress vector solutions for the porous region are given by:

$$\mathbf{v}_H^{PSV}(k,m,z,\omega) = \mathbf{P}^{PSV}(z,0)\mathbf{v}_{H0}^{PSV}(k,m,\omega) \tag{3.16a}$$

$$\mathbf{v}_H^{SH}(k,m,z,\omega) = \mathbf{P}^{SH}(z,0)\mathbf{v}_{H0}^{SH}(k,m,\omega) \tag{3.16b}$$

where

$$\mathbf{v}_{H0}^{PSV}(k,m,\omega) = \mathbf{v}_H^{PSV}(k,m,0,\omega) \tag{3.17a}$$

$$\mathbf{v}_{H0}^{SH}(k,m,\omega) = \mathbf{v}_H^{SH}(k,m,0,\omega) \tag{3.17b}$$

The components of vectors $\mathbf{v}_{H0}^{PSV}$ and $\mathbf{v}_{H0}^{SH}$ comprise a total of 8 coefficients: 6 for the PSV problem and 2 for the SH problem. The coefficients are in general functions of k, m, and ω, and are determined by satisfaction of boundary conditions with the source solutions, or particular integrals.

The particular integrals for the porous region are developed by specifying a discontinuity in the displacement-stress vector at the source location, $z = z_0$. For $z < z_0$, the displacements and stresses are set to zero. For $z > z_0$, the displacement-stress components are given by the propagators:

$$\mathbf{v}_I^{PSV}(z) = \mathbf{P}^{PSV}(z,z_0)\mathbf{q}^{PSV}(z_0) \tag{3.18a}$$

$$\mathbf{v}_l^{SH}(z) = \mathbf{P}^{SH}(z, z_0)\mathbf{q}^{SH}(z_0) \tag{3.18b}$$

The particular integral at the same plane as the source, $z = z_0$, is simply one half the stress discontinuity.

By appropriate specification of the discontinuity, Green's functions or their gradients are determined. In general, there may be a displacement-stress vector discontinuity for each harmonic mode number m and for each wavenumber k. For point loads acting in a vertically heterogeneous and isotropic material such as considered here, only the values of $m = \pm 1$ and $m = 0$ are required; the displacement-stress discontinuities are zero for all other values of m, as discussed below with respect to construction of the Green's functions.

3.2.4 Hybrid Multiple Layer Solution Method

When propagating over large distances, the above single layer approach suffers from lack of numerical precision in the presence of evanescent waves. To remove this problem without excessive reformulation, propagators are numerically computed for a set of sublayers, and then substituted into a banded matrix representing the boundary conditions between each of the layers. Stress discontinuities represented by inhomogeneous terms in the banded matrix equation are introduced at a given sublayer boundary. The coefficients are determined by Gaussian elimination and back substitution. Smoothly varying velocity profiles are maintained in the model, using a total of perhaps 10 to 20 layers.

Whether or not the hybrid approach is preferable to use of, for example, 1000 homogeneous layers and conventional reflectivity solution procedures involving propagator matrices for up and down going waves (Kennett, 1983) has not been determined. The procedure appears to be efficient for smoothly varying velocity profiles. For large homogeneous regions, propagating up- and down-going waves and solving by one of various matrix manipulation methods would be more appropriate than numerical integration of the displacement stress problem. (See Chin, et. al., 1984, for a comparison of various matrix reflectivity methods) The multiple layer hybrid method is the approach eventually selected for use here. Furthermore, the procedure may be competitive with conventional matrix methods for computing synthetic seismograms for anisotropic vertically heterogeneous solids.

Chin points out that Gaussian elimination and back substitution techniques (applied to tridiagonal systems of 2x2 matrices) are closely related or equivalent to invariant embedding procedures (Meyer,

1973). There is evidently a deep and fascinating relationship between matrix methods, Gaussian elimination, and invariant embedding (involving Ricatti transformations and initial value methods) procedures for solving ordinary differential equations.

3.3 Representation of Semi-Infinite Solid Regions

The semi-infinite solid regions are assumed to be homogeneous isotropic visco-elastic solids with complex Lamé parameters λ and μ. Complex Lamé parameters are incorporated to simplify numerical integration of the Hankel transform inversions beyond the branch points and poles which would otherwise be located on the real axis of the complex wave-number plane. The displacements for the solid are expressed as gradients of the potentials (Harkrider, 1964): $\phi(\mathbf{x},\omega)$, $\Psi(\mathbf{x},\omega)$, and $\chi(\mathbf{x},\omega)$:

$$\mathbf{u}^S(\mathbf{x},\omega) = \nabla\phi(\mathbf{x},\omega) + \nabla\times\nabla\times\Psi(\mathbf{x},\omega) + \nabla\times\chi(\mathbf{x},\omega) \tag{3.19}$$

where

$$\Psi(\mathbf{x},\omega) = \psi(\mathbf{x},\omega)\hat{\mathbf{z}} \tag{3.20a}$$

and

$$\chi(\mathbf{x},\omega) = \chi(\mathbf{x},\omega)\hat{\mathbf{z}} \tag{3.20b}$$

The scalar potentials ϕ, ψ, and χ satisfy the Helmholtz wave equations:

$$(\lambda+2\mu)\nabla^2\phi(\mathbf{x},\omega) = -\rho_s\omega^2\phi(\mathbf{x},\omega) \tag{3.21a}$$

$$\mu\nabla^2\psi(\mathbf{x},\omega) = -\rho_s\omega^2\psi(\mathbf{x},\omega) \tag{3.21b}$$

$$\mu\nabla^2\chi(\mathbf{x},\omega) = -\rho_s\omega^2\chi(\mathbf{x},\omega) \tag{3.21c}$$

Solutions for the scalar potentials are:

$$\phi(\mathbf{x},\omega) = \frac{1}{4\pi}\sum_{m=-\pi}^{m=+\pi}\int_0^{+\infty}\left\{A^+e^{-\zeta_p z} + A^-e^{+\zeta_p z}\right\}Y_k^m(r,\theta)kdk \tag{3.22a}$$

$$\psi(\mathbf{x},\omega) = \frac{1}{4\pi}\sum_{m=-\pi}^{m=+\pi}\int_0^{+\infty}\left\{B^+e^{-\zeta_s z} + B^-e^{+\zeta_s z}\right\}Y_k^m(r,\theta)kdk \tag{3.22b}$$

$$\chi(\mathbf{x},\omega) = \frac{1}{4\pi}\sum_{m=-\pi}^{m=+\pi}\int_0^{+\infty}\left\{C^+e^{-\zeta_s z} + C^-e^{+\zeta_s z}\right\}Y_k^m(r,\theta)kdk \tag{3.22c}$$

where $Y_k^m(r,\theta)$ is the cylindrical harmonic defined above regarding the displacement-stress representation for the porous region:

$$Y_k^m(r,\theta) = e^{im\theta} J_m(kr) \tag{3.6}$$

The spectral solutions for the solid region are represented by Hankel inverse transforms and Fourier sums over m.

The vertical wavenumbers, ζ_p and ζ_s are given by the principal branches:

$$\zeta_p = \sqrt{k^2 - k_p^2} \tag{3.23a}$$

$$\zeta_s = \sqrt{k^2 - k_s^2} \tag{3.23b}$$

where:

$$k_p = \frac{\omega}{c_p} \tag{3.24a}$$

$$k_s = \frac{\omega}{c_s} \tag{3.24b}$$

The parameters c_p and c_s are complex velocities of propagation for dilatation and shear waves, respectively. The complex Lamé parameters are related to the complex velocities by:

$$c_s(\omega) = \sqrt{\frac{\mu(\omega)}{\rho}} \tag{3.25a}$$

$$c_p(\omega) = \sqrt{\frac{\lambda(\omega) + 2\mu(\omega)}{\rho}} \tag{3.25b}$$

The complex Lamé parameters used for the solid region were set to the equivalent parameters for the porous matrix at the edge of the layer to provide a smooth transition for the "fast" pressure wave and the shear wave in propagating from the porous layer to the solid region. The equivalent parameters were evaluated by constraining the fluid displacement to equal the solid displacement at the boundary, thus simulating a non-conductive condition for the fluid, and the transition from a porous material to a solid material. The relations are:

$$\lambda(\omega) = A(\pm h,\omega) + 2N(\pm h,\omega) + 2Q(\pm h,\omega) + R(\pm h,\omega) \tag{3.26a}$$

$$\mu(\omega) = N(\pm h,\omega) \tag{3.26b}$$

where A, N, Q, and R, are the Biot moduli discussed above.

Dispersion is incorporated into the compression and shear wave velocities for the solid material making up the porous matrix to displace branch points and poles away from the real axis of the complex wavenumber plane during evaluation of the Hankel inversion integrals. The frequency dependence does not involve effects due to fluid viscosity, but enters the Biot parameters via the the complex velocity dispersion introduced into the prescription for the Lamé parameters of the solid material. The solid region velocity dispersion is equivalent to that of the solid material making up the porous region.

3.3.1 Radiation Conditions

To obtain bounded solutions for all values of k, A^-, B^-, and C^- are set to zero for $z \geq +h$, and A^+, B^+, and C^+ are set to zero for $z \leq -h$. These selections represent branch cuts with branch points $\pm k_s$, and $\pm k_p$. For the elastic case, the branch points are on the real axis, and the branch cuts follow the real axis from the branch point to the origin, and from there follow the imaginary axis to $\pm\infty$. If the Lamé parameters, λ and μ, are complex, the branch points are depressed away from the real axis, bypassing the origin. As illustrated in Figure 3.2, the branch points in the right-half plane descend into the fourth quadrant, while the branch points in the left hand plane rise from the real axis into the second quadrant. The branch cuts bypass the origin and do not cross either the real or imaginary axes but approach the imaginary axis asymptotically. Therefore, with slightly complex Lamé parameters, the Hankel transform inversions can be computed numerically by following the real axis without directly encountering singularities. With the above branch selections, the solutions remain bounded for arbitrary kz, yielding at most a homogeneous wave for wavenumber k lying on the branch line. (A discussion of the contour of integration is presented in Chapter 4, Section 4.3.2, regarding Hankel inversion procedures.)

3.3.2 Displacement-Stress Representation for the Solid Region

The displacements and stresses for the solid region are expressed as components of PSV and SH displacement-stress vectors, analogous to those for the displacements and partial stresses associated with the porous matrix. Transformation formulae between the displacement-stress components for the solid region and the displacement potential coefficients are determined by comparing the integral

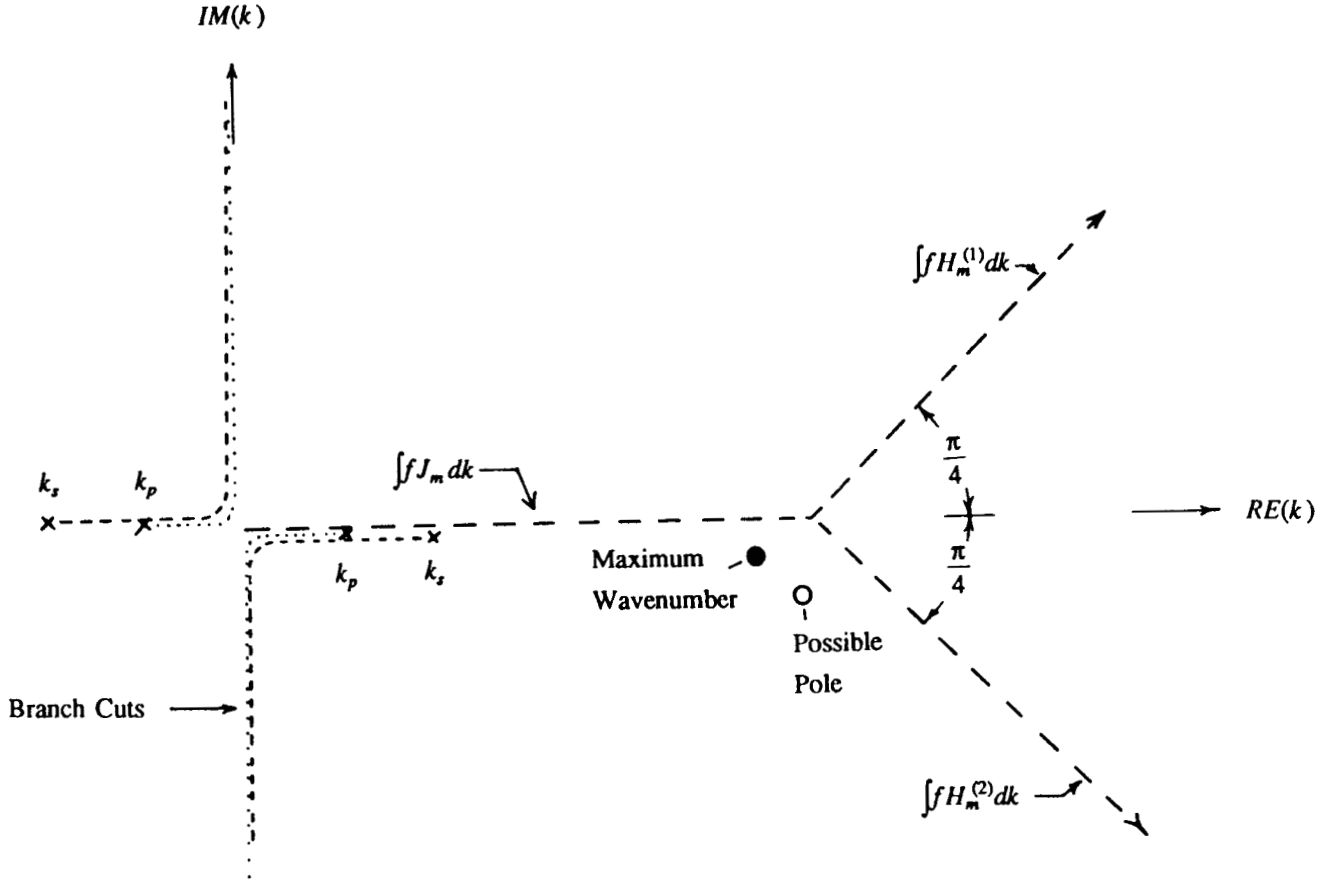

FIGURE 3.2 SPLIT CONTOUR AND BRANCH CUTS

expressions for the displacements and stresses in the potential representation with those in the displacement-stress representation. The following relations are obtained for $z>+h$:

$$l_1(z)=kC^+e^{-\zeta_s z} \tag{3.27a}$$

$$l_2(z)=-k\mu\zeta_s C^+e^{-\zeta_s z} \tag{3.27b}$$

$$r_1(z)=kA^+e^{-\zeta_p z}-k\zeta_s B^+e^{-\zeta_s z} \tag{3.27c}$$

$$r_2(z)=+\zeta_p A^+e^{-\zeta_p z}-k^2B^+e^{-\zeta_s z} \tag{3.27d}$$

$$r_3(z)=-k2\mu\zeta_p A^+e^{-\zeta_p z}+k\mu(2k^2-k_s^2)B^+e^{-\zeta_s z} \tag{3.27e}$$

$$r_4(z)=-\mu(2k^2-k_s^2)A^+e^{-\zeta_p z}+2\mu k^2\zeta_s B^+e^{-\zeta_s z} \tag{3.27f}$$

Similar expressions are obtained for the region $z<-h$:

$$l_1(z)=kC^-e^{+\zeta_s z} \tag{3.28a}$$

$$l_2(z)=+k\mu\zeta_s C^-e^{+\zeta_s z} \tag{3.28b}$$

$$r_1(z)=kA^-e^{+\zeta_p z}+k\zeta_s B^-e^{+\zeta_s z} \tag{3.28c}$$

$$r_2(z)=-\zeta_p A^-e^{+\zeta_p z}-k^2B^-e^{+\zeta_s z} \tag{3.28d}$$

$$r_3(z)=+k\mu2\zeta_p A^-e^{+\zeta_p z}+k\mu(2k^2-k_s^2)B^-e^{+\zeta_s z} \tag{3.28e}$$

$$r_4(z)=-\mu(2k_s^2-k^2)A^-e^{+\zeta_p z}-2\mu k^2\zeta_s B^-e^{+\zeta_s z} \tag{3.28f}$$

Except for the factor k multiplying $B^{\pm}$ and $C^{\pm}$, and differences in sign convention, these expressions are equivalent to expressions given by Aki and Richards (1980) for the displacement-stress vector components of up- and down-going components of compression and shear waves.

3.4 Boundary Conditions

General boundary conditions between porous and solid regions are discussed in Appendix A. These boundary conditions are restated here for the case of horizontal plane boundaries, perpendicular to the z -axis, where the unsuperscripted field quantities are assigned to the porous material and those with the superscript, S, to the solid material:

(1) Continuity of porous matrix displacements with solid region displacements:

$$\mathbf{u}(r,\theta,\pm h,\omega)=\mathbf{u}^S(r,\theta,\pm h,\omega) \tag{3.29a}$$

(2) Balance of total tractions acting on the porous region with the traction acting on the solid region:

$$\mathbf{T}(r,\theta,\pm h,\omega)+\mathbf{S}(r,\theta,\pm h,\omega)+\mathbf{T}^S(r,\theta,+/-h,\omega)=0 \tag{3.29b}$$

(3) Zero fluid injection normal to the boundary:

$$U_z(r,\theta,\pm h,\omega)-u_z(r,\theta,\pm h,\omega)=0 \tag{3.29c}$$

By expressing these boundary conditions in terms of the displacement-stress components for the porous and solid regions, the following boundary conditions are obtained for the displacement-stress components at $z=\pm h$, where, again, the superscript, S, refers to the solid region displacement-stress vector components.

For the SH problem:

$$l_1=l_1^S \tag{3.30a}$$

$$l_2=l_2^S \tag{3.30b}$$

For the PSV problem:

$$r_1=r_1^S \tag{3.31a}$$

$$r_2=r_2^S \tag{3.31b}$$

$$r_3=r_3^S \tag{3.31c}$$

$$r_4+s_2=r_4^S \tag{3.31d}$$

$$r_2-s_1=0 \tag{3.31e}$$

For problems involving a single porous layer, the above boundary conditions between the displacement stress vectors for the porous and solid regions provide a total of fourteen relations, seven for the upper boundary at $z=h$ and seven for the lower boundary at $z=-h$, determining eight coefficients for the porous region, representing the six components of the PSV displacement stress vector and the two components of the SH displacement stress vector at the central plane, $z=0$, and six potential

coefficients for the elastic regions; three for the region $z \geq +h$ and three for the region $z \leq -h$. The displacement potential coefficients are determined along with the porous region displacement-stress vector components.

For the hybrid solution procedure employing sub-layers for the porous region, additional boundary conditions are incorporated at each intermediate boundary. These conditions are simply continuity of the displacement stress components across the intermediate boundary in the absence of a stress discontinuity due to applied load. Thus, for each intermediate boundary, an additional eight equations are obtained, sufficient to solve for the additional eight displacement stress components arising for each additional porous layer.

3.5 Hankel Inversion and Fourier Summation

Once the displacement-stress components and potential coefficients are determined for a given value of ω and k, they are substituted into Hankel transform inversion formulae to obtain spectral responses at arbitrary radial distance, r, and vertical position, z. For uniformity in computation, the displacement-stress representation is used in forming the Green's functions for the solid regions as well as the porous region, employing a simple transformation between the two representations.

3.5.1 Displacement Components and Fluid Partial Stress

The components of the displacements of the porous matrix or solid region are expressed in terms of the displacement-stress vector components by contracting the vector expressions for displacements (Equation 3.3a) with the respective unit vector:

$$u_r(r,\theta,z,\omega) = \frac{1}{2\pi}\sum_{m=-\infty}^{m=+\infty} e^{im\theta}\int_0^{\infty}\left[l_1(k,m,z,\omega)\frac{im}{kr}J_m(kr) + r_1(k,m,z,\omega)\frac{1}{k}\frac{\partial J_m(kr)}{\partial r}\right]kdk \quad (3.31a)$$

$$u_\theta(r,\theta,z,\omega) = -\frac{1}{2\pi}\sum_{m=-\infty}^{m=+\infty} e^{im\theta}\int_0^{\infty}\left[l_1(k,m,z,\omega)\frac{1}{k}\frac{\partial J_m(kr)}{\partial r} - r_1(k,m,z,\omega)\frac{im}{kr}J_m(kr)\right]kdk \quad (3.31b)$$

$$u_z(r,\theta,z,\omega) = -\frac{1}{2\pi}\sum_{m=-\infty}^{m=+\infty} e^{im\theta}\int_0^{\infty} r_2(k,m,z,\omega)J_m(kr)kdk \quad (3.31c)$$

The normal fluid isotropic partial stress is given by:

$$s(r,\theta,z,\omega)=\frac{-1}{2\pi}\sum_{m=-\infty}^{m=+\infty}e^{im\theta}\int_0^{\infty}s_2(k,m,z,\omega)J_m(kr)kdk \tag{3.32}$$

Expansions can be obtained for the fluid vertical displacement or matrix stresses by similar means.

3.5.2 Point Load Representation

The specification of appropriate point loads for the displacement-stress representation is well described by Aki and Richards (1980, p. 309) for the case of loads applied to a solid. Briefly, the stress discontinuities due to radial, transverse, and vertical point loads are expanded in vector cylindrical harmonics, with F_T, F_S, and F_R components. The corresponding terms in the expansion couple with corresponding terms in the displacement-stress representation, subject to the orthogonality relations between the vector cylindrical harmonic functions.

The stress traction discontinuity associated with a point load acting on the porous matrix across a plane, $z = z_0$, is:

$$\mathbf{T}(z_0+)-\mathbf{T}(z_0-)=-\mathbf{F}(z_0) \tag{3.33}$$

Writing the traction discontinuity as

$$\mathbf{T}(z_0+)-\mathbf{T}(z_0-)= \tag{3.34}$$

$$\frac{1}{2\pi}\sum_m\int_0^{\infty}[F_T\mathbf{T}_k^m(r,\theta)+F_S\mathbf{S}_k^m(r,\theta)+F_R\mathbf{R}_k^m(r,\theta)]kdk \tag{3.35}$$

and employing the orthogonality relation

$$\int_0^{2\pi}d\theta\int_0^{\infty}\mathbf{T}_k^{m'}(r,\theta)\mathbf{T}^*{}_k^m(r,\theta)rdr=\frac{2\pi\delta(k-k')\delta_{mm'}}{\sqrt{kk'}} \tag{3.36}$$

and similar rel,θ), $_k^m$ $_k^m$ Aki and Richards obtain the following result:

$$F_T(k,\pm1)=\frac{1}{2}(+iF_x\pm F_y) \tag{3.37a}$$

$$F_S(k,\pm1)=\frac{1}{2}(\mp F_x+iF_y) \tag{3.37b}$$

$$F_R(k,0)=F_z \tag{3.37c}$$

Using their results and transformations between cylindrical and Cartesian coordinates, the following transformation is derived between the load components in the cylindrical harmonic expansion and the physical components in cylindrical coordinates.

$$F_T(k,\pm 1,z_0;\omega)=\frac{1}{2}e^{\mp i\theta}\left[iF_r\pm F_\theta\right] \tag{3.38a}$$

$$F_S(k,\pm 1,z_0;\omega)=\frac{1}{2}e^{\mp i\theta}\left[\mp F_r+iF_\theta\right] \tag{3.38b}$$

$$F_R(k,0,z_0,\omega)=F_z \tag{3.38c}$$

All other F_T, F_S, and F_R are zero.

When calculating the Green's functions, stress discontinuities $[r_i]=r_i(z_0+)-r_i(z_0-)$ are set to $+1$, rather than -1, a consequence of incorporating the minus sign in the above formula for the traction discontinuity. The minus sign is included in the representations for F_r, F_θ, and F_z.

The following holds for the displacement-stress component responses to the load components F_T, F_S, and F_R, applied to the porous matrix:

$$l_1(k,m,z,\omega)=l_1^T(k,z,\omega;z_0)F_T(k,m,z_0,\omega) \tag{3.39a}$$

$$r_1(k,m,z,\omega)=r_1^S(k,z,\omega;z_0)F_S(k,m,z_0,\omega)+r_1^R(k,z,\omega;z_0)F_R(k,m,z_0,\omega) \tag{3.39b}$$

$$r_2(k,m,z,\omega)=r_2^S(k,z,\omega;z_0)F_S(k,m,z_0,\omega)+r_2^R(k,z,\omega;z_0)F_R(k,m,z_0,\omega) \tag{3.39c}$$

$$s_2(k,m,z,\omega)=s_2^S(k,z,\omega;z_0)F_S(k,m,z_0,\omega)+s_2^R(k,z,\omega;z_0)F_R(k,m,z_0,\omega) \tag{3.39d}$$

The azimuthal mode number, m, does not appear in the response functions l_1^T, r_1^S, etc., a consequence of isotropy and azimuthal symmetry.

The Green's functions for radial, transverse, and vertical point loads are determined by decomposing the displacement-stress vector components into responses for each respective load, and identifying the appropriate Green's function by inspection.

Point loads acting on the fluid admit the same expansion as given above. The vertical component of a point load acting on the fluid gives a discontinuity in the normal partial stress associated with the fluid. Horizontal loads are less easily represented, and appear as traction discontinuities acting on the porous matrix with a coefficient representing the "drag" of the fluid on the porous matrix. An

additional term also appears as a discontinuity of vertical fluid displacement for the PSV case. The representation also fails at zero frequency, a consequence of lack of fluid shear. The application of fluid loads is guided by inspection of the first-order set of displacement-stress differential equations, derived in Appendix B. Thus, the fluid load components give the following discontinuities:

$$l_2(z_0+)-l_2(z_0-)=F_T^F \tag{3.40a}$$

$$r_3(z_0+)-r_3(z_0-)=-\frac{\tilde{\rho}_{12}(z_0,\omega)}{\tilde{\rho}_{22}(z_0,\omega)}F_S^F \tag{3.40b}$$

$$s_1(z_0+)-s_1(z_0-)=-\frac{k}{\omega^2\tilde{\rho}_{22}(z_0,\omega)}F_S^F \tag{3.40c}$$

$$s_2(z_0+)-s_2(z_0-)=F_R^F \tag{3.40d}$$

The superscript, F, indicates that the load is applied to the fluid.

The specification of point loads acting on the fluid is discussed in detail in Chapter 4, regarding numerical implementation.

3.5.3 Point Load Green's Functions

Substituting the expressions for the components of the point loads into the above, carrying out the lengthy algebra, and identifying the Green's functions for the various unit loads as the terms multiplying each of the F_r, F_θ, and F_z, expressions for the Green's functions in cylindrical coordinates are obtained.

The Green's functions for point loads applied at $r=0$ are presented first. The first subscript refers to the physical component of displacement in cylindrical coordinates. The second subscript following the semi-colon refers to the physical component of the point load, again in cylindrical coordinates. Thus, the radial component of the displacement Green tensor at r, θ, and z, due to a radially directed unit point load is:

$$G^{\alpha}_{r;r}(r,z,\omega|z_0)=-\frac{1}{2\pi}\int_0^{\infty}\left[l_1^{T\alpha}\frac{1}{kr}J_1(kr)+r_1^{S\alpha}\frac{1}{k}\frac{\partial J_1(kr)}{\partial r}\right]kdk \tag{3.41a}$$

Continuing:

$$G^{\alpha}_{r;\theta}(r,z,\omega|z_0)=0 \tag{3.41b}$$

$$G^{\alpha}_{r;z}(r,z,\omega|z_0)=\frac{1}{2\pi}\int_0^{\infty} r_1^{R\alpha}\frac{\partial J_0(kr)}{\partial r}dk \tag{3.41c}$$

$$G^{\alpha}_{\theta;r}(r,z,\omega|z_0)=0 \tag{3.41d}$$

$$G^{\alpha}_{\theta;\theta}(r,z,\omega|z_0)=\frac{-1}{2\pi}\int_0^{\infty}\left[l_1^{T\alpha}\frac{\partial J_1(kr)}{\partial r}+\frac{1}{r}r_1^{S\alpha}J_1(kr)\right]dk \tag{3.41e}$$

$$G^{\alpha}_{\theta;z}(r,z,\omega|z_0)=0 \tag{3.41f}$$

$$G^{\alpha}_{z;r}(r,z,\omega|z_0)=\frac{1}{2\pi}\int_0^{\infty} r_2^{S\alpha}J_1(kr)kdk \tag{3.41g}$$

$$G^{\alpha}_{z;\theta}(r,z,\omega|z_0)=0 \tag{3.41h}$$

$$G^{\alpha}_{z;z}(r,z,\omega|z_0)=\frac{-1}{2\pi}\int_0^{\infty} r_2^{R\alpha}J_0(kr)kdk \tag{3.41i}$$

The fluid Green partial stresses are:

$$s^{G\alpha}_{;r}(r,z,\omega|z_0)=\frac{1}{2\pi}\int_0^{\infty} s_2^{S\alpha}J_1(kr)kdk \tag{3.42a}$$

$$s^{G\alpha}_{;\theta}(r,z,\omega|z_0)=0 \tag{3.42b}$$

$$s^{G\alpha}_{;z}(r,z,\omega|z_0)=\frac{-1}{2\pi}\int_0^{\infty} s_2^{R\alpha}J_0(kr)kdk \tag{3.42c}$$

The superscript, α, indicates whether the load is applied to the matrix ($\alpha=M$) or to the fluid ($\alpha=F$). These formulae for the displacement response apply to either the porous matrix or the solid region, by appropriate choice of the displacement-stress components. That is, the Green's functions for the solid regions are obtained by substituting the potential coefficients into the expressions for the displacement-stress vector, and using the above relations.

An important feature of the form of the Green's functions in cylindrical coordinates for azimuthal symmetry is that they do not have azimuthal dependence, thus simplifying their representation. The Green's functions in Cartesian coordinates may be obtained from the Green's functions in cylindrical coordinates by a tensor transformation.

Identities between the Bessel functions and their derivatives are used to cast the formulas into a form for numerical integration. These identities are:

$$\xi \frac{d}{d\xi} J_m(\xi) + m J_m(\xi) = \xi J_{m-1}(\xi) \tag{3.43a}$$

$$\xi \frac{d}{d\xi} J_m(\xi) - m J_m(\xi) = -\xi J_{m+1}(\xi) \tag{3.43b}$$

Using these identities, and extracting a factor of $\frac{1}{r^2}$, the following integrals for the non-trivial Green's functions are obtained, where $\xi = kr$:

$$G^{\alpha}_{r;r}(r,z,\omega|z_0) = -\frac{1}{2\pi r^2}\int_0^{\infty}\left[l_1^{T\alpha}\frac{1}{\xi}J_1(\xi) + r_1^{S\alpha}\left[J_0(\xi) - \frac{1}{\xi}J_1(\xi)\right]\right]\xi d\xi \tag{3.44a}$$

$$G^{\alpha}_{r;z}(r,z,\omega|z_0) = \frac{1}{2\pi r^2}\int_0^{\infty} r_1^{R\alpha}\left[\frac{1}{\xi}J_0(\xi) - J_1(\xi)\right]\xi d\xi \tag{3.44b}$$

$$G^{\alpha}_{\theta;\theta}(r,z,\omega|z_0) = \frac{-1}{2\pi r^2}\int_0^{\infty}\left[l_1^{T\alpha}\left[J_0(\xi) - \frac{1}{\xi}J_1(\xi)\right] + \frac{1}{\xi}r_1^{S\alpha}J_1(\xi)\right]\xi d\xi \tag{3.44c}$$

$$G^{\alpha}_{z;r}(r,z,\omega|z_0) = \frac{1}{2\pi r^2}\int_0^{\infty} r_2^{S\alpha}J_1(\xi)\xi d\xi \tag{3.44d}$$

$$G^{\alpha}_{z;z}(r,z,\omega|z_0) = \frac{-1}{2\pi r^2}\int_0^{\infty} r_2^{R\alpha}J_0(\xi)\xi d\xi \tag{3.44e}$$

The fluid partial Green stresses are:

$$s^{G\alpha}_{;r}(r,z,\omega|z_0) = \frac{1}{2\pi r^2}\int_0^{\infty} s_2^{S\alpha}J_1(\xi)\xi d\xi \tag{3.45a}$$

$$s_{;z}^{G\alpha}(r,z,\omega|z_0)=\frac{-1}{2\pi r^2}\int_0^{\infty}s_2^{R\alpha}J_0(\xi)\xi d\xi \tag{3.45b}$$

3.5.4 Gradients of the Green's Tensors

The representation of responses due to dislocation sources requires computing the gradients of the Green tensors. The above expressions for the point load Green's functions are for the physical components of the corresponding tensors in cylindrical coordinates. To compute the displacement gradient for the Green's functions, they are expressed in their tensor form and subjected to covariant differentiation with respect to each of the coordinates, r_0, θ_0, and z_0, and then re-expressed in physical components. The derivative with respect r_0 and θ_0 can be replaced by the negative of the the derivatives with respect to r and θ receiver coordinates, because the material is homogeneous as a function of r and θ. The derivative with respect to z_0 can not be replaced by the derivative at z because of vertical heterogeneity. The results are summarized below. The first, second, and third subscripts denote the component of displacement, the component of the point load, and the gradient component, respectively.

For the matrix or solid region displacements, the Green displacement gradients are:

$$G_{r;r,r}^{\alpha}(r,z,\omega;z_0)=\frac{1}{2\pi}\int_0^{\infty}\left[l_1^{T\alpha}\frac{\partial}{\partial r}\left[\frac{J_1(kr)}{r}\right]+r_1^{S\alpha}\frac{\partial^2}{\partial r^2}J_1(kr)\right]dk \tag{3.46a}$$

$$G_{r;r,\theta}^{\alpha}(r,z,\omega;z_0)=0 \tag{3.46b}$$

$$G_{r;r,z}^{\alpha}(r,z,\omega;z_0)=\frac{-1}{2\pi}\int_0^{\infty}\left[\frac{\partial l_1^{T\alpha}}{\partial z_0}\frac{J_1(kr)}{r}+\frac{\partial r_1^{S\alpha}}{\partial z_0}\frac{\partial J_1(kr)}{\partial r}\right]dk \tag{3.46c}$$

$$G_{r;\theta,r}^{\alpha}(r,z,\omega;z_0)=\frac{-1}{r}G_{r;\theta}^{\alpha}=0 \tag{3.46d}$$

$$G_{r;\theta,\theta}(r,z,\omega;z_0)=\frac{1}{r}\left[G_{\theta;\theta}^{\alpha}-G_{r;r}^{\alpha}\right]=\frac{-1}{2\pi r}\int_0^{\infty}\left[l_1^{T\alpha}-r_1^{S\alpha}\right]\left[\frac{\partial J_1(kr)}{\partial r}-\frac{J_1(kr)}{r}\right]dk \tag{3.46e}$$

$$G_{r;\theta,z}^{\alpha}(r,z,\omega;z_0)=0 \tag{3.46f}$$

$$G_{r;z,r}(r,z,\omega;z_0)=\frac{-1}{2\pi}\int_0^{\infty} r_1^{R\alpha}\frac{\partial^2 J_0(kr)}{\partial r^2}dk \tag{3.46g}$$

$$G^{\alpha}_{r;z,\theta}(r,z,\omega;z_0)=0 \tag{3.46h}$$

$$G^{\alpha}_{r;z,z}(r,z,\omega;z_0)=\frac{1}{2\pi}\int_0^{\infty}\frac{\partial r_1^{R\alpha}}{\partial z_0}\frac{\partial J_0(kr)}{\partial r}dk \tag{3.46i}$$

The gradients of the θ-component of displacement are:

$$G^{\alpha}_{\theta;r,r}(r,z,\omega;z_0)=0 \tag{3.47a}$$

$$G^{\alpha}_{\theta;r,\theta}(r,z,\omega;z_0)=\frac{-1}{r}\left[G_{r;r}-G_{\theta;\theta}\right]= \tag{3.47b}$$

$$\frac{1}{2\pi r}\int_0^{\infty}\left[l_1^{T\alpha}-r_1^{S\alpha}\right]\left[\frac{J_1(kr)}{r}-\frac{\partial J_1(kr)}{\partial r}\right]dk$$

$$G^{\alpha}_{\theta;r,z}(r,z,\omega;z_0)=0 \tag{3.47c}$$

$$G^{\alpha}_{\theta;\theta,r}(r,z,\omega;z_0)=\frac{1}{2\pi}\int_0^{\infty}\left[l_1^{T\alpha}\frac{\partial^2 J_1(kr)}{\partial r^2}+r_1^{S\alpha}\frac{\partial}{\partial r}\frac{J_1(kr)}{r}\right]dk \tag{3.47d}$$

$$G^{\alpha}_{\theta;\theta,\theta}(r,z,\omega;z_0)=0 \tag{3.47e}$$

$$G^{\alpha}_{\theta;\theta,z}(r,z,\omega;z_0)=\frac{-1}{2\pi}\int_0^{\infty}\left[\frac{\partial l_1^{T\alpha}}{\partial z_0}\frac{\partial J_1(kr)}{\partial r}+\frac{\partial r_1^{S\alpha}}{\partial z_0}\frac{J_1(kr)}{r}\right]dk \tag{3.47f}$$

$$G^{\alpha}_{\theta;z,r}(r,z,\omega;z_0)=0 \tag{3.47g}$$

$$G^{\alpha}_{\theta;z,\theta}(r,z,\omega;z_0)=-\frac{G^{\alpha}_{r;z}}{r}=\frac{1}{2\pi r}\int_0^{\infty} r_1^{R\alpha}\frac{\partial J_0(kr)}{\partial r}dk \tag{3.47h}$$

$$G^{\alpha}_{\theta;z,z}(r,z,\omega;z_0)=0 \tag{3.47i}$$

The gradients of the z-component of the Green's functions are:

$$G^{\alpha}_{z;r,r}(r,z,\omega;z_0)=\frac{-1}{2\pi}\int_0^{\infty} r_2^{S\alpha}\frac{\partial J_1(kr)}{\partial r}kdk \tag{3.48a}$$

$$G^{\alpha}_{z;r,\theta}(r,z,\omega;z_0)=0 \tag{3.48b}$$

$$G^{\alpha}_{z;r,z}(r,z,\omega;z_0)=\frac{1}{2\pi}\int_0^{\infty}\frac{\partial r_2^{S\alpha}}{\partial z_0}J_1(kr)kdk \tag{3.48c}$$

$$G^{\alpha}_{z;\theta,r}(r,z,\omega;z_0)=0 \tag{3.48d}$$

$$G^{\alpha}_{z;\theta,\theta}(r,z,\omega;z_0)=-\frac{G^{\alpha}_{z;r}}{r}=\frac{-1}{2\pi r}\int_0^{\infty} r_2^{S\alpha}J_1(kr)kdk \tag{3.48e}$$

$$G^{\alpha}_{z;\theta,z}(r,z,\omega;z_0)=0 \tag{3.48f}$$

$$G^{\alpha}_{z;z,r}(r,z,\omega;z_0)=\frac{1}{2\pi}\int_0^{\infty} r_2^{R\alpha}\frac{\partial J_0(kr)}{\partial r}kdk \tag{3.48g}$$

$$G^{\alpha}_{z;z,\theta}(r,z,\omega;z_0)=0 \tag{3.48h}$$

$$G^{\alpha}_{z;z,z}(r,z,\omega;z_0)=\frac{-1}{2\pi}\int_0^{\infty}\frac{\partial r_2^{R\alpha}}{\partial z_0}J_0(kr)kdk \tag{3.48i}$$

The gradients of the fluid partial stress is:

$$s^{G\alpha}_{;r,r}(r,z,\omega;z_0)=-\frac{1}{2\pi}\int_0^{\infty} s_2^{S\alpha}\frac{\partial J_1(kr)}{\partial r}kdk \tag{3.49a}$$

$$s^{G\alpha}_{;r,\theta}(r,z,\omega;z_0)=s^{G\alpha}_{;\theta,r}(r,z,\omega;z_0)=0 \tag{3.49b}$$

$$s^{G\alpha}_{;r,z,\omega;z_0}(r,z,\omega;z_0)=\frac{1}{2\pi}\int_0^{\infty}\frac{\partial s_2^{S\alpha}}{\partial z_0}J_1(kr)kdk \tag{3.49c}$$

$$s^{G\alpha}_{;\theta,\theta}(r,z,\omega;z_0)=-\frac{s^{G\alpha}_{;r}}{r}=-\frac{1}{2\pi r}\int_0^{\infty} s_2^{S\alpha}J_1(kr)kdk \tag{3.49d}$$

$$s^{G\alpha}_{;\theta,z}(r,z,\omega;z_0)=0 \tag{3.49e}$$

$$s^{G\alpha}_{;z,r}(r,z,\omega;z_0)=\frac{1}{2\pi}\int_0^{\infty}s_2^{R\alpha}\frac{\partial J_0(kr)}{\partial r}kdk \tag{3.49f}$$

$$s^{G\alpha}_{;z,\theta}(r,z,\omega;z_0)=0 \tag{3.49g}$$

$$s^{G\alpha}_{;z,z}(r,z,\omega;z_0)=-\frac{1}{2\pi}\int_0^{\infty}\frac{\partial s_2^{R\alpha}}{\partial z_0}J_0(kr)kdk \tag{3.49h}$$

Using the above identities for the derivatives of the Bessel functions, the following integrals are obtained for the matrix or solid nontrivial displacement gradients, where the factor $\frac{1}{r^3}$ is extracted from the integrals and $\xi=kr$:

$$G^{\alpha}_{r;r,r}(r,z,\omega;z_0)=\frac{1}{2\pi r^3}\int_0^{\infty}\left[l_1^{T\alpha}\left\{\xi J_0(\xi)-2J_1(\xi)\right\}+r_1^{S\alpha}\left\{\left[2-\xi^2\right]J_1(\xi)-\xi J_0(\xi)\right\}\right]d\xi \tag{3.50a}$$

$$G^{\alpha}_{r;r,z}(r,z,\omega;z_0)=\frac{-1}{2\pi r^3}\int_0^{\infty}\left[r\frac{\partial l_1^{T\alpha}}{\partial z_0}J_1(\xi)+r\frac{\partial r_1^{S\alpha}}{\partial z_0}\left\{\xi J_0(\xi)-J_1(\xi)\right\}\right]d\xi \tag{3.50b}$$

$$G^{\alpha}_{r;\theta,\theta}(r,z,\omega;z_0)=\frac{-1}{2\pi r^3}\int_0^{\infty}\left\{l_1^{T\alpha}-r_1^{S\alpha}\right\}\left\{\xi J_0(\xi)-2J_1(\xi)\right\}d\xi \tag{3.50c}$$

$$G^{\alpha}_{r;z,r}(r,z,\omega;z_0)=\frac{-1}{2\pi r^3}\int_0^{\infty}r_1^{R\alpha}\left\{\xi J_1(\xi)-\xi^2 J_0(\xi))\right\}d\xi \tag{3.50d}$$

$$G^{\alpha}_{r;z,z}=\frac{-1}{2\pi r^3}\int_0^{\infty}r\frac{\partial r_1^{R\alpha}}{\partial z_0}\xi J_1(\xi)d\xi \tag{3.50f}$$

For the transverse θ-components of the displacement gradient:

$$G^{\alpha}_{\theta;r,\theta}(r,z,\omega;z_0)=\frac{-1}{2\pi r^3}\int_0^{\infty}\left\{l_1^{T\alpha}-r_1^{S\alpha}\right\}\left\{\xi J_0(\xi)-2J_1(\xi)\right\}d\xi \tag{3.51a}$$

$$G^{\alpha}_{\theta;\theta,r}(r,z,\omega;z_0)=\frac{-1}{2\pi r^3}\int_0^{\infty}\left[l_1^{T\alpha}\left\{\xi J_0(\xi)-\left[2+\xi^2\right]J_1(\xi)\right\}-r_1^{S\alpha}\left\{\xi J_0(\xi)-2J_1(\xi)\right\}\right]d\xi \tag{3.51b}$$

$$G^{\alpha}_{\theta;\theta,z}(r,z,\omega;z_0)=\frac{-1}{2\pi r^3}\int_0^{\infty}\left[r\frac{\partial l_1^{T\alpha}}{\partial z_0}\left\{\xi J_0(\xi)-J_1(\xi)\right\}+r\frac{\partial r_1^{S\alpha}}{\partial z_0}J_1(\xi)\right]d\xi \tag{3.51c}$$

$$G^{\alpha}_{\theta;z,\theta}(r,z,\omega;z_0)=+\frac{1}{2\pi r^3}\int_0^{\infty}r_1^{R\alpha}\xi J_1(\xi)d\xi \tag{3.51d}$$

The z-components of the displacement gradient are:

$$G^{\alpha}_{z;r,r}(r,z,\omega;z_0)=\frac{-1}{2\pi r^3}\int_0^{\infty}r_2^{S\alpha}\xi\left\{\xi J_0(\xi)-J_1(\xi)\right\}d\xi \tag{3.52a}$$

$$G^{\alpha}_{z;r,z}(r,z,\omega;z_0)=\frac{1}{2\pi r^3}\int_0^{\infty}r\frac{\partial r_2^{S\alpha}}{\partial z_0}J_1(\xi)\xi d\xi \tag{3.52b}$$

$$G^{\alpha}_{z;\theta,\theta}(r,z,\omega;z_0)=\frac{-1}{2\pi r^3}\int_0^{\infty}r_2^{S\alpha}J_1(\xi)\xi d\xi \tag{3.52c}$$

$$G^{\alpha}_{z;z,r}(r,z,\omega;z_0)=\frac{-1}{2\pi r^3}\int_0^{\infty}r_2^{R\alpha}\xi^2J_1(\xi)d\xi \tag{3.52d}$$

$$G^{\alpha}_{z;z,z}(r,z,\omega;z_0)=\frac{-1}{2\pi r^3}\int_0^{\infty}r\frac{\partial r_2^{R\alpha}}{\partial z_0}J_0(\xi)\xi d\xi \tag{3.52e}$$

The gradients of the fluid partial Green isotropic stresses are:

$$s^{G\alpha}_{;r,r}(r,z,\omega;z_0)=\frac{-1}{2\pi r^3}\int_0^{\infty}s_2^{S\alpha}\left\{\xi J_0(\xi)-J_1(\xi)\right\}\xi d\xi \tag{3.53a}$$

$$s^{G\alpha}_{;r,z}(r,z,\omega;z_0)=+\frac{1}{2\pi r^3}\int_0^{\infty}r\frac{\partial s_2^{S\alpha}}{\partial z_0}J_1(\xi)\xi d\xi \tag{3.53b}$$

$$s^{G\alpha}_{;\theta,\theta}(r,z,\omega;z_0)=\frac{-1}{2\pi r^3}\int_0^{\infty} s_2^{S\alpha}J_1(\xi)\xi d\xi \tag{3.53c}$$

$$s^{G\alpha}_{;z,r}(r,z,\omega;z_0)=\frac{-1}{2\pi r^3}\int_0^{\infty} s_2^{R\alpha}J_1(\xi)\xi^2 d\xi \tag{3.53d}$$

$$s^{G\alpha}_{;z,z}(r,z,\omega;z_0)=\frac{-1}{2\pi r^3}\int_0^{\infty} r\frac{\partial s_2^{R\alpha}}{\partial z_0}J_0(\xi)\xi d\xi \tag{3.53e}$$

Further simplifications are obtained for the responses due to fluid sources, because the moment tensor representing the fluid source is an isotropic tensor. Only the trace of the gradient of the fluid point load Green's functions are required:

$$G^F_r(r,z,\omega;z_0)=G^F_{r;r,r}+G^F_{r;\theta,\theta}+G^F_{r;z,z}= \tag{3.54a}$$

$$\frac{-1}{2\pi r^3}\int_0^{\infty}\left[r_1^{SF}\xi+r\frac{\partial r_1^{RF}}{\partial z_0}\right]J_1(\xi)\xi d\xi$$

$$G^F_\theta(r,z,\omega;z_0)=0 \tag{3.54b}$$

$$G^F_z(r,z,\omega;z_0)=\frac{-1}{2\pi r^3}\int_0^{\infty}\left[\xi r_2^{SF}+r\frac{\partial r_2^{RF}}{\partial z_0}\right]J_0(\xi)\xi d\xi \tag{3.54c}$$

The trace of the gradient of the fluid isotropic Green partial stress due to fluid loads is:

$$s^{GF}(r,z,\omega;z_0)=s^{GF}_{;r,r}+s^{GF}_{;\theta,\theta}+s^{GF}_{;z,z}=\frac{-1}{2\pi r^3}\int_0^{\infty}\left\{s_2^{SF}\xi+r\frac{\partial s_2^{RF}}{\partial z_0}\right\}J_0(\xi)\xi d\xi \tag{3.55}$$

The above relations for the trace of the gradient of the Green's functions for fluid point loads, Equations 3.54a,b, and c, and Equation 3.55, would have been more satisfying if the responses r_1^{SF}, r_2^{SF}, and s_2^{SF}, were absent, since these involve horizontal fluid loads acting in the "S" direction. As indicated above, the fluid loads acting in the "S" and "T" directions are singular at zero frequency. Absence of these solutions would remove any concern about singularity of the solutions. However,

these relations have been rederived several times without any further simplification. The presence of the solution for the "S" load component can be argued on the basis of requiring a nontrivial result for the radial displacement at a receiver located on the same plane as the source. The term involving l_1^{TF}, obtained for a horizontal "T" load component, is canceled when taking the trace, because an isotropic source cannot give rise to purely SH motion.

The moment tensor representing dislocation sources in the absence of externally applied couples are symmetric with respect to interchange of indices. Therefore, only the symmetric parts of the gradients of the Green's functions are required for construction of responses due to fracture sources. For calculation of the matrix or solid region displacement response to a point dislocation source in the porous matrix, only ten components of the displacement gradient are required. For a fluid volume source, only the three components of the trace of the displacement gradient for fluid sources are required. To calculate the fluid partial stress, only the four independent components of the symmetric part of the stress gradient for matrix dislocations and the trace of the stress gradient for fluid volume sources are required. Thus, a total of 18 functions determine the fluid partial stress and matrix displacement for arbitrary matrix moment and fluid isotropic moment source terms.

Only ten displacement-stress vector components enter the Hankel transform inversion formulae for the displacement response of the matrix or solid region due to porous matrix dislocations. These are l_1^{TM}, r_1^{SM}, r_2^{SM}, r_1^{RM}, r_2^{RM}, and their derivatives with respect to z_0. A similar result is obtained by Stump (1978) for the Green's functions for elastic isotropic solids.

Chapter 4: Numerical Solution Procedures

The numerical procedures used for calculating the Green's functions and their derivatives include numerical integration of the displacement stress vectors to obtain propagators for PSV and SH waves in the porous layer, numerical solution of the equations expressing the boundary conditions between the porous and solid regions, and inversion of the Hankel transforms in the complex plane. These procedures and details regarding the specification of loads for calculating the Green's functions and associated derivatives are discussed here.

4.1 Integration of the Displacement Stress Equations

Solutions for PSV and SH waves for the porous layer are represented by numerically computed propagator matrices mapping displacements and stresses from one vertical position to another. The differential equations of motion for the displacements and stresses, discussed in Chapter 3 and in Appendix B, are:

$$\frac{\partial \mathbf{P}(z;z_0)}{\partial z} = \mathbf{A}(z)\mathbf{P}(z;z_0) \tag{4.1}$$

The initial value for the propagator is the unit matrix.

Numerical integration of the displacement stress equations over the layer thickness is complicated by the presence of fluid diffusion in the low frequency limit and evanescence at large imaginary vertical wave number, leading to exponentially growing displacements and stresses. The decaying solutions must be extracted from the growing solutions, requiring high precision. For a thin layer, this is not a great difficulty, but for a broad layer, more sophisticated procedures are required, several of which are discussed in the literature.

Several numerical techniques were employed to numerically integrate the displacement stress vector over the layer thickness. The first of these was a Runge-Kutta method, implemented in the NAG Fortran subroutine package (Numerical Algorithms Group, 1984). The Runge-Kutta procedure was not entirely stable over the full width of the fractured zone, regardless of starting step size or error criterion used. The difficulty manifested itself in lack of convergence of the fluid pressure and displacement for decreasing error criterion.

An alternative to the Runge Kutta method included discretization of the layer and use of a global finite element procedure. The approach was dropped because of excessive computer time, and was never thoroughly developed or debugged. The approach was roughly ten times slower than the Runge-Kutta procedure.

The Bulirsch-Stoer technique described and praised by Press, et al, (1986, pg. 563) was used with good results. The method is an elegant procedure relying on a modified midpoint rule with successive reduction of integration step size followed by an extrapolation of computed intermediate results to zero step size. The procedure supplied in the reference was modified for the present problem, but was dropped after determining that speed enhancements could be obtained by pregridding of function parameters, which would make the adaptive step size control in the Bulirsch Stoer technique awkward to apply. Thus, adaptive step size control was dropped in favor of selecting a step-size consistent with the Nyquist limit or some fraction thereof, and pregridding in the vertical direction. Euler and second order midpoint rules were tested with varying degrees of success. A stable second order modified midpoint rule used in the Bulirsch-Stoer technique discussed by Press, et al, (1986, pg. 560), was selected as the core integrator. The rule is similar to trapezoidal integration, but with modifications at the beginning and ending points.

If the result of a modified midpoint integration is followed by a second modified midpoint integration over the same interval, but with half as many steps, the two results can be combined according to the following rule to obtain fourth order accuracy (Press, et al, 1986):

$$y = \frac{(4y_n - y_{n/2})}{3} \tag{4.2}$$

The rule requires only one and one half derivative evaluations per step where the Runge-Kutta procedure requires four for the same order of accuracy. If the coarse step size is selected to satisfy the Nyquist criterion, a very efficient integration rule without convergence testing is obtained. However, for the evanescent case, a course step size of about 1/3 the Nyquist step size was required for reasonable accuracy.

To increase accuracy further, a 6th order rule was developed, again using the modified midpoint rule as a core integrator:

$$y = \frac{84}{35}y_n - \frac{64}{35}y_{2n/3} + \frac{15}{35}y_{n/2} \tag{4.3}$$

The rule is similar to the two step rule discussed above, but incorporates an additional integration with two thirds the number of original steps. The original number of steps was selected to be a multiple of 6, so that it could be divided evenly by the factors 2 and 3. The 6th order rule is very accurate and does not require a great penalty in cpu time over the 4th order rule, requiring only 2 1/6 derivative evaluations per step.

The numerical execution time is reduced by an order of magnitude by simultaneous integration of all of the propagator matrix components, pregridding for each frequency, precomputing terms independent of wavenumber, and use of the above 6th order rule. When simultaneously integrating the propagator matrix components, a total of eight initial value problems are solve simultaneously; six for the PSV problem and two for the SH problem. Real arithmetic is employed in the current code, resulting in the simultaneous integration of eighty displacement-stress components at one pass, taking advantage of the vector optimization of the CRAY computers at Lawrence Livermore National Laboratory.

To determine the maximum step size for integration of the displacement stress components, dispersion relations obtained from a potential representation of wave propagation in homogeneous fluid-saturated porous media of the Biot type are used to calculate phase velocities for the two coupled compression waves and the single shear wave associated with a homogeneous porous material with the same properties as the heterogeneous material at a given position. The dispersion relations are equivalent to expressions for phase velocity derived by Biot (1956a). By searching over the entire width of the fractured layer, the maximum wavenumber magnitude for any of the wave types and at any position within the layer is used to define the minimum wavelength within the layer. The Nyquist limit is one-half the characteristic wavelength. That is, the Nyquist limit is taken as

$$\Delta_{nyq} = \frac{c_\alpha}{2f} \tag{4.4}$$

where c_α is the wave velocity for either of the two Biot PSV waves or the shear wave. The fine step size for computation of results presented here was selected to be 1/24 of the Nyquist limit for very high accuracy, and therefore the coarse step size was 1/8 of the Nyquist limit. Selection of the step size is an option specified in the input parameter list for the program, and larger step sizes may be appropriate for practical computation. However, the presence of exponentially increasing and decreasing evanescent solutions requires that the step size be smaller than typically used for calculating sinusoidal solutions, as with finite-difference procedures.

To conserve computer time, the displacement stress components were integrated from the center plane, $z = 0$, to the upper boundary, relying on symmetry about the central plane to determine propagator matrices for the region below the plane of symmetry. For an asymmetric porous layer, the propagators would be computed by numerical integration over the entire layer width.

4.2 Solution of the Boundary Value Problem

Two solution procedures were used for solving the boundary value problem. The first procedure included representing the solutions for the porous layer by displacement-stress components at $z = 0$ and propagators from the central plane of symmetry to the boundaries with the elastic region. Superposition with a particular integral at the boundary and solving for the displacement-stress components at $z = 0$ gives the desired general solution. The approach is adequate for thin layers and low frequencies, but suffers from insufficient numerical precision for thick layers or higher frequencies.

A second approach, referred to here as a "hybrid" procedure, incorporates the efficiency of the numerical integration procedure for the displacement-stress vector while avoiding problems with numerical precision at high wave-number. The procedure involves subdividing the porous layer into sub-layers, computing propagators for each of the sublayers, and solving a global boundary value problem for the displacement-stress components at each of the layer interfaces. Only the latter procedure is discussed, because it is the most effective for thick layers, and because only results for the latter procedure are presented. The resulting matrix of boundary conditions is an extension of that obtained for the single layer treatment.

Two matrix equations are obtained; one for the PSV problem and another for the SH problem.

$$\mathbf{B}^{PSV}\mathbf{a}^{PSV} = \mathbf{q}^{PSV} \tag{4.5a}$$

$$\mathbf{B}^{SH}\mathbf{a}^{SH} = \mathbf{q}^{SH} \tag{4.5b}$$

The vectors **a** for the PSV and SH cases consist of the displacement stress components at each of the layer interfaces and the potential coefficients for the solid regions.

$$\mathbf{a}=\begin{Bmatrix} \phi^{+} \\ \mathbf{v}(z_n) \\ \mathbf{v}(z_{n-1}) \\ \vdots \\ \mathbf{v}(z_2) \\ \mathbf{v}(z_1=0+) \\ \mathbf{v}(z_{-1}=0-) \\ \mathbf{v}(z_{-2}) \\ \vdots \\ \mathbf{v}(z_{-n+1}) \\ \mathbf{v}(z_{-n}) \\ \phi^{-} \end{Bmatrix} \tag{4.6}$$

The subvectors for the PSV problem are:

$$\phi^{\pm PSV}=\begin{Bmatrix} A^{\pm}e^{\mp\zeta_p h} \\ B^{\pm}e^{\mp\zeta_s h} \end{Bmatrix} \tag{4.7a}$$

$$\mathbf{v}^{PSV}(z_i)=\begin{Bmatrix} r_1(z_i) \\ r_2(z_i) \\ r_3(z_i) \\ r_4(z_i) \\ s_1(z_i) \\ s_2(z_i) \end{Bmatrix} \tag{4.7b}$$

Similarly, for the SH case:

$$\phi^{SH\pm}=\left\{C^{\pm}e^{\mp\zeta_s h}\right\} \tag{4.8a}$$

$$\mathbf{v}^{SH}(z_i)=\begin{Bmatrix} l_1(z_i) \\ l_2(z_i) \end{Bmatrix} \tag{4.8b}$$

The matrix, $\mathbf{B}^{PSV}$, is of the form:

$$\mathbf{B}^{PSV}(k,\omega)= \tag{4.9}$$

$$\begin{bmatrix}
\mathbf{H}(+h) & -\mathbf{Q}(+h) & 0 & 0 & . \\
0' & \mathbf{I} & -\mathbf{P}(z_n,z_{n-1}) & 0 & . \\
0' & 0 & \mathbf{I} & -\mathbf{P}(z_{n-1},z_{n-2}) & . \\
0' & 0 & 0 & \mathbf{I} & . \\
. & . & . & . & .
\end{bmatrix}$$

$$\begin{bmatrix}
. & . & . & . \\
. & \mathbf{I} & -\mathbf{P}(z_2,z_1) & 0 & . \\
. & 0 & \mathbf{I} & -\mathbf{I} & . \\
. & . & 0 & \mathbf{P}(z_{-2},z_{-1}) & . \\
. & . & . & 0 & .
\end{bmatrix}$$

$$\begin{bmatrix}
. & . & . & . & . \\
. & -\mathbf{I} & 0 & 0 & 0' \\
. & \mathbf{P}(z_{-n+1},z_{-n+2}) & -\mathbf{I} & 0 & 0' \\
. & 0 & \mathbf{P}(z_{-n},z_{-n+1}) & -\mathbf{I} & 0' \\
. & 0 & 0 & -\mathbf{Q}(-h) & \mathbf{H}(-h)
\end{bmatrix}$$

The sub-matrices $\mathbf{H}^{PSV}(\pm h)$ appearing above are:

$$\mathbf{H}^{PSV}(\pm h)=\begin{bmatrix}
k & \mp k\zeta_s \\
\pm\zeta_p & -k^2 \\
\mp 2\mu k\zeta_p & \mu(2k^2-k_s^{\,2})k \\
-2\mu\zeta_s^{\,2} & \mp 2\mu k^2\zeta_s \\
0 & 0
\end{bmatrix} \tag{4.10}$$

Again, the + sign refers to $z>h$, and the − sign refers to $z<h$. The matrix, $\mathbf{Q}$, is a 6 by 5 matrix, expressing the boundary conditions between the displacement-stress components at the edge of the porous region and the potential coefficients for the solid region. The components of $\mathbf{Q}^{PSV}$ are:

$$\mathbf{Q}^{PSV}=\begin{bmatrix}
1 & 0 & 0 & 0 & 0 & 0 \\
0 & 1 & 0 & 0 & 0 & 0 \\
0 & 0 & 1 & 0 & 0 & 0 \\
0 & 0 & 0 & 1 & 0 & 1 \\
0 & -1 & 0 & 0 & 1 & 0
\end{bmatrix} \tag{4.11}$$

The matrices, 0′ and 0, are trivial 2 by 5 and 6 by 6 matrices, respectively.

The porous region displacement-stress components at the boundary between the layer and the solid region are included in the solution. They could be deleted, reducing the size of the matrix, thus saving some computer time, but were included to simplify bookkeeping and debugging, and allow computing the fluid partial stress at the boundary, if desired, though this was not done.

Analogous expressions are obtained for the SH problem. For this case, the trivial matrices 0′ and 0 are 1 by 2 and 2 by 2, respectively. The matrix **H** is:

$$\mathbf{H}^{SH}(\pm h, k, \omega) = \begin{bmatrix} k \\ \mp \mu k \zeta_s \end{bmatrix} \tag{4.12}$$

and the matrix, **Q**, is simply the unit 2 by 2 matrix:

$$\mathbf{Q}^{SH} = \mathbf{I} \tag{4.13}$$

The point $z = 0$ is divided into two locations, $z_{+1} = 0+$, and $z_{-1} = 0-$, to allow application of a stress discontinuity at the point $z = 0$. The need for this is a consequence of using symmetry and determining propagators for $z < 0$ from the propagators for $z > 0$. The extra coefficients would not be necessary if upward going propagators were used throughout the porous region.

4.2.1 Inhomogeneous Terms for Stress Discontinuities.

The inhomogeneous term representing a stress discontinuity at z_i is given by:

$$\mathbf{q} = \begin{Bmatrix} 0' \\ 0 \\ \cdot \\ \cdot \\ 0 \\ \mathbf{q}_i \\ 0 \\ \cdot \\ \cdot \\ 0 \\ 0' \end{Bmatrix} \tag{4.14}$$

The subscript, i, ranges from n to 1 and -1 to $-n$.

The load vector, $\mathbf{q}$, depends on the nature of the stress discontinuity. For the PSV case, the loads are:

Transverse load "*SM*" applied to the porous matrix in the "*S*" direction, representing a discontinuity, $[r_3](z_i) = r_3(z_i+) - r_3(z_i-) = +1$:

$$\mathbf{q}_i^{SM} = \begin{Bmatrix} 0 \\ 0 \\ 1 \\ 0 \\ 0 \\ 0 \end{Bmatrix} \tag{4.15a}$$

Vertical load, "*RM*", acting on the porous matrix in the "*R*" direction, representing a discontinuity $[r_4](z_i) = r_4(z_i+) - r_4(z_i-) = +1$:

$$\mathbf{q}_i^{RM} = \begin{Bmatrix} 0 \\ 0 \\ 0 \\ 1 \\ 0 \\ 0 \end{Bmatrix} \tag{4.15b}$$

Transverse fluid load "*SF*" acting in the "*S*" direction, giving a discontinuity in transverse matrix shear, $[r_3] = r_3(z_i+) - r_3(z_i-) = -\dfrac{\breve{\rho}_{12}}{\breve{\rho}_{22}}$, and vertical fluid displacement, $[s_1] = s_1(z_i+) - s_1(z_i-) = -k/(\omega^2 \breve{\rho}_{22})$:

$$\mathbf{q}_i^{SF} = \begin{Bmatrix} 0 \\ 0 \\ -\dfrac{\breve{\rho}_{12}}{\breve{\rho}_{22}} \\ 0 \\ -\dfrac{k}{\omega^2 \breve{\rho}_{22}} \\ 0 \end{Bmatrix} \tag{4.15c}$$

Vertical load "*RF*" applied to the fluid in the "*R*" direction, representing a discontinuity $[s_2](z_i) = s_2(z_i+) - s_2(z_i-) = +1$:

$$\mathbf{q}_i^{RF} = \begin{Bmatrix} 0 \\ 0 \\ 0 \\ 0 \\ 0 \\ 1 \end{Bmatrix} \tag{4.15d}$$

The trivial sub vectors for the PSV load vector are:

$$0' = \begin{Bmatrix} 0 \\ 0 \\ 0 \\ 0 \\ 0 \end{Bmatrix}, \qquad 0 = \begin{Bmatrix} 0 \\ 0 \\ 0 \\ 0 \\ 0 \\ 0 \end{Bmatrix} \tag{4.16}$$

The transverse loads for the SH problem are:

Transverse load "*TM*" applied to the porous matrix in the "*T*" direction, representing the discontinuity, $[l_2](z_i) = l_2(z_i+) - l_2(z_i-) = +1$:

$$\mathbf{q}_i^{TM} = \begin{Bmatrix} 0 \\ 1 \end{Bmatrix} \tag{4.17a}$$

Transverse load "*TF*" applied to the fluid in the "*T*" direction, giving a discontinuity in the transverse matrix shear, $[l_2] = l_2(z_i+) - l_2(z_i-) = -\dfrac{\sigma_{12}}{\sigma_{22}}$, is:

$$\mathbf{q}_i^{TF} = \begin{Bmatrix} 0 \\ -\dfrac{\sigma_{12}}{\sigma_{22}} \end{Bmatrix} = -\frac{\sigma_{12}}{\sigma_{22}} \mathbf{q}_i^{TM} \tag{4.17b}$$

The transverse "*T*" loads applied to the fluid and matrix are not independent, so that one solution may be obtained from the other for each frequency. Further, the transverse "*T*" fluid load is not required for representing responses to the isotropic fluid moment tensor, as discussed in Chapter 3, and is therefore not used, except for inspection of point load solutions to verify code performance.

The point load solutions are singular for zero frequency as may be observed in the load representation for $\mathbf{q}^{SF}$, involving a factor of ω^2 in the denominator. When combined with the visco-dynamic density ρ_{22}, the load component varies as ω^{-1}.

The trivial sub vectors for the SH problem are:

$$0' = \begin{Bmatrix} 0 \\ 0 \end{Bmatrix}, \qquad 0 = \begin{Bmatrix} 0 \\ 0 \end{Bmatrix} \tag{4.18}$$

4.2.2 Inhomogeneous Terms for Derivative Evaluations

The inhomogeneous equations required for computing the derivatives of the point load Green's functions with respect to source vertical coordinate, z_0, are obtained by differentiating the inhomogeneous matrix equations for the point load case. To do this, one must allow the source to be moved vertically. Let $\mathbf{q}^{\alpha}(z_i)$ be the inhomogeneous contribution at z_i due to a source $\mathbf{q}^{\alpha}(z_0)$ at z_0, differentiate with respect to z_0, and let z_0 approach z_i:

$$\mathbf{q}^{\alpha}(z_i) = \mathbf{P}(z_i, z_0)\mathbf{q}^{\alpha}(z_0) \tag{4.19}$$

The components of $\mathbf{q}^{\alpha}$ are simply the vector components discussed above. Thus, $\alpha=SM$ refers to a transverse load in the S direction applied to the porous matrix, and so forth. Then, the derivative with respect to z_0 is

$$\frac{\partial \mathbf{q}^{\alpha}(z_i)}{\partial z_0} = \frac{\partial \mathbf{P}(z_i, z_0)}{\partial z_0}\mathbf{q}^{\alpha}(z_0) + \mathbf{P}(z_i, z_0)\frac{\partial \mathbf{q}^{\alpha}(z_0)}{\partial z_0} \tag{4.20}$$

The derivative of the propagator with respect to z_0 is obtained by differentiating the inverse relation for the propagator:

$$\mathbf{P}(z_i, z_0)\mathbf{P}(z_0, z_i) = \mathbf{I} \tag{4.21}$$

Obtain:

$$\frac{\partial \mathbf{P}(z_i, z_0)}{\partial z_0}\mathbf{P}(z_0, z_i) + \mathbf{P}(z_i, z_0)\frac{\partial \mathbf{P}(z_0, z_i)}{\partial z_0} = 0 \tag{4.22}$$

Using the differential equation of motion:

$$\frac{\partial \mathbf{P}(z_0, z_i)}{\partial z_0} = \mathbf{A}(z_0)\mathbf{P}(z_0, z_i)$$

and post-multiplying from the right with $\mathbf{P}(z_i, z_0)$, and using the inverse relation again:

$$\frac{\partial \mathbf{P}(z_i, z_0)}{\partial z_0} = -\mathbf{P}(z_i, z_0)\mathbf{A}(z_0) \tag{4.23}$$

When $z_0 = z_i$, the propagator, **P**, is just the unit matrix. Then:

$$\frac{\partial \mathbf{q}^{\alpha}(z_i)}{\partial z_0} = -\mathbf{A}(z_0)\mathbf{q}^{\alpha}(z_0) + \frac{\partial \mathbf{q}^{\alpha}(z_0)}{\partial z_0} \tag{4.24}$$

For loads applied to the porous matrix in the "*S*", "*T*", or "*R*" directions, and the load applied to the fluid in the "R" direction, the components of $\mathbf{q}^{\alpha}(z_0)$ are independent of z_0. For the transverse loads applied to the fluid, the derivative of $\mathbf{q}^{\alpha}(z_0)$ are non-zero because of the z-dependence of the visco-dynamic densities appearing in the components of the load vectors. However, these particular gradients are not needed in the representation of responses to isotropic point fluid moment tensors, and are not computed.

4.2.3 Summary

In summary, the above derivative formulas give three additional load vectors for the derivative evaluations of the PSV problem, and one additional load vector for the derivative evaluation of the SH problem. Thus, a total of seven PSV solutions and two SH solutions are obtained for each source location.

For convenience, the required source vectors, or inhomogeneous terms, for the SH problem are: $\mathbf{q}^{TM}$, and $\frac{\partial \mathbf{q}^{TM}}{\partial z_0}$. For the PSV problem, the required source vectors are: $\mathbf{q}^{SM}$, $\mathbf{q}^{SF}$, $\mathbf{q}^{RM}$, $\mathbf{q}^{RF}$, $\frac{\partial \mathbf{q}^{SM}}{\partial z_0}$, $\frac{\partial \mathbf{q}^{RM}}{\partial z_0}$, and $\frac{\partial \mathbf{q}^{RF}}{\partial z_0}$.

All of the independent solutions are obtained by back-substitution into the global banded matrices decomposed by Gaussian elimination. Solutions for additional sources are also obtained without further decomposition of the banded matrix, so that a number of sources may be considered without substantial increase of computer time.

When computing the displacement-stress components at the central plane of symmetry in response to a source at the same plane, the displacement-stress coefficients at $z_1 = 0+$ and $z_{-1} = 0-$ are averaged together to account for the load discontinuity. An alternative is to add 1/2 the load discontinuity to the displacement-stress solution at z_{-1}. In principal, using the above averaging procedure should not

be necessary, since the Hankel inversion should be continuous in z for finite r. In practice, convergence of trivial solutions or near trivial solutions is improved if the averaging is done. The procedure does not affect displacement vector components for assigned stress discontinuities, but shows up mainly in the derivative evaluations, and in the transverse fluid load specifications. In general, inverting solutions under this condition is a difficult process, requiring extensive computer time and effort.

4.2.4 Discussion

An interesting feature of the global matrix approach for solving the reflectivity problem over multiple layers is that for evanescent waves, the global matrix becomes poorly conditioned, suffering from insufficient numerical precision. However, conditioning improves as the sublayer thicknesses are reduced. In the limit of infinitesimal layer thickness, ill-conditioning should be absent, but solution time for solving the banded matrix equation is roughly proportional to the number of layers. A practical choice for the number of layers is therefore necessary.

Fortunately, if the conditioning of the individual propagators is reasonable, then the solutions for the displacement stress vector near the source are found to be well determined, while those far from the source may be dominated by numerical "noise", the magnitude of which depends on sub-layer thickness. For sufficiently small sub-layer thickness, the noise dominated solutions at large distance from the source are of extremely small magnitude, and, therefore, do not contribute significantly to the Hankel transform inversion integral. This effect was observed for the same LU decomposition of the banded matrix, independent of source location. Evidently, one need only reduce the sublayer thicknesses sufficiently to obtain a reasonable "signal-to-noise" ratio for solving the problem. No criteria for layer thicknesses have been established, except that of obtaining reasonable looking results. Lack of precision produces noisy looking and non-causal response functions which can usually be identified. Moreover, the condition number of the matrix, obtained during LU decomposition, provides an indicator of the adequacy of sub-layer thickness. For severe ill-conditioning, indicated by a positive result of a conditioning test, results were found to be unsatisfactory.

From a physical point of view, the results obtained with LU decomposition and Gaussian elimination are consistent with the requirement that, in the presence of severe evanescence, boundaries at large distance from the source should not have a significant physical effect on the near-field response. Requiring that evanescent solutions at large distances from the source be accurately computed may be

unnecessary, as well as impractical, provided that the wavenumber is not too close to a pole, as revealed by the condition number for the banded matrix.

As mentioned in Chapter 3, Gaussian elimination is related to methods of invariant embedding, whereby a Ricatti transform is used to circumvent the effects of evanescence. Invariant embedding is described by Meyer (1973) regarding the solution of boundary value problems via initial value methods (the approach used here, though not strictly invariant embedding).

As mentioned in Chapter 3, Chin, et al, (1984) provide an excellent discussion of the relationship of invariant embedding, Gaussian elimination, and matrix methods (Kennet, 1983) for solving the reflectivity problem. A new method is proposed by Chin, et al, as an alternative to Kennet's algorithm for homogeneous layers.

The hybrid approach used here differs again from the matrix procedures discussed by Chin, et al. Smoothly varying stiffness profiles are preserved in the model by numerical integration of propagator matrices, but Gaussian elimination techniques are applied to individual components to obtain solutions for a limited number of sub-layers, avoiding an otherwise poorly conditioned problem. Branch points, associated branch cuts (not actually present for interior layers), and turning points need not be evaluated or be of concern. The integration procedure is therefore robust. Moreover, the speed with which the numerical integration may be performed may make the technique preferable to using a large number of homogeneous layers to approximate the stiffness profile and solving by one of the more usual matrix reflectivity methods. This has not been evaluated, however. The procedure should be equally effective for anisotropic elastic regions.

4.3 Hankel Inversion Procedures

The displacement-stress solutions are inserted into the integral expressions listed in Chapter 3 for the Green's functions and gradients of the Green's functions.

4.3.1 Constant Q Velocity Dispersion

To avoid branch points or poles on the real axis of the wavenumber plane during numerical integration of the Hankel transforms, complex velocities of propagation are assigned to the dilatational and rotational waves in the material making up the porous matrix and solid regions.

The complex Lamé parameters for the solid material are then determined by the usual formulae.

To preserve causality of the computed results, the constant Q model for velocity dispersion developed by Kjartansson (1979) is used. The complex velocities are given by:

$$c_p = c_{0p}\left[\frac{i\omega}{\omega_0}\right]^{\gamma} \tag{4.24a}$$

$$c_s = c_{0s}\left[\frac{i\omega}{\omega_0}\right]^{\gamma} \tag{4.24b}$$

$$\gamma = \frac{1}{\pi}\arctan\left[\frac{1}{Q}\right] \tag{4.25}$$

The reference radian frequency, ω_0, is selected to be within the frequency range of interest. For reasonable values of Q, eg. $Q \geq 30$, the factor γ is much less than unity, and the complex velocity closely approximates the real valued phase velocity except for a small imaginary component. Only at very low frequencies does the complex velocity differ appreciably from the real valued phase velocity for the elastic case.

Other models of complex velocity dispersion have been introduced to describe attenuation of body waves in visco-elastic media. Futterman (1962) presents a model (predating Kjartanssons work) including a non-constant Q, indicating that although Q may be assumed constant over the frequency range of interest, Q must become infinite below some arbitrarily small but finite frequency. Evidently, the arbitrariness of this small but finite frequency allows one to set Q to infinity for frequencies below the first spectral point used for computation, in effect providing a constant Q velocity dispersion over the frequency range of study. Kjartansson's model avoids the problem of selecting an arbitrary low frequency behavior for Q by specifying the above form for the velocity dispersion, though this is done at the expense of selecting an arbitrary reference frequency, ω_0. Kjartansson points out that for reasonable frequencies and Q-factors, his model closely approximates the usual models of velocity dispersion and amplitude attenuation for a constant Q material.

Complex velocities associated with the Lamé parameters for a Voigt solid would also be suitable, because the velocity dispersion satisfies the necessary requirements for causality and integrability conditions.

The Voigt model is most attractive from a physical point of view, though it is not a constant Q model. Because the loss factor included in the solid material moduli is very small, the constant Q

model of Kjartansson is considered adequate for displacing singularities away from the real axis.

4.3.2 Integration Contour

The Hankel inversion integrals were initially evaluated with a trapezoidal rule, integrating along the real wavenumber axis. This is a satisfactory approach for computing responses in the semi-infinite solid regions, because of natural evanescent roll-off at high wavenumber, but the approach is inadequate for the response of the porous layer, especially for source and receiver on the same plane, because of poor convergence and excessive computer time. The resolution of this problem required substantial effort.

To achieve rapid convergence of the Hankel inversions for responses in the porous layer, the contour of integration is modified as illustrated in Figure 3.2 to exploit the exponential character of Hankel the functions off the real axis of the k-plane. The Bessel functions appearing in the integral expressions for the Green's functions are expressed as Hankel functions of the first and second kind for integration in the complex plane.

$$J_m(kr) = \frac{1}{2}\left[H_m^{(1)}(kr) + H_m^{(2)}(kr)\right] \tag{4.26}$$

For large kr, the Hankel functions behave asymptotically as:

$$H_m^{(1)}(kr) \approx \sqrt{\frac{2}{\pi kr}}\, e^{-i\left(\frac{m\pi}{2}-\frac{\pi}{4}\right)} e^{iRe(kr)} e^{-Im(kr)} \tag{4.27a}$$

$$H_m^{(2)}(kr) \approx \sqrt{\frac{2}{\pi kr}}\, e^{i\left(\frac{m\pi}{2}+\frac{\pi}{4}\right)} e^{-iRe(kr)} e^{Im(kr)} \tag{4.27b}$$

The Hankel function of the first kind attenuates exponentially with increasing positive imaginary part of k, while the Hankel function of the second kind attenuates exponentially with decreasing negative imaginary part of k. To exploit these properties, the contour of integration begins at the origin and follows the real axis to a point just beyond the highest wave number associated with any of the characteristic wave velocities within the fractured layer. At this point, the Bessel function is split into the Hankel functions of the first and second kind, and the part of the integral with kernel involving Hankel functions of the first kind are evaluated along a contour entering the first quadrant of the complex plane, while the remaining part of the integral with kernel involving the Hankel function of the second kind are evaluated over a reflected contour entering the fourth quadrant. The upper and lower contours are rejoined at $k = \infty$. Provided that no poles are contained within the region bounded by the

deformed contours beyond the demarcation point, the result will be the same by Cauchy's theorem as if the integration were carried out entirely on the real axis.

The angle at which the contours depart from the real axis is arbitrarily set to $\frac{\pi}{4}$ to further increase the chances of including all poles in the calculation. Frazer and Gettrust (1984) suggest that the angle be set to $\tan^{-1}(x/|(z_r - z_s|)$, where z_r and z_s are the receiver and source elevations, respectively, for maximum convergence rate. The angle, $\frac{\pi}{4}$, is selected as a reasonable compromise between large and small vertical offsets. Winding number evaluations for the determinants of the banded matrices could have been used to detect an imbalance of poles and zeroes within the contour, but this was not done.

The poles representing normal mode or "trapped wave" solutions, will likely have phase velocities comparable with or greater than the slowest characteristic wave velocity for the medium, as for a "normally dispersive" medium (Achenbach, 1973). Unfortunately, a pole may conceivably exist which represents a mode with phase velocity less than the slowest characteristic velocity for the medium. A canonical example is the Rayleigh wave for a semi-infinite half space. The phase velocity of the Rayleigh wave is slightly lower than the shear wave velocity for the medium, and, thus, its pole lies just beyond the branch point for the shear wave number. To capture this type of pole, the contour of integration was extended about 10 to 20 percent above the largest characteristic wavenumber for the layer before entering the complex plane, following the recommendation of Frazer and Gettrust (1984).

To partially test the above procedure, two test runs were made for an assumed set of porous layer parameters. One run was with the demarcation point just beyond the wavenumber for the slowest wave, the other for twice the wave number of the slowest wave. No difference in the computed result was obtained. However, setting the demarcation point to less than the wave number of the slowest wave, while avoiding branch cuts, did in fact produce a change in the computed response, signifying the presence of an excluded pole. Rigorous testing and searching for poles was not carried out.

In practice, convergence of the integrands was achieved very rapidly, especially at large radius, for which the argument to the Hankel function changes rapidly with wavenumber. Often, only an additional 10 percent of computer time was required to complete the integration along the split portions of the contour. Moreover, Bessel functions of the first kind on the real axis are well behaved near the

origin; their use is more attractive than use of Hankel functions along the "Chapman contour" discussed by Frazer and Gettrust (1984) for which the path of integration passes through the origin.

Frazer and Gettrust (1984) discuss the use of Filon's method for approximating Hankel inversion integrals for rapidly varying Hankel functions and slowly varying integrands. The procedure involves approximating the non-Hankel portion of the integrand by a polynomial of order 1 or more over a finite increment of the argument. The procedure can give a substantial reduction of the number of integration steps for large Hankel function argument. The procedure was not attempted here, but combining the procedure with a Romberg (Press, 1986) integration scheme may yield substantial reduction of computer time.

A custom subroutine was developed for computing Hankel functions of the second kind for order 0 and 1, because no suitable package was available in the NAG, IMSL, or SLATEC libraries. Hankel functions of the first kind were computed by supplying the complex conjugate argument and taking the complex conjugate of the result. The subroutines are recursive implementations of the series representations and large argument approximations given by Stegun and Abramowitz (1964) and by Gradshteyn and Ryzhik (1965) for Bessel and Neuman functions of complex argument. The subroutines were checked against standard tables and found to be accurate up to at least 4 or 5 significant figures, except adjacent to the branch cut along the negative real axis where the large argument approximation is not valid. The dimensionless transition radius for kr between the series representation and the large argument approximation is 5.

4.4 Computers

Original model development was carried out on the Numerical Modeling Machine at the Center for Computational Seismology at Lawrence Berkeley Laboratories. For large scale runs, the model was transferred to the Cray II at Lawrence Livermore National Laboratories MFE computer facility. Finally, the model was transferred to the Cray-XMP, also at the MFE computer center. The Cray-XMP is about a factor of 2 faster than the Cray II, in spite of the widely advertised speed advantages of the Cray II. The reason for this is lack of large-scale vectorization and use of complex variables in the model. The Cray II is particularly well suited to real arithmetic and large-scale vectorization. Execution time on the Cray-XMP ranged from less than an hour to several hours, depending on model input parameters. The model is being considered for adaptation on the Center for Computational

Seismology's Convex computer, where execution time may be on the order of several tens of hours. In batch mode, this is not a disadvantage, and turn around time may be less than that achieved on the Cray-XMP, which involved several days, running at low priority.

The math package used on the Cray-XMP for solving the matrices was included in the OMNILIB library, a vectorized version of the SLATEC library, also resident on the Cray. The OMNILIB routines were significantly faster than the NAG or IMSL library routines, also available on the Cray. Though the OMNILIB routines were faster, there was some evidence of less numerical accuracy than that achieved with the NAG library, though the differences were minor.

4.5 Verification

The model was checked in a number of ways. By outputting the point load solutions reciprocity relations between the various point load Green's functions, as discussed in Appendix A, were verified. Since these involved comparison of the matrix Green's functions with Green's functions for the solid regions, essential consistency between the potential and displacement-stress formulations was verified. Symmetry properties also require that certain Green's functions for the response at the plane of symmetry must be zero for certain types of sources. For example, the transverse horizontal response at $z = 0$ due to a dilatational source was verified to be zero. During the early phase of model development, potential representations for a homogeneous porous layer were used to compute displacement stress vectors and derivatives. These were compared with those computed via numerical integration techniques, and were found to agree within 3 to 4 significant figures, thus verifying the basic displacement-stress representation presented in Appendix B.

The most important verification was obtained by setting the porosity to a very small value, and equating the fluid bulk modulus and mass with those of the solid material, and thereby simulating a homogeneous infinite solid region. The computed results for matrix point loads and gradient solutions were compared with exact solutions for a homogeneous elastic region obtained analytically by Fourier transforming the temporal solutions provided by Aki and Richards (1980, pg. 73-79). The results agreed to within 3 to 4 significant figures. The agreement verified the construction formulae for the point load Green's functions and their gradients, the displacement-stress formulation, the load representations, and the Hankel inversion procedure. In fact, an error in sign was detected and thereby corrected as a result of these comparisons.

No direct validation of the effect of fluid source solutions was attempted. Rather, detailed derivations and assumptions were checked and rechecked, and essential symmetries in the specification of the load components were verified. Most importantly, inspection of the response functions due to fluid volume sources satisfy physical intuition, and the solutions for a vertical point fluid load applied at the edge of the boundary agree exactly with the solution obtained for a vertical point matrix load applied at the same location, as they should, because of the nature of the boundary conditions. As will be discussed in the following chapter, the fluid load representation is verified by certain low frequency or long-time response behaviors for fluid volume sources located at the central plane of symmetry. Response characteristics for fluid supplies at the boundary edge were less satisfactory, however.

Chapter 5: Application to Hydraulic Fracture

Time integrated Green's functions are computed for a broad hydraulicly conductive fracture zone of width 60 meters containing a high porosity interior region of width approximately 10 meters. The model parameters roughly reflect the model parameters used by Mauk, et al (1987), for finite difference modeling of hydraulicly fractured rock, though the geometries differ considerably. The profile used by Mauk includes a 30 meter wide low velocity zone with a surrounding 15 meter wide transition zone between the low velocity zone and the surrounding competent rock. A major difference is that the model used by Mauk, et al, is two dimensional, including a finite size two-dimensional fracture zone. The present model is three dimensional, but homogeneous in the lateral directions. Because of the bounded two dimensional geometry used by Mauk and the unbounded three dimension geometry used here, the results obtained from the two approaches are not directly comparable. Further, Mauk includes a 3 millimeter wide crack filled with water along the center line of the low velocity zone, though fluid pressure is not modeled. A highly conductive region is simulated in the present model by the densely fractured region, using a maximum crack aperture of 1 millimeter.

5.1 Input Parameters

The parameters describing the fracture zone are summarized in Table 5.1. Dimensionless parameters are employed to maintain reasonable number size during numerical computation. Dimensioned "physical" parameters corresponding to the dimensionless parameters are also listed at the right hand side of Table 5.1. The normalizing quantities are the density and shear wave velocity of unfractured "infinite-Q" rock, and a nominal length. The quantities are:

Velocity:	3000m/sec	(Shear-Wave Velocity of Solid Rock)
Length:	1m	(Nominal Width)
Density:	2,500Kg/m	(Density of Solid Rock)

The normalizing time unit is thus 1/3000 sec, corresponding to a normalizing frequency of 3000 Hz.

Results for other frequency ranges, layer widths, etc., are obtained by appropriate scaling. For example, assuming a length scale of 0.1 m, the corresponding upper frequency limit rises from 256 Hz to 2,560 Hz.

Table 5.1 Input Parameters

Parameter	Dimensionless	Dimensioned
Solid Material Density	1.0	(2,500Kg/m^3)
Fluid Material Density	0.4	(1000Kg/m^3)
Solid Material P-Wave Velocity	2.0	(6,000m/sec)
Solid Material S-Wave Velocity	1.0	(3,000m/sec)
Fluid Material P-Wave Velocity	0.5	(1,500m/sec)
Solid Material Q-Factor	40.0	
Fluid Viscosity	1.33333×10^{-10}	(0.001N–sec/m^2)
β_0:	0.02	
β_1:	0.005	
β_2:	0.005	
High Porosity Region Width, $2z_f$:	10.0	(10.0m)
Conductive Fracture Zone Width, $2h$:	60.0	(60m)
Micro-Fracture Maximum Aperture, $2h_f$:	.001	(.001m)
Maximum Porosity	.03	
Micro-Fracture Aspect Ratio:	0.003333	
Tortuosity:	2.0	
Sinuosity:	2.0	
Frequency Step Size:	6.666667×10^{-4}	(2 Hz)
Number of Frequencies	128	
Upper Frequency Limit	0.085325	(256 Hz)

5.1.1 Porosity Profile

The porosity profile is given by:

$$\beta(z)=\beta_0 e^{-\frac{z^2}{z_f^2}}+\beta_1\left[1-\frac{z^2}{h^2}\right]+\beta_2 \tag{5.1}$$

The parameters h, z_f, β_0, β_1, and β_2, are listed in Table 5.1 as input parameters.

The porosity profile, illustrated in Figure 5.1, has a Gaussian shape near the center of the fracture zone, with concave downward parabolic profile for the flanks, decreasing to a finite edge porosity of 1/2 %.

The porosity profile is within the range of fracture porosities listed by Weber and Bakker (1981) for fractured petroleum reservoir rock. These authors indicate that some fractured chert porosities are 5% to 8%, with crack apertures of several millimeters and spacings of about 5 centimeters, and that important aquifers and oil fields are contained in fractured tuffs and igneous rocks with apertures ranging from "hairlines to nearly 4 cm width". They further indicate that in the USSR, oil fields exist in basaltic rocks containing cooling joints and "intersected vesicles" with fracture porosities of up to 6%. At the low end, fracture porosities of limestones, dolomites, and siltstones range from 0.01% to 0.3%. The profile employed here thus falls within the range of observed natural fracture porosities. Hydraulic fracturing would presumably increase these natural porosities, may simply induce connectivity between naturally occurring fractures, or introduce additional fractures.

5.1.2 Total Aperture and Fracture Conductivity

The total aperture, equal to the sum of the micro-crack apertures over the fractured zone, 0.6772 meters for a normalizing length scale of 1 meter, substantially larger than for a single discrete fracture. Part of the porosity can be rationalized as existing prior to fracturing. If the preexisting porosity is equivalent to that at the boundary of the zone, or 0.5%, then, over the 60 meter width of the fracture zone, the preexisting integrated aperture would be about 0.3 meters. The remainder, 0.3772 meters, would presumably be contributed by fracture zone expansion, though this may be much larger than normally assumed in models of hydraulic fracturing processes. Much of the contribution to the total aperture is in the flanks of the porosity profile from $z > z_f$ to $z < h$. The porosity in this region, controlled by the parameter, β_1, is selected to provide a shear wave velocity roughly comparable to that used by Mauk for the transition zone between the high porosity region and competent rock regions. An induced fracture zone expansion of 0.3 to 0.4 meters would imply a fracture volume of 3000 to 4000 cubic meters for a fracture extent of perhaps 100 x 100 meters, of the same order of magnitude as the fluid volume of 5,500 cubic meters discussed by Green and Baria (1987), with respect to hydraulic fracturing of a hot dry rock geothermal system.

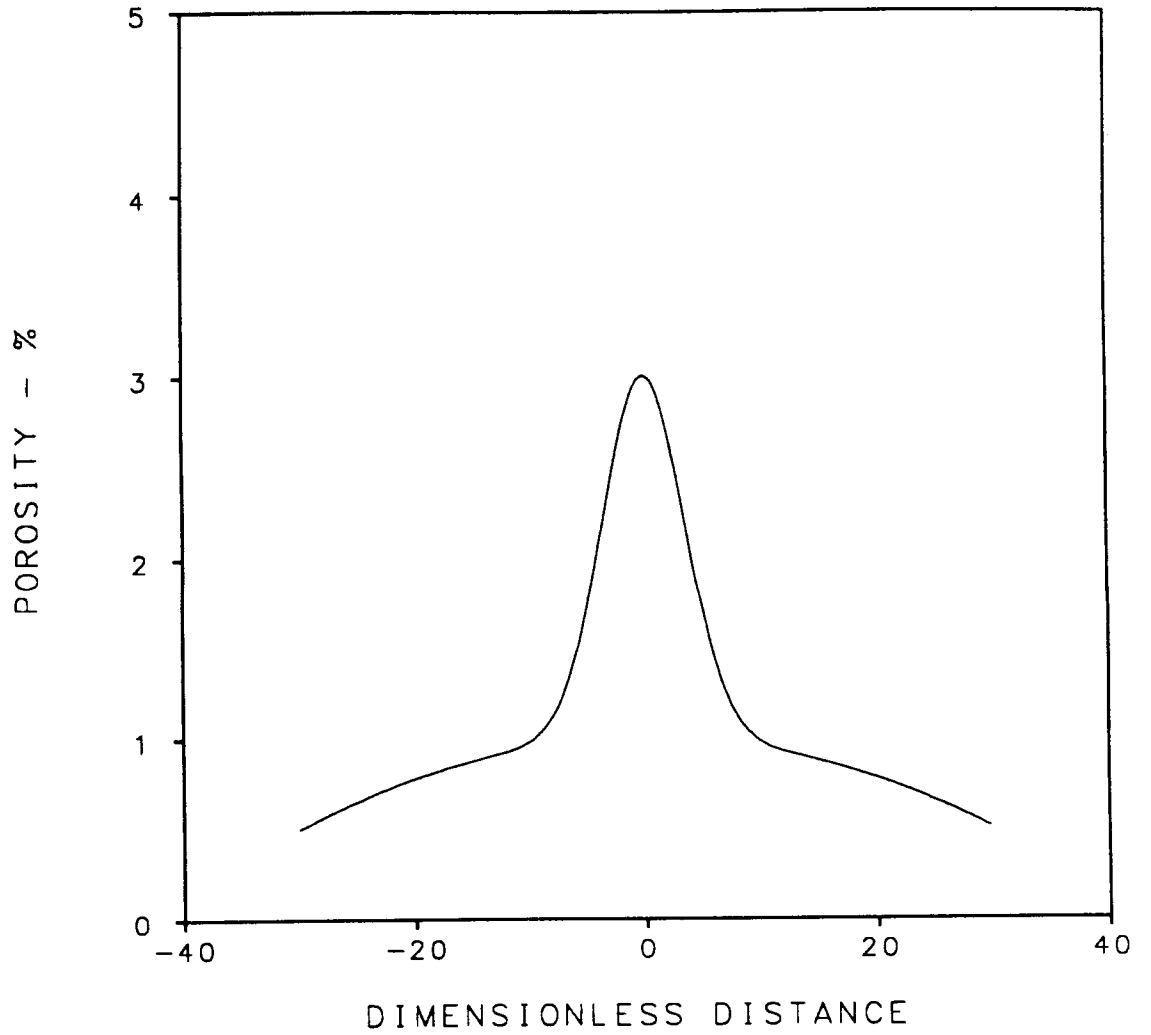

FIGURE 5.1 POROSITY PROFILE OF FRACTURE ZONE

The total aperture can be reduced substantially by reducing the size of the conductive zone, or by reducing its porosity. Lower fracture porosities can be handled by the model, though the assumption of connectivity becomes questionable without further reduction of crack aspect ratio. Reduction of porosity will increase the shear wave velocity in the low velocity zone, which increase can also be compensated by reducing the crack aspect ratio, which increases the crack density for a given crack aperture.

The fracture conductivity, C_f, is equal to the sum of the individual conductivities of the fractured zone. The conductivity of an individual fracture is given by wk_f (Palen and Narasimhan, 1981, p. 39), where $w = 2h_f$ is the fracture width and $k_f = \frac{1}{12}w^2 = \frac{1}{3}h_f^2$ is the fracture permeability (Narasimhan, 1987, p. 10). Thus, the fracture conductivity of an individual fracture is

$$C_f = wk_f = \frac{1}{12}w^3 \tag{5.2}$$

For a fracture aperture of 0.005 meter, the fracture conductivity is:

$$C_f = \frac{1}{12} \times (0.005m)^3 = 1.04 \times 10^{-8} m^3$$

The total fracture conductivity for a porous zone of interconnected micro-fractures is defined here as:

$$C_f = \int_{-h}^{+h} k_f(z)\,dz \tag{5.3}$$

where $k_f(z)$ is the intrinsic permeability of the porous material at position z (Biot, 1956):

$$k_f(z) = \frac{\beta(z)}{3\xi} h_f^2(z) \tag{5.4}$$

The dimensionless parameter, ξ, is the sinuosity of the porous material. The micro-crack aperture is assumed to vary in proportion to the porosity, so that the intrinsic permeability profile is:

$$k_f(z) = \beta^3(z) \frac{h_f^2(0)}{3\xi\beta^2(0)} \tag{5.5}$$

and the total conductivity may be expressed as:

$$C_f = k_f(0) \int_{-h}^{+h} \left\{ \frac{\beta(z)}{\beta(0)} \right\}^3 dz \tag{5.6}$$

The profile of the ratio of the intrinsic permeability to fluid viscosity is illustrated in Figure 5.2 in

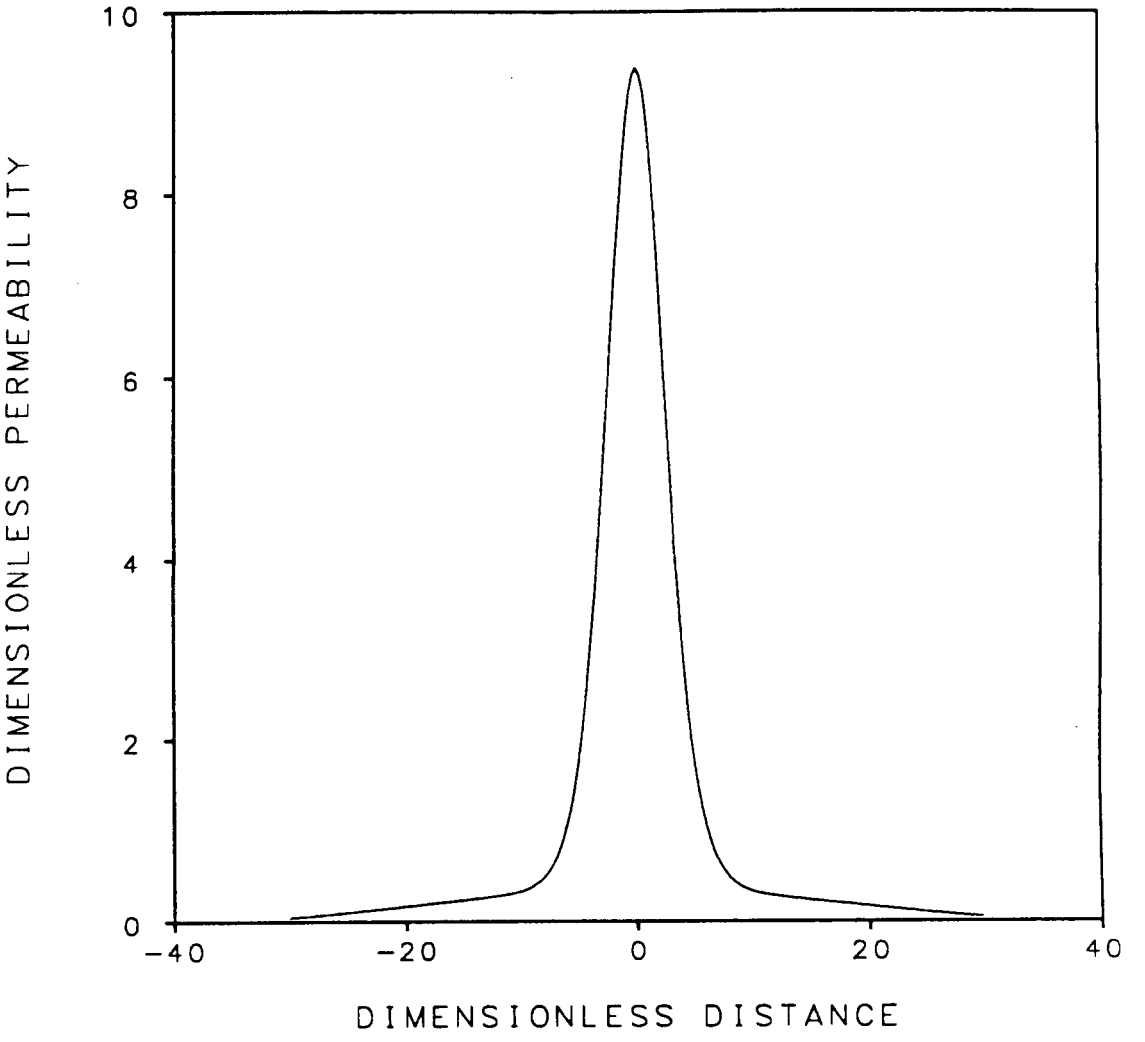

FIGURE 5.2 PERMEABILITY PROFILE: k_f/η

dimensionless form. The ratio is the usual Darcy coefficient of permeability (Jaeger and Cook, 1979, pg. 210), and scales as the ratio of the square of the micro-fracture aperture to fluid viscosity. The full scale is equivalent to approximately 1.333 millidarcy. For comparison, the permeabilities of limestones, shales, and siltstones, are less than 0.05 millidarcy, and the permeability of Berea sandstone is about 200 millidarcy (Jaeger and Cook, 1979, pg. 210). Note that the natural formation permeability is ignored in the model development.

The fracture conductivity varies as h_f^2 and is very dependent on the porosity profile, represented by the integral over the fracture zonal width. Most of the fracture conductivity is contributed in the high porosity region, $|z| < z_f$. The model parameters given in Table 5.1 are adjusted to give a fracture conductivity roughly similar to that of a 0.005 meter wide single fracture, of the same order of magnitude as that used by Mauk, et al.

5.1.3 Crack Density Parameter

The crack density parameter, ε, is directly related to the porosity profile for constant aperture cracks, as discussed in Chapter 2. The shape of the crack density profile is therefore represented by the porosity profile illustrated in Figure 5.1. The crack density varies from a low of about 0.25 at the edge of the fracture zone to a high of 1.43 at the center. These values represent dense fracture networks, necessary for the assumption of fluid conductivity. The crack density at the edge of the fracture zone represents a minimum value capable of supporting fluid conduction, though larger crack densities are necessary for reasonably isotropic flow (See Chapter 2).

5.1.4 Characteristic Velocity Profiles

The phase velocity profiles, computed from the real parts of the characteristic wavenumbers of the individual wave types, are presented in Figure 5.3a. The characteristic wavenumbers are those which would exist in an unbounded homogeneous porous material with constitutive parameters corresponding to those found at position z within the porous layer. Thus, the wavenumbers and phase velocities are not due to poles associated with bound-state modes, such as for a waveguide, but to the local properties of the material.

Frequencies of f=0.0006666... (2 Hz), f = 0.00666... (20 Hz), and f = 0.0666... (200 Hz), are represented in Figures 5.3a, b, and c, respectively. At 2 Hz, the phase velocities of the shear and fast

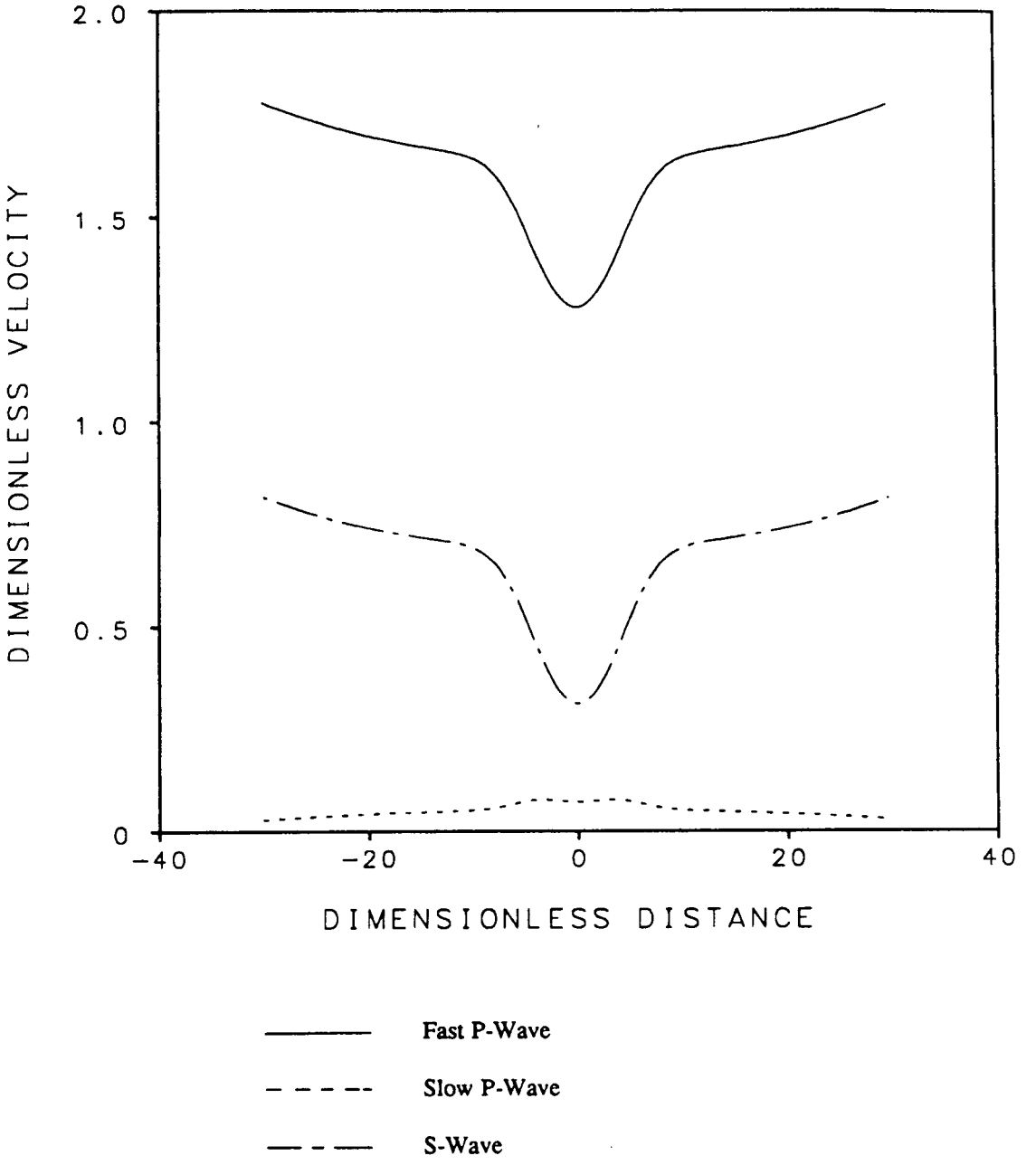

FIGURE 5.3A PHASE VELOCITY PROFILE AT FREQUENCY = .00066666... (2 Hz)

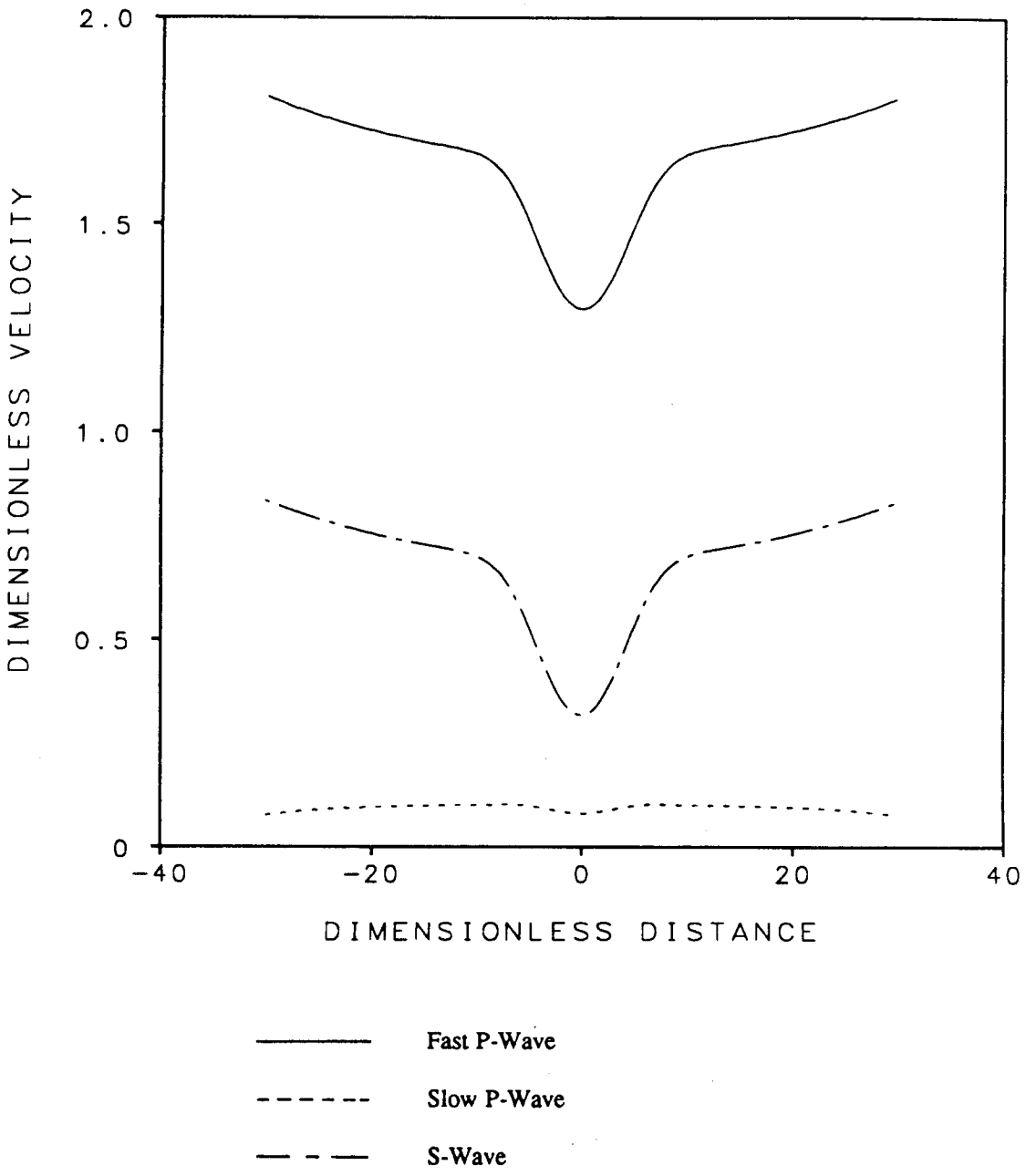

FIGURE 5.3B PHASE VELOCITY PROFILE AT FREQUENCY = 0.00666... (20 Hz)

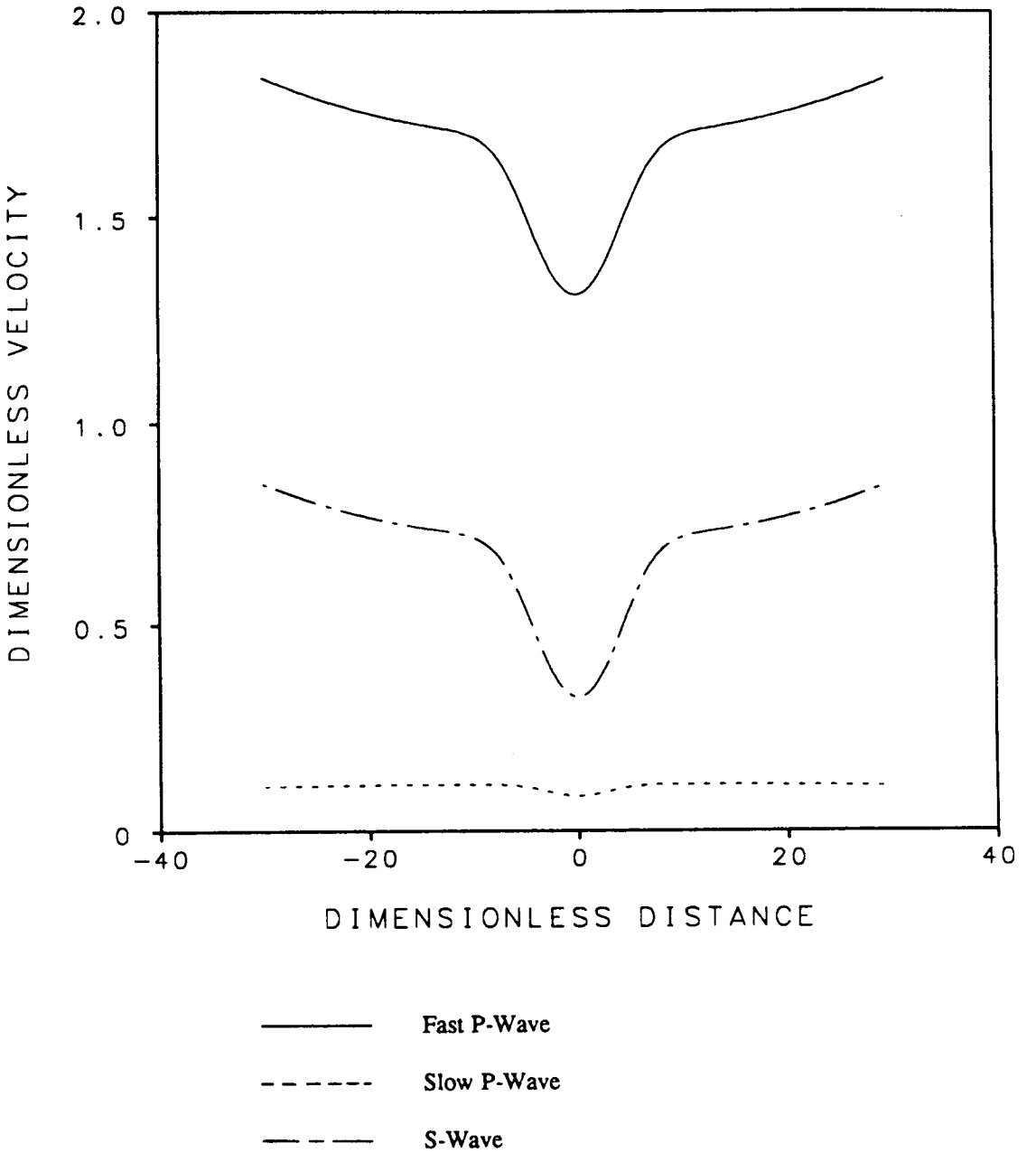

FIGURE 5.3C PHASE VELOCITY PROFILE AT FREQUENCY = 0.066666... (200 Hz)

mode compression waves are slightly less than the corresponding velocities at 20 Hz and 200 Hz. A constant-Q velocity dispersion for $Q = 40$ is incorporated in the input velocity data for the solid portion of the porous matrix, as discussed in Chapter 2. The reference frequency is 100 Hz, and at 2 Hz, the reduction of dilatational and shear wave phase velocities of the solid material making up the porous matrix is about 3%, comparable to the velocity differences observed between the dilatational and shear wave velocities of Figure 5.3a and Figure 5.3c. Also, the velocity differences are roughly unchanged as a function of position. Thus, the velocity differences between the fast compression and shear waves at 2 Hz relative to 20 Hz and 200 Hz are primarily due to the porous material's constant-Q velocity dispersion incorporated in the model, and not to relative motion between fluid and solid constituents.

As pointed out by Zimmerman (1985), for the porosities and constitutive parameters assumed for this case, the fast mode dilatational wave velocity is relatively insensitive to fluid bulk modulus. Although the fluid bulk modulus is much smaller than the that of the solid, the volume of the fluid is a small percentage of the total volume, so that the effective bulk modulus of the saturated cracked solid is approximately the same if the constituent fluid bulk modulus were set to infinity. The reduction of the fast dilatational wave velocity within the high porosity layer is thus due to shear stiffness reduction caused by increased crack density.

The slow compressional wave phase velocity is much lower than the fast compressional and shear wave velocities, and is much more strongly influenced by porosity profile and frequency, due to the viscosity of the fluid, and to the apparent bulk modulus of the fluid. As a function of position, the slow dilatational wave phase velocity increases slightly from its value at the fracture zone boundary, reaching a maximum near the edge of the high porosity central region. Within the high porosity region, the phase velocity dips to a local minimum. The overall velocity of the slow dilatational wave is roughly one fifth or less of the acoustic velocity of the fluid alone, because the pressure of the slow mode wave is relieved by the bulk compliance of the solid material making up the porous matrix.

If the porosity were increased substantially, the dilatational velocity of the fast mode would decrease to the phase velocity of acoustic waves in the fluid, so that the acoustic velocity of the fluid is recovered by the fast-mode wave for the mixture in the limit of unit porosity. In the limit of zero porosity, the fast-mode wave velocity approaches the dilatational wave velocity of the unfractured

elastic solid. Thus, the fast-mode wave is the principal propagating wave while the slow-mode wave is diffusive in character, and only resembles a propagating wave at sufficiently high frequencies. Regardless of the diffusive nature of the second- or slow-mode wave, its arrival is causal because of the inclusion of fluid density in the equations of motion.

5.1.5 Loss Factor Profile

The loss factor is the negative of the ratio of the imaginary part of the characteristic wavenumber to the real part, and represents the deviation of the complex characteristic wavenumber from the real axis. The logarithmic decrement is obtained directly from the loss factor by multiplying by 2π; the logarithmic decrement and loss factor are equivalent descriptors, except for the multiplier. Relationships between various descriptors of attenuation are discussed by Johnston and Toksoz, (1981).

Characteristic loss factor profiles are illustrated in Figures 5.4a, 5.4b, and 5.4c for frequencies of 0.000666... (2 Hz), 0.006666... (20 Hz), and 0.0666... (200 Hz), respectively. Throughout the fracture zone, the loss factors for the fast dilatational wave and shear wave are on the order of 1 per cent, controlled by the loss factor of the constant-Q material making up the porous matrix, for which the loss factor is approximately $1/(2Q) = 1/80$. For zero porosity, the loss factors for both the fast dilatational wave and shear wave would be identical. The profiles illustrated in Figures 5.4a, b, and c, indicate a separation of loss factors in the relatively high porosity region. The loss factor for the fast dilatational wave decreases significantly in the high porosity region, while the loss factor for the shear wave is essentially unchanged.

The loss factor for the slow dilatational wave is substantially higher than that of either the fast dilatational wave or the shear wave, because the fluid displacement is out of phase with the solid displacement for the slow dilatational mode. The slow dilatational mode loss factor increases with decreasing frequency, and, in the limit of zero frequency, the slow dilatational wave becomes diffusive, in which case the loss factor is infinite.

The loss factor for the slow mode wave becomes substantial near the edges of the fracture zone, where the crack aperture is 1/6 of the aperture at the center of the fracture zone. Near the center of the fracture zone, the loss factor is least, on the order of 10 percent, indicating that the slow dilatational wave is more efficiently propagated in the region of high porosity, as expected.

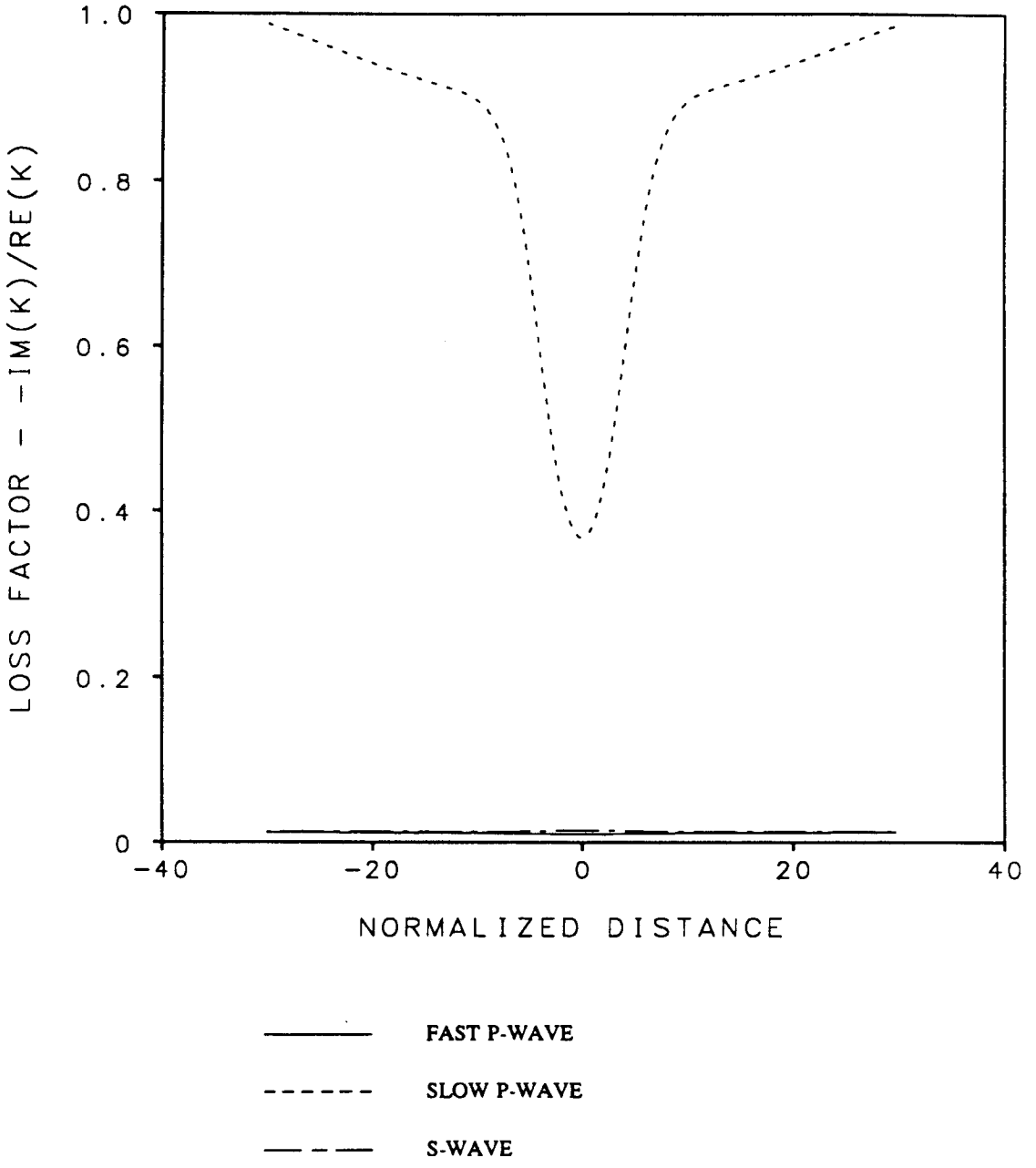

FIGURE 5.4A LOSS FACTOR PROFILE AT FREQUENCY = .00066666... (2 Hz)

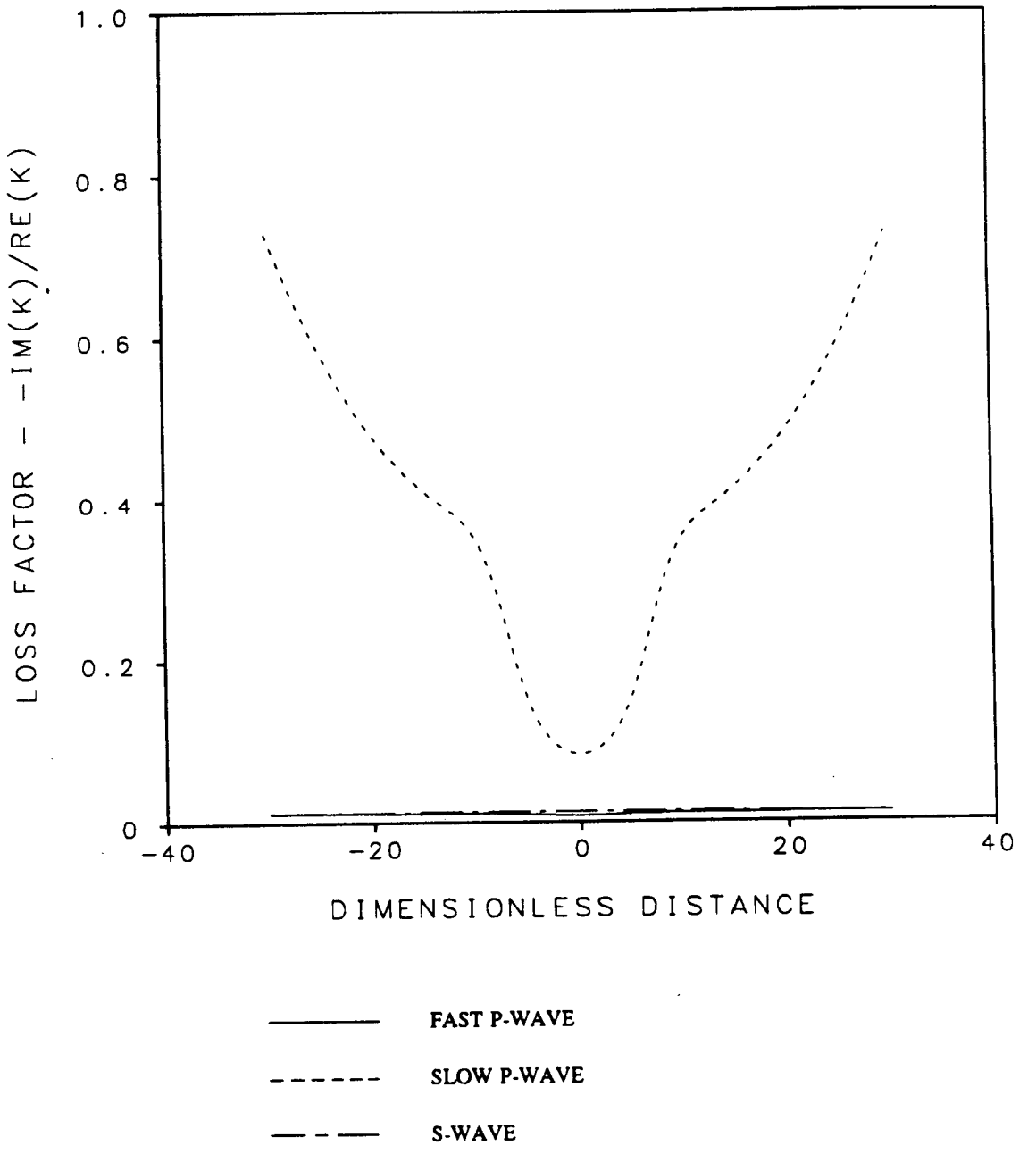

FIGURE 5.4B LOSS FACTOR PROFILE AT FREQUENCY = 0.0066666... (20 Hz)

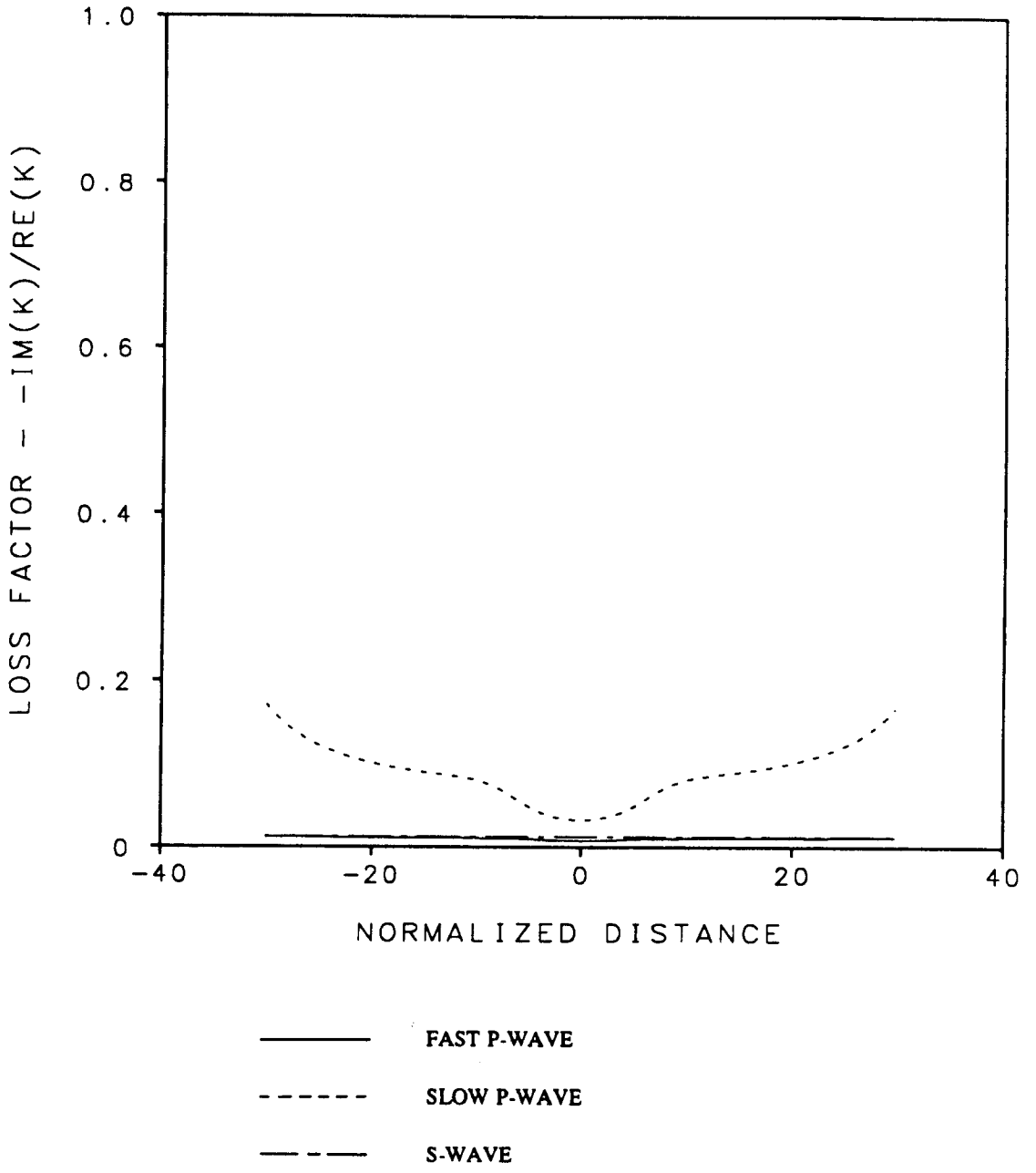

FIGURE 5.4C LOSS FACTOR PROFILE AT FREQUENCY = 0.066666... (200 Hz)

Attenuation rate profiles in dB per unit distance for each of the wave types are presented in Figures 5.5a, 5.5b, and 5.5c, for each of the above frequencies, respectively. The attenuation rate in dB per unit distance is related to the loss factor, Δ, by:

$$\alpha(\text{dB/unit distance}) = 8.686 Im(k) = 8.686 \Delta 2\pi \frac{f}{c_\phi} \tag{5.7}$$

where c_ϕ is the phase velocity of the associated wave, indicated in Figures 5.3a, b, and c.

The attenuation rates are very low for the fast dilatational wave, and moderate for the shear wave. The attenuation rate of the shear wave reaches a maximum at the center of the fracture zone, the plane of highest porosity and lowest shear wave velocity. At frequency 0.000666.. (2 Hz), the rate is roughly 0.145 dB per unit distance (per meter).

The attenuation rate of the slow dilatational wave is very much higher than for either the fast dilatational wave or shear wave, (Figure 5.5b). The rate is almost 6 dB per unit distance (per meter) at the edge of the fracture zone at 200 Hz, decreasing to roughly 1.5 dB per unit distance at the center. At frequency 0.000666... (2 Hz), the attenuation rate is roughly about 0.2 dB per unit distance at the center of the fracture zone. The attenuation rate profile for the slow dilatational wave thus indicates that the second mode wave will be most efficiently propagated in the high porosity region.

5.2 Fundamental Response Functions

Plots of computed response functions for Heaviside step point loads and point moments are presented in Appendices C, D, and E. Appendix C contains plots of the porous solid displacement and fluid partial stress response functions along the central plane of symmetry. These responses are perhaps the most interesting and novel information regarding the wave propagation in a fractured zone. Displacement responses are given in Appendices D and E for the solid exterior regions. Appendix D includes responses along a line perpendicular to the fracture plane, beginning at the boundary between the fracture zone and solid region. The receiver line is offset radially by 10 distance units. Appendix E includes responses along the upper boundary between the fractured zone and solid region, beginning at a radial offset of 10 units (10 meters). The results given in Appendix E are thus directly comparable with those of Appendix C with respect to propagation parallel with the fracture plane.

Each of the response functions are computed from the spectral Green's functions for delta function sources by first performing an inverse Fourier transform with the Cooley-Tukey FFT algorithm

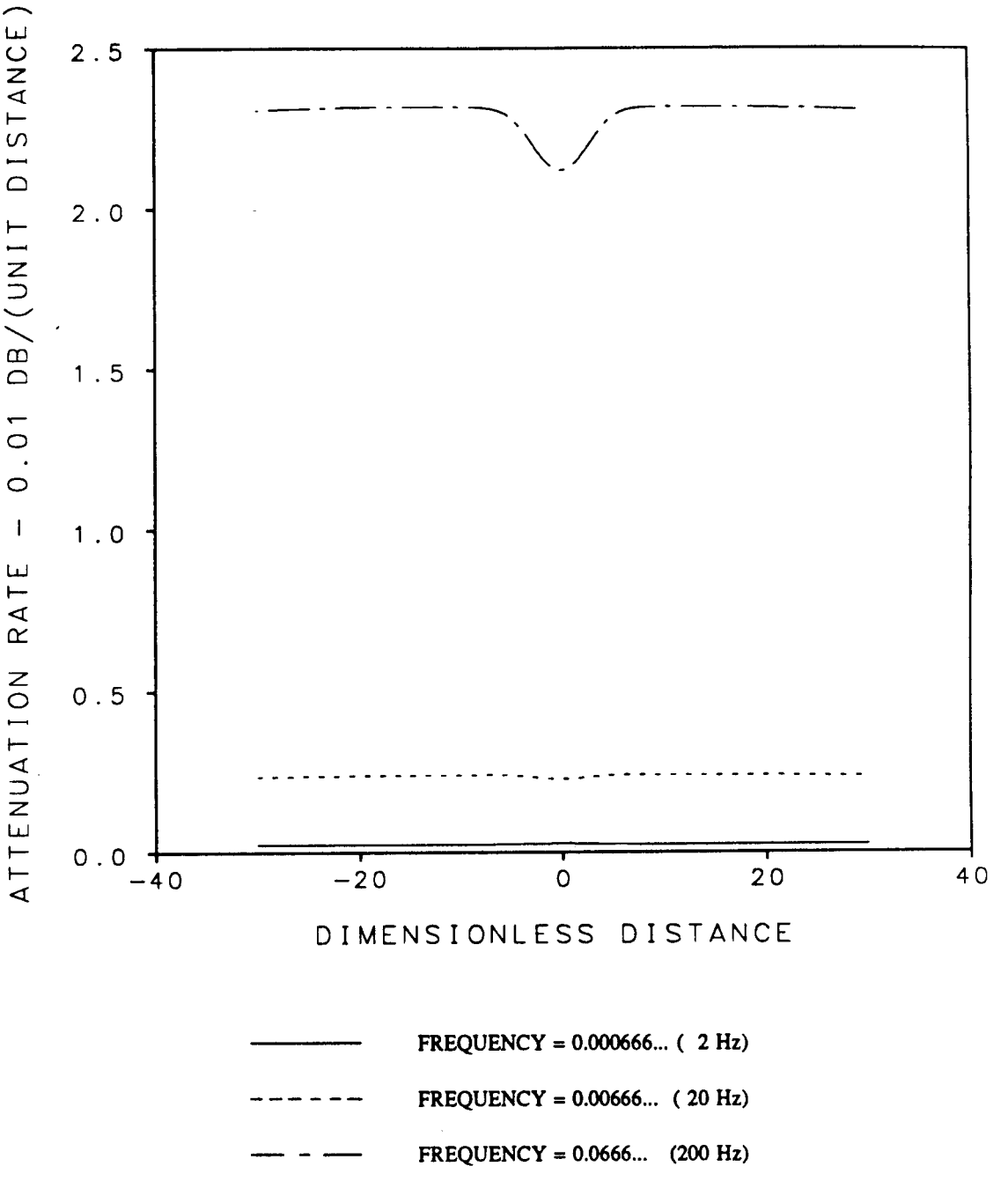

FIGURE 5.5A ATTENUATION RATE OF FAST P-WAVE

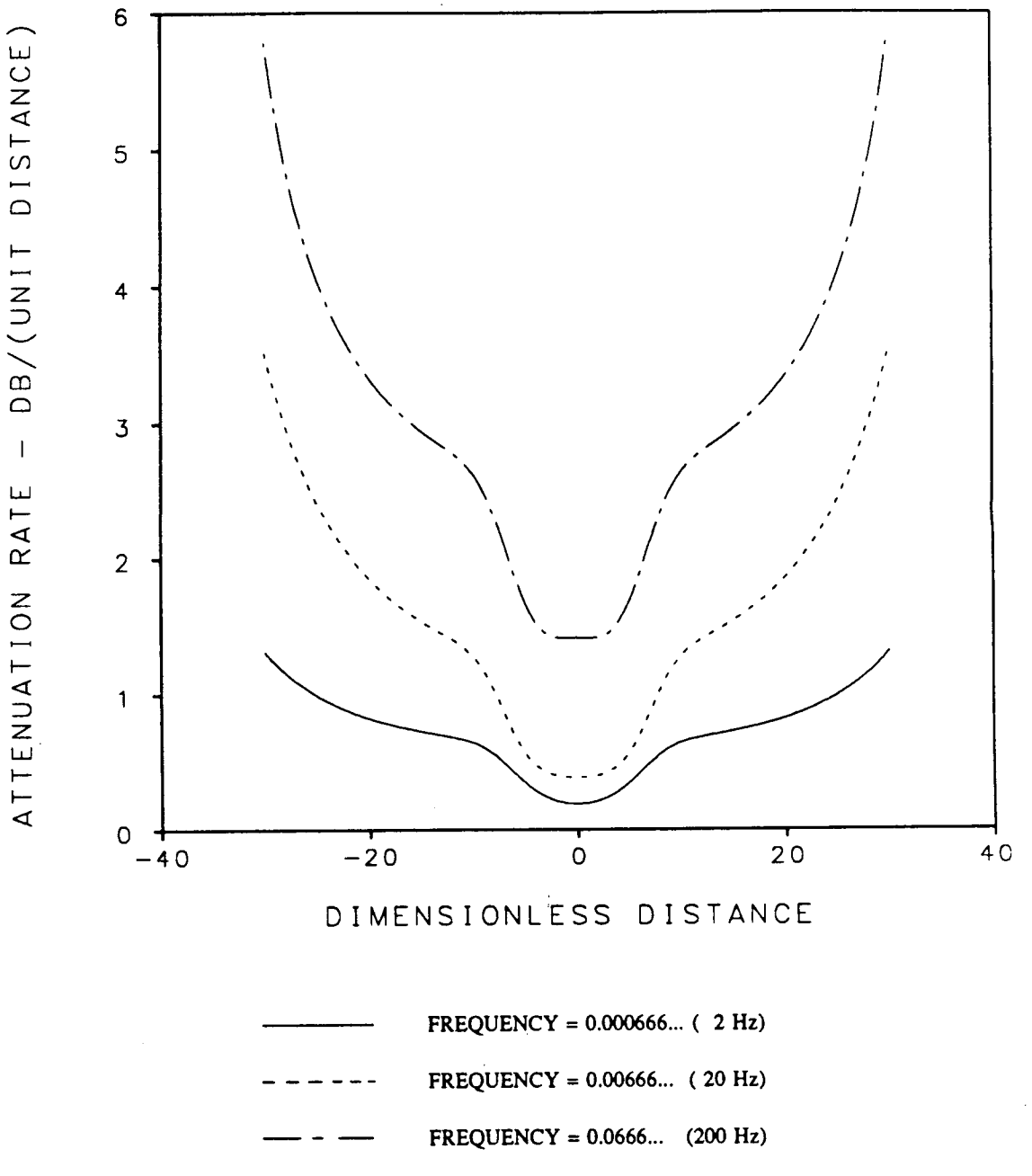

FIGURE 5.5B ATTENUATION RATE OF SLOW P-WAVE

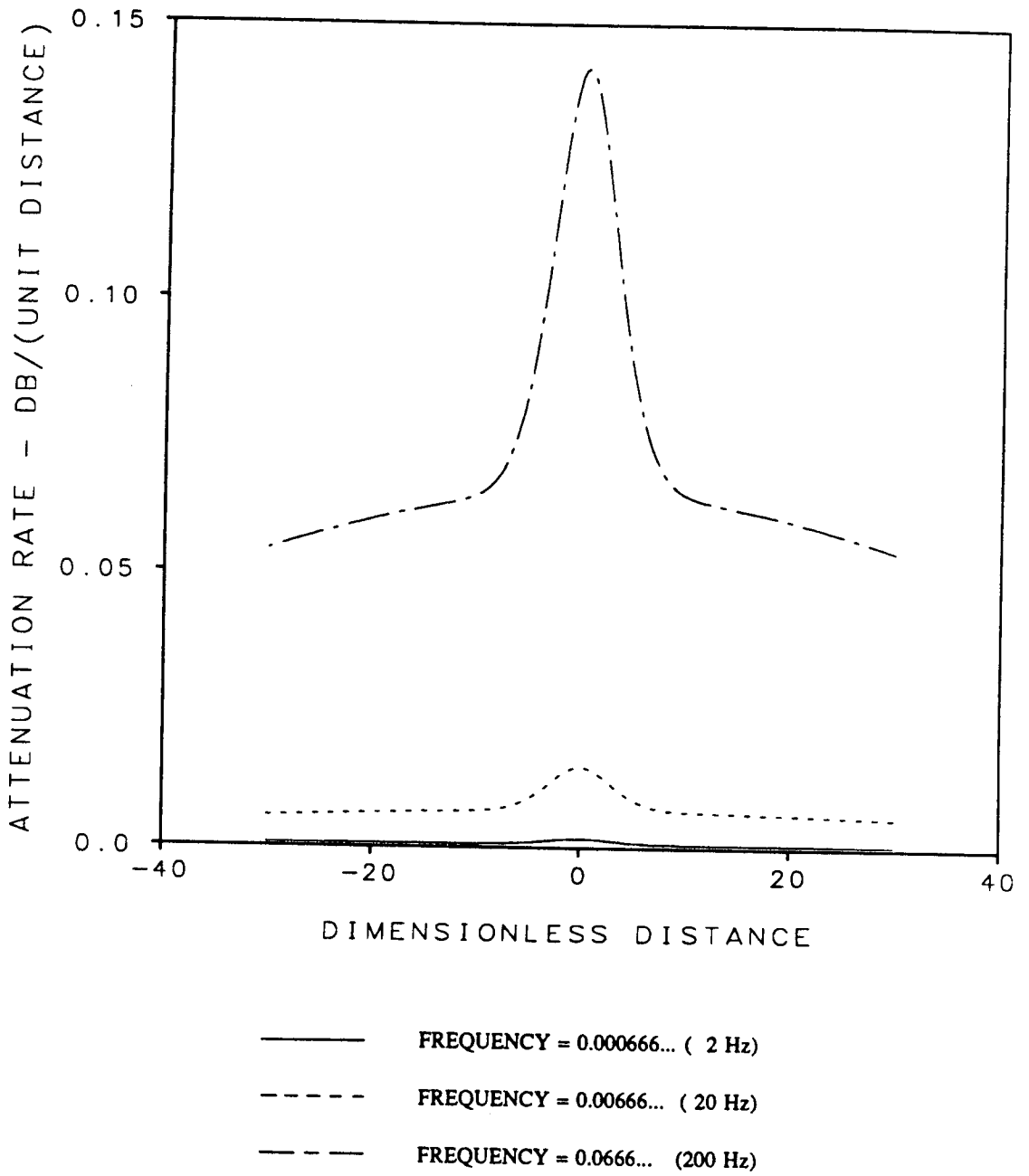

FIGURE 5.5C ATTENUATION RATE OF SHEAR WAVE

described by Claerbout (1976), and then directly integrating the temporal responses by a trapezoidal rule. Prior to Fourier inversion, a small linear phase shift corresponding to a time delay of less than one time step was included to enforce continuity of phase at the Nyquist frequency of 0.085 (256 Hz). An additional linear phase shift corresponding to a time delay of 5% of the total time window was included to provide a small quiescent time immediately prior to the first arrival and, thus, define an initial offset. The offset was then subtracted from the waveform so that the static displacement will be determined after integration of the waveform, necessary because of the lack of computed static displacements. Subtraction of the initial offset enforces zero slope for the integrated responses at the beginning and ending of the integrated waveforms. The long-time response is thus representative of the static displacement remaining after cessation of motion, provided that the responses attain quiescence within the time window.

The static displacements existing at the end of each trace do not reflect the actual static displacement if significant relaxation due to fluid flow occurs. The Green function response at the beginning and ending points of the time record are continuous and smooth, due to the nature of the finite Fourier transform. The effect is referred to as "wrap around." If significant relaxation persists near the end of the record, the effect will influence the computed early time record, and thus produce an acausal result. The effect can be reduced by reducing the frequency interval, thus increasing the time window.

Amplitudes of the traces are indicated by scale factors at the extreme right hand end of each trace. The scale factors are the vertical spans for the display range, equivalent to twice the maximum absolute value of the waveform.

The response amplitudes are dimensionless. Conversion factors for physical dimensions can be determined by recalling the definition of the Green's function. The displacement response is given by a convolution of the Green's function with the applied point load over time. Thus the unit of the displacement Green's function is distance per force-time, or, in MKS units, "meters per Newton-second". Because the normalizing quantities are the density of the competent rock, 2500kg/m^3, the shear wave velocity of the competent rock, 3000 m/s, and a length of one meter, the conversion factor for the displacement Green's functions is $0.1333...\times10^{-6}$ m/(N-sec). The responses given in the appendices are integrated over time, so that the conversion factor must be multiplied by an additional time unit of 1/3000 s. The conversion factor in MKS for the integrated displacement responses is thus

$44.444...\times10^{-12}$ m/N. For example, the span indicated in Figure C5.1 for the radial response of the porous layer at the center plane and radial distance 10 m due to a radially directed point load acting at the center plane is $0.10\times44.444..\times10^{-12}$m/N = 4.444... pico-meters per Newton.

The conversion factor for the gradients of the Heaviside response functions in physical units is 44.444... pico-meters per Newton-meter, obtained by dividing the factor for the point load responses by the reference distance, L.

The conversion factor for the Green's function for fluid partial stress has units of force per unit area per force-time, and the conversion factor for the response to the Heaviside point load is simply L^{-2}, $1m^{-2}$ for a normalizing distance of 1 meter. The conversion factor for the gradient of the fluid partial stress Green's function, integrated with respect to time, is $1m^{-3}$ for a normalizing distance of 1 meter. For example, the fluid partial stress responses given in Figure C4 for symmetric fluid moments are of order $10^{-3}m^{-3}$. Assuming a pressure drop of 5000 psi, or 35 mega-Newtons per square meter, over a volume of 0.01 cubic meter, the order of magnitude partial pressure response would be about 350 Newtons per square meter, or 0.05 psi, plus or minus an order of magnitude. The fracture (pore) pressure, is equivalent to the partial stress divided by the porosity, so that the fracture pressure at 10 m from a source at the central plane would be about 1.3 psi for 3% porosity, small considering the magnitude of hydraulic fracturing pressures, but well above the resolution of piezo-electric pressure transducers.

The time axes are in units of L/V, where L is the normalizing distance and V is the normalizing velocity. Again, for the application here, these are 1 m and 3000 m/s, respectively. Thus, the time axis for the traces are units of 1/3000 s, and the maximum time span for each trace is thus precisely 0.5 second, corresponding to the real frequency step size of 2 Hz for the spectral response functions.

5.2.1 Center Plane Responses

The displacement responses of the porous structure for moments acting on the porous structure are presented in Figures C1.1 through C1.10. Response functions are given for two sources: one at the central plane of symmetry, and the other at the upper boundary. Symmetry can be used to determine the responses due to sources at the lower boundary; the conversion being a multiplication by +1 or −1, depending on symmetry.

Some of the responses are trivial for sources located at the central plane of symmetry. An example is the radial displacement due to a symmetric shearing moment, M_{rz}. Other examples include the transverse horizontal response to a symmetric $M_{\theta z}$ moment, designated as θ-Z in Figure C1.6, and the vertical displacement responses (Figures C1.7, C1.8, and C1.9) to the diagonal moment components, M_{rr}, $M_{\theta\theta}$, and M_{zz}.

Similarly, the fluid partial stress responses in Figure C2.4 to the symmetric M_{rz} moment component acting on the porous structure at the center plane are trivial, as well as the vertical displacement response to isotropic fluid moments acting at the center plane. Other trivial responses are obtained as a result of symmetry for some of the responses to point loads.

The fluid partial stress response in Figure C2.1 contains acausal arrivals propagating at the second mode velocity from spurious or fictitious sources. These sources are the result of insufficient step size in the Hankel inversion process. Reduction of wavenumber step-size, or use of a sufficiently small constant wave-number step rather than a constant slowness step will, presumably, reduce or eliminate this effect, though at the cost of substantial computer time. Also, higher precision may be required in solving the boundary value problem in vertical coordinate, z, in the neighborhood of the second mode pole. During Hankel inversion, the contour of integration proceeds into the complex plane at just beyond the second mode pole; the acausal arrivals may be related to this.

Most of the responses given in Appendix C exhibit quiescent long term behavior, including a static displacement. Some of the response functions are not quiescent at long time, but appear to relax, presumably because of fluid diffusion. Principal examples include the displacement and fluid partial stress responses to isotropic fluid moments acting at the upper (or lower) boundary, illustrated in Figures C3.1 through C4. Moreover, the responses tend to exhibit a substantial static offset at long time for the fluid moment source. When computing the response to a fluid injection, the static displacement should be canceled at long time by combination with the response due to an isotropic moment acting on the porous matrix, or structure. This is discussed below with respect to computed responses to fluid dilatation.

5.2.2 Solid Region Responses

Responses at positions along a line normal to the fracture plane, each separated by 10 distance units (10 m), with the first position at the upper boundary, $z = h$, and offset from the z-axis by 10 units (10 m), are presented in Appendix D. These results illustrate the radial, transverse, and vertical responses which might be measured in a borehole intersecting the fracture zone normal to the fracture plane of symmetry. Responses along receiver lines offset at greater distances from the vertical axis were also computed, but are not presented.

Each figure in Appendix D contains responses for three source locations. The upper set of traces is for a source a $z = h$, the middle set for a source at $z = 0$, the central plane of symmetry, and the bottom set for a source at $z = -h$. The first trace (labeled as #1) of the top set is with receiver position on the same elevation as the source. In this case, some of the response functions would be trivial if not for the presence of the fracture zone. An example is the radial displacement response to a symmetric M_{rr} moment component, illustrated in Figure D1.4. In this example, the response is an order of magnitude less than the responses at higher elevations above the upper boundary.

Point load responses are given in Figures D3.1 through D3.5 for loads applied to the porous solid. The radial response to radial point loads and the transverse response to transverse point loads are similar in shape regardless of source position, though differ significantly in amplitude. These responses are primarily SH in nature (pure SH for the transverse-to-transverse response) due to the primarily vertical direction of propagation. At zero radial offset, both responses would be identical. The high degree of similarity of these responses provides a partial check of the correctness of the overall algorithm.

The transverse displacement response to a transverse point load is a pure shear-horizontal SH response, and thus can be used to evaluate attenuation of shear waves through the fracture zone. The static amplitude at the upper boundary is about 0.0024 for the source at the lower boundary, about distance 60 below the receiver. This can be compared with the response at distance 50 above the upper boundary for the source at the upper boundary to evaluate the attenuation of the shear wave by the layer. The discrepancy in travel distance, 60 versus 50, is minor for the purpose of qualitative evaluation. The static and dynamic amplitudes of the two responses are of the same order-of-magnitude, indicating that the fracture zone does not substantially attenuate the wave, in spite of the very low shear wave velocity in the high porosity zone. This may be because the smooth, Gaussian

shaped, velocity profiles used in the model are not very reflective.

5.2.3 Responses Along the Upper Boundary

Responses along the upper boundary at $z = h$ to Heaviside step point moments and point loads are given in Appendix E. Three source positions are again represented; one at $z = -h$, one at $z = 0$ and the third at $z = +h$. The receiver locations are each separated by 10 distance units, beginning with receiver #1 at $(r, z) = (10,30)$. Thus, the final receiver location, receiver #6, is at $(r, z) = (70,30)$.

The moment sources, M_{rr}, $M_{\theta\theta}$, M_{zz}, etc., are designated as R-R, θ–θ, Z-Z, etc.

The radial responses in Figure E1.4 to a symmetric M_{rz} moment component and the transverse responses in Figure E1.6 to a symmetric $M_{\theta z}$ moment component acting on the porous solid at the upper boundary are slightly noisy. The static displacements are ill-defined, and there is evidence of a reverse traveling acausal arrival at the second mode dilatational velocity of the fracture zone at the center of the layer. These results are obtained with the same LU decomposition as all of the other results. The "noise" is probably due to insufficient step size during Hankel inversion.

Point load response acting on the porous structure are presented in Figures E3.1 through E3.5. The point load responses all exhibit significant static displacements, particularly the diagonal components (radial response to radial load, etc.) The transverse response in Figure E3.2 to a transverse point load is a pure SH response, and includes a near-field effect propagating at P-wave velocity. The reflection and transmission of pure SH motion across the layer are contained in this figure. The amplitude of SH wave propagation is not significantly attenuated by transmission across the layer, when the effect of propagation distance is removed.

The radial displacement responses in Figure E3.4 to vertical load at $z = h$ and the transverse displacement responses in Figure E3.5 to radial load at $z = h$ would be identically zero with the layer absent. The essential condition of reciprocity between these two sets of responses is satisfied if a sign change for interchanging source and receiver is included.

Reciprocity is satisfied by the responses at the center plane to point loads at the upper boundary, and the responses at the upper boundary to point loads applied to the porous solid at the center plane.

Examples include the radial responses to radial load components, Figures C5.1 (top), and E3.1 (center), or the center plane vertical response to a radial load, Figure C5.4 (top), and, with a change of sign, the upper boundary radial response to center plane vertical load, Figure E3.4, and so forth. The satisfaction of reciprocity indicates that point loads at various locations are being applied in a consistent manner and that the two methods of constructing the Green's functions are equivalent. Recall that the upper boundary Green's functions are constructed from potential coefficients and that the center plane Green's functions are constructed from the displacement-stress components.

Displacement responses to point loads applied to the fluid were calculated for finite frequencies, but are not presented here. Reciprocity between solid material displacement responses to fluid point loads and fluid displacement responses to solid material point loads were not checked because the fluid displacements were not computed.

5.3 Responses to Isotropic Dilatational Sources

Responses are presented for fluid and porous matrix isotropic dilatational sources, both with Heaviside step function time dependences. The responses are constructed with the gradients of the Green's functions according to the representation formulae given in Appendix A. The primary purpose for this section is to illustrate the model's capability for modeling responses to fluid dilatation, produced by injection. For comparison, responses to unit matrix dilatations are included also. A second purpose for presenting responses to isotropic sources is that the isotropic source is convenient for illustrating arrival times versus distance and receiver radial offset.

In the simplest case, fluid is pumped into the fracture zone and the decay of fluid pressure with time after shut-in is observed and used to infer certain properties of the "fracture". An alternative is to inject fluid from the primary borehole and monitor fracture fluid pressure and solid material displacement at an observation well. The model developed here can be used to study the high-frequency characteristics of such cross-hole tests.

The responses to unit dilatations of the fluid phase are presented here. Responses to unit volume fluid injections are obtained by dividing the response to a unit fluid dilatation by the porosity at the point of injection. That is, given a certain porosity, the volume of "pure" fluid injected is equal to the product of the dilatation of the porous "fluid" and porosity.

The responses were computed in a manner slightly different from that used for computing the fundamental step responses presented in Appendices C, D, and E. In the former case, direct numerical integration of the temporal Green's tensors after first subtracting the initial offset of the delta function response prior to first arrivals produced zero-slope of the step function response at the edges of the time window, a non-physical characteristic if significant relaxation is occurring over times longer than the window.

As discussed in Chapter 3, and in Appendix A, representing isotropic matrix or fluid dilatations requires determining responses to isotropic moments for both the porous matrix and fluid. With the present computer code, calculating the zero-frequency spectral component for isotropic fluid moments requires evaluating the r_1^S, and r_2^S, displacement-stress components for the horizontally directed fluid point load component, S. This load component is singular at zero frequency, and the computer code is incapable of handling this condition, although a solution for the fluid dilatation must exist. The code has not been revised to handle this condition. If the zero-frequency spectral components can be determined, then numerical Fourier inversion followed by direct numerical integration will produce the step responses to porous matrix dilatations, though the effects of wrap-around will still remain. Because of persistent or long-time responses due to fluid flow, producing relaxation, estimates of the zero-frequency spectral components were made.

In lieu of direct numerical evaluation of the zero-frequency component, various interpolation schemes were attempted. The routine, RATINT.FOR, discussed by Press, et al (1986), was used with little success for interpolating over the real parts of the spectral components for both positive and negative frequencies, giving an indication of a singularity at zero frequency. The analogous polynomial interpolation routine, POLINT.FOR, also discussed by Press, et al (1986), was used with stable performance, but unrealistic results. Recognizing that the spectral components are complex, the routine RATINT.FOR was converted to complex double precision arithmetic and used for rational fraction interpolation in the complex plane. The results were very encouraging, usually giving realistic static displacement responses to moments applied to the porous solid after direct numerical integration of the delta function responses without first subtracting the initial offset (the usual procedure). In the presence of significant relaxation due to fluid flow, offsets at the end of the time window were usually between zero (obtained by direct numerical integration of the responses with trivial zero-frequency spectral component) and the offset obtained by direct numerical integration after first subtracting the initial offset of the delta-function response. The procedure is not fool proof, and where unrealistic

results were obtained, the standard temporal integration with zero initial offset was used. In practice, the results obtained with rational fraction interpolation were qualitatively more favorable than those obtained by initial offset removal for only a small number of cases, giving roughly equivalent results for most of the remaining cases. Those cases which gave the greatest difficulty for rational fraction interpolation were also those cases subject to significant fluid relaxation. In view of this, rational fraction interpolation is not necessarily more effective than initial offset removal, though it is interesting from a mathematical point of view.

The static displacement produced by injection of fluid over a finite time interval without a static porous matrix dilatation is expected to be identically zero, because the porous matrix should relax and relieve stresses built up during injection. A zero static displacement requires that the zero-frequency component of the spectral Green's function (impulse response spectrum) must be identically zero. However, substitution of zero for the zero-frequency component, use of discrete Fourier inversion, followed by numerical integration, gives a step-function response which is zero at both ends of the time window, but with non-zero slope at these endpoints due to wrap-around.

As an experiment, rational fraction interpolation was applied to the responses to fluid volume sources and was noticed to give "reasonable looking" results. This is surprising, because the interpolator produces a non-zero estimate where zero is expected. Because the results obtained for fluid volume supplies using rational fraction interpolation appear in many cases to be more realistic than those obtained either by zeroing the zero-frequency spectral component prior to Fourier inversion, or by initial offset removal prior to numerical integration, the interpolation procedure was applied to fluid volume sources as well, though no theoretical justification is provided. Further, the effects of wrap-around are not necessarily removed, and, in several cases, the results were qualitatively less desirable than those obtained by initial offset removal.

5.3.1 Responses Along Center Plane

Examples of responses along the center plane of the fracture zone to a unit fluid dilatation are provided in Figures 5.6A through Figures 5.6C for the radial displacement, vertical displacement, and fluid partial stress, respectively. The transverse matrix displacements are trivial. The first receiver location is at a radius of 10 units (10 meters), and each of the receivers are separated by 10 units (10 meters).

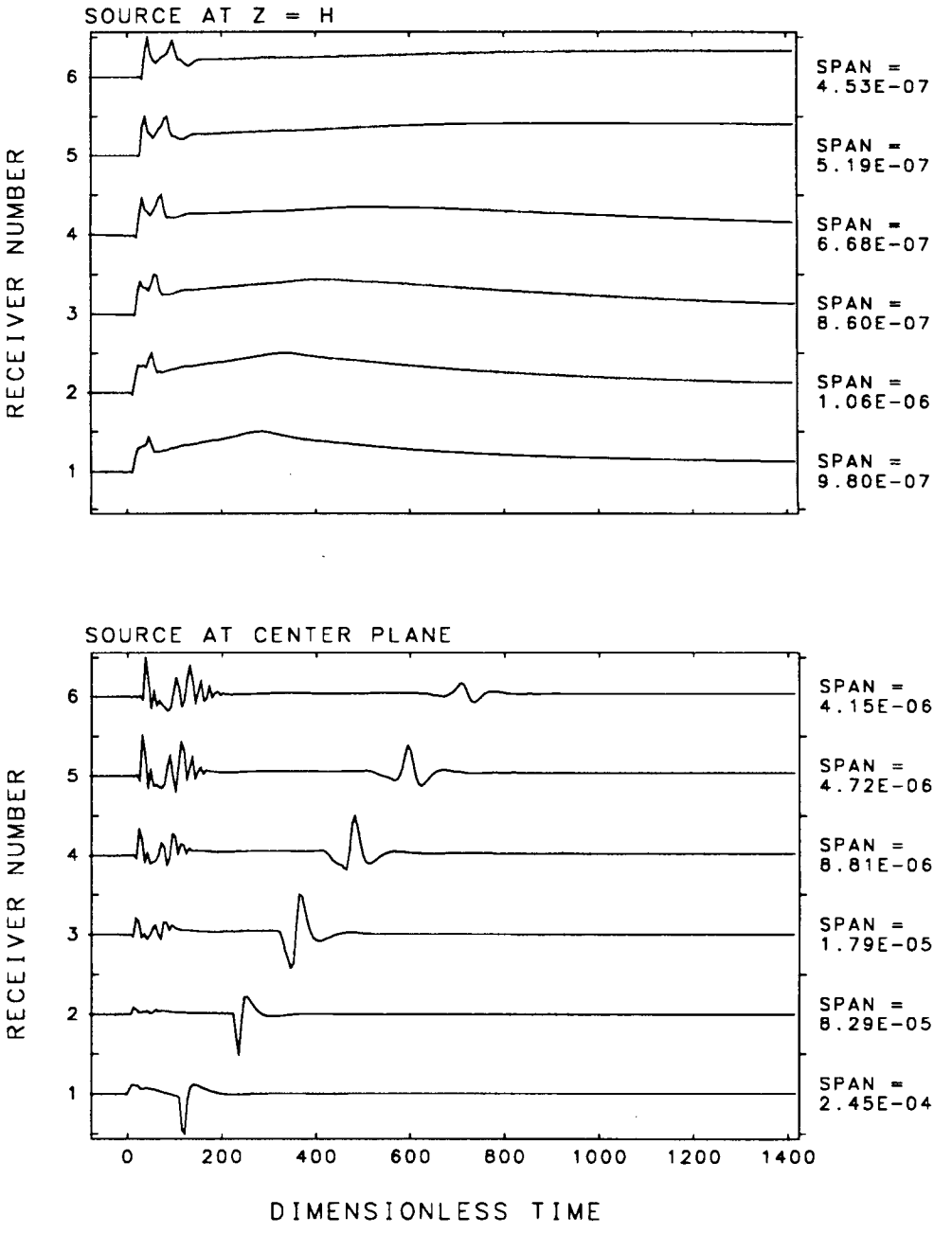

FIGURE 5.6A RADIAL RESPONSE AT CENTER PLANE TO TO A UNIT VOLUME FLUID DILATATION

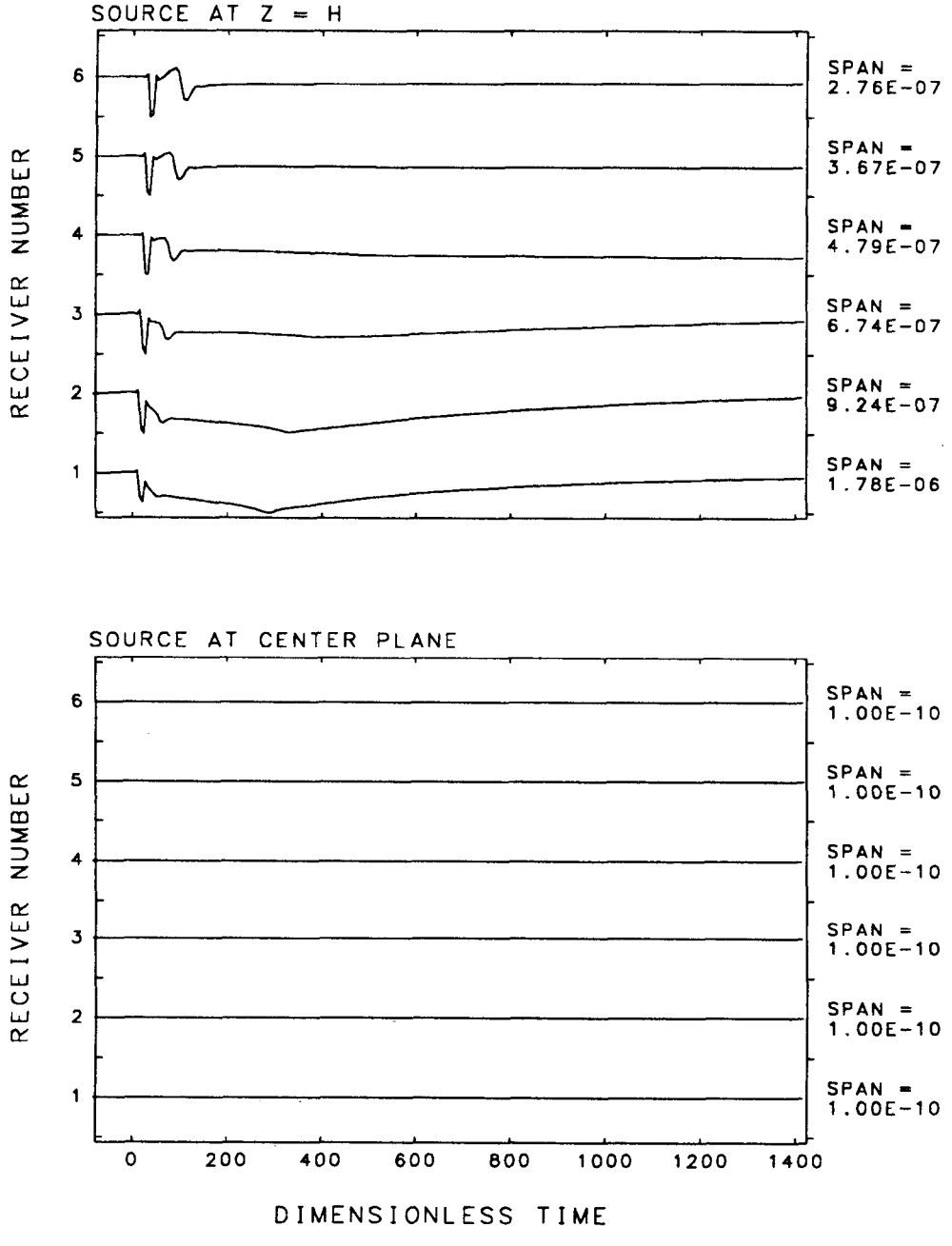

FIGURE 5.6B VERTICAL DISPLACEMENT RESPONSE AT CENTER PLANE TO A UNIT VOLUME FLUID DILATATION

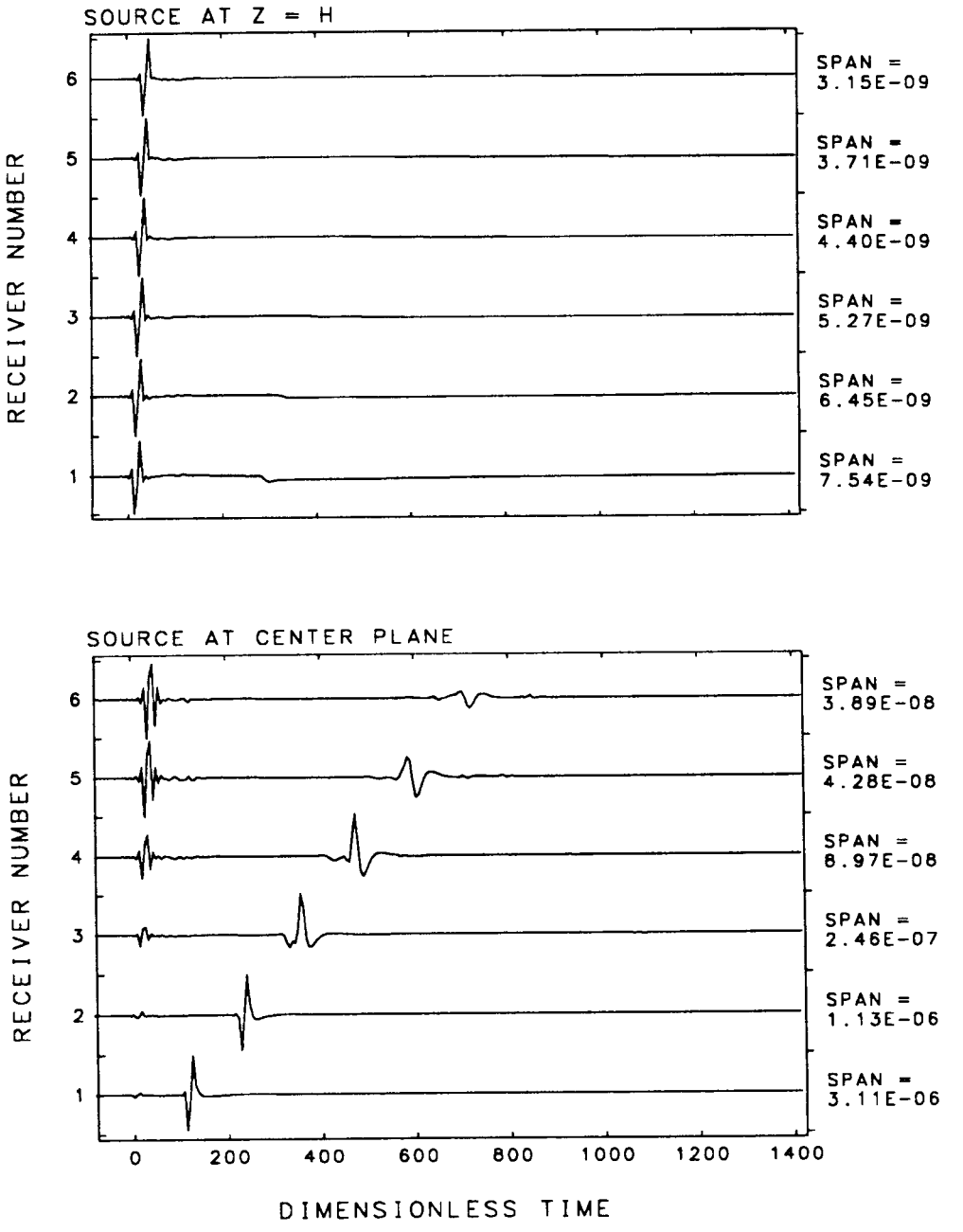

FIGURE 5.6C FLUID PARTIAL STRESS RESPONSE AT CENTER PLANE TO UNIT VOLUME FLUID DILATATION

Two sets of responses are given in each figure. The lower set is for a source at the origin, located on the center plane at $z = 0$, and the upper set is for a source at the upper boundary of the fracture zone, $z = h$.

The responses contain initial P-wave arrivals with velocity corresponding to that of a head wave propagating in the high-velocity portion of the layer or at the boundary with the solid region, the region of highest P-wave velocity. Immediately following the P-wave, an SV-wave appears, corresponding to a critically refracted shear wave propagating in the outlying region, for the source at the upper boundary. For the source at the center, strong oscillatory responses occur, produced by a trapped mode in the layer.

The most notable feature of the response functions for the fluid dilatational source is the arrival of a pulse propagating at a velocity consistent with the second mode P-wave velocity for the saturated porous region. The arrival is sharply defined for the source at the center, but is highly diffused for the source at the upper boundary, where the porosity and micro-fracture apertures are significantly lower than at the center of the layer. The second mode wave must propagate over a substantial distance of 30 units before reaching the high porosity region. The arrival of the second mode wave from the upper boundary is marked by the broad peak occurring at between time 250 and 300, the time required for the wave to travel from the upper boundary to the first center plane receiver. For the upper boundary source, there exists considerable relaxation of the porous matrix after arrival of the second mode wave. Preceding the second mode arrival, the matrix displacements "ramp" to their extreme values.

For the fluid partial stress, given in Figure 5.6C, the second mode response is strongest for the source at the center, and barely observable for the source at the upper boundary, for which the head-wave produces the greatest fluid partial stress response. The fluid partial stress response to a source at the center plane is dominated by the second mode arrival for distances up to about 50 units from the source (50 meters for the example scaling used here.) In a field situation, low-pass filtering of the data would substantially reduce the amplitude of the short period responses produced by trapped modes and head-wave arrivals, allowing the second mode arrival to be more easily identified.

The response to isotropic porous matrix dilatations are presented in Figures 5.7A, 5.7B, and 5.7C. A remarkable feature is that the responses are very similar in shape to the responses to fluid dilatations, but differ substantially in amplitude. The ratio of the bulk modulus for the porous matrix, $A + 2N/3$,

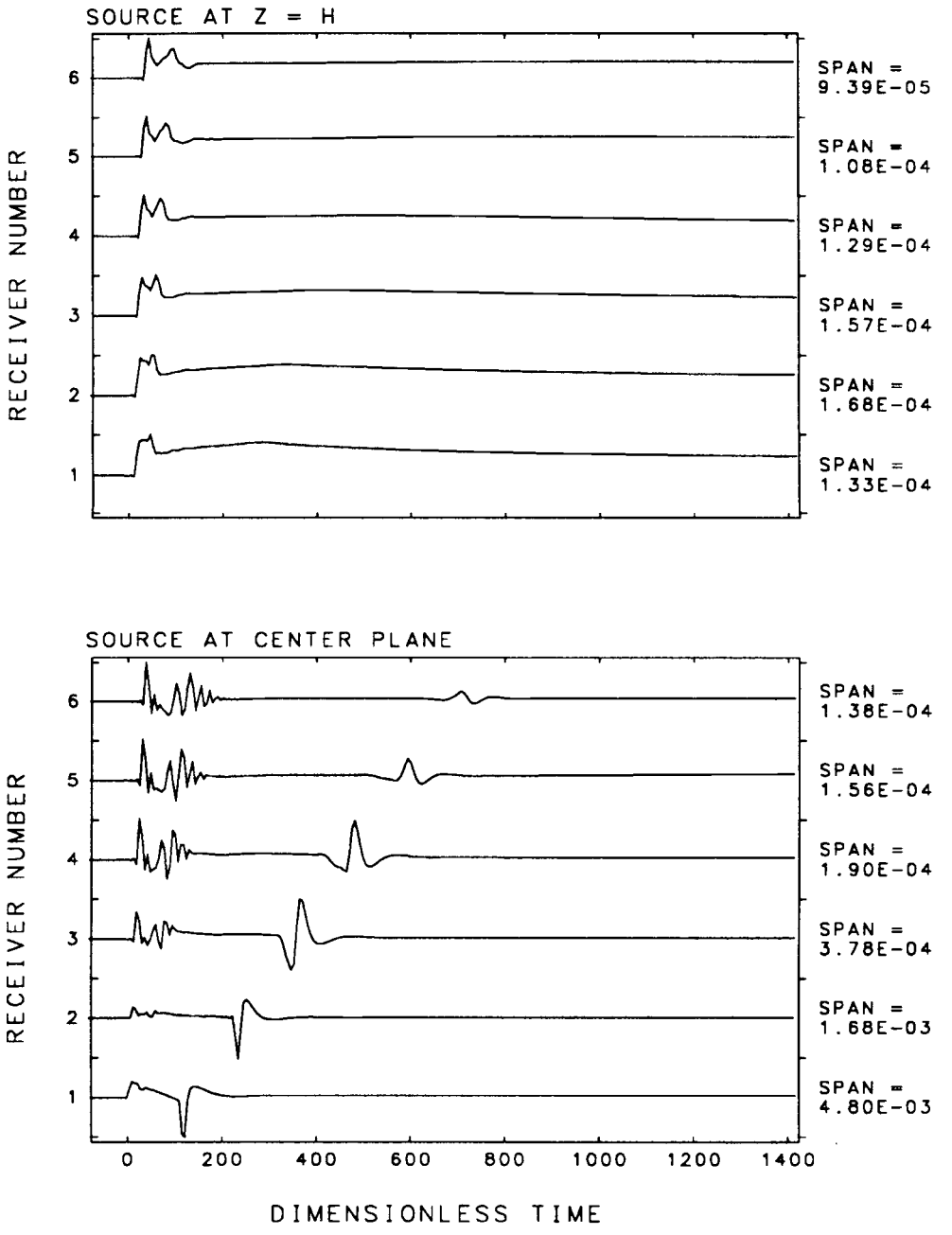

FIGURE 5.7A RADIAL DISPLACEMENT RESPONSE AT CENTER PLANE DUE TO A UNIT POROUS MATRIX ISOTROPIC DILATATION

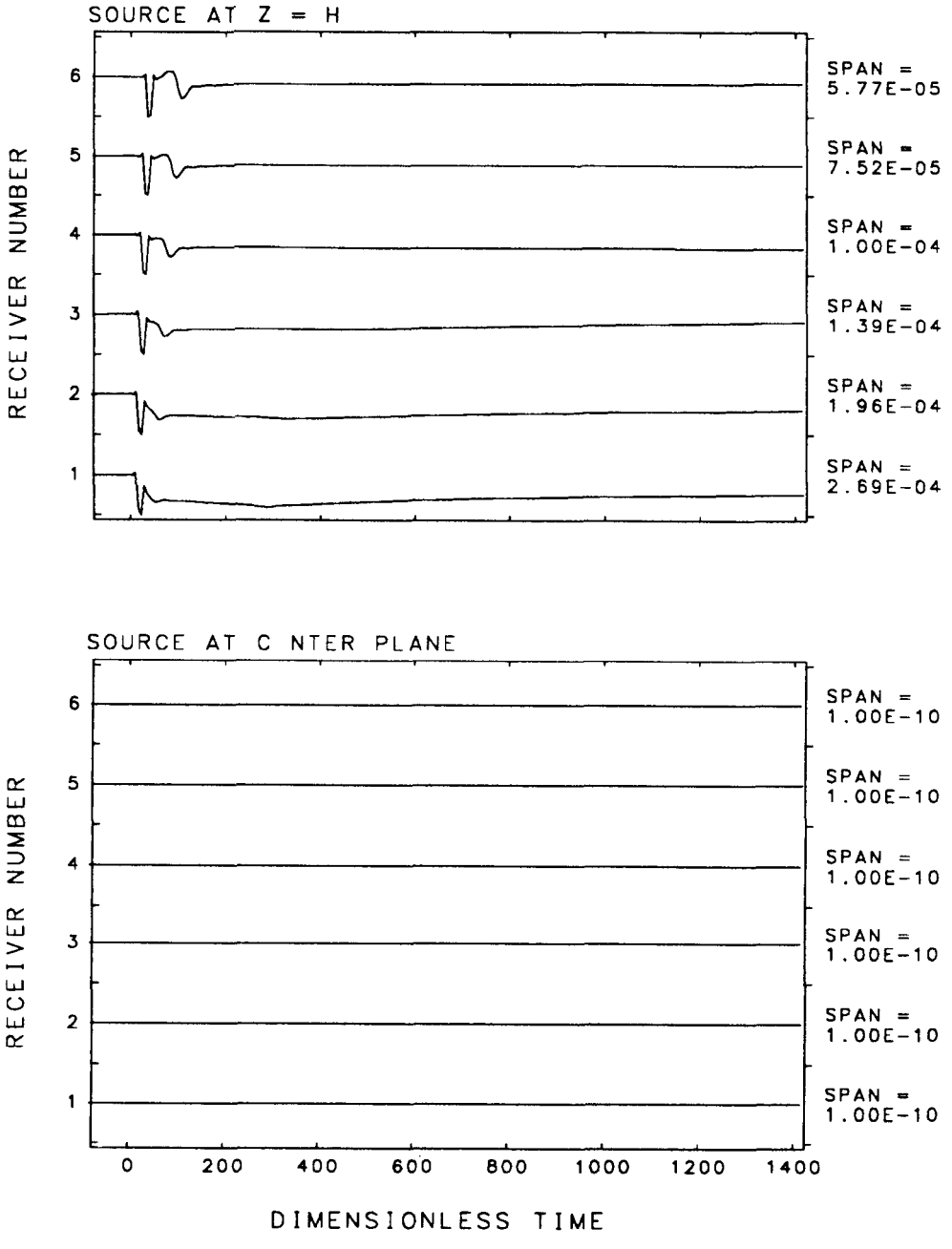

FIGURE 5.7B VERTICAL DISPLACEMENT RESPONSE AT CENTER PLANE DUE TO A UNIT POROUS MATRIX ISOTROPIC DILATATION

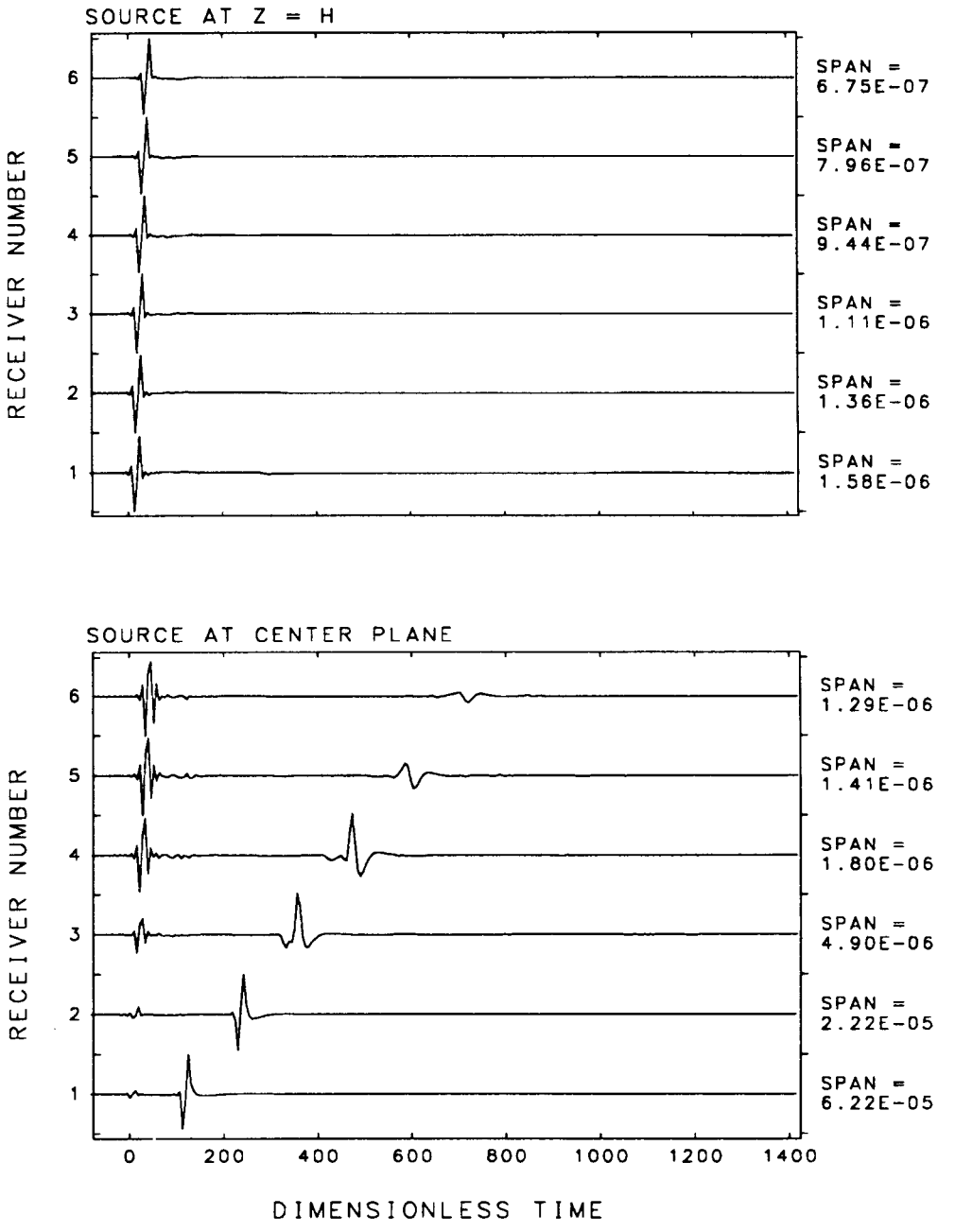

FIGURE 5.7C FLUID PARTIAL STRESS RESPONSE AT CENTER PLANE DUE TO A UNIT POROUS MATRIX ISOTROPIC DILATATION

to the coupling modulus, Q, is roughly similar to the ratio of the coupling modulus to the fluid bulk modulus, R. The ratios are not identical, though, and there are observable differences between the responses to the two types of sources. Further, if the responses to fluid isotropic dilatations are divided by the porosity of the sources, the resulting magnitudes of the the two types of sources become comparable.

5.3.2 Responses Along Upper Boundary

Radial and vertical solid displacement responses along the upper boundary, $z = 30$, to fluid dilatational sources are presented in Figures 5.8A and 5.8B, respectively. Corresponding responses to porous matrix isotropic dilatations are given in Figures 5.9A and 5.9B. As with the center plane receivers, the first receiver is located at $r = 10$, and receiver spacing is 10.

The initial arrivals are critically refracted waves propagating at the P-wave velocity for the solid region. There is some numerical noise arriving prior to the first P-wave arrival in the trace for receiver #1 located at $(r,\theta,z) = (10,0,30)$.

The radial response at $r = 10$ (receiver no. 1) to a source at the upper boundary is similar to a step function until approximately time 90, when the radial response abruptly begins to decrease (Figure 5.8A) The abrupt decay does not appear at the more distant receivers, which is puzzling.

The non-trivial vertical responses along the upper boundary (Figure 5.8B and 5.9B) to sources at the upper boundary are a direct consequence of the presence of the layer; without the layer, these responses would be zero. As a result, the first arrivals have lower amplitude compared to those from sources at the center and lower boundary of the layer.

The long-term responses at $r=10$ to fluid dilatation (Figure 5.8A and 5.8B) appear to approach zero asymptotically, while those at larger offsets appear to contain a substantial static displacement, which, for fluid dilatation, should be zero. The responses given in Figure 5.8B for fluid volume sources were computed by the standard technique of numerically integrating the impulse response functions after removing the initial offset prior to the first arrival. Rational fraction interpolation did not produce realistic results. The persistent static displacement appears to be stabilized by the end of the trace, so that these results are disappointing.

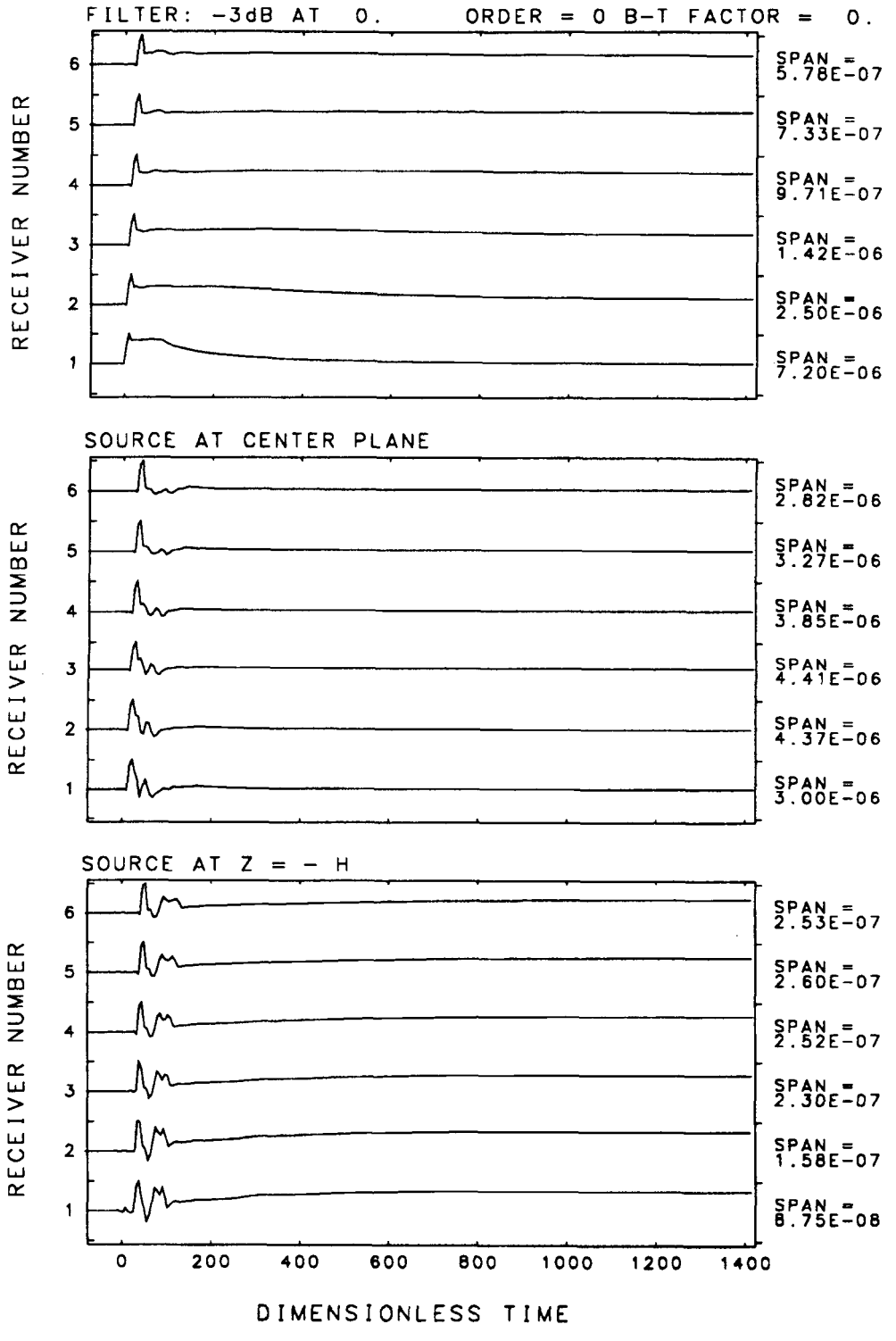

FIGURE 5.8A RADIAL DISLPLACEMENT RESPONSE ALONG UPPER BOUNDARY TO A UNIT FLUID ISOTROPIC DILATATION

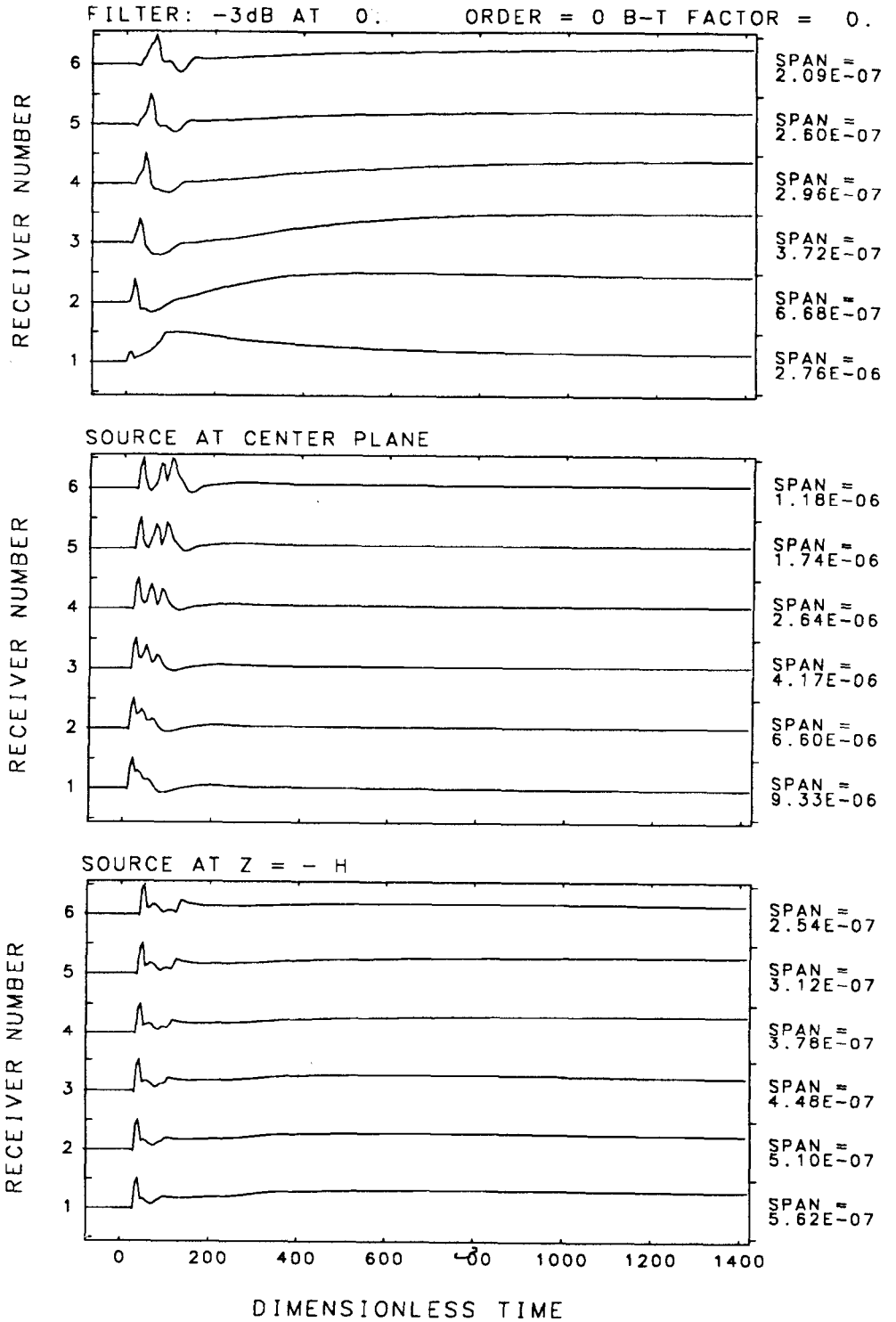

FIGURE 5.8B VERTICAL DISLPLACEMENT RESPONSE ALONG UPPER BOUNDARY DUE TO A UNIT FLUID ISOTROPIC DILATATION

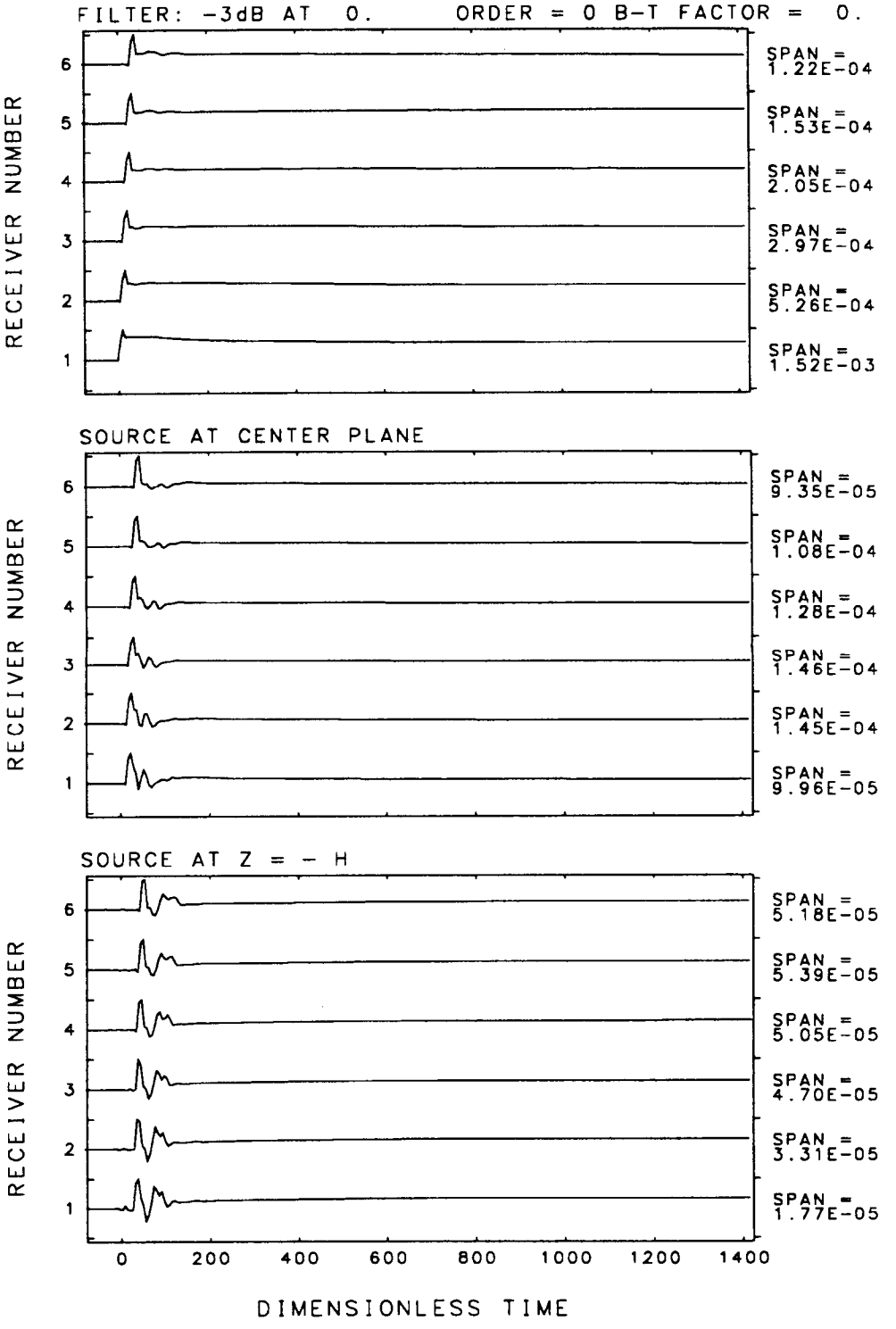

FIGURE 5.9A RADIAL DISPLACEMENT RESPONSE ALONG UPPER BOUNDARY DUE TO A UNIT POROUS MATRIX ISOTROPIC DILATATION

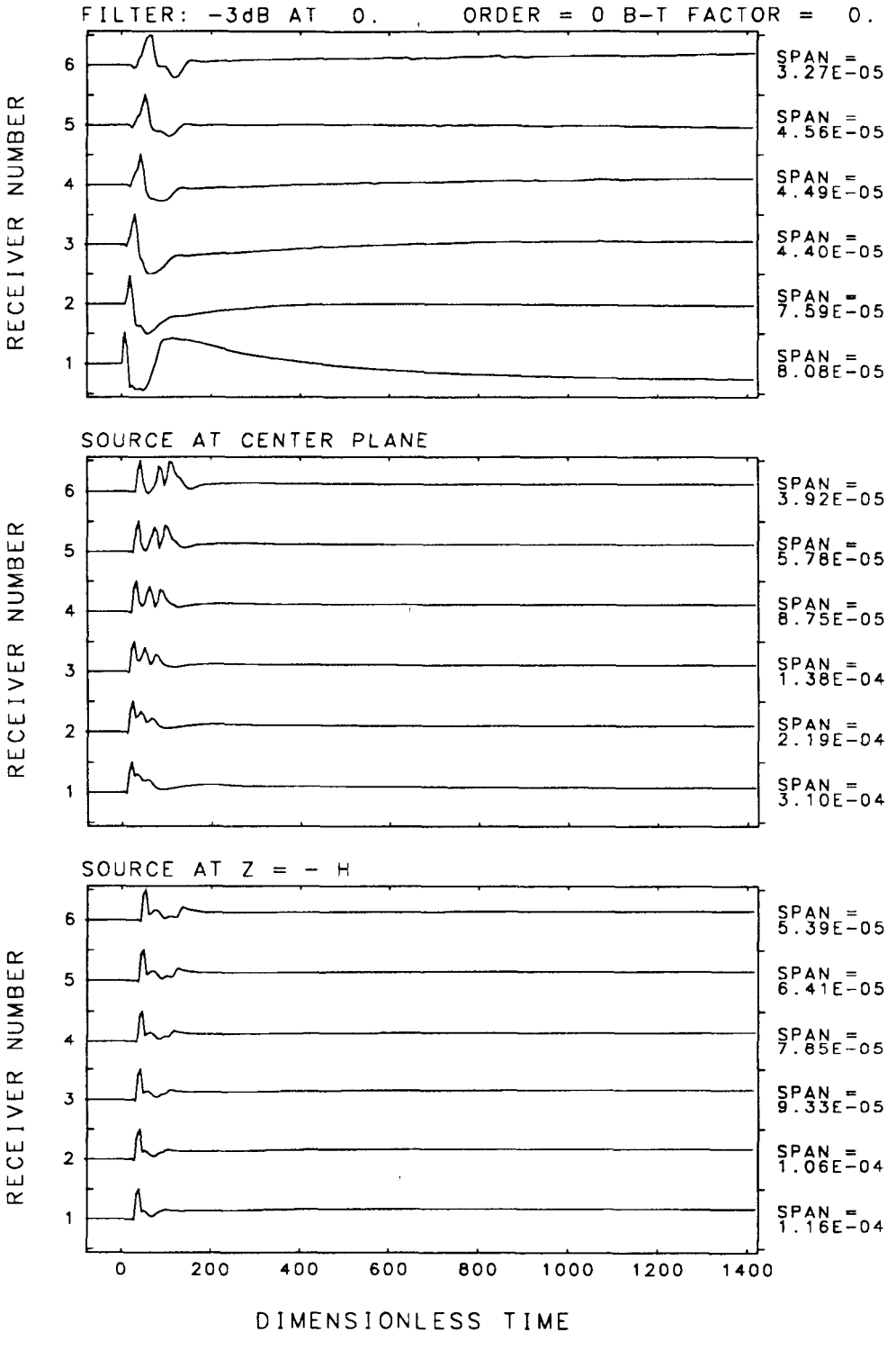

FIGURE 5.9B VERTICAL DISPLACEMENT RESPONSE ALONG UPPER BOUNDARY DUE TO A UNIT POROUS MATRIX ISOTROPIC DILATATION

5.3.3 Responses In Solid Region

The radial and vertical displacement responses along a line normal to the fracture layer for fluid and matrix dilatational sources are presented in Figures 5.10A,B and 5.11A,B, respectively. The receiver locations are at $r = 10$ and $z = 30, 40, 50, 60, 70, 80, 90, 100, 110$. The responses for the first receiver are thus identical to those shown above for the responses at the first receiver along the upper boundary. (Fundamental response functions were not presented in the appendices for the receivers at the highest locations, $z = 90, 100, 110$.)

The radial displacement responses (Figures 5.10A and 5.11A) contain significant numerical noise at time $t = 0$. The cause of the noise is probably due to insufficient step size in the Hankel inversion process at high frequencies. The noise was discovered after forming the dilatational source responses, by summation over gradients of Green's functions for both matrix and fluid sources, as discussed in Appendix A. Evidently, some cancellation of the P- and SV- wave arrivals occurred, reducing the signal-to-noise ratio of the computed waveforms. The problem does not appear in the vertical response functions, which are an order of magnitude greater than the radial responses, consistent with a longitudinal polarization of the radiated wave. Had the radial offset of the receiver locations been 0, the radial response would have been identically zero.

The vertical responses at the layer boundary to a source also on the boundary (trace #1 of the upper set of vertical displacement response functions, Figures 5.10B and 5.11B) are substantially different from and have much lower magnitude than the responses at higher elevations, due to radiation angle. As indicated above, the vertical response at the boundary would be zero without the layer present.

The long term displacement responses to fluid dilatational sources at the center plane appear to approach zero as expected. However, apparent static displacements exist for fluid dilatational sources at the upper and particularly the lower boundaries (Figures 5.10A 5.10B). As discussed above regarding the procedure for computing the integrated responses, the time window may be insufficient for capturing the long term static displacement. However, because the long-time response appears to stabilize, the results are questionable.

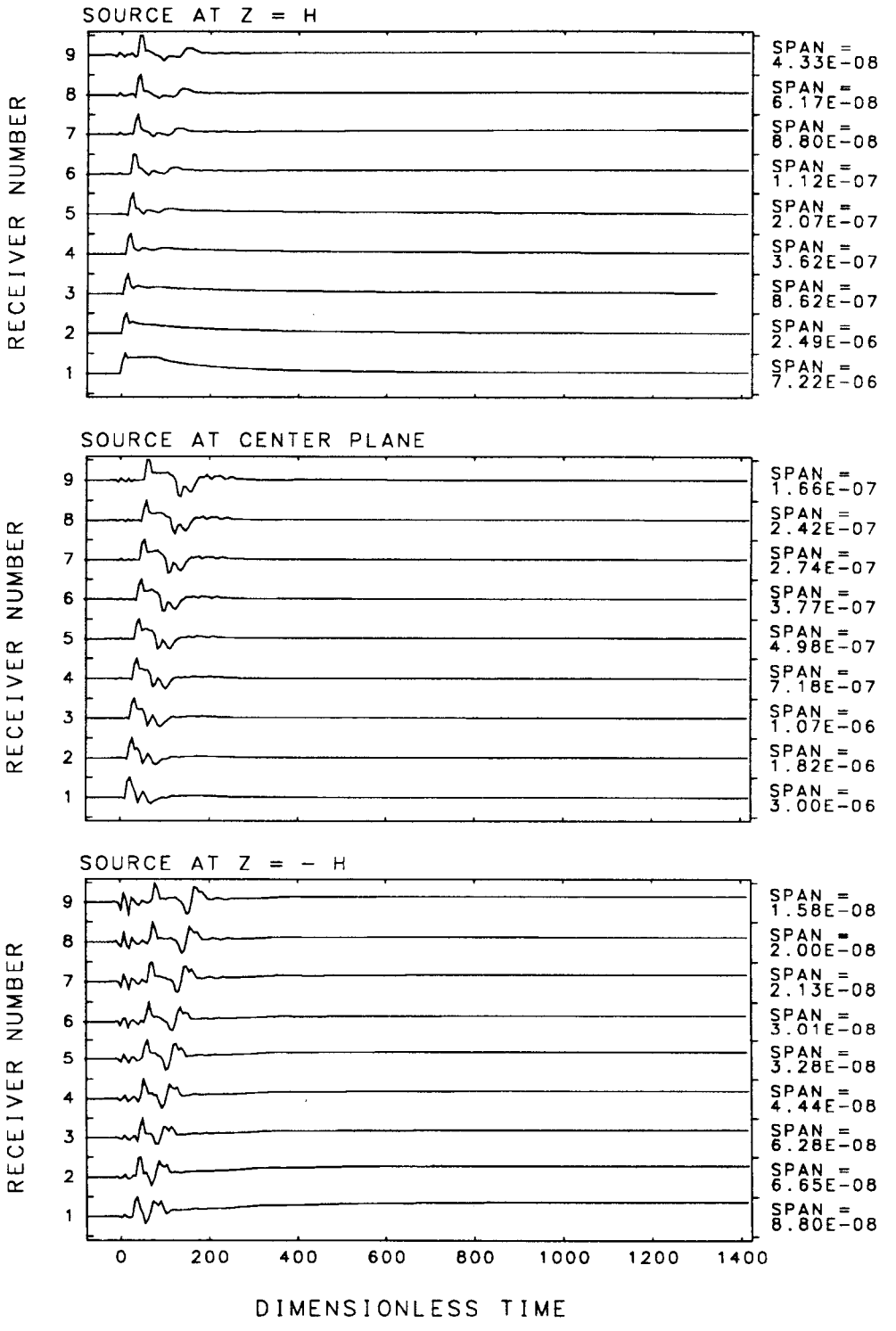

FIGURE 5.10A RADIAL DISPLACEMENT RESPONSE OF SOLID REGION AT VARIOUS ELEVATIONS AND RADIAL OFFSET 10 TO A UNIT FLUID ISOTROPIC DILATATION

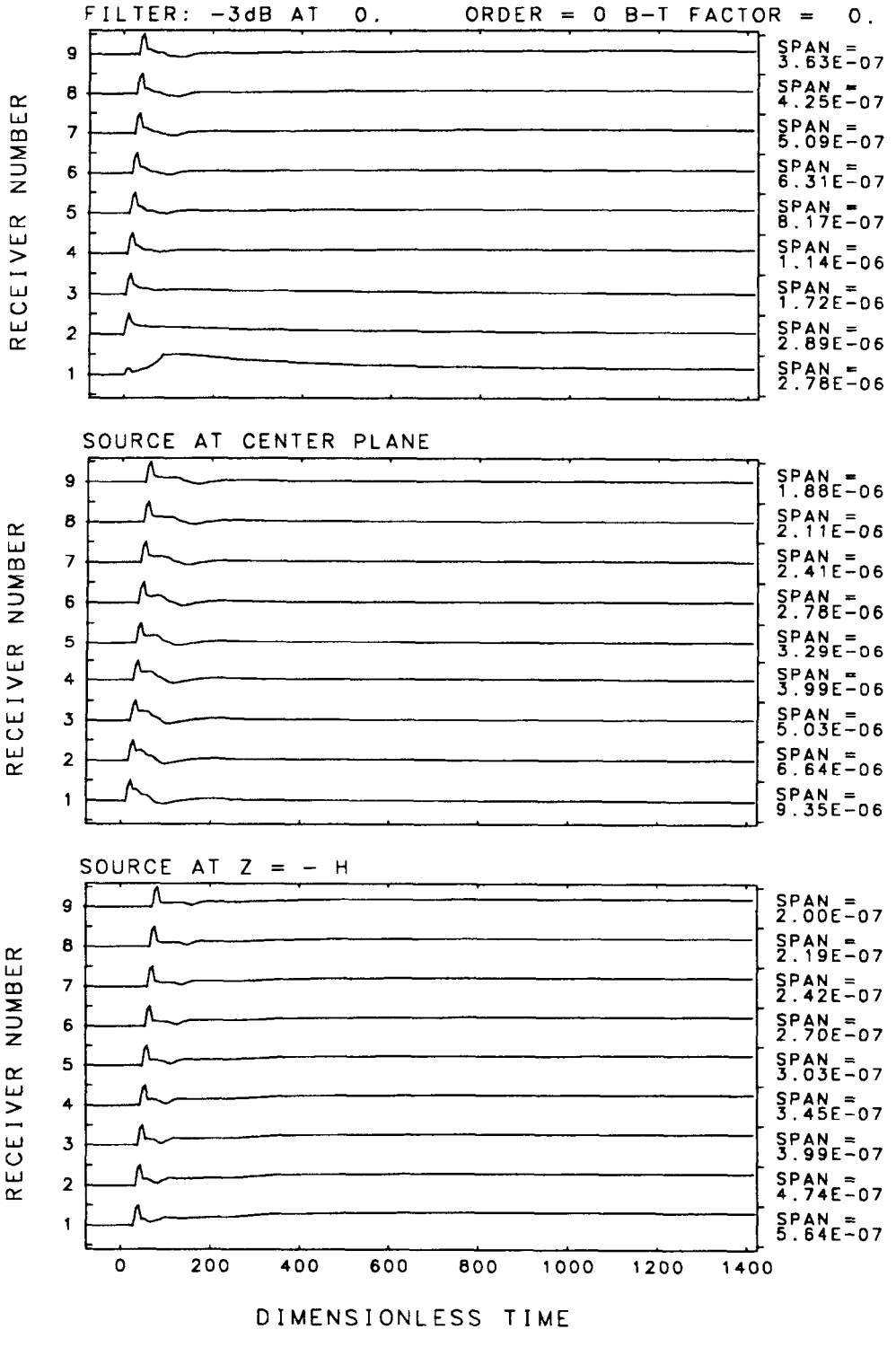

FIGURE 5.10B VERTICAL DISLPLACEMENT RESPONSE OF SOLID REGION AT VARIOUS ELEVATIONS TO A UNIT FLUID ISOTROPIC DILATATION

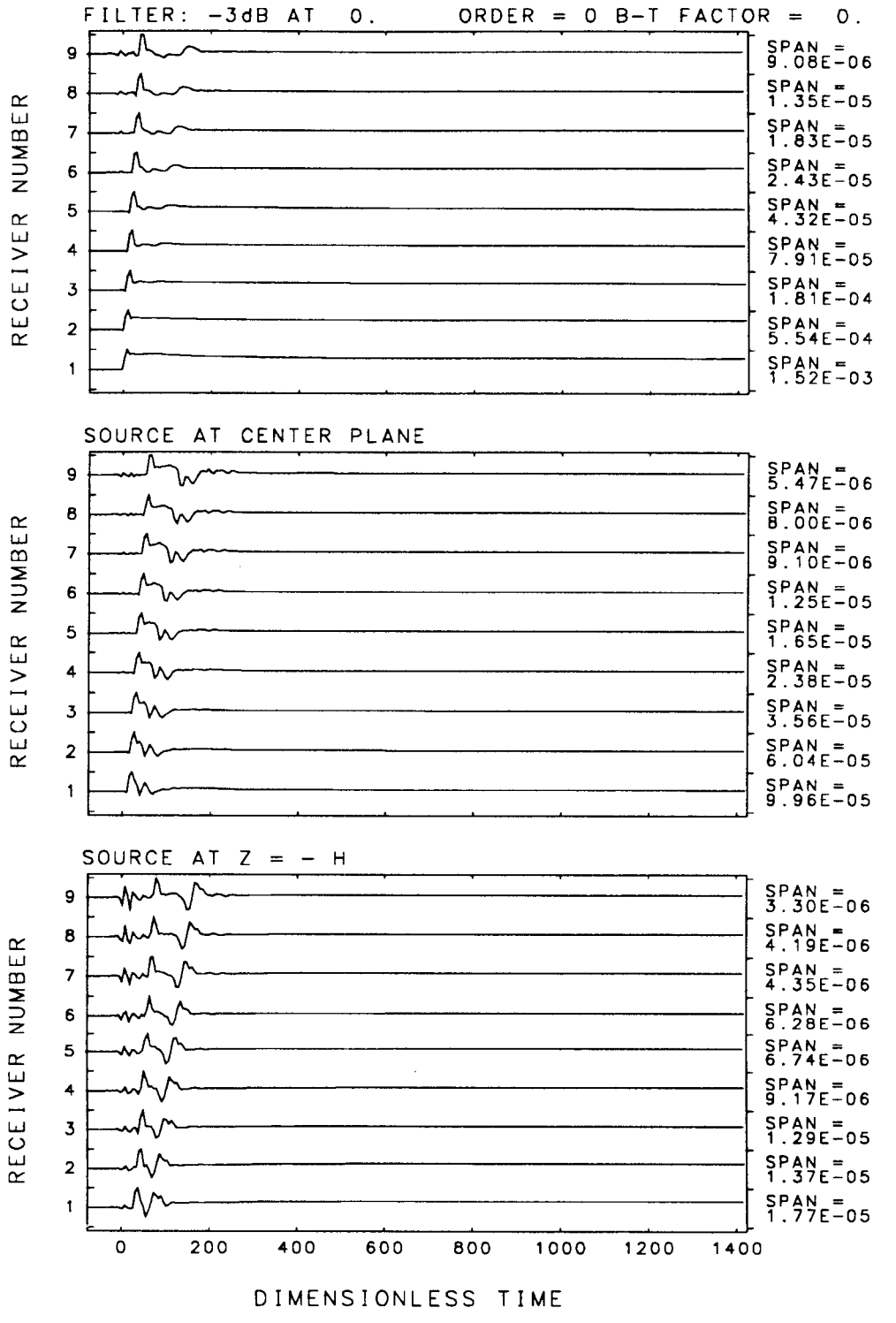

FIGURE 5.11A RADIAL DISPLACEMENT RESPONSE OF THE SOLID REGION AT VARIOUS ELEVATIONS AND RADIAL OFFSET 10 TO A UNIT ISOTROPIC DILATATION OF THE POROUS MATRIX

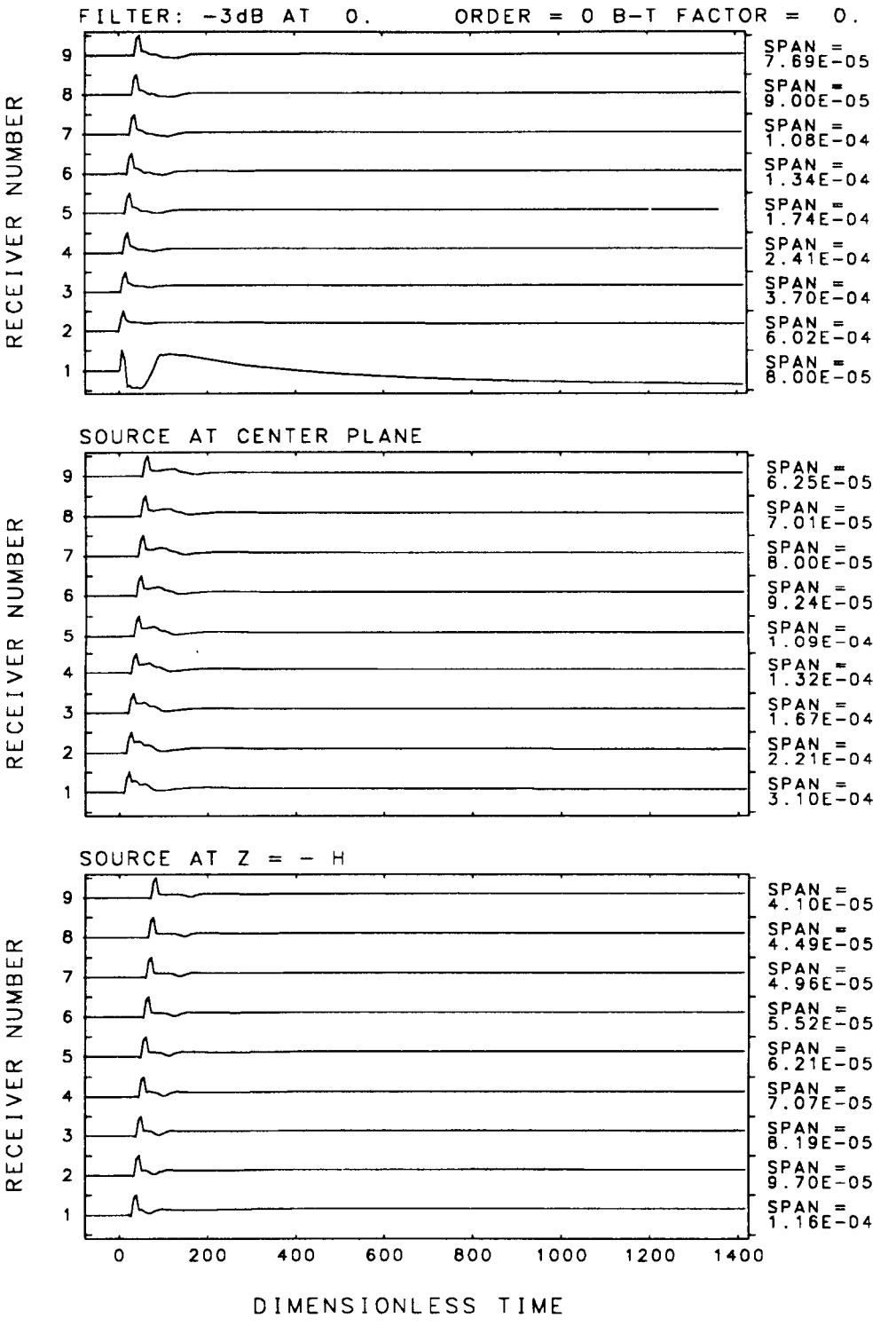

FIGURE 5.11B VERTICAL DISPLACEMENT RESPONSE OF THE SOLID REGION AT VARIOUS ELEVATIONS AND RADIAL OFFSET 10 TO A UNIT ISOTROPIC DILATATION OF THE POROUS MATRIX

5.4 Responses to Fracturing Events - Acoustic Emission

The principal purpose of this thesis is the modeling of solid material displacement and fluid partial stress responses to fracturing within the porous layer. Acoustic emission sources in a porous material involve a combination of dilatational or shear failures of the porous structure. These responses are discussed below separately for each type of source.

5.4.1 Responses to Dilatational Failures

In the event of a dilatational failure, fluid backflow into the void left by the fracture may occur, depending on the static pore pressure. A fluid backflow profile is proposed in Figure 5.12. Fracture of the solid material forming the porous structure is assumed to be instantaneous, with displacement discontinuity proportional in time to a Heaviside step function. The fluid dilatation, Δ_F, is assumed to be initially equal to the dilatation of the matrix, Δ_M with zero fluid pressure in the void left by the fluid and porous matrix inclusion. For shear failures, the dilatations of the structure, and, thus, the fluid, are zero.

Following initial expansion, the static fluid pressure driving the hydraulic fracturing process forces the fluid back into the volume left by the fracture. The rate of fluid backflow is dependent on the driving pressure, and fracture network permeability. However, the rate of fluid backflow must be input as an independent parameter, in the same manner as the porous matrix displacement discontinuity. Regardless of the rate of fluid backflow, the backflow must cease when the cavity produced by the fracture process is filled with fluid.

The volume of fluid backflow after initial expansion is $\frac{\Delta_M}{\beta}$. Because this includes the initial volume of fluid expansion, assumed equal to Δ_M, the extreme negative fluid dilatation due to fluid backflow is:

$$\Delta_M - \frac{\Delta_M}{\beta} = \Delta_M \left[\frac{\beta - 1}{\beta} \right] \tag{5.8}$$

To compute responses to matrix dilatation and fluid backflow, spectral moment tensors are constructed according to the representation formulas given in Appendix A for point moment sources. The moment tensor for the matrix is:

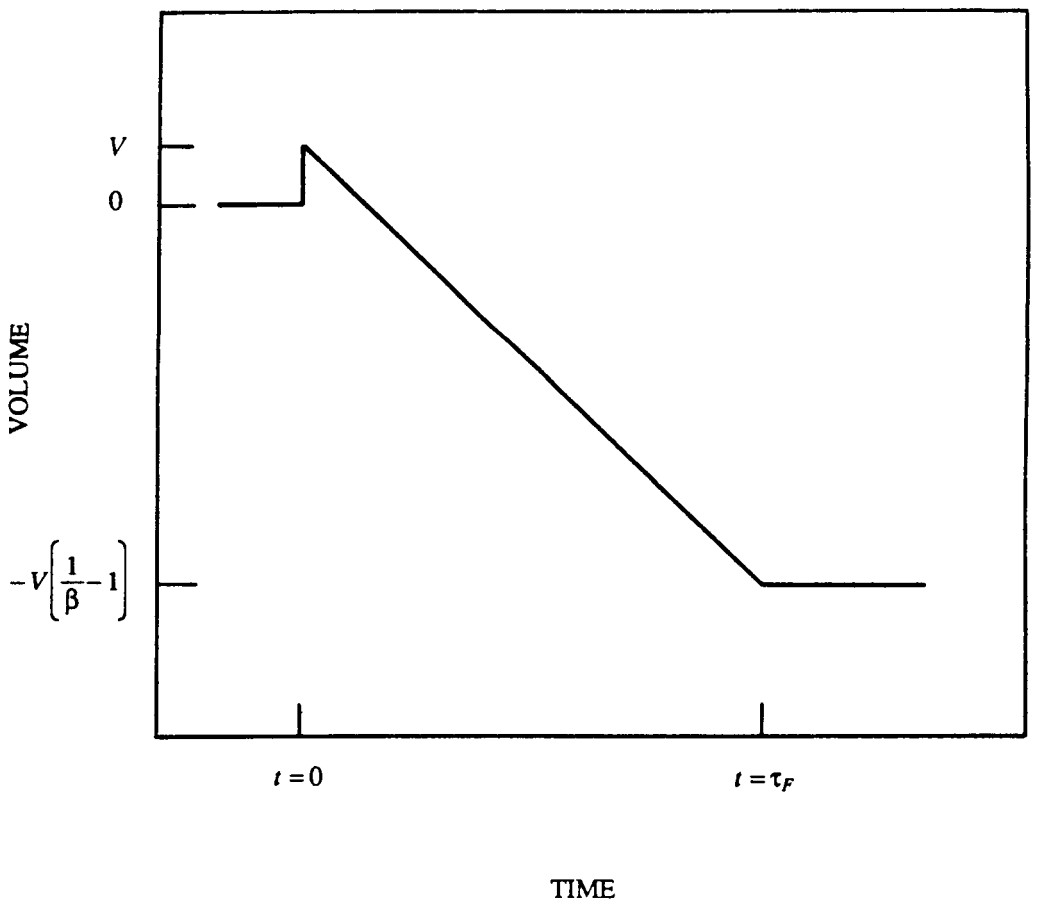

FIGURE 5.12 FLUID BACK-FLOW PROFILE

$$M_{ij}^{M} = A\,\delta_{ij}\Delta_M + 2N\left([u_i]\nu_j + [u_j]\nu_i\right) + Q\,\delta_{ij}\Delta_F \tag{5.9}$$

The isotropic scalar moment for the fluid is:

$$M^F = Q\,\Delta_M + R\,\Delta_F \tag{5.10}$$

where:

$$\Delta_M = [u_i]\nu_i \tag{5.11}$$

and:

$$\Delta_F = \Delta_M\left\{1 - \frac{1}{i\,\omega\tau_F\,\beta}\left[1 - \exp^{-i\,\omega\tau_F}\right]\right\} \tag{5.12}$$

The above spectral components for the moments correspond to a delta function time dependence for the porous matrix moment. The responses to Heaviside step matrix dislocation time dependence were obtained by numerical integration of the impulse response functions obtained by discrete inverse Fourier transformation of the spectral impulse responses. Zero frequency spectral components were estimated by rational fraction interpolation across positive and negative frequencies. Where rational fraction interpolation produced a poor result, integration of the Green's function was preceded by removal of the initial offset of the response, producing zero slope in the response functions at either end of the time window. In most cases, the interpolation procedure produces the same result as the standard procedure of initial offset removal, especially when the static displacements are clearly defined.

5.4.1.1 Center Plane Responses to Dilatational Failures

Displacement and fluid partial stress responses in the fracture zone at the central plane of symmetry and radial offset of 40 to dilatational displacement discontinuities across fracture planes are presented in Figures 13A, B, and C for instantaneous fluid backflow. Three types of failures are represented in each of these figures, one for each of the axes of the coordinate system. The upper set of traces is for a source at the upper boundary, and the lower set for a source at the center.

The initial radial displacement for the center source is positive going for an $r-r$ failure, and negative-going for $\theta-\theta$ and $z-z$ failures. The vertical displacement responses given in Figure 5.13B to center plane dilatational sources are all zero, as they should be by symmetry. If the fracture plane were oriented along a direction not parallel with one of the coordinate axis, symmetry would be

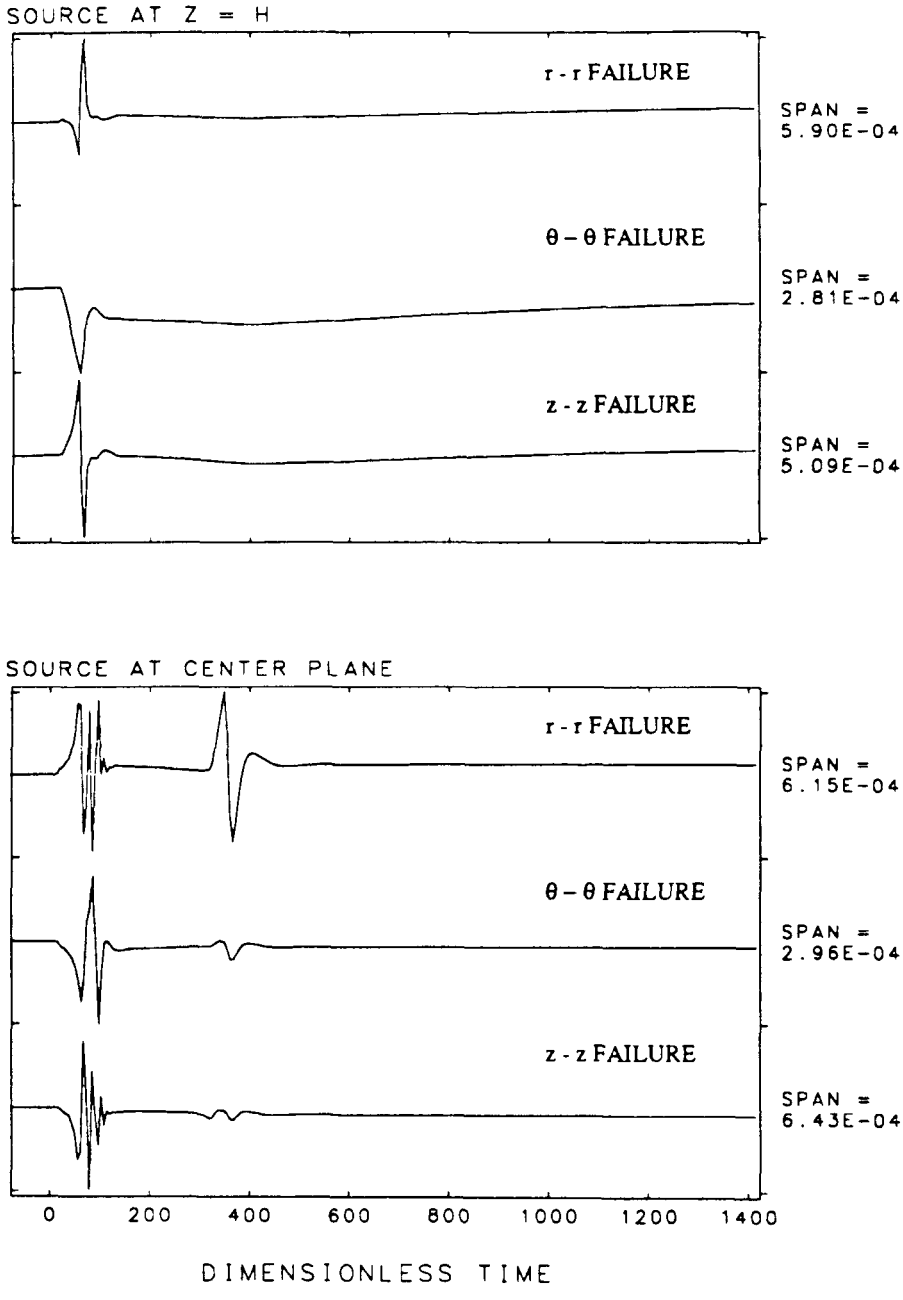

FIGURE 5.13A RADIAL DISPLACEMENT AT CENTER PLANE, RADIUS 40, TO DILATATIONAL FAILURES WITH INSTANTANEOUS FLUID BACKFLOW

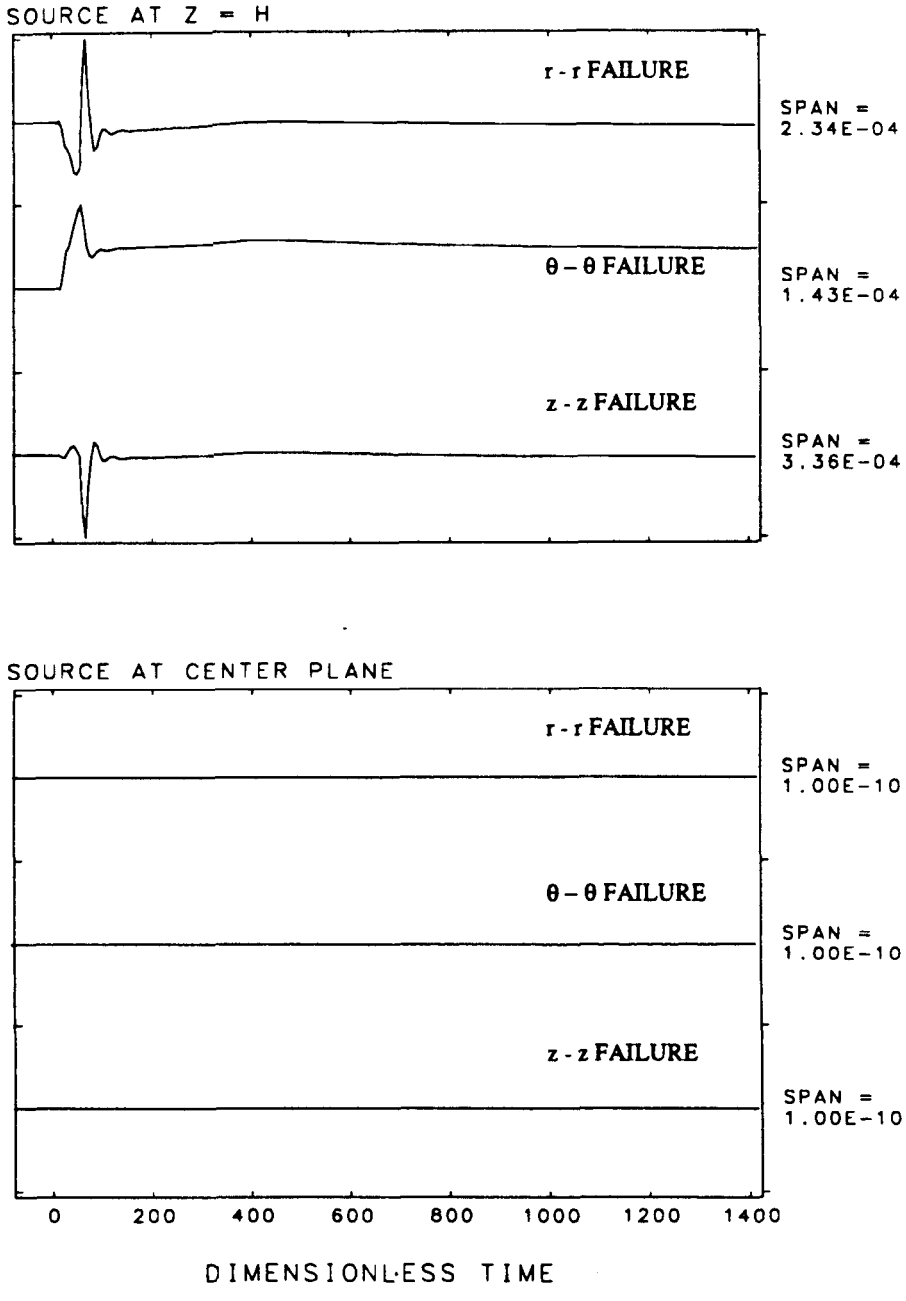

FIGURE 5.13B VERTICAL DISPLACEMENT AT CENTER PLANE, RADIUS 40, TO DILATATIONAL FAILURES WITH INSTANTANEOUS FLUID BACKFLOW

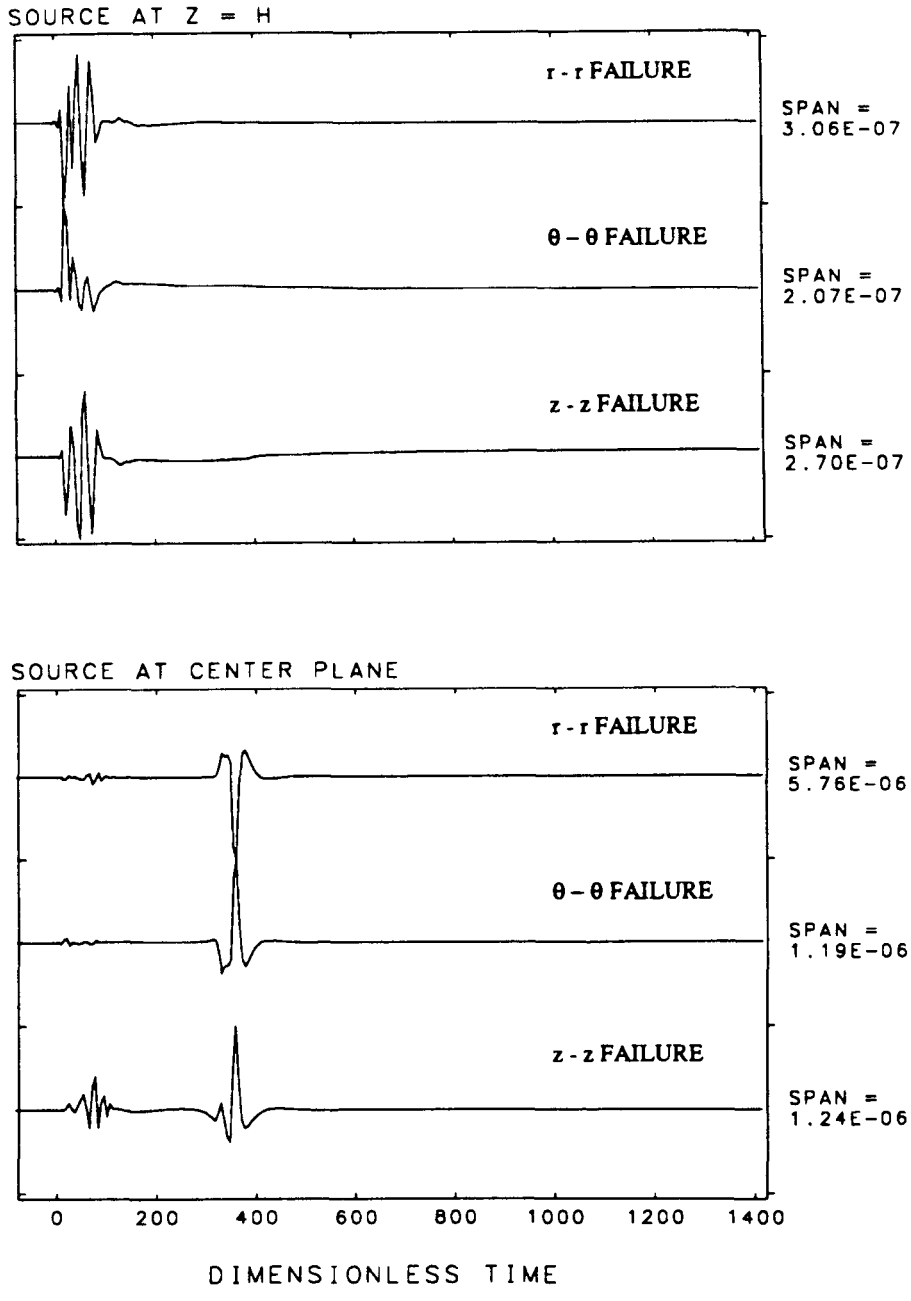

FIGURE 5.13C FLUID PARTIAL STRESS RESPONSE AT CENTER PLANE, RADIUS 40, TO DILATATIONAL FAILURES WITH INSTANTANEOUS FLUID BACKFLOW

destroyed and a vertical response would be obtained.

At about time 300 to 350 for the source at the center, a strong pulse representing the arrival of the Biot second mode wave appears in the radial displacement response of Figure 5.13A. The pulse is strongest for the r-component of displacement for an $r-r$ failure. The pulse is also clear in the fluid partial stress response shown in Figure 5.13C, again strongest for the $r-r$ failure. There is no well defined pulse marking the arrival of the second mode wave from the source at the upper boundary, though there appears to be a slight relaxation effect beginning at about the time of arrival of the highly attenuated second mode.

Some static pressure is observable in fluid stress responses to failures at the upper boundary (Figure 5.13C). However, these particular responses to Heaviside step sources were computed by the standard numerical integration procedure of initial offset removal, thus forcing a non-physical zero-slope in the responses at the end of the time window. Rational fraction interpolation produced erratic results in this case, and was not used.

Center plane responses to dilatational failures and fluid backflow time of 300 (0.1 second) are presented in Figures 5.14A, B, and C. These responses may be compared directly with those of Figures 5.13A, B, and C.

These responses with finite backflow time differ considerably from those given above for instantaneous backflow. The relaxation time for fluid backflow is not necessarily very significant in determining the waveforms of the short-period initial arrivals provided that the backflow time is much longer than the period of the early arrivals. For sources at the center plane, the end of the backflow is signaled by a very small arrival at about time 650 ($\approx$ 0.22 second).

No static pressure is apparent in the fluid partial stress response to failures at the upper boundary (Figure 5.14C), as expected.

The arrival of the second-mode wave causes a substantial radial displacement for the θ–θ and $z-z$ failure modes relative to the $r-r$ modes for central plane sources (Figure 5.14A). The response to the $r-r$ failure is much lower than for the instantaneous backflow case. Fluid backflow has a strong effect on the long-period behavior of the radial and vertical responses to sources located at the upper boundary.

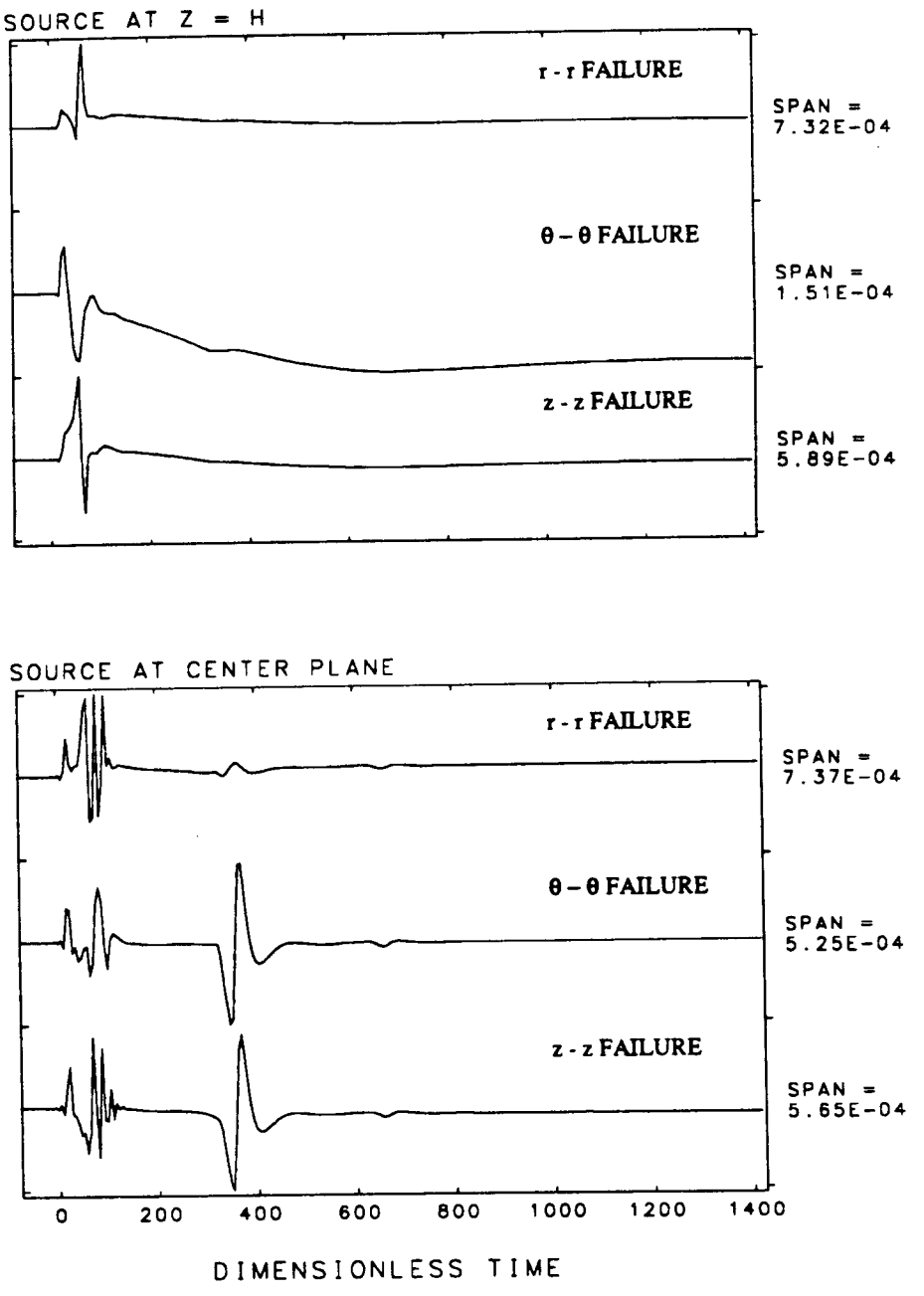

FIGURE 5.14A RADIAL DISPLACEMENT RESPONSE AT CENTER PLANE, RADIUS 40, TO DILATATIONAL FAILURES WITH FLUID BACKFLOW TIME 300

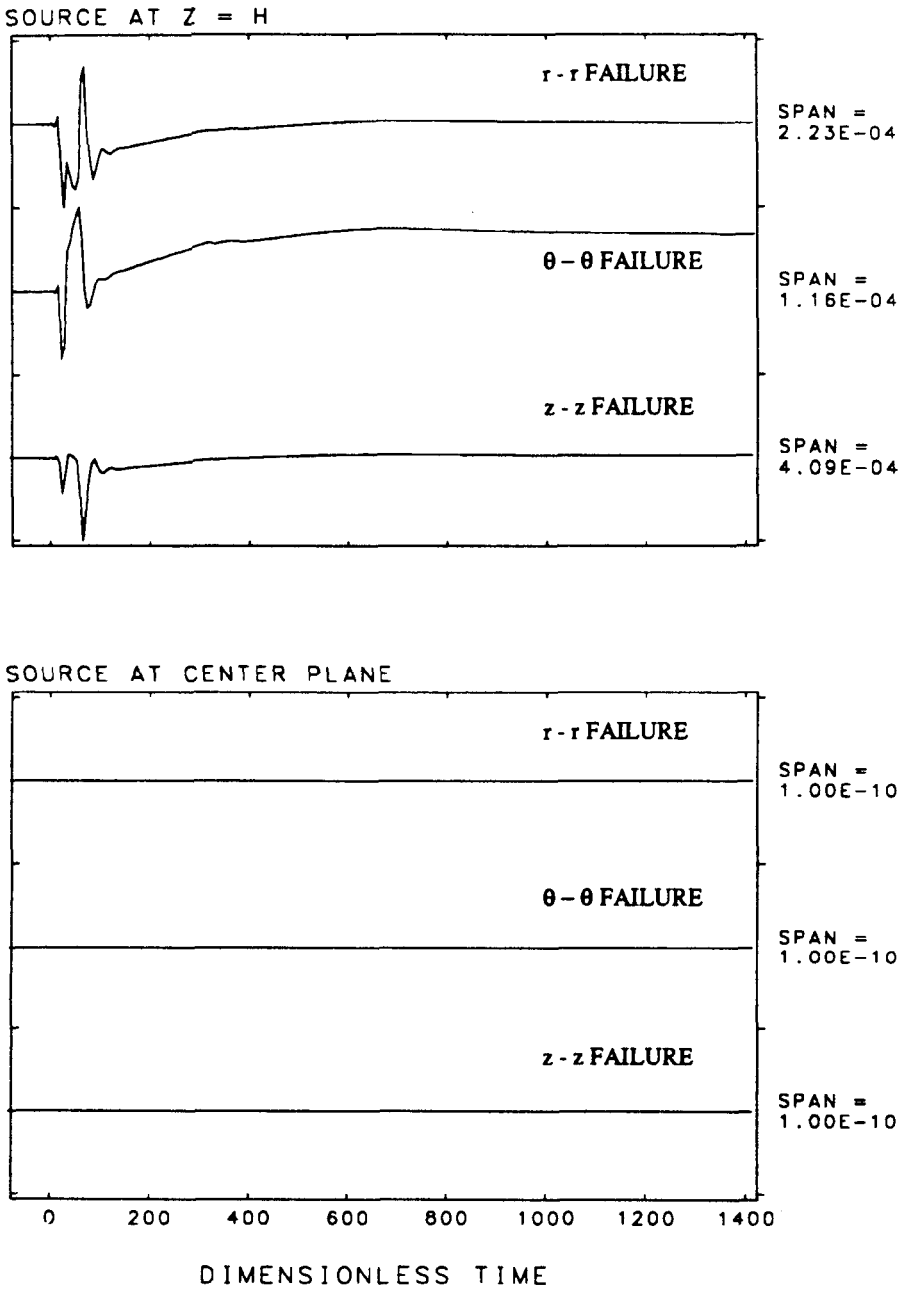

FIGURE 5.14B VERTICAL DISPLACEMENT RESPONSE AT CENTER PLANE, RADIUS 40, TO DILATATIONAL FAILURES WITH FLUID BACKFLOW TIME 300

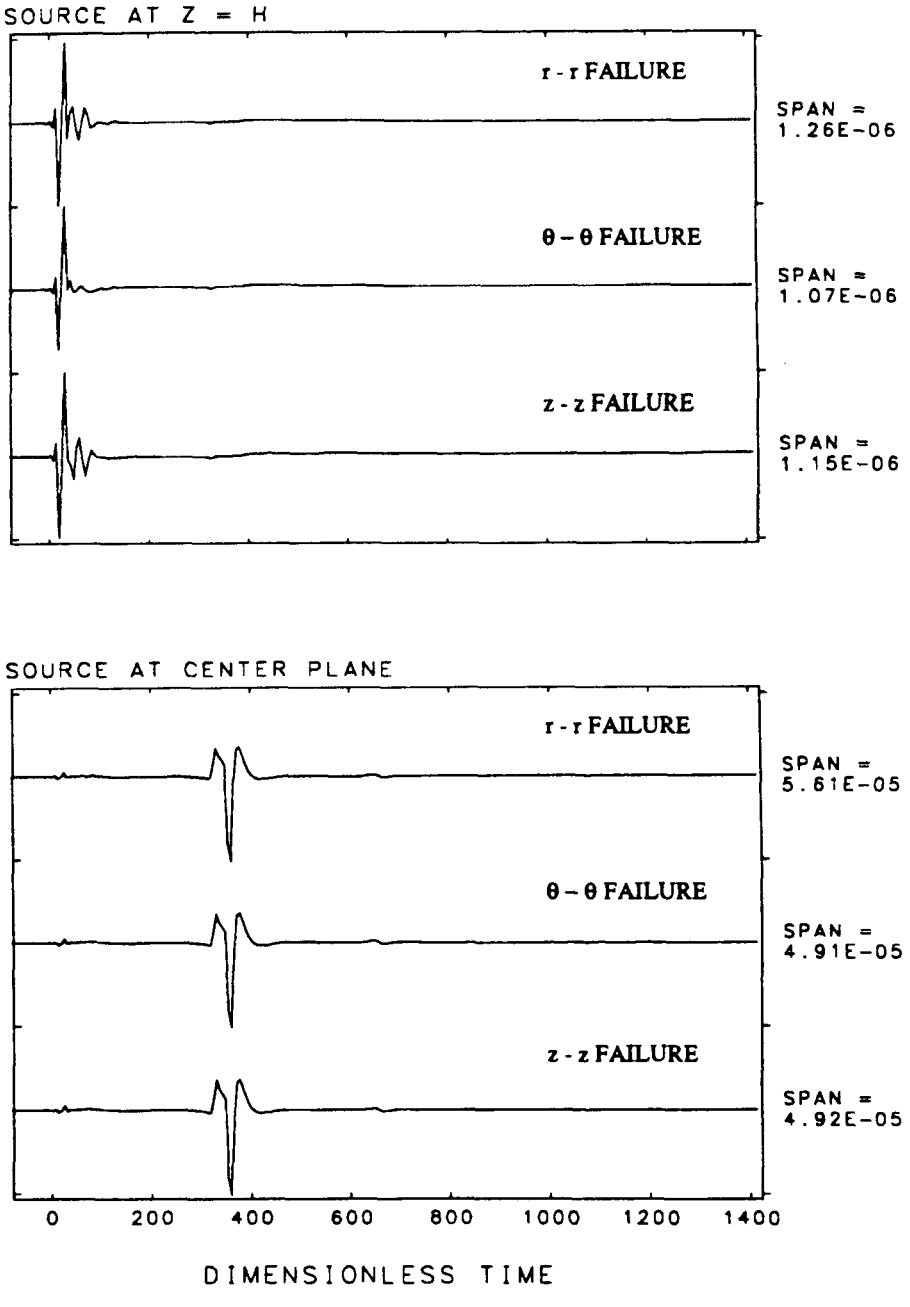

FIGURE 5.14C FLUID PARTIAL STRESS RESPONSE AT CENTER PLANE, RADIUS 40, TO DILATATIONAL FAILURES WITH FLUID BACKFLOW TIME 300

For center plane sources, the fluid partial stress response to an $r-r$ failure is much reduced relative to the instantaneous backflow case, while the responses to $\theta-\theta$ and $z-z$ failures are increased by an order of magnitude. For sources at the upper boundary, the magnitude of short period fluid stress responses are an order of magnitude higher than for the case of instantaneous backflow.

5.4.1.2 Upper Boundary Responses to Dilatational Failures

Displacement responses at the upper boundary of the fracture zone, $z=30$, and at a radial distance $r=40$ from the z-axis, are presented in Figures 5.15A through 5.16B. The responses are for dilatational failures located on the z-axis at $z=-h$, $z=0$, and $z=+h$.

Displayed in Figures 5.15A and 5.15B are radial and vertical responses, respectively, for dilatational failures with instantaneous fluid backflow. These responses are thus the counterparts to the center plane responses given in Figures 5.13A and 5.13B.

The vertical component of displacement in Figure 5.15B for sources at the upper boundary are an order of magnitude less than for sources at other locations, and would have been zero if not for the presence of the porous layer. Reflection of P and SV waves from the high-porosity region of the layer occur roughly between time 50 and 100. The long-time response appears to be poorly defined.

The second mode wave propagating within the high-porosity layer is not observable in the responses at the upper boundary, as expected for a bound state or trapped mode.

Radial and vertical displacement responses to dilatational sources with fluid backflow time of 300 (0.1 second) are presented in Figures 5.16A and Figures 5.16B, respectively. Comparison of these results with those for the instantaneous fluid backflow case indicate that at least the initial part of the backflow has a substantial effect on the first P- and S- wave arrivals. After the first arrival, a "ramp" occurs for sources at the upper boundary, directly related to the fluid backflow.

One would expect that the static displacement would be the same regardless of fluid backflow rate. Although the static displacements are of the same order-of-magnitude for both cases, there are differences. No such static displacement is observable for the response to a pure isotropic fluid dilatation at the center plane, illustrated in Figure 5.8A and 5.8B, though for sources at the upper and lower boundaries, the static displacements are rather substantial.

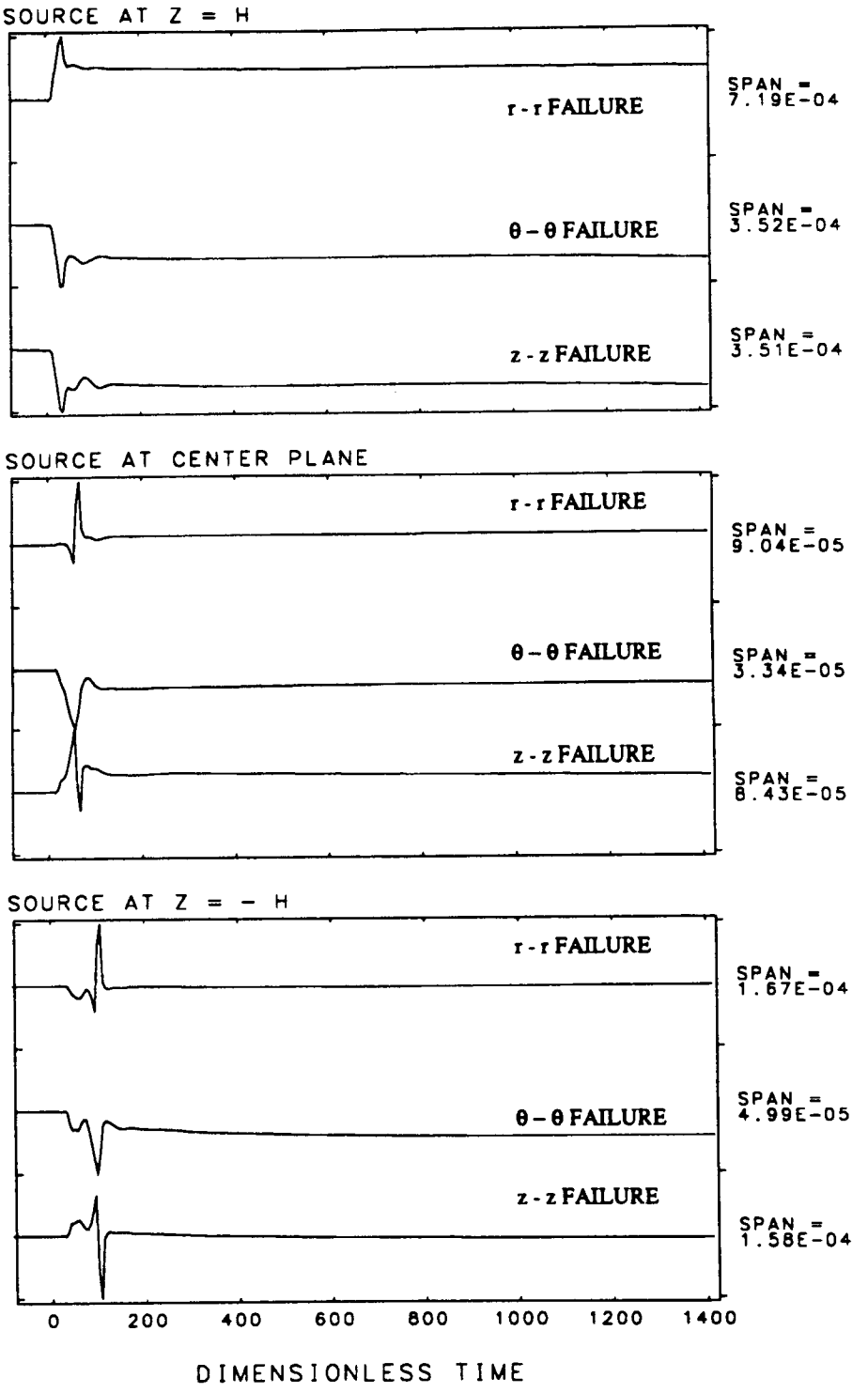

FIGURE 5.15A RADIAL DISPLACEMENT RESPONSE AT UPPER BOUNDARY, RADIUS = 30, TO DILATATIONAL FAILURES WITH INSTANTANEOUS FLUID BACKFLOW

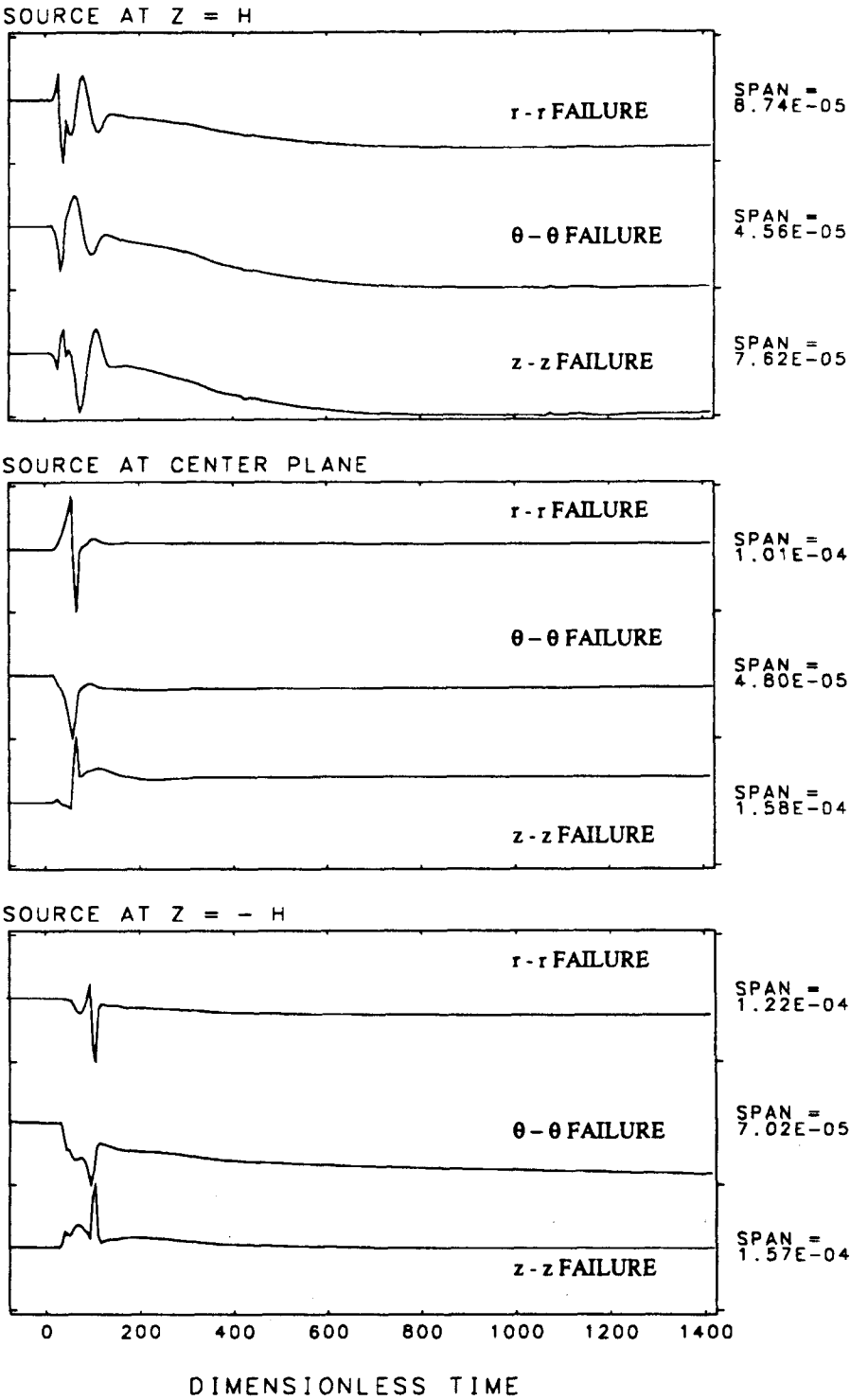

FIGURE 5.15B VERTICAL DISPLACEMENT RESPONSE AT UPPER BOUNDARY, RADIUS = 30, TO DILATATIONAL FAILURES WITH INSTANTANEOUS FLUID BACKFLOW

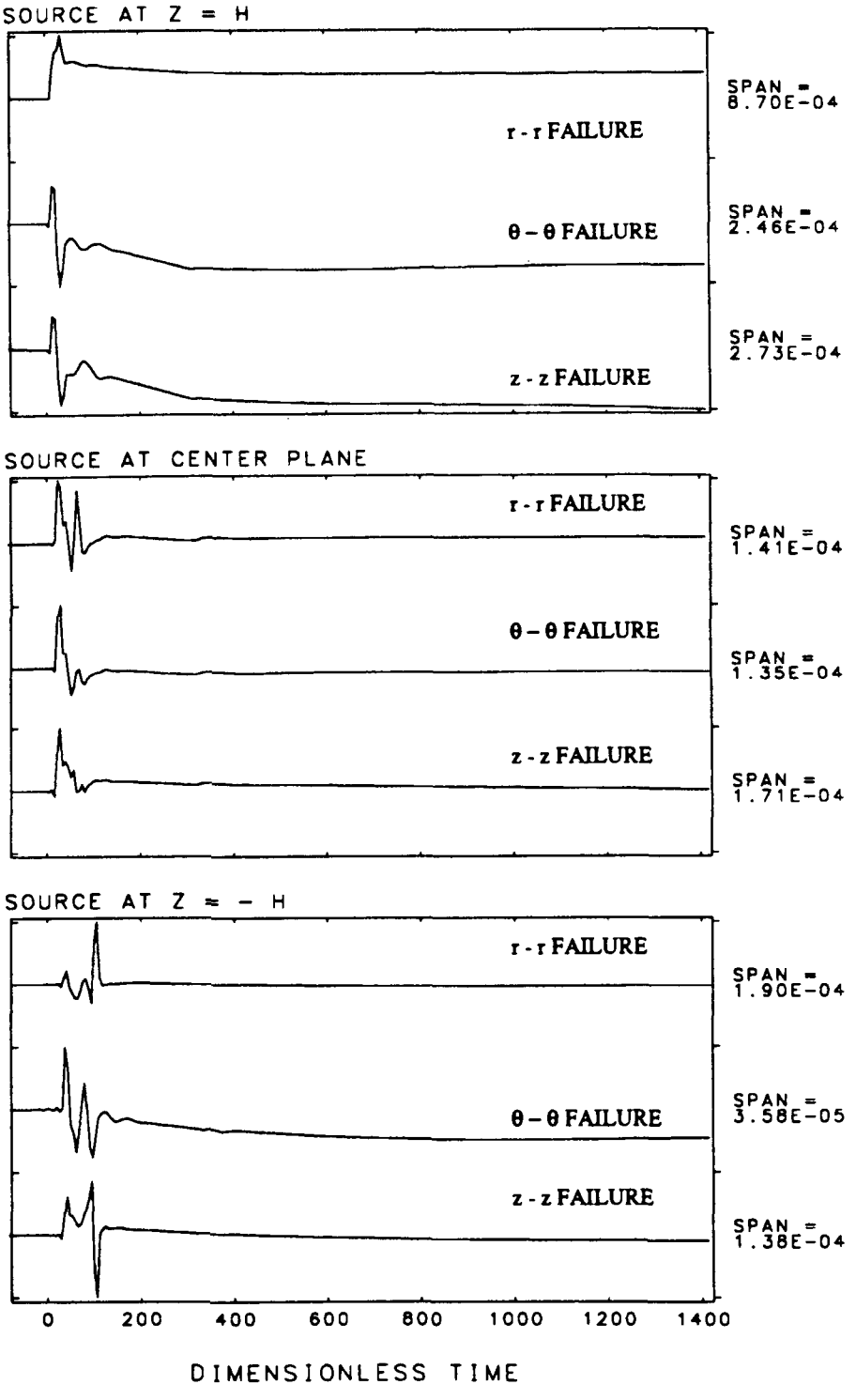

FIGURE 5.16A RADIAL DISPLACEMENT RESPONSE AT UPPER BOUNDARY, RADIUS 30, TO DILATATIONAL FAILURES WITH FLUID BACKFLOW TIME 300

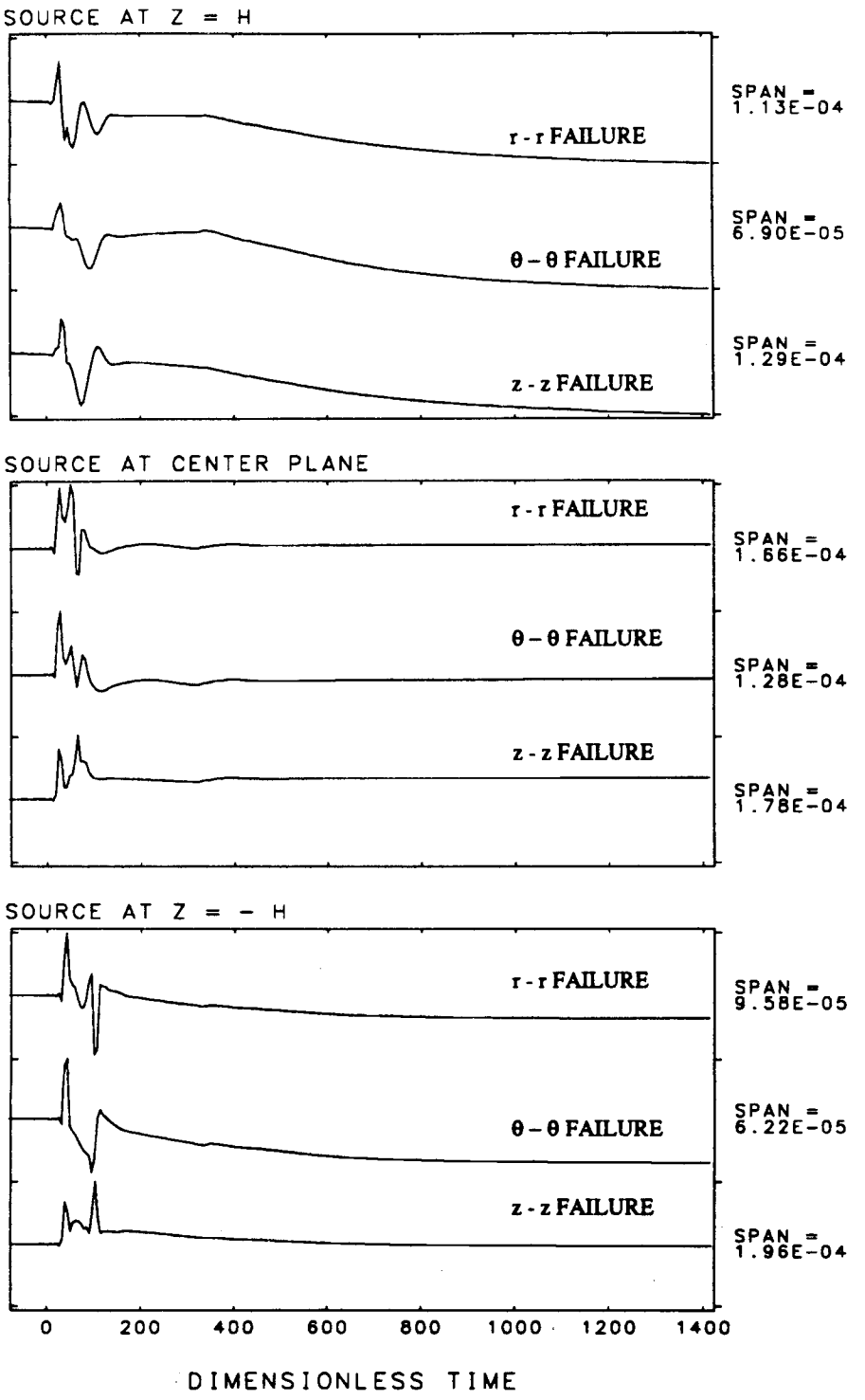

FIGURE 5.16B VERTICAL DISPLACEMENT RESPONSE AT UPPER BOUNDARY, RADIUS 30, TO DILATATIONAL FAILURES WITH FLUID BACKFLOW TIME 300

5.4.1.3 Discussion

These results indicate that the fluid backflow can have a very significant effect on displacement and fluid partial stress response waveforms at the center of the layer. The responses at the upper boundary are representative of the responses well removed from the high porosity region, and are thus representative of the responses in the elastic region, at least close to the boundary. In this region, the effect of fluid backflow is again significant. Chouet (1986) assumed that the fluid advances behind an expanding crack without cavitation. This assumption is convenient for numerical analysis and justifiable for studying propagating modes, However, the above results suggest that the assumption of instantaneous fluid backflow is not necessarily appropriate for inverting field data to obtain source displacement discontinuities, and that such backflow may have to be included as an additional quantity to be determined by inversion.

5.4.2 Responses to Deviatoric Failures

This section concerns the responses to deviatoric, or shear, failures. Responses along the center plane are presented first for a variety of failure orientations. Following this, responses along the upper boundary are considered. In the former case, the effect of fracture plane orientation is considered. In the latter, only a limited of number of source orientations with fracture plane unit normal parallel with one of the coordinate axes are discussed. In all cases, the representation formulae given in Appendix A are used.

5.4.2.1 Center Plane Responses to $r-\theta$ Shear Failures

Responses to deviatoric, or pure shear, displacement discontinuities are presented in Figures 5.17A through 5.17D for failures in the $r-\theta$ plane, that is, horizontal displacement discontinuities across a plane with horizontal unit normal. Figure 5.17A illustrates the transverse displacement response to a failure with unit normal parallel to the r-coordinate axis, referred to as "zero-degree orientation". The displacement discontinuity is parallel to the θ-coordinate axis, and is positive in the θ-direction. Only the transverse component of displacement is non-trivial for this orientation of the dislocation.

Radial and vertical displacements and fluid partial stress responses are given in Figure 5.17B through 5.17D for a 45-degree orientation of the fracture plane unit normal relative to the r-coordinate axis. In Figure 5.17C, the vertical response is again trivial for the center plane source.

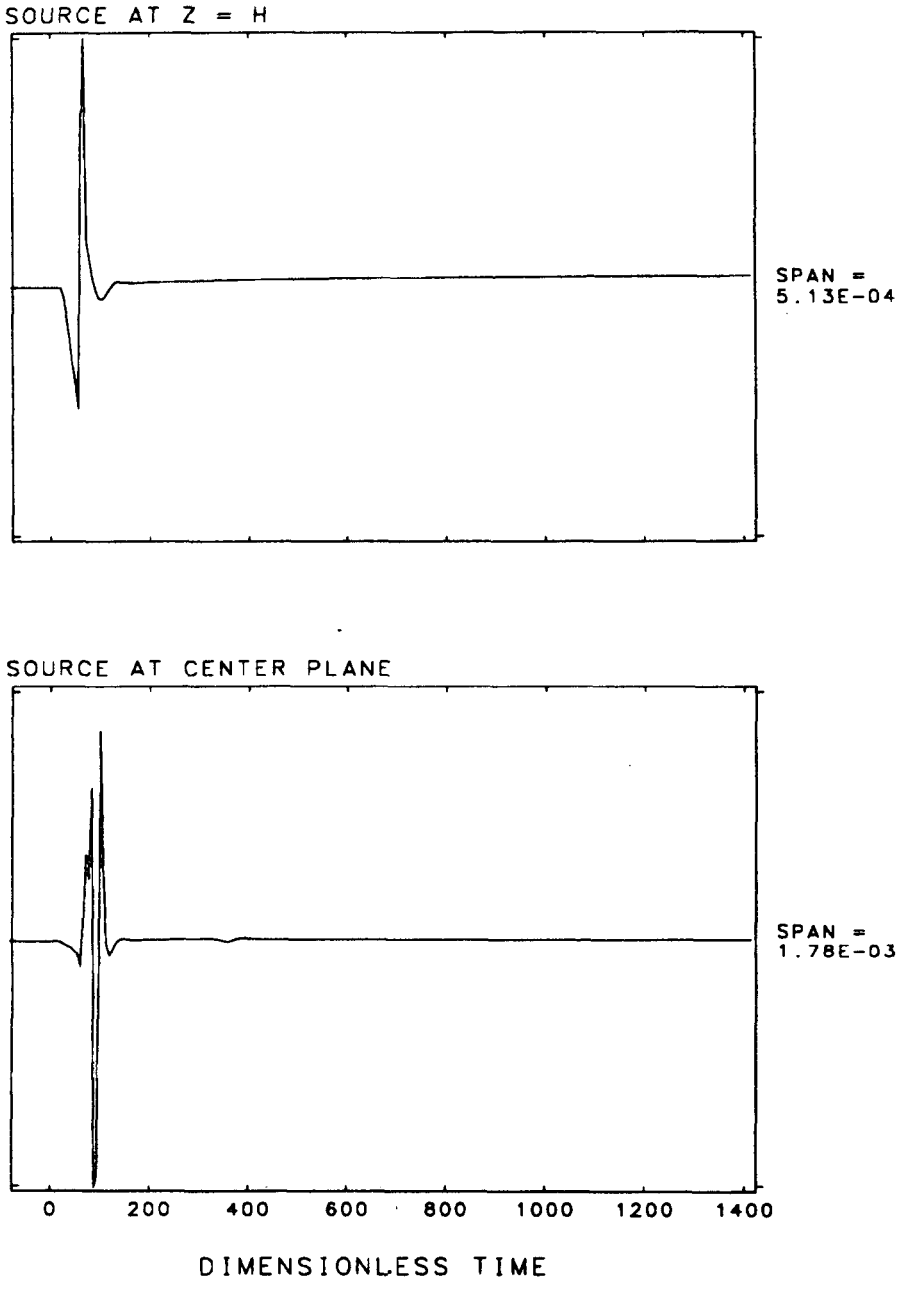

FIGURE 5.17A TRANSVERSE DISPLACEMENT AT CENTER PLANE, RADIUS 30, TO A UNIT R - θ SHEAR FAILURE AT 0-DEGREE ORIENTATION

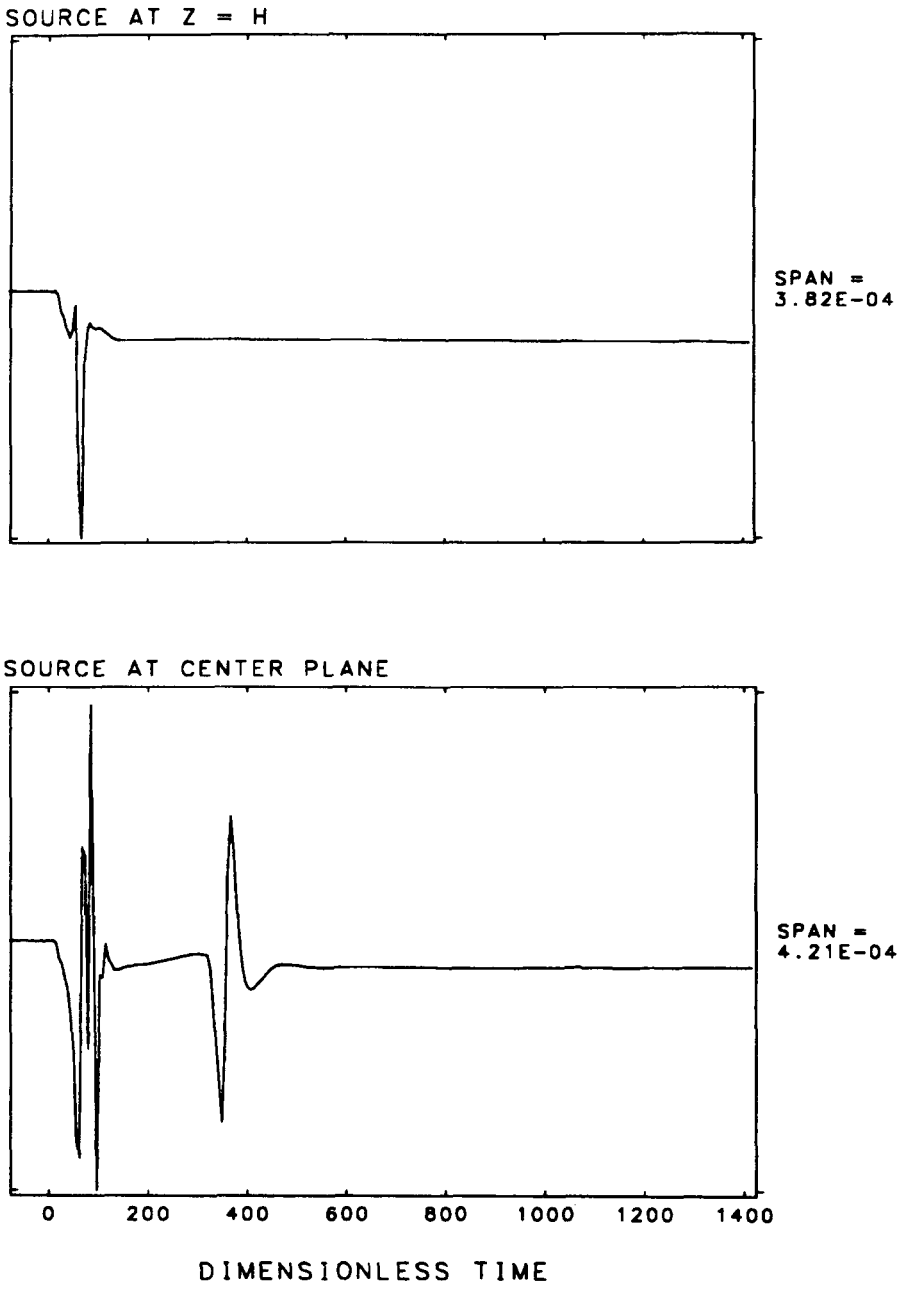

FIGURE 5.17B RADIAL DISPLACEMENT RESPONSE AT CENTER PLANE, RADIUS 30, TO AN R - θ SHEAR FAILURE ORIENTED AT 45 DEGREES

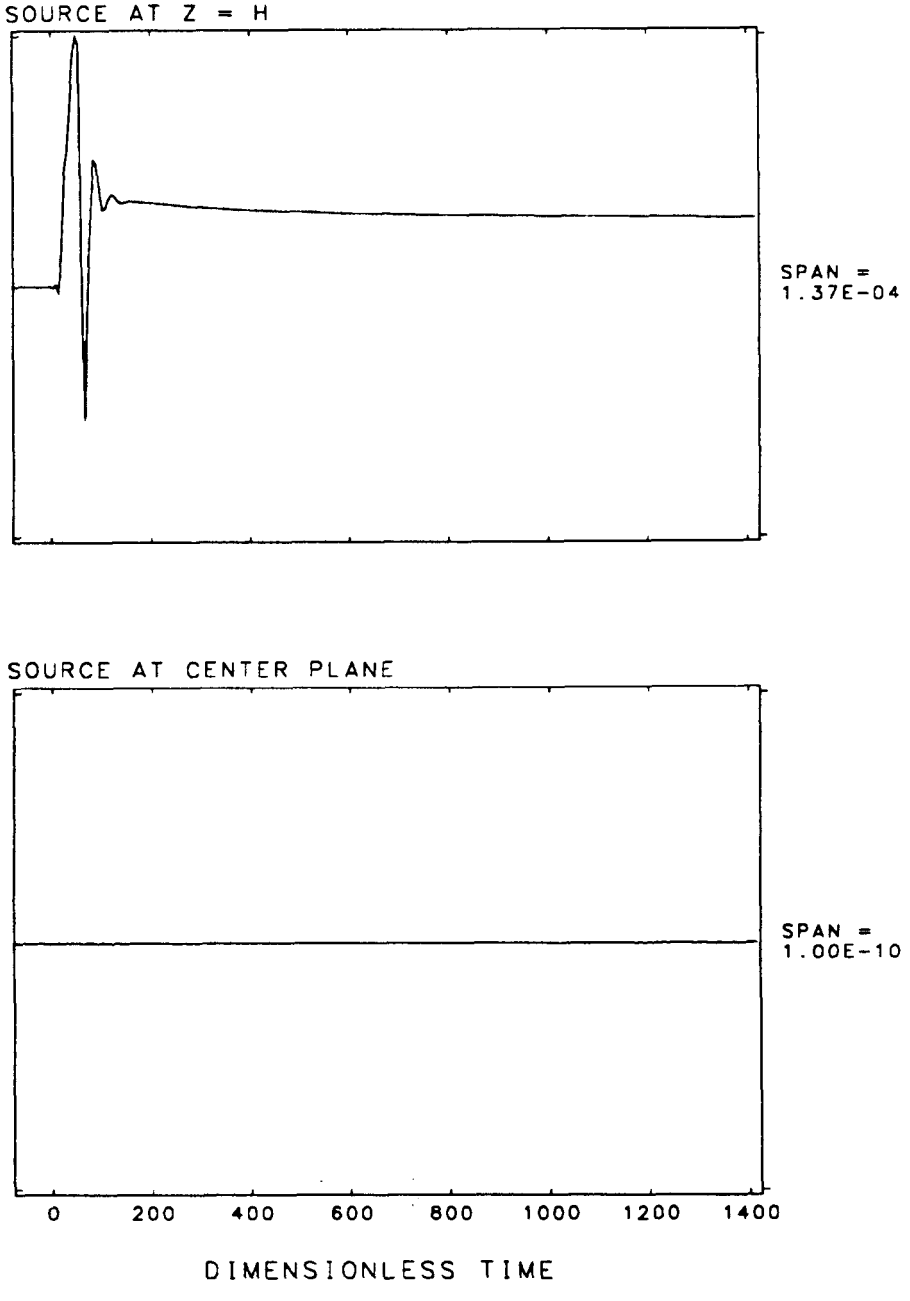

FIGURE 5.17C VERTICAL DISPLACEMENT RESPONSE AT CENTER PLANE, RADIUS 30, TO AN R - θ SHEAR FAILURE ORIENTED AT 45 DEGREES

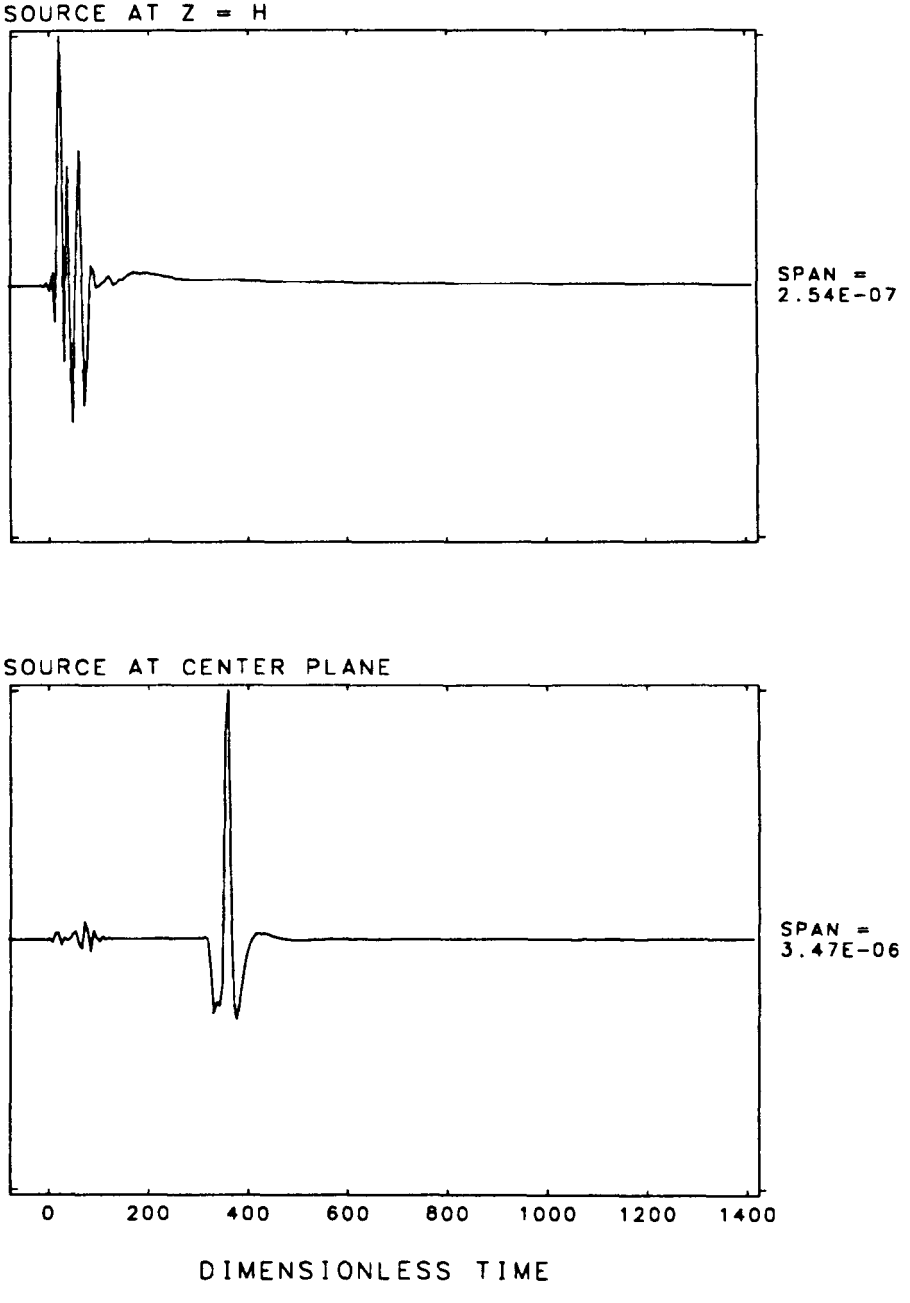

FIGURE 5.17D FLUID PARTIAL STRESS RESPONSE AT CENTER PLANE, RADIUS 30, TO AN R - θ SHEAR FAILURE ORIENTED AT 45 DEGREES

In Figure 5.17A, there exists a small hint of a second mode arrival, which, for transverse motion, represents a pure shear motion, and is analogous to the near-field motion of the fast elastic wave. In the radial displacement (Figure 5.17B) and fluid partial stress (Figure 5.17D) responses to r–θ sources oriented at 45 degrees, there are very substantial second mode arrivals at about time 390 to 400, relative to the earlier shorter period first-mode dilatational and shear arrivals. The shorter period early arrivals are of very much lower amplitude than the second mode arrival in the fluid partial stress response, very surprising because of the lack of source dilatation. Evidently, for a 45 degree orientation, a pure shear failure may produce a substantial second mode wave.

For sources at the upper boundary, the second mode arrivals are virtually unobservable, though there is a slight relaxation of the vertical response illustrated in Figure 5.17C.

5.4.2.2 Center Plane Responses to θ–z Shear Failures

Responses to θ–z shear dislocations are presented in Figures 5.18A through 5.18D. The orthogonal displacement discontinuity and fracture plane unit normal both lie in the θ–z plane. At zero degree orientation (Figure 5.19A), the unit normal is parallel with the θ-axis, and the displacement discontinuity is parallel with the z-axis. The transverse displacement is the only non-trivial response for for zero-degree orientation, and only for sources not on the center plane of symmetry. For non-zero-degree orientation, the radial and vertical displacement and fluid partial stress responses are non-trivial, and maximum responses are achieved for a 45-degree orientation of the fracture plane unit normal relative to the θ-axis (Figures 5.18B, C, and D). The waveforms are essentially unaffected by fracture plane orientation. The vertical displacement response in Figure 5.18C remains zero for a source at the center plane.

There is a small second-mode arrival in the radial response relative to the shorter period, earlier arrivals, illustrated in Figure 5.18B. In Figure 5.18D, the fluid partial stress contains a large second-mode contribution relative to the earlier arrivals. A second mode wave is visible in the radial and vertical displacement and especially in the fluid partial stress responses to sources at the upper boundary, though these responses are severely attenuated because of propagation through the low permeability region.

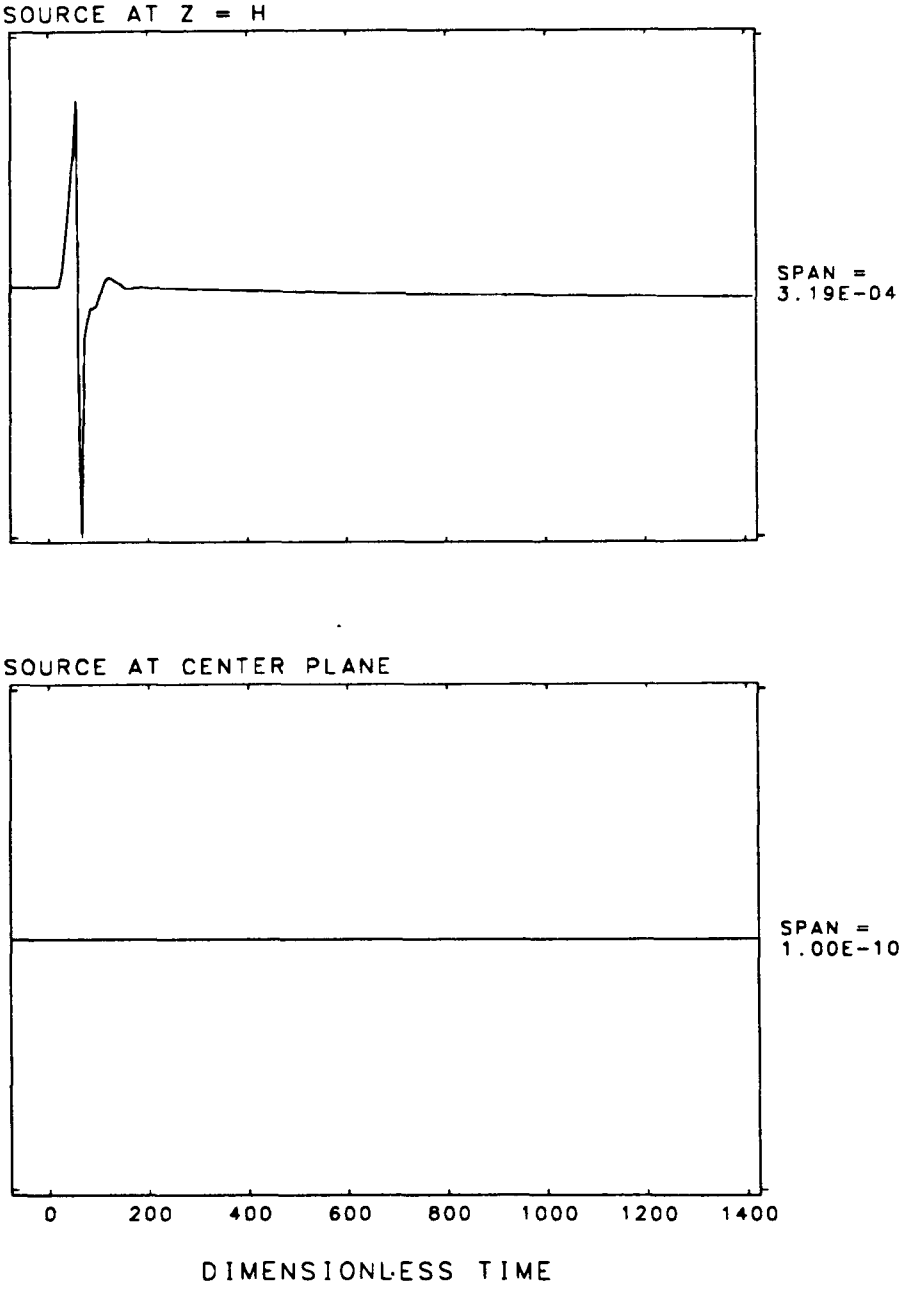

FIGURE 5.18A TRANSVERSE DISPLACEMENT RESPONSE AT CENTER PLANE, RADIUS 30, TO A UNIT θ - Z SHEAR FAILURE ORIENTED AT 0 DEGREES

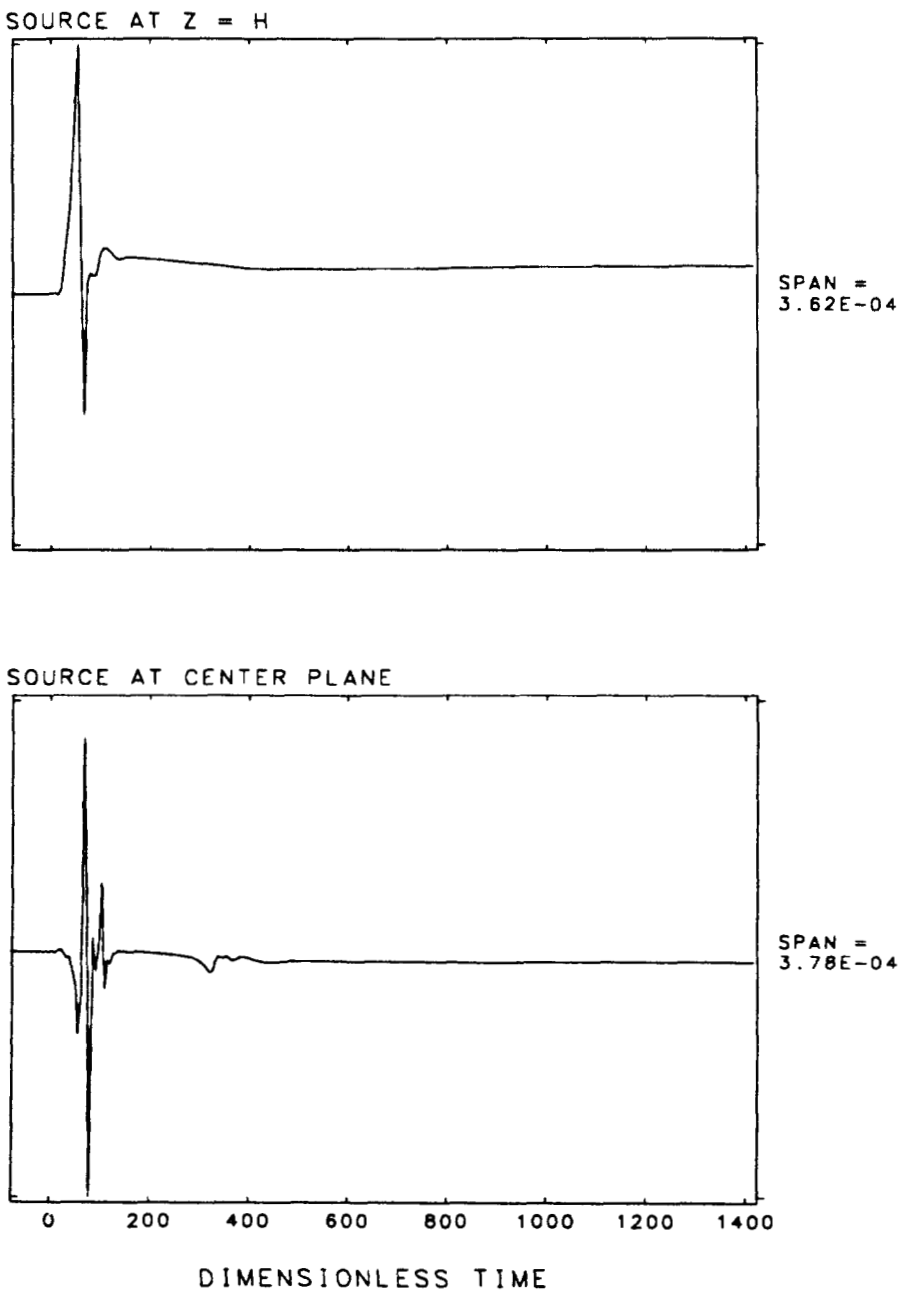

FIGURE 5.18B RADIAL DISPLACEMENT RESPONSE AT CENTER PLANE, RADIUS 30, TO A θ - Z SHEAR FAILURE ORIENTED AT 45 DEGREES

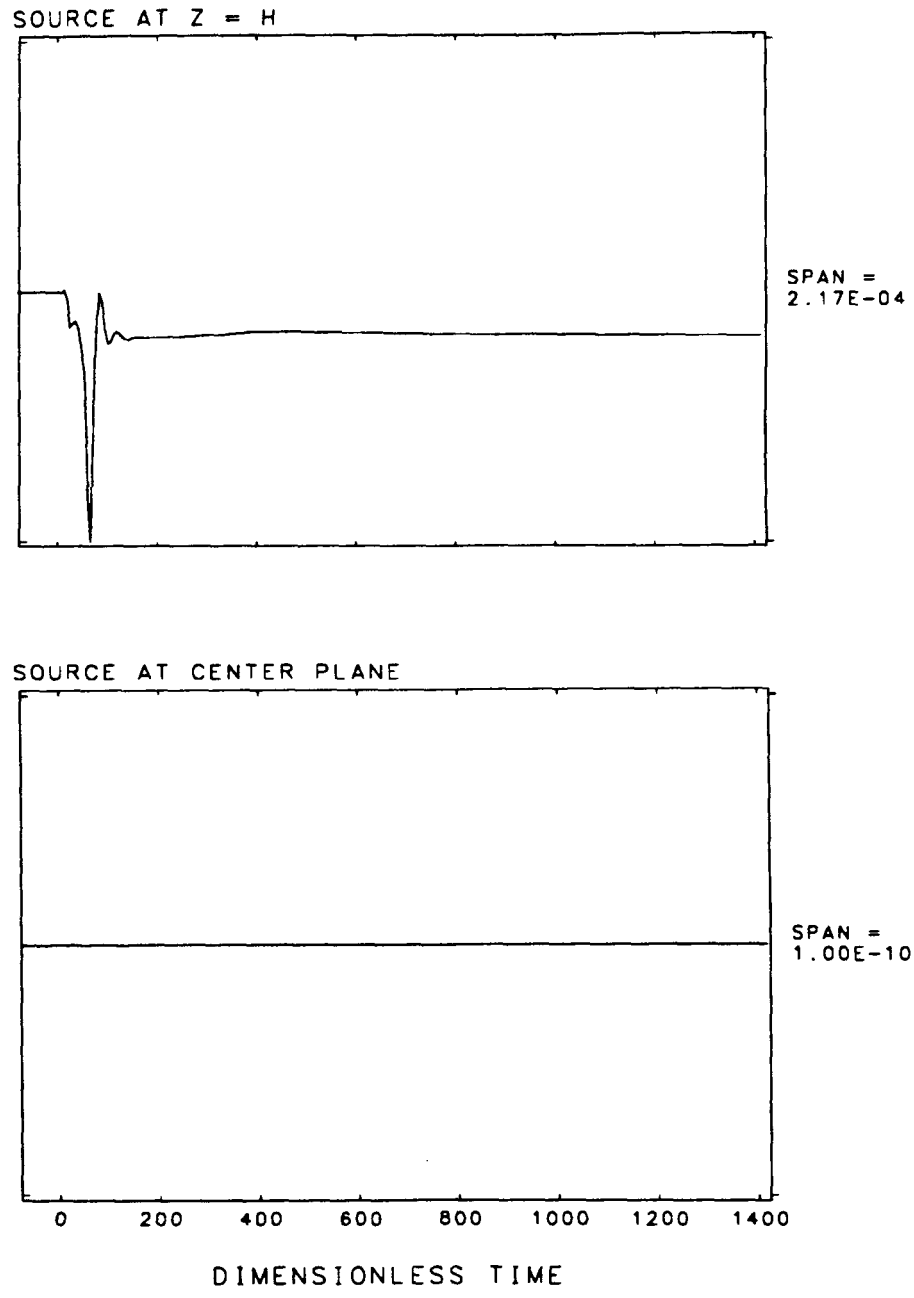

FIGURE 5.18C VERTICAL DISPLACEMENT RESPONSE AT CENTER PLANE, RADIUS 30, TO A θ - Z SHEAR FAILURE ORIENTED AT 45 DEGREES

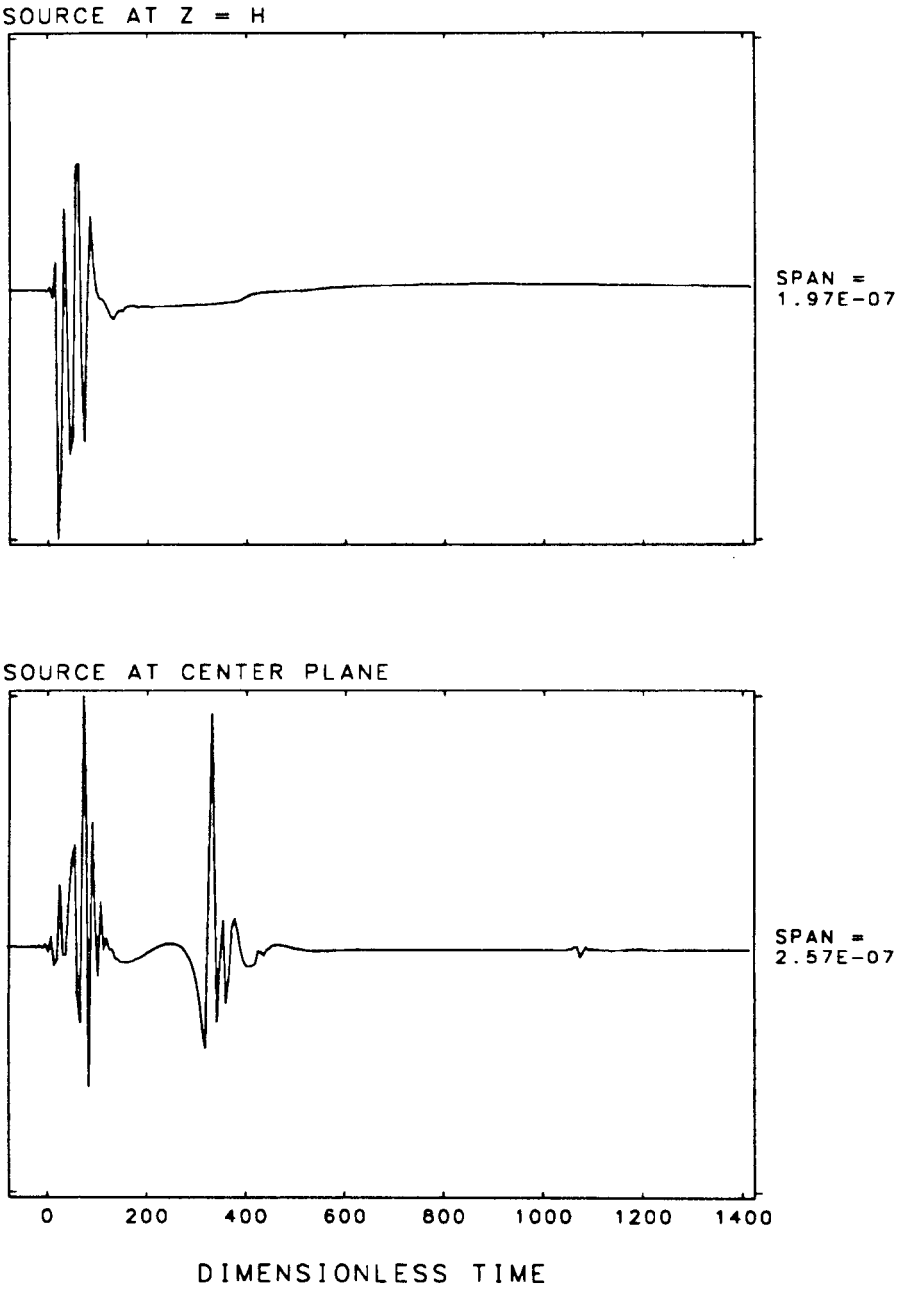

FIGURE 5.18D FLUID PARTIAL STRESS RESPONSE AT CENTER PLANE, RADIUS 30, TO A θ - Z SHEAR FAILURE ORIENTED AT 45 DEGREES

5.4.2.3 Center Plane Responses to $z-r$ Shear Failures

Radial and vertical displacement and fluid partial stress responses to $z-r$ shear dislocations at various orientations are presented in Figures 5.19A through 5.19C, respectively. The zero-degree orientation is with the fracture plane unit normal parallel to the r-axis. Results for multiple orientations are presented because the waveforms are dependent on fracture plane orientation for sources not on the center plane. The responses to sources at the upper boundary are primarily composed of the fast dilatational and shear waves, though if the results were plotted at higher resolution, the second mode arrivals may also be observable, as in the earlier figures. The second-mode arrivals are very significant in the radial displacement and especially fluid partial stress responses shown in Figures 5.19A and 5.19C, respectively.

In Figures 5.17A there is a slight indication of a second mode arrival at about time 400 (0.13 seconds). These responses are transverse to the direction of propagation, involving pure SH motion, in the absence of radial and vertical displacement and fluid partial stress. The second mode arrival is analogous to the near-field P-wave arrival found in the elastic case for transverse waves (Aki and Richards, pg. 79, 1980). Though this may be a "new wave," the formalism developed by Norris (1985) should similarly exhibit a second mode near-field transverse wave. A similar second mode arrival is observable in the vertical displacement response to a center plane $z-r$ failure oriented at 0 or 90 degrees (Figure 5.19B), for which orientation the second-mode radial displacement and fluid stress is zero.

5.4.2.4 Upper Boundary Responses

Upper boundary responses to shear dislocations are presented in Figures 5.20A through 5.20D. In these figures, the shear failures are all across fracture planes with unit normals parallel with one of the coordinate axis. Thus, an $r-\theta$ dislocation has fracture plane unit normal parallel with the r-axis and displacement discontinuity parallel with the θ-axis. Responses for 45-degree fracture orientations are not presented, though they can be computed easily.

Figures 5.20A and 5.20B contain transverse responses to $r-\theta$ and $\theta-z$ shear failures. Because of symmetry, the transverse response given in Figure 5.20B to a $\theta-z$ shear failure at the upper boundary would have been zero without the presence of the porous layer. As a result, this response is an order of magnitude less than the responses to the sources at the other positions. There is considerable

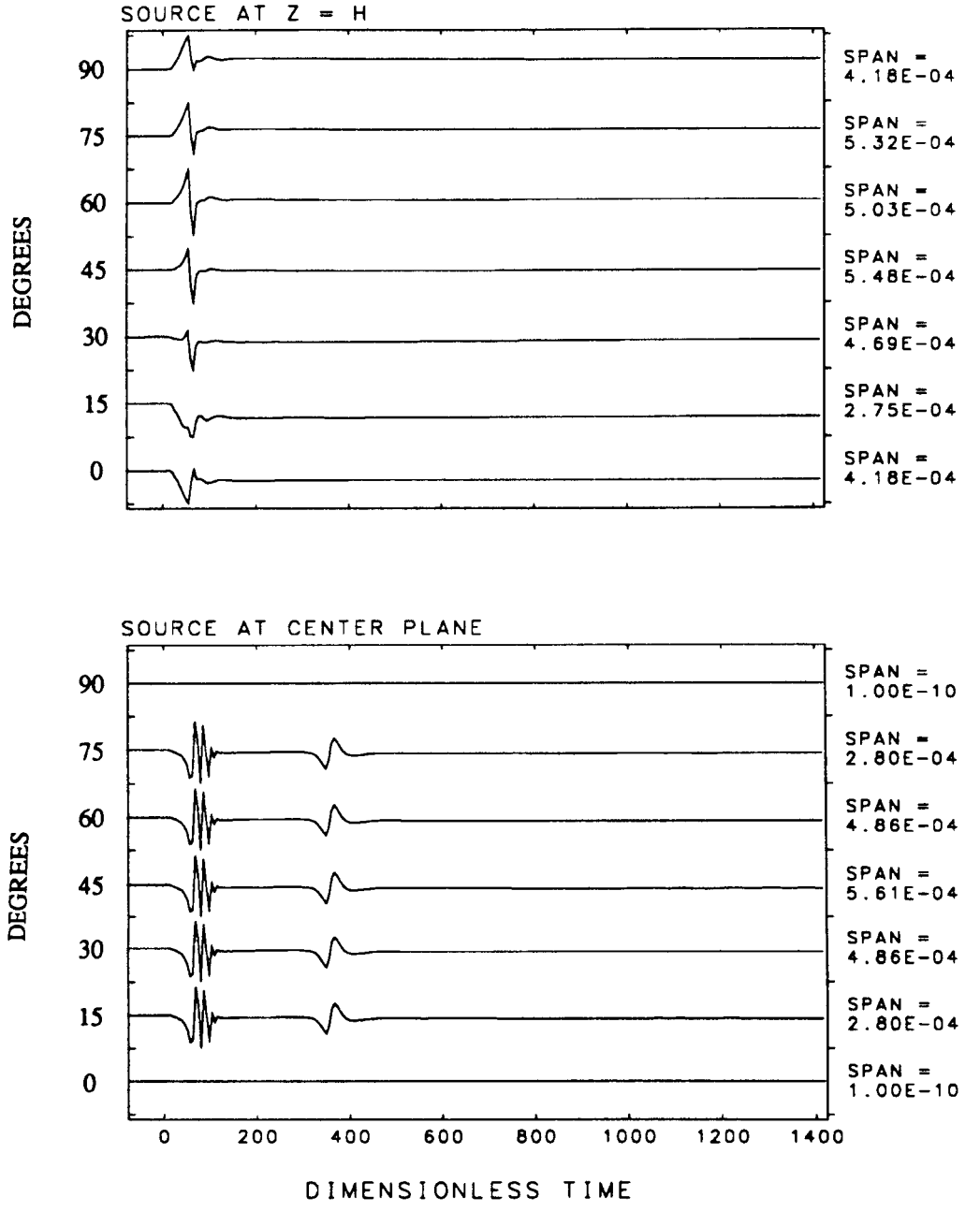

FIGURE 5.19A RADIAL DISPLACEMENT RESPONSE AT CENTER PLANE, RADIUS 30, TO Z-R SHEAR FAILURES ORIENTED AT VARIOUS ANGLES RELATIVE TO VERTICAL

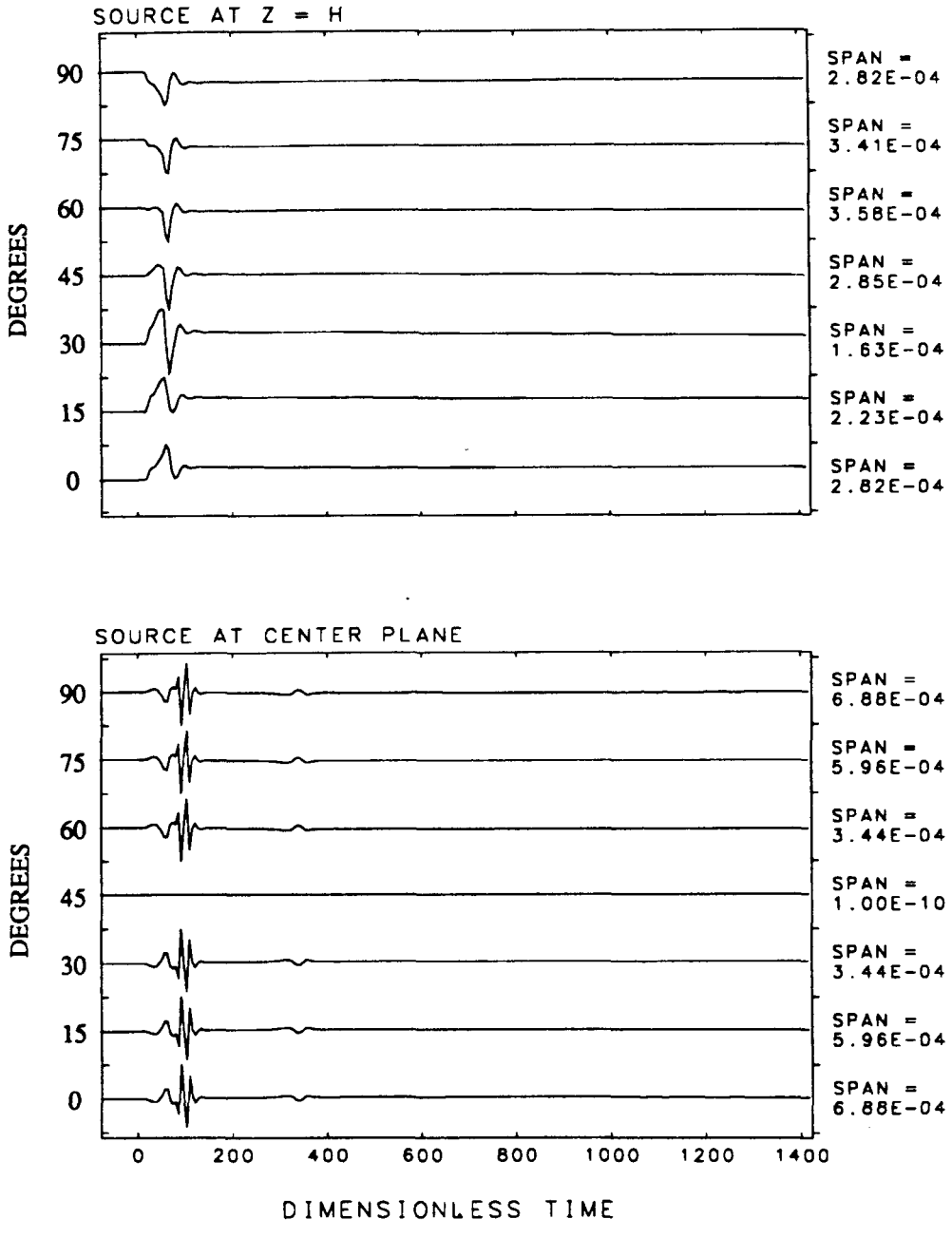

FIGURE 5.19B VERTICAL DISPLACEMENT RESPONSE AT CENTER PLANE, RADIUS 30, TO Z-R SHEAR FAILURES ORIENTED AT VARIOUS ANGLES RELATIVE TO VERTICAL

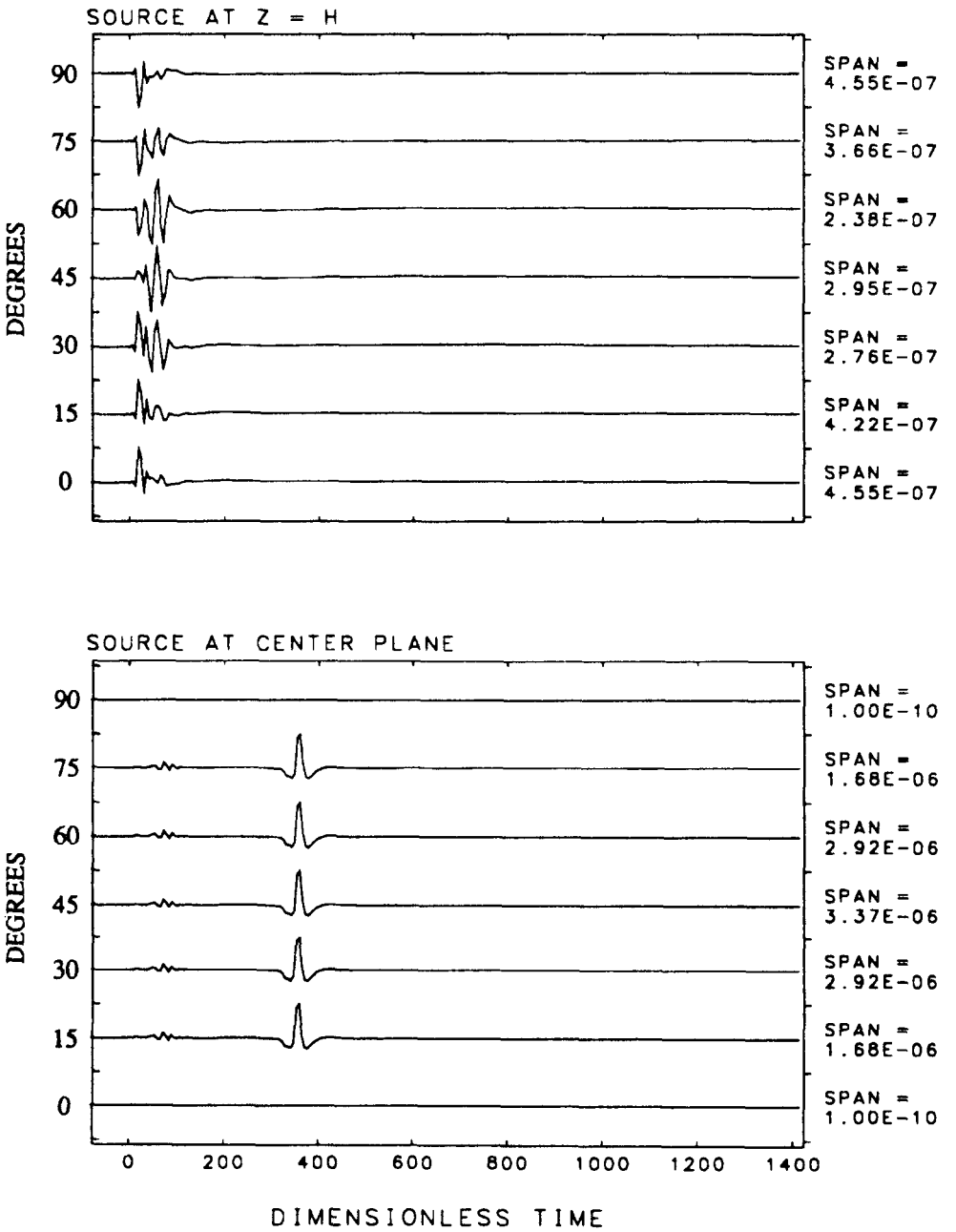

FIGURE 5.19C FLUID PARTIAL STRESS RESPONSE AT CENTER PLANE, RADIUS 30, TO Z-R SHEAR FAILURES AT VARIOUS ANGLES RELATIVE TO VERTICAL

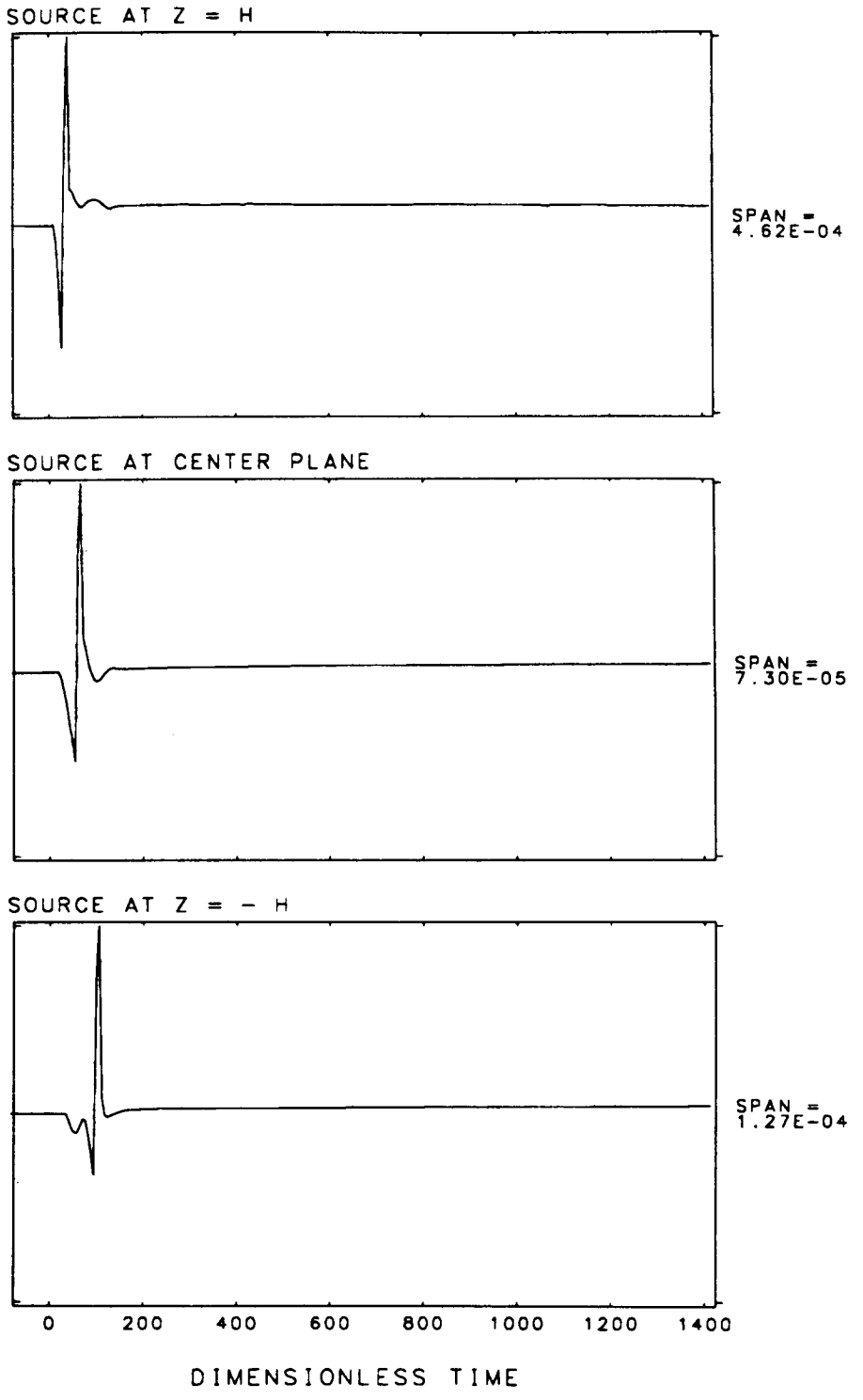

FIGURE 5.20A TRANSVERSE DISPLACEMENT RESPONSE AT UPPER BOUNDARY, RADIUS 30, TO R - θ
SHEAR FAILURES

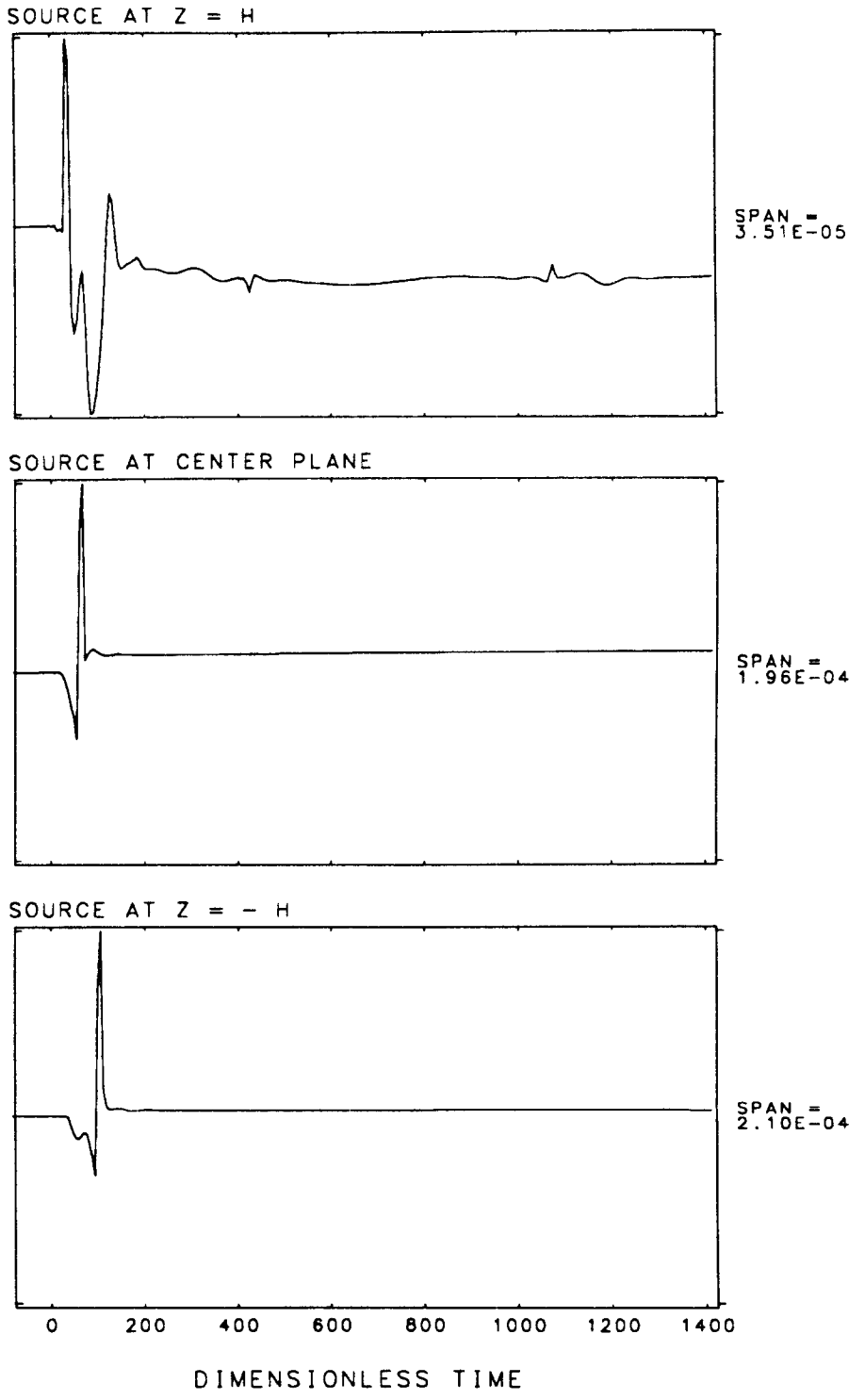

FIGURE 5.20B TRANSVERSE DISPLACEMENT RESPONSE AT UPPER BOUNDARY, RADIUS 30, TO θ - Z
SHEAR FAILURES

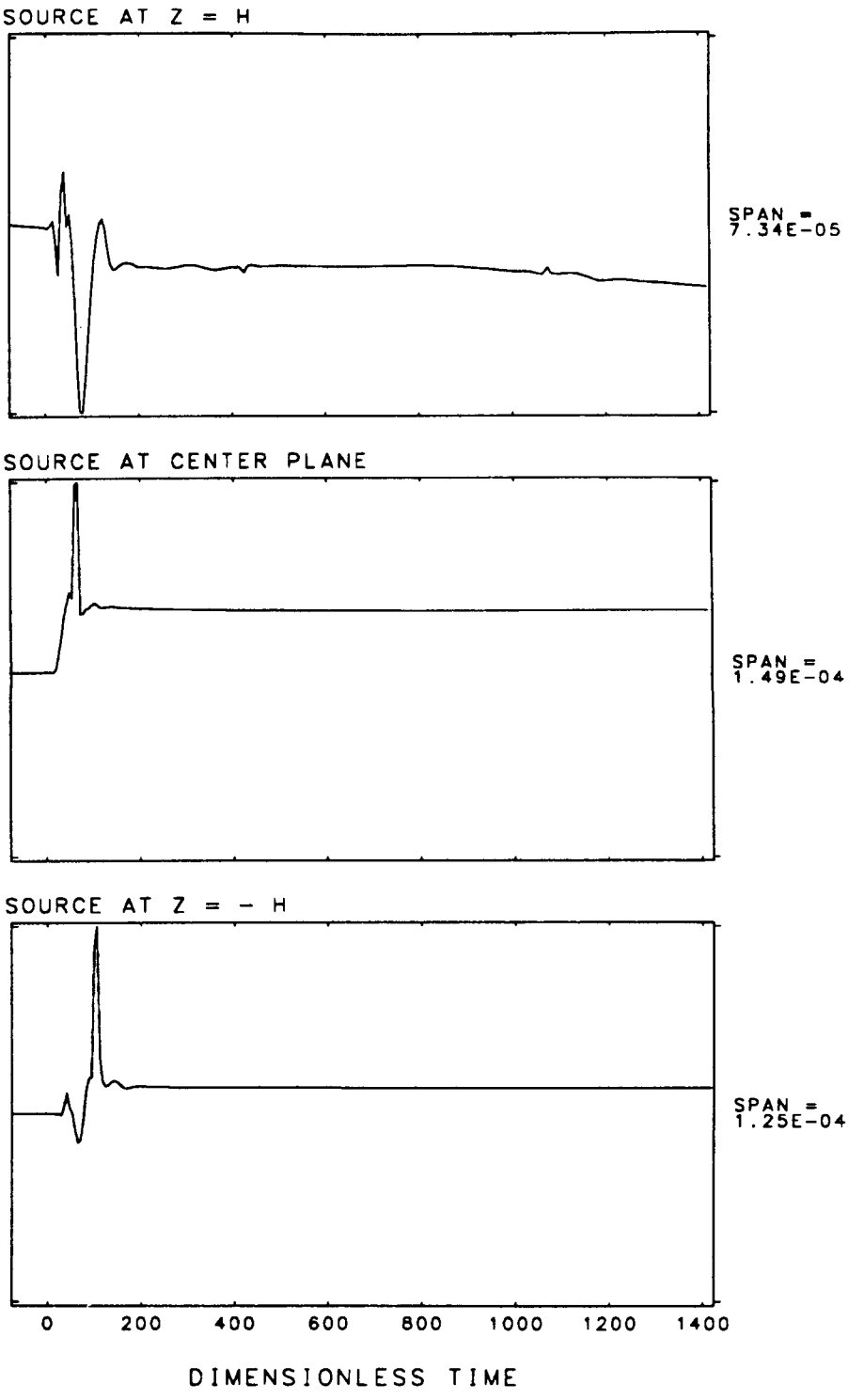

FIGURE 5.20C RADIAL DISPLACEMENT RESPONSE AT UPPER BOUNDARY, RADIUS 30, TO "Z-R" SHEAR FAILURES

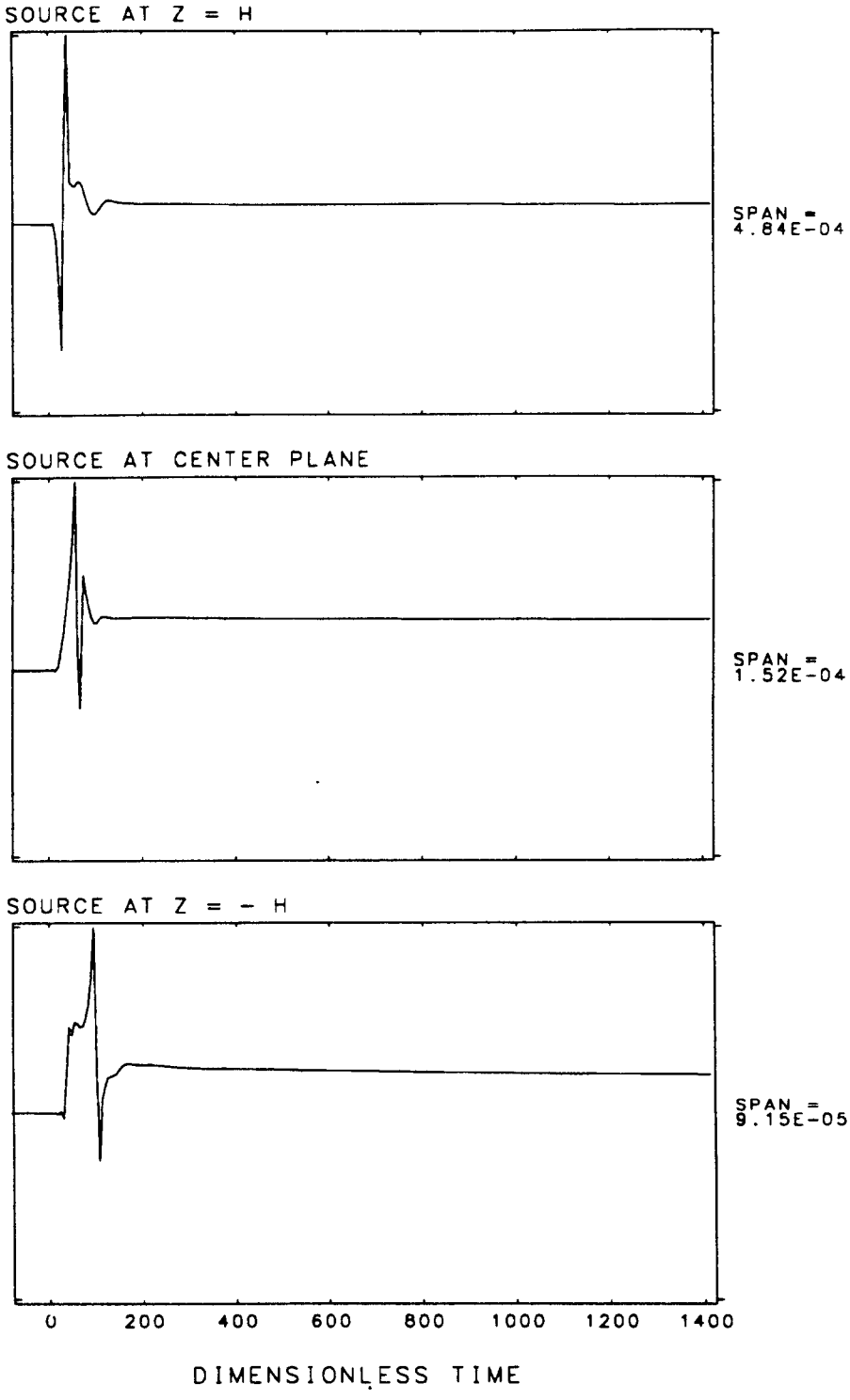

FIGURE 5.20D VERTICAL DISPLACEMENT RESPONSE AT UPPER BOUNDARY, RADIUS 30, TO "Z-R" SHEAR FAILURES

"noise" present in the response, related to insufficient step size during Hankel inversion. The noise arrives at the time of the second-mode dilatational wave velocity for the high-porosity zone. An acausal arrival from an "image source" is observable at time 1050, again due to insufficient wavenumber step size.

Radial and vertical displacement responses to $z-r$ shear failures are presented in Figures 5.20C and 5.20D. Again, because of symmetry, the radial response to the source at $z=+h$ would have been zero without the presence of the porous layer. As with the transverse response to a $\theta-z$ failure, shown in Figure 5.18B, the radial component of displacement plotted in Figure 5.20C is much lower than for sources at the other locations, and the signature contains numerical "noise".

Responses to shear dislocations at other orientations can be computed, producing non-trivial displacement responses for non-zero-degree orientations.

5.5 Discussion

The foregoing results illustrate the ability of a reflectivity model to represent sources of various types, including fluid volume supply as well as arbitrary porous matrix dislocations. Responses may be computed for any fracture surface orientation and discontinuity, as well as fluid dilatation.

Unfortunately, the results for fluid volume supply are less than satisfactory for source locations in low permeability regions, where diffusion dominates the long time response, producing apparent static displacements. The interpretation is that the long time diffusion effect is so strong that quiescence is not obtained until long after the end of the time window employed here.

Part of the problem of apparent static displacement may involve numerical imprecision, because when calculating the response to fluid volume supplies, the long term static displacements of the gradients of the Green's functions for matrix and fluid loads must be canceled. If these functions are not well computed, complete cancellation may not be obtained, in which case some residual static displacement may result. The long-time responses to fluid injection are uniform and of are all of similar character, depending on position, suggesting that if there are numerical errors, they are systematic, rather than random.

The above latter observation suggests that a reformulation of the problem may be appropriate, specifically involving propagation of the fluid stress and fluid divergence, rather than the fluid stress and fluid vertical displacement. Fluid load terms would then be represented as fluid volume supplies directly. Bonnet, 1987, represents the fluid volume supply by just such an approach, though using Green's functions for homogeneous regions and boundary element procedures for modeling layers. A. Norris, in a private conversation, indicated that his development of the representation theorems for point loads in porous materials (Norris, 1985) is equivalent to that of Bonnet if the divergence of the Green's tensors for fluid point loads is taken, as is the approach used here. This is expected. Reformulation of the problem should be straight-forward, and may involve only the method by which the fundamental loads are applied to the fluid in solving the boundary value problem in coordinate z. Reformulation has not been investigated here.

The problem can be recomputed with much finer frequency step size to lengthen the time window. This would require much more computer time than the already substantial time expended for the present example. An alternative procedure is to employ a complex frequency during numerical solution of the reflectivity problem and Hankel inversion to introduce attenuation in time. After Fourier inversion of the spectral Green's functions, temporal responses may be multiplied by a simple exponential to recover the long-time response. This relatively simple procedure has not been tested here, however.

The zero static displacement observed for fluid dilatational sources at the center plane where the porosity is high indicates that the Green's functions for fluid volume supplies are being constructed properly. These responses were constructed from the gradients of the Green's functions for both porous matrix and fluid point sources. These functions contain static displacements which, when combined with the moment tensor for fluid volume supplies, cancel, at least for sources at the center plane, providing an important check for consistency of the the solution and correctness of the fluid load representation. Recall that the load representations for sources acting on the porous matrix at extremely small porosity were verified against those for a homogeneous elastic medium. The zero static displacement thus provides a verification of the fluid load representation for sources at the center plane. The check would be more gratifying if the static displacements for the fluid dilatational sources in the low permeability regions at the layer boundaries were zero also. Again, cancellation might have been obtained if a much larger time window were considered.

The major motivation for applying Biot's theory to acoustic emission in hydraulic fractures is to provide a tool for studying fluid pressure transients which may launch tube waves within the primary borehole. The model does in fact predict second mode responses of the Biot type for hydraulicly fractured rock. Moreover, significant second mode responses are obtained for pure shear failures, though these depend strongly on radiation patterns. The second mode response is relatively strong and should be easily detected in the field, even if the detailed signature may actually be distorted by the actual fracture geometry relative to that predicted by a continuum representation.

Chapter 6: Summary Discussion and Conclusion

Three tasks have been accomplished. The first was the development of a reflectivity model for computing displacement and fluid stress responses to general dislocation sources in a heterogeneous fluid saturated porous layer. The second task was the development of a constitutive model for wave propagation in hydraulicly conductive fracture networks using conventional relations for porous media. The third task consisted of applying the results of the first and second tasks to the problem of acoustic emission in a fluid saturated hydraulicly conductive fracture network.

6.1 Reflectivity Model

The reflectivity model employs Biot's (1956) equations of motion for isotropic porous materials, solutions of which are expanded in cylindrical harmonics using the procedures described by Aki and Richards (1980). Numerical integration procedures are used for computing propagators for displacement and stress over a limited number of regions. These propagators are substituted into a global matrix representing boundary conditions between contiguous regions. The matrix is solved by Gaussian elimination and back-substitution to obtain solutions to point loads to the set of ordinary differential equations resulting from the expansion. The spectral solutions in three dimensions for point loads and moments are then obtained by Hankel inversion procedures, and temporal responses are computed via Fourier inversion. The procedure is distinct from other procedures such as those used by Chin (1984) employing matrix methods to solve the reflectivity problem with a set of homogeneous layers approximating continuously varying material properties. Arbitrary dislocations of the porous matrix and fluid dilatation can be included, though the representation is limited to point sources. The fluid dilatation is input as an quantity independent of the matrix dislocation. The numerical integration approach is fast and practical for inhomogeneous layers, but is not competitive with matrix methods for large homogeneous layers.

There are a number of practical limitations of the model. The principal limitation is that if second-mode P-wave velocities are very much smaller than the first-mode P- or S-wave velocities, substantial computer time is required to compute the Hankel inversion integral. A similar problem arises if the porous matrix shear stiffness is very low, resulting in a low S-wave velocity relative to the fast P-wave velocity. The ordinary differential equations become stiff, requiring care during numerical integration of the propagators. Evanescence becomes a major problem, in this case. A second limitation is that a fluid volume source is represented as a scalar moment, requiring intermediate

computation of responses to point loads applied to the fluid constituent. The solutions become singular as the frequency approaches zero, perhaps contributing to numerical error at very low frequencies. A third limitation is that the procedure becomes uneconomical for large homogeneous layers, in which case the more standard procedures used by Chin (1984) are attractive.

The model is applied here to hydraulicly conductive fracture networks. There are other potential applications as well. These include modeling of the seismic response of porous seabeds, (Yamamoto, 1983), fault zone responses to acoustic emission sources, and vibration generation and propagation in porous saturated soils with continuously varying shear stiffness and porosity. The latter problem is of significance to the prediction of ground vibration from industrial and transportation sources (Nelson, et al, 1987).

6.2 Constitutive Model

The constitutive model developed here for propagation of waves in hydraulicly conductive fracture networks employs well established relations for porous materials (Biot and Willis, 1957). Assuming that a porous material model is valid for representing fracture networks in rock, the principal problems involve estimation of the tortuosity and sinuosity for the network, evaluating the effect of crack density on shear and bulk stiffnesses for the fractured rock, and specifying the limits of model application.

The tortuosity describes the effect of network geometry on fluid flow and the kinetic energy of the system, and is determined by equating the micro-mechanical and macro-mechanical kinetic energy densities in the presence of relative motion of between the fluid and rock. The sinuosity describes the effect of network geometry on energy dissipation, and should be determined by comparing the micro-mechanical and macro-mechanical dissipation rates for fluid flow relative to the rock. However, for the present problem, the sinuosity is assumed equivalent to the tortuosity.

The shear and bulk stiffnesses of the fractured rock under drained conditions is determined of formulae derived by Bruner (1976), offered as improvements over the self-consistent formulae given by O'Connell and Budiansky (1976). These formulas give the modulus of elasticity and Poisson's ratio as a function of crack density parameter. Given the crack aspect ratio and crack geometry, the crack density parameter may be directly related to porosity. Once the stiffnesses are determined for the drained condition, the relations of Biot and Willis (1957) complete the specification of the constitutive

parameters appearing in Biot's (1956) equations of motion.

The fracture network is not conductive for insufficient crack density. Therefore, as the crack density (and porosity) decreases with increasing distance from the center of the layer, the network becomes non-conductive. Selection of the critical crack density is based on the work and discussion given by Long and Witherspoon (1985). For crack densities less than the critical value, the porous material is assumed to be solid, with material properties equivalent to those of the porous material, but with the fluid constrained within the solid, unable to flow.

6.3 Hydraulic Fractures

The variable porosity model was used to study a hypothetical symmetric 60 meter wide hydraulicly fractured rock layer with maximum fracture porosity of 3% at the plane of symmetry and 0.5% at the boundary. The layer was bounded above and below by semi-infinite solid regions with P- and S-wave velocities equivalent to those of the saturated fractured rock with constrained fluid at the layer boundary. The porosity profile and the directly proportional crack density parameter were of approximately Gaussian shape near the center of the layer and monotonously decreasing away from the boundary. The region of high permeability was about 10 meters wide. Fluid properties were those of water. The micro-crack aperture was assumed proportional to the porosity, with maximum micro-crack aperture of 1.0 mm at the center. A crack aspect ratio of 1/3 % was employed throughout.

The principal outcome of the model application is the prediction of a second mode P-wave arrival of substantial magnitude, observable in the the porous matrix displacement and the fluid partial stress responses at the center of the porous layer. The second mode P-wave arrival is diffusive at low frequencies, is attenuated at high frequencies, and has a much lower velocity than those of the faster first-mode P- and S-waves. The second mode wave is not observable outside the fracture zone, because the wave is a bound-state or trapped mode propagating within the fractured layer.

The second mode arrival is preceded by arrivals which have group velocities consistent with the P-wave and S-wave velocities of the solid region. Both of these early arrivals are thus presumed to be refracted head-waves. Following the initial arrivals are dispersive channel waves or trapped modes which also precede the second mode arrival.

The waveforms of displacement and fluid partial stress responses due to the Biot second-mode wave are generally of longer period than the early arriving refracted headwaves and relatively fast trapped modes for receiver locations up to at least 60 meters from the source, and are clearly separated in time from early arrivals. The second mode responses are dominant at the center of the fracture zone for distances as far as 30 meters from dilatational sources, depending on fracture orientation and source characteristics. The results suggest that low-pass filtering of field data will reduce the amplitude of shorter period fast P- and S-wave arrivals relative to the longer period second-mode P-wave arrivals, thus perhaps aiding detection and analysis of slow second-mode waves which may exist in down-hole fluid pressure transient signatures and seismic responses.

For the porosity profile employed above, the second-mode response is very diffusive for dilatational sources at the extreme boundary between the porous and solid regions, presumably because of low permeability. Significant relaxation due to fluid diffusion is observable for both dilatation and shear dislocations in the low permeability zone. However, the time window used for modeling was too short to capture the long-time response to these sources.

The transverse displacement response to a transverse $r-\theta$ shear dislocation (transverse displacement discontinuity in the θ-direction across a plane with unit normal along the r-axis) contains an arrival at a time coincident with the second-mode wave. A transverse fast-mode arrival is also contained in the transverse displacement response of the porous matrix to the $r-\theta$ source. These arrivals are the counterparts to the transverse displacement near field response occurring at the P-wave arrival time for a wave in an elastic solid. Both of the fast and slow mode arrivals occur in the absence of a fluid partial stress response, identically zero by symmetry. Rotation of the failure surface, disturbing the symmetry, results in a non-trivial fluid partial stress response. These near-field responses would be observed for homogeneous porous materials, and should be predicted by the theories given by Norris (1985), and Burridge, et al (1979).

Acoustic emission waves involving dilatation (as with Mode-I failures) in the fracture zone and in the solid region are strongly influenced by fluid backflow into the void left by the event. Fluid backflow is often assumed to be instantaneous, as in the model developed by Chouet, et al (1985). These results indicate that fluid backflow should be taken into account when inverting detected seismic waveforms for source characteristics.

The slow-mode P-wave contribution to the displacement and fluid partial stress responses at the center plane to dilatational "Mode I" failures is significantly influenced by the orientation of the failure surface. In the case of the fluid partial stress, θ–θ and $z-z$ dilatational failures produce second mode responses of opposite sign to that produced by an $r-r$ failure for the instantaneous fluid backflow case. For finite fluid backflow time, the fluid partial stress initial response is approximately independent of fracture plane orientation.

Long term near-field relaxation is observable in the response functions, especially for sources in the low-permeability region near the layer boundary. However, the relaxation effect is most pronounced for dilatational failures, and is evidently related to flow of fluid in the immediate vicinity of the failure. Relaxation effects are very dependent on fluid backflow. Very little relaxation effects are observed for pure shear dislocations.

A number of other conclusions may be derived from the model. Yet to be performed is a parametric study of the effect of porosity, porosity profile, micro-crack aperture, crack aspect ratio, tortuosity and sinuosity, etc, on response functions. Parametric studies are limited by CPU time requirements. A number of test runs were performed during the course of model development, involving various maximum porosities, micro-crack apertures, layer widths, and so forth. The results of these test runs do indicate that increasing the porosity, thus increasing the permeability, produces lower rates of attenuation of the second mode response. In fact, for a maximum porosity on the order of 10% and relatively large micro-crack aperture, reflections of the second mode wave as well as the fast dilatational and shear waves from the layer boundaries can be observed. These results were not presented since the porosities involved were judged to be unrepresentative of hydraulicly fractured rock. These early runs indicate that the period of high frequency oscillation due to trapped modes following the first arrival of the fast mode wave or critically refracted head wave is significantly influenced by porosity profile, (or fracture zone width), as might be expected.

6.4 Suggestions for Research

Prior to model development, a number of alternative procedures were considered for modeling hydraulic fractures. Some of these involve approximations which may be applied to the reflectivity model, and others concern the basic assumptions used in the model.

The model porosity used for the hydraulicly fractured zone has such low porosity that, for example, the bulk modulus of the fluid has little effect (provided that it is reasonably high) on the fast-mode P-wave velocity, determined primarily by the bulk-modulus for the fractured rock under saturated conditions. Therefore, the Biot second mode wave might be computed independently of the first mode wave, requiring solution of a diffusive acoustic wave problem. The 6X6 propagator employed for the PSV problem might then be decomposed into a 4X4 propagator for the porous matrix and a 2X2 propagator for the Biot second mode. The SH problem would remain as a 2X2 problem. Significant reduction of CPU time would be obtained, though the actual saving has not been determined. The Hankel function step size might be increased significantly for the second-mode contribution, providing a further reduction of CPU time. The advantage of the present model is that arbitrarily high porosities can be included without reformulation. Porosities on the order of 10% can be argued for certain vuggy porosities of oil-bearing rock, for which the exact formulation is appropriate.

Early in the study of fluid pressure waves in a fracture zone, a fluid sheet representation (Green and Naghdi, 1984) and boundary element methods (Brebbia, 1978) were considered for modeling discrete fracture networks. The approach remains untried but may be particularly effective for studying the effect of fracture network geometry on displacement and fluid stress responses to acoustic emission sources. Incorporation of fluid sheet elements into a boundary or finite element formulation for the fracture zone should be a natural extension of these numerical procedures, and would represent a level of realism similar to that now used for studies of fluid diffusion in fracture networks.

A boundary element method would involve significant CPU time and a large number of elements for a realistic fracture network and short wave-lengths, in which case the Biot representation is perhaps more attractive, though it loses validity at high-frequencies where wavelengths become short with respect to fracture spacing. The boundary element method is most useful for studying a network of a limited number of large aperture discrete fractures. Such a method would be very realistic, and might be useful for "validating" a Biot representation for fracture networks.

The finite difference approach used by McNiven and Mengi (1977) is attractive, but requires convolution of response functions for visco-dynamic effects due to fluid flow relative to the porous matrix at high frequencies. A major advantage is that finite geometry fracture zones can be modeled, as was done by Mahrer and Mauk (1987). Secondly, CPU time should be small relative to the reflectivity method, and finite difference methods lend themselves to large scale vectorization of computer code.

Current methods of field evaluation of fracture zone anisotropy include vertical seismic profiling (Majer, 1988). Incorporation of anisotropy would be a natural extension of the present model. Azimuthal isotropy could be incorporated in a straight-forward way, and would capture the effect of fracture planes which favor an orientation with unit normal parallel with the z-axis, while perhaps permitting use of the cylindrical harmonic expansion and Hankel inversion procedures. Higher levels of anisotropy, such as azimuthal anisotropy, would require Fourier inversion with respect to the k_x and k_y axis, and thus require significant additional development. However, including more than just simple anisotropy would involve specification of an excessive number of constitutive parameters. Identification of appropriate parameters for an isotropic fracture network is already a formidable task. Experimental evaluation of a Biot model including more than simple anisotropy would probably not be feasible.

The results indicate that there should be substantial seismic and fluid pressure slow-mode P-wave responses at substantial distances from acoustic emission sources in hydraulicly conductive fractured rock. By expanding monitoring of hydraulic fracturing to include down-hole fluid pressure in the fracture zone and seismic response both within and without the fracture zone, and comparing these results with model predictions, significantly more information regarding fracture properties might be obtained. The acquisition of such data is thus greatly encouraged for subsequent research.

6.5 Conclusion

The study of mixture theory and Biot's equations of motion in particular has been very rewarding. In tribute to Biot, if good agreement, at least qualitative, is obtained between model predictions and experimental data for acoustic emission in hydraulic fractures, further evidence will be acquired testifying to the robustness of Biot's equations and the contribution which the late scientist has made to the study of solid-fluid mixtures.

References

Abramowitz, M. and I. Stegun, 1964. *Handbook of Mathematical Functions* Applied Mathematics Series, 55, Washington National Bureau of Standards,

Achenbach, J. D., 1973. *Wave Propagation in Elastic Solids*, North-Holland Publishing Company, Amsterdam, 425 pp.

Aki, Keiiti, and Paul G. Richards, 1980. *Quantitative Seismology, Theory and Methods, Volume I and II*, W. H. Freeman and Company, San Francisco, 932 pp.

Amsden, A. A., H. M. Ruppel, C. W. Hirt, 1980. SALE: A Simplified ALE Computer Program for Fluid Flow at all Speeds, Los Alamos Report #LA-8095/UC-32.

Archambeau, C. B., and J. B. Minster, 1976. Theory of Failure as a Transition Process in a Stressed Medium, *Report of the Workshop on Application of Elastic Waves in Electrical Devices, Non-Destructive Testing, and Seismology*, ed. J. D. Achenbach, Y. H. Pao, and H. F. Tiesten, Held at Northwester University, May 24-26, 1976. p. 196

Berryman, James G., 1980. *Applied Physics Letters, 37*, p. 382.

Berryman, James G., 1981a. Elastic Wave Propagation in Fluid-Saturated Porous Media, *Journal Acoustical Society of America, 69(2)*, pp. 416-424.

Berryman, James G., 1981b. Elastic Wave Propagation in Fluid-Saturated Porous Media II, *Journal Acoustical Society of America, 70(6)*, pp. 1754-1756

Berryman, J. G., B. P. Bonner, R. C. Y. Chin, G. W. Hedstrom, 1983. Theory of Pulse Propagation in Fluid-Saturated Porous Layers, *1983 Ultrasonics Symposium Proceedings, 2*, Conference held 31 October - 2 November, 1983, Atlanta, GA. Publ. IEEE, New York,

Biot, M. A., 1956a. Theory of Propagation of Elastic Waves in a Fluid-Filled Porous Solid. I. Low-Frequency Range, *Journal Acoustical Society of America, 28(2)*, pp. 168-178.

Biot, M. A., 1956b. Theory of Propagation of Elastic Waves in a Fluid-Filled Porous Solid. II. Higher Frequency Range, *Journal Acoustical Society of America, 28(2)* pp. 179-191.

Biot, M. A. and D. G. Willis, 1957. The Elastic Coefficients of the Theory of Consolidation, *Journal Applied Mechanics*, Dec. 1957. pp. 594-601.

Biot, M. A., 1962. Generalized Theory of Acoustic Propagation in Porous Dissipative Media, *Journal Acoustical Society of America, 34(9)*, pp. 1254-1264.

Biot, M. A., 1962. Mechanics of Deformation and Acoustic Propagation in Porous Media, *Journal of Applied Physics, 13(4)* pp. 1482-1498.

Bonnet, G., 1987. Basic Singular Solutions and Boundary Integral Equations for a Poroelastic Medium in the Dynamic Range, *Journal of the Acoustical Society of America*, pp.

Bowen, R. M., and R. R. Locket, 1983. Inertial Effects in Poroelasticity, *Journal Applied Mechanics, 50,* pp. 335-342.

Boutin, C., G. Bonnet, P. Y. Bard, 1987. Green Functions and Associated Sources in Infinite and Stratified Poroelastic Media, *Geophysical Journal of the Astronomical Society, 90,* pp. 521-550.

Brebbia, C. A., 1978. *The Boundary Element Method for Engineers,* John Wiley and Sons, New York. 189 pages.

Bruner, W. M., 1976. Comment on 'Seismic Velocities in Dry and Saturated Cracked Solids' by Richard J. O'Connell and Bernard Budiansky, *Journal of Geophysical Research, 81(14),* pp. 2573-2576.

Burridge, R., and C. A. Vargas, 1979. The Fundamental Solution in Dynamic Poroelasticity, *Geophysical Journal Royal Astronomical Society, No. 58,* pp. 61-90

Chin, R. C. Y., G. W. Hedstrom, and L. Thigpen, 1984. Matrix Methods in Synthetic Seismograms, *Geophysical Journal Royal Astronomical Society., 77* pp. 483-502

Chouet, B., B. R. Julien, 1985. Dynamics of an Expanding Fluid-Filled Crack, *Journal of Geophysical Research, 90(B13),* pp. 11,187-11,198.

Chouet, B., 1986. Dynamics of a Fluid Driven Crack in Three Dimensions by the Finite Difference Method, *Journal of Geophysical Research, 91(B14),* pp. 13,967-13,992.

Claerbout, Jon F., 1976. *Fundamentals of Geophysical Data Processing,* McGraw-Hill, 274 pp.

Deresiewicz, H., and J. T. Rice, 1964. The Effect of Boundaries on Wave Propagation in a Liquid-Filled Porous Solid: V. Transmission Across a Plane Interface, *Bulletin of the Seismological Society of America, 54(1)* pp. 409-416.

Drew, Donald A., 1971. Averaged Field Equations for Two -Phase Media, *Studies in Applied Mathematics, V. L No. 2,* Massachusettes Institute of Technology, June 1971 pp. 133-166.

Engelman, R., Y. Gur, and Z. Jaeger, 1983. Fluid Flow Through a Crack Network in Rocks, *Journal Applied Mechanics, 50,* December 1983, pp. 707-711.

Ferrazzini, V., and Keiiti Aki, 1987. Slow Waves Trapped in a Fluid-Filled Infinite Crack: Implication for Volcanic Tremor, *Journal of Geophysical Research, 92(B9),* pp. 9215-9223.

Frazer, L., and Joseph F. Gettrust, 1984. On a Generalization of Filon's Method and the Computation of the Oscillatory Integrals of Seismology, *Geophysical Journal Royal Astronomical Society, 76,* pp. 461-481.

Futterman, W. I., 1962. Dispersive Body Waves, *Journal of Geophysical Research, 67, pp. 5279-5291.*

Fung, Y. C., 1965. *Foundations of Solid Mechanics,* Prentice-Hall, Englewood Cliffs, New Jersey, 525 pp.

Gradshteyn, I. S., and I. M. Ryzhik, 1965. *Table of Integrals, Series, and Products,* Translated from the Russian, Academic Press, New York, 1086 pp.

Green, A. E., and P. M. Naghdi, 1984. A Direct Theory of Viscous Fluid Flow in Channels, *Archive for Rational Mechanics and Analysis, 86(1)* Springer-Verlag, pp. 39-63

Green, A. S. P., and R. Baria, 1987. Active Seismics To Determine Reservoir Characteristics of a Hot Dry Rock Geothermal System, *Proceedings, Twentieth Workshop on Geothermal Reservoir Engineering, Stanford University, Stanford, CA.* pp. 131-137.

Gubernatis, J. E., E. Domany, and J. A. Krumhansi, 1977. Formal Aspects of the Theory of the Scattering of Ultrasound by Flaws in Elastic Materials, *Journal of Applied Physics, 48(7),* p. 2806.

Harkrider, D. G., 1964. Surface Waves in Multilayered Elastic Media, Part I: Rayleigh and Love Waves from Buried Sources in a Multilayered Elastic Halfspace, *Bull. Seis. Soc. Am., No. 71,* pp. 1011-1029.

Jaeger, J. C., and N. G. W. Cook, 1979. *Fundamentals of Rock Mechanics, 3rd Ed.,* Chapman and Hall, New York, 593 pp.

Johnston, David H., and M. Nafi Toksoz, 1981. Editors of *Seismic Wave Attenuation,* Geophysics Reprint Series, No. 2, Society of Exploration Geophysicists, pp. 1-5.

Kennett, B. L. N., 1983. *Seismic Wave Propagation in Stratified Media,* Cambridge University Press.

Kjartansson, E., 1979. Constant Q-Wave Propagation and Attenuation, *Journal of Geophysical Research, 84,* pp. 4737-4748.

Korringa, J., 1981. On the Biot-Gassman Equations for the Elastic Moduli of Porous Rocks (Critical Comment on a Paper by J. G. Berryman), *Journal Acoustical Society of America, 70(6)* pp. 1752-1753.

Hull, L. C., and T. M. Clemo, 1987. Effects of Using a Continuum Representation to Simulate Discrete Fracture Networks, *Geothermal Resources Council Transactions, 11,* pp. 593-599.

Long, Jane C. S., and Paul A. Witherspoon, 1985. The Relationship of the Degree of Interconnection to Permeability in Fracture Networks, *Journal of Geophysical Research, 90(B4)* pp. 3087-3098

Lovera, Oscar M., 1987. Boundary Conditions for a Fluid-Saturated Porous Solid, *Geophysics, 52(2)* pp. 174-187.

Madden, Theodore R., 1983. Microcrack Connectivity in Rocks: A Renormalization Group Approach to the Critical Phenomena of Conduction and Failure in Crystalline Rocks, *Journal of Geophysical Research, 88(B1),* pp. 585-592.

Mahrer, K. D. and F. J. Mauk, 1987. Seismic Wave Motion for a New Model of Hydraulic Fracture With an Induced Low Velocity Zone, *Journal of Geophysical Research, 92(B9),* pp. 9293-9309.

Majer, E. L., T. V. McEvilly, F. S. Eastwood, and L. R. Meyer, 1988. Fracture Detectin Using P-Wave and S-Wave Vertical Seismic Profiling at the Geysers, *Geophysics, 53(1)* pp. 76-84.

McNiven, H. D., and Y. Mengi, 1977. Reflection and Refraction of Transient Waves in Fluid-Filled Porous Media, *Journal Acoustical Society of America, 61(4),* pp. 972-981.

Mengi, Y., and H. D. McNiven, 1977. Response of Fluid-Filled Porous Media to a Transient Input, *Journal of the Acoustical Society of America, 61(1),* pp. 84-94.

Meyer, Gunter H., 1973. *Initial Value Methods for Boundary Value Problems, Theory and Application of Invariant Imbedding,* Academic Press, New York, 220 pp.

Minzoni, A. A., and C. A. Vargas, 1981, A Note on the Propagation of Precursors in Poroelastic Media, *Geophysical Journal Royal Astronomical Society, 67,* pp. 673-677.

Morland, L. W., 1974. Continuum Model of Regularly Jointed Mediums, *Journal Geophysical Research, 79(2)* pp. 357-362

Narasimhan, T. N., 1987. Hydrodynamics of a Vertical Hydraulic Fracture, Earth Sciences Division, *Lawrence Berkeley Laboratory, Report No. LBL-23175,* Prepared for U.S. Geological Survey, Menlo Park, CA. Under U.S. DOE Contract DE-AC03-76SF00098 87 pp.

NAG, 1984. Numerical Algorithms Group, Downers Grove, Illinois (Comprehensive Fortran subroutine package)

Nelson, James Tuman, and Hugh J. Saurenman, 1987. A Prediction Procedure for Groundborne Noise and Vibration from Rail Transportation Systems, *Transportation Research Board Record, No. 1143, Environmental Issues: Noise, Rail Noise and High Speed Rail,* Transportation Research Board, National Science Foundation, Washington, D.C. pp. 26-35.

Norris, Andrew N., 1985. Radiation from a Point Source and Scattering Theory in a Fluid-Saturated Porous Solid, *Journal of the Acoustical Society of America, 77(6),* pp. 2012-2023.

O'Connell, Richard J., and Bernard Budiansky, 1974. Seismic Velocities in Dry and Saturated Cracked Solids, *Journal of Geophysical Research, 79* pp. 5412-5426

O'Connell, Richard J., and Bernard Budiansky, 1976. Reply, *Journal of Geophysical Research 81(14)*

O'Connell, Richard J., and Bernard Budiansky, 1977. Viscoelastic Properties of Fluid-Saturated Cracked Solids, *Journal of Geophysical Research, 82,* pp. 5719-5735.

Palen, W. A., and T. N. Narasimhan, 1981. The Roles of Pore Pressure and Fluid Flow in the Hydraulic Fracture Process, (PhD. Thesis) *Lawrence Berkeley Laboratory Report No. LBL-13049* Prepared for U.S. DOE, Contract W-7405-ENG-48 196 pp.

Palmer, I. D., C. T. Luiskutty, H. R. Craig, (no date) Interpretation of Phase I MWX Stimulation Results Using Hydraulic Fracture Models, National Institute for Petroleum Research, 5034-04217/23

Pipes, Louis A., and Shahen A. Hovanessian, 1969. *Matrix-Computer Methods in Engineering*, John Wiley & Sons, New York. 333 pp.

Plona, T. J., 1980. Observation of a Second Bulk Compressional Wave in a Porous Medium at Ultrasonic Frequencies, *Applied Physics Letters, 36(4)* p. 259

Plona, T. J., and David L. Johnson, 1984. Acoustic Properties of Porous Systems: I. Phenomenological Description, *Physics and Chemistry of Porous Media, AIP Conference Proceedings, No. 107,Hy?cPyaX}M]¯l1}qp* Schlumberger-Doll Research, Ed. D. L. Johnson, and P. N. Sen, Publisher: American Institute of Physics

Press, W. H., B. P Flanner, S. A. Teukolsky, W. T. Vetterling, 1986. *Numerical Recipes, The Art of Scientific Computing*, Cambridge University Press, Cambridge, 818 pp.

Stump, B., 1978. *Investigation of Seismic Sources by Linear Inversion of Seismograms, (Ph.D. Thesis)*, University of California, Berkeley, California

Weber, Koenraad Johan, and Margot Bakker, 1981. Fracture and Vuggy Porosity, SPE Paper No. 10332, Presented at the 56th Annual Fall Technical Conference and Exhibition of the Society of Petroleum Engineers of AIME, San Antonio, Texas, October 5-7, 1981. Society of Petroleum Engineers,

Yamamoto, Tokuo, 1983. Propagator Matrix for Continuously Layered Porous Seabeds, *Bulletin of the Seismological Society of America, 73(6)*, pp. 1599-1620.

Zimmerman, R., 1985a. Propagation of Acoustic Waves Through Cracked Rock, *Proc. 26th Symposium on Rock Mechanics*, Rapid City, So. Dakota,

Zimmerman, Robert, 1985b. The Effect of Microcracks on the Elastic Moduli of Brittle Materials, *Journal of Materials Science Letters, 4*, pp. 1457-1460

(For number sequence only)

Appendix A:
Representation Theorem and Reciprocity Relations

Norris's (1985) development of a representation theorem and reciprocity relations for a fluid saturated porous material is applied to dislocation and point sources in a porous material embedded in a solid. The procedure is a straight forward extension of standard derivations of the representation theorem for linear elastic heterogeneous solids (Aki and Richards, 1980). A prescription for the seismic responses of the elastic or porous region and fluid pressure response are obtained for either point loads or moments applied to the porous matrix or isotropic moments applied to the fluid. Following the derivation of the representation theorem, the moment tensor source representation is discussed with respect to scattering theory for elastic solids. Finally, the moment tensors are specialized to an infinitesimal fracture surface in the manner of Aki and Richards (1980).

A1 Generalization of Betti's Reciprocal Theorem

A porous region denoted by P and a surrounding elastic region denoted by S are illustrated in Figure A-1. The surface ∂V_{PS} is the boundary between the porous and elastic regions, and the surface ∂V_F encloses a portion of the porous region which will later be identified with a dislocation. The elastic region extends to infinity, and the solutions in the elastic region are required to approach zero in the limit of infinite distance from the surface ∂V_{PS}. The unit vector, $\mathbf{n}^P$, is the unit normal to the surface ∂V_{PS} pointing away from the porous region. Similarly, $\mathbf{n}^S$ is the unit normal to the surface ∂V_P pointing away from the solid region. At a common point on ∂V_{PS}, $\mathbf{n}^S$ and $\mathbf{n}^P$ are oppositely directed. The unit normal $\mathbf{n}^F$ is directed towards the interior of the volume enclosed by the surface ∂V_F.

Following Norris, (1985) if u_i^A, and U_i^A, are solutions of the equations of motion for the displacement fields of the matrix and fluid constituents, respectively, resulting from respective body force distributions f_i^A and F_i^A, and u_i^B, and U_i^B are another set of solutions for the displacement fields with body force distributions denoted by superscript B, then:

$$\omega^2\left\{\rho_{11}u_i^A+\rho_{12}U_i^A\right\}+\sigma_{ij,j}^A=-f_i^A \tag{A1a}$$

$$\omega^2\left\{\rho_{12}u_i^A+\rho_{22}U_i^A\right\}+s_j^A=-F_i^A \tag{A1b}$$

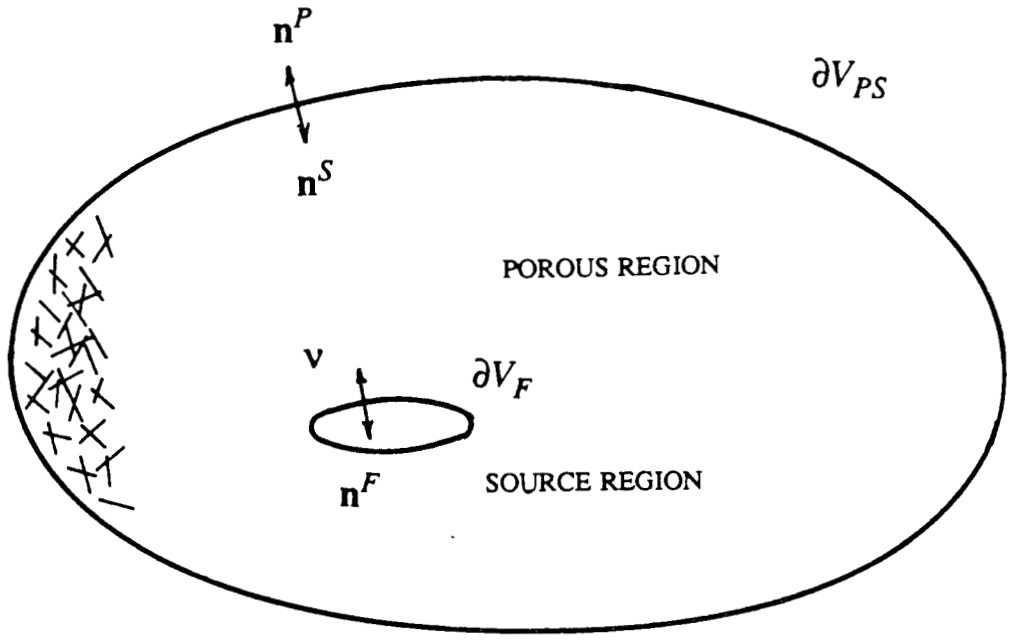

FIGURE A1 EMBEDDED PORO-ELASTIC MEDIUM WITH SOURCE INCLUSION

$$\omega^2\left\{\tilde{\rho}_{11}u_i^B+\tilde{\rho}_{12}U_i^B\right\}+\sigma_{ij,j}^B=-f_i^B \tag{A2a}$$

$$\omega^2\left\{\tilde{\rho}_{12}u_i^B+\tilde{\rho}_{22}U_i^B\right\}+s_{,i}^B=-F_i^B \tag{A2b}$$

The visco-dynamic densities $\tilde{\rho}_{\alpha\beta}$, where $\tilde{\rho}_{\alpha\beta}=\tilde{\rho}_{\beta\alpha}$, are defined in Appendix B and Chapter 2, and are the sums of the densities $\rho_{\alpha\beta}$ and terms representing friction between the constituents. The fields, σ_{ij}^A, and s^A are the partial stresses for the matrix and fluid constituents, respectively, corresponding to solution set A, and σ_{ij}^B, s^B, are the partial stresses corresponding to solutions B. The partial stresses are given by the constitutive relations:

$$\sigma_{ij}=(A\,\delta_{ij}\delta_{kl}+N\,\delta_{ik}\delta_{jl})u_{k,l}+Q\,\delta_{ij}U_{k,k} \tag{A3a}$$

$$s=Qu_{k,k}+RU_{k,k} \tag{A3b}$$

The moduli, A, N, Q, and R, are functions of position, and are discussed in Chapter 2 and Appendix B.

A2 Reciprocity

Multiplying the first of the equations of motion for the solutions "A" by u_i^B, the second by U_i^B, and add the results. Then multiply the first of the equations of motion for the solutions "B" by u_i^A, and the second by U_i^A, and add the results. Subtracting the second result from the first, obtain:

$$\sigma_{ij,j}^A u_i^B+s_{,i}^A U_i^B-\sigma_{ij,j}^B u_i^A-s_{,i}^B U_i^A=-f_i^A u_i^B-F_i^A U_i^B+f_i^B u_i^A+F_i^B U_i^A \tag{A4}$$

Integrating Equation (A4) over the volume V_P bounded by the surfaces ∂V_F and ∂V_{PS}, and using the divergence theorem and the symmetry of the constitutive relations:

$$\int_{V_P}\left\{f_i^A u_i^B+F_i^A U_i^B-f_i^B u_i^A-F_i^B U_i^A\right\}dv= \tag{A5}$$

$$-\int_{\partial V_{PS}}\left[\sigma_{ij}^A u_i^B-\sigma_{ij}^B u_i^A+s^A U_i^B-s^B U_i^A\right]n_i^P da$$

$$-\int_{\partial V_F}\left[\sigma_{ij}^A u_i^B-\sigma_{ij}^B u_i^A+s^A U_i^B-s^B U_i^A\right]n_i^F da$$

In the solid region, the solutions for the displacement field corresponding to body force distributions f_i^{SA} and f_i^{SB} for solution set A and B, respectively, satisfy Betti's reciprocal theorem, obtained by procedures similar to the above.

$$\int_{V_S}\left\{f_i^{SA}u_i^{SB}-f_i^{SB}u_i^{SA}\right\}dv = \tag{A6}$$

$$-\int_{\partial V_{SP}}\left\{\sigma_{ij}^{SA}u_i^{SB}-\sigma_{ij}^{SB}u_i^{SA}\right\}n_j^S da$$

Adding the reciprocal relations for both the solid and porous regions:

$$\int_{V_S}\left[f_i^{SA}u_i^{SB}-f_i^{SB}u_i^{SA}\right]dv+\int_{V_P}\left[f_i^{A}u_i^{B}-f_i^{B}u_i^{A}+F_i^{A}U_i^{B}-F_i^{B}U_i^{A}\right]dv \tag{A7}$$

$$=-\int_{\partial V_{PS}}\left[\sigma_{ij}^{SA}u_i^{SB}-\sigma_{ij}^{SB}u_i^{SA}\right]n_j^S da$$

$$-\int_{\partial V_{PS}}\left[\sigma_{ij}^{A}u_i^{B}-\sigma_{ij}^{B}u^{iA}+s^A U_i^B-s^B U_i^A\right]n_j^P da$$

$$-\int_{\partial V_F}\left[\sigma_{ij}^{A}u_i^{B}-\sigma_{ij}^{B}u_i^{A}+s^A U_j^B-s^B U_j^A\right]n_j^F da$$

Boundary conditions on the surface ∂V_{PS} govern the coupling of the porous region with the solid region. H. Deresiewicz (1964) provides an analysis and discussion of the boundary conditions between a fluid-saturated porous material and a solid. The boundary conditions are:

Balance of total tractions acting on the surface ∂V_{PS}

$$\sigma_{ij}^S n_j^S+[\sigma_{ij}+s\,\delta_{ij}]n_j^P=0 \tag{A8a}$$

Continuity of porous matrix displacements with solid region displacements

$$u_i^S=u_i \tag{A8b}$$

Zero relative fluid flux across the boundary

$$\left[U_j-u_j\right]n_j^P=0 \tag{A8c}$$

Only the total stress at the boundary, giving rise to the total traction, and not the individual partial stresses, enter the boundary conditions. For a "dry" condition, the fluid partial stress would be zero, and the total stress would be born by the porous matrix. The lack of individual specifications for the matrix and fluid stresses is related to the requirement that there be no fluid flow across the boundary. Had the surface been free without externally applied tractions, there would be no restriction on net fluid flow across the boundary, and an additional boundary condition of zero fluid partial stress, or, equivalently, zero pore pressure, would be required. Because the total traction would be zero at a free surface, the matrix partial stress would also be zero.

As mentioned in Chapter 3, boundary conditions for general surface geometries are described by O. Lovera (1987). While discussing the case of a fluid-saturated porous material in contact with an impervious solid, Lovera equates the fluid pore pressure with the normal component of the total traction acting on any surface in a porous material, and proceeds to derive boundary conditions based on this assumption. The assumption is without physical justification, however. A condition of zero pore pressure may easily be obtained in the presence of non-zero total traction acting on the surface of a porous solid, because the partial stress of the porous matrix can support the traction. The proper boundary condition is that the sum of the tractions due to fluid partial stress, matrix partial stress, and solid stress, balance. The result is that the sum of the fluid partial normal stress and matrix partial normal stress equals the normal stress of the solid.

The two boundary integrals in Equation A7 over the common surface ∂V_{PS} can be combined into one, using the relation $n_j^P = -n_j^S$:

$$\int_{\partial V_{PS}} \cdots = \int_{\partial V_{PS}} \left[\left\{ \sigma_{ij}^{SA} n_j^S u_i^{SB} - \sigma_{ij}^{A} n_j^S u_i^{B} - s^A \delta_{ij} n_j^S U_i^B \right\} \right. \tag{A9}$$

$$\left. - \left\{ \sigma_{ij}^{SB} n_j^S u_i^{A} - \sigma_{ij}^{B} n_j^S u_i^{A} - s^B \delta_{ij} n_j^S U_i^A \right\} \right] da$$

Breaking up the displacements into normal and transverse components

$$u_i = u_k n_k n_i + (u_i - u_k n_k n_i) \tag{A10a}$$

$$U_i = U_k n_k n_i + (U_i - U_k n_k n_i) \tag{A10b}$$

and using the above boundary conditions, the integral over the boundary ∂V_{PS} becomes zero. With this result, a general reciprocal relation between the solutions for the porous and solid regions is

obtained:

$$\int_{V_S}\left[f_i^{SA}u_i^{SB}-f_i^{SB}u_i^{SA}\right]dv+\int_{V_P}\left[f_i^{A}u_i^{B}-f_i^{B}u_i^{A}+F_i^{A}U_i^{B}-F_i^{B}U_i^{A}\right]dv= \tag{A11}$$

$$\int_{\partial V_F}\left[\sigma ij^{A}u_i^{B}-\sigma_{ij}^{B}u_i^{A}+s^{A}U_j^{B}-s^{B}U_j^{A}\right]n_j^{F}da$$

A3 Representation Theorem

Let $\mathbf{x}_1$ represent a point in the porous region, V_P, and be assigned to the porous matrix. Let $\mathbf{x}_2$ also represent a point in the porous region, V_P, and be assigned to the fluid. Finally, let $\mathbf{x}_3$ represent a point in the solid region, V_S. Let the body force f_i^{SB} acting on the solid at $\mathbf{x}_3$ be given by a concentrated force:

$$f_i^{SB}(\mathbf{x})=\delta_{ik}\,\delta(\mathbf{x}-\mathbf{x}_3) \tag{A12}$$

and the corresponding solution for the displacements and stresses in the solid region be given by Green's tensors:

$$u_i^{SB}(\mathbf{x})=G_{i;k}^{SS}(\mathbf{x},\mathbf{x}_3) \tag{A13a}$$

$$\sigma_{ij}^{SB}(\mathbf{x})=\sigma_{ij;k}^{GSS}(\mathbf{x},\mathbf{x}_3) \tag{A13b}$$

The superscript SS refers to the response of the solid region due to a source in the solid region. Similarly, the displacement and stress responses of the porous matrix due to a source in the solid region are:

$$u_i^{B}(\mathbf{x})=G_{i;k}^{MS}(\mathbf{x},\mathbf{x}_3) \tag{A13c}$$

$$\sigma_{ij}^{B}(\mathbf{x})=\sigma_{ij;k}^{GMS}(\mathbf{x},\mathbf{x}_3) \tag{A13d}$$

and the displacement and stress responses of the fluid due to the source in the solid region are:

$$U_i^{B}(\mathbf{x})=G_{i;k}^{FS}(\mathbf{x},\mathbf{x}_3) \tag{A13e}$$

$$s^{B}(\mathbf{x})=s_{;k}^{GFS}(\mathbf{x},\mathbf{x}_3) \tag{A13f}$$

The superscripts, MS and FS, denote the respective responses of the porous matrix and fluid due to a source in the solid region.

Substituting the above into the reciprocal relations, dropping the superscript A, and employing the properties of the delta function,

$$\int_{V_S} \delta_{ik}\,\delta(\mathbf{x}-\mathbf{x}_3)u_i(\mathbf{x})dv = u_k(\mathbf{x}_3) \tag{A14}$$

the following representation is obtained for the solid displacement at $\mathbf{x}_3$ for arbitrary body force distributions.

$$u_k^S(\mathbf{x}_3) = \tag{A15}$$

$$\int_{V_S} f_i^S(\mathbf{x})G_{i;k}^{SS}(\mathbf{x};\mathbf{x}_3)dv + \int_{V_P}\left[f_i(\mathbf{x})G_{i;k}^{MS}(\mathbf{x};\mathbf{x}_3) + F_i(\mathbf{x})G_{i;k}^{FS}(\mathbf{x};\mathbf{x}_3)\right]dv$$

$$+\int_{\partial V_F}\left[\sigma_{ij}(\mathbf{x})G_{i;k}^{MS}(\mathbf{x};\mathbf{x}_3) - \sigma_{ij;k}^{GMS}(\mathbf{x};\mathbf{x}_3)u_i(\mathbf{x}) + s(\mathbf{x})G_{j;k}^{FS}(\mathbf{x};\mathbf{x}_3) - s_{;k}^{GFS}U_j(\mathbf{x})\right]n_j^F da$$

Thus, the response of the solid region at $\mathbf{x}_3$ due to an arbitrary distribution of body forces over the volumes, V_S and V_P, and displacements and stresses over the boundary of the inclusion, ∂V_F, are determined by integrals of these quantities with the Green's functions for the displacements and stresses for a point source at position $\mathbf{x}_3$ in V_S.

If the inclusion bounded by ∂V_F and fluid body forces are nonexistent, and the body force acting on the porous matrix is a point load in the direction i, then $u_k^S(\mathbf{x}_3)$ is simply the Green's function for displacement at $\mathbf{x}_3$ for a source at, say, $\mathbf{x}_1$ in the porous region V_P, represented by $G_{k;i}^{SM}(\mathbf{x}_3,\mathbf{x}_1)$. Following this reasoning, general reciprocity relations between the Green's functions are obtained:

Solid-solid, with $\mathbf{x}_1 \varepsilon V_S$ and $\mathbf{x}_2 \varepsilon V_S$

$$G_{k;i}^{SS}(\mathbf{x}_1;\mathbf{x}_2) = G_{i;k}^{SS}(\mathbf{x}_2;\mathbf{x}_1) \tag{A16a}$$

Solid-matrix, with $\mathbf{x}_1 \varepsilon V_S$ and $\mathbf{x}_2 \varepsilon V_P$

$$G_{k;i}^{SM}(\mathbf{x}_1;\mathbf{x}_2) = G_{i;k}^{MS}(\mathbf{x}_2;\mathbf{x}_1) \tag{A16b}$$

Solid-fluid, with $\mathbf{x}_1 \varepsilon V_S$ and $\mathbf{x}_2 \varepsilon V_P$

$$G_{k;i}^{SF}(\mathbf{x}_1;\mathbf{x}_2) = G_{i;k}^{FS}(\mathbf{x}_2;\mathbf{x}_1) \tag{A16c}$$

Matrix-matrix, with $\mathbf{x}_1 \varepsilon V_P$ and $\mathbf{x}_2 \varepsilon V_P$

$$G_{k;i}^{MM}(\mathbf{x}_1;\mathbf{x}_2) = G_{i;k}^{MM}(\mathbf{x}_2;\mathbf{x}_1) \tag{A16d}$$

Matrix-fluid, with $\mathbf{x}_1 \varepsilon V_P$ and $\mathbf{x}_2 \varepsilon V_P$

$$G_{k;i}^{MF}(\mathbf{x}_1;\mathbf{x}_2) = G_{i;k}^{FM}(\mathbf{x}_2;\mathbf{x}_1) \tag{A16e}$$

Fluid-fluid, with $\mathbf{x}_1 \varepsilon V_P$ and $\mathbf{x}_2 \varepsilon V_P$

$$G_{k;i}^{FF}(\mathbf{x}_1;\mathbf{x}_2) = G_{i;k}^{FF}(\mathbf{x}_2;\mathbf{x}_1) \tag{A16f}$$

Summarizing:

$$G_{k;i}^{\alpha\beta}(\mathbf{x}_1;\mathbf{x}_2) = G_{i;k}^{\beta\alpha}(\mathbf{x}_1;\mathbf{x}_2) \tag{A17}$$

Here, $\alpha,\beta=S,M,F$ refer to the Green tensor for the solid, porous matrix, or fluid phases, respectively. Thus, u_k^S is the solid region displacement, $u_k^M=u_k$ is the displacement of the porous matrix, and $u_k^F=U_k$ is the displacement of the fluid.

Using the above reciprocal relations for the Green tensors, the following representations are obtained for the displacement fields:

$$u_k^{\alpha}(\mathbf{x}_1) = \tag{A18}$$

$$\int_{V_S} G_{k;i}^{\alpha S}(\mathbf{x}_1;\mathbf{x}) f_i^S(\mathbf{x}) dv + \int_{V_P} \left[G_{k;i}^{\alpha M}(\mathbf{x}_1;\mathbf{x}) f_i(\mathbf{x}) + G_{k;i}^{\alpha F}(\mathbf{x}_1;\mathbf{x}) F_i(\mathbf{x}) \right] dv$$

$$+ \int_{\partial V_F} \left[G_{k;i}^{\alpha M}(\mathbf{x}_1;\mathbf{x}) \sigma_{ij}(\mathbf{x}) - \sigma_{ij;k}^{G\alpha M}(\mathbf{x};\mathbf{x}_1) u_i(\mathbf{x}) + G_{k;j}^{\alpha F} s(\mathbf{x}) - s_{;k}^{G\alpha M}(\mathbf{x};\mathbf{x}_1) U_j(\mathbf{x}) \right] n_j^F da$$

Now, using the constitutive relations and making use of the reciprocal relations for the displacement Green tensors, the Green stresses are expressed in terms of gradients of the Green tensors. The partial Green stresses associated with the porous matrix at $\mathbf{x}$ resulting from loads acting on the porous matrix ($\alpha=M$), fluid ($\alpha=F$), or solid ($\alpha=S$), at $\mathbf{x}_1$, become:

$$\sigma_{ij;k}^{GM\alpha}(\mathbf{x};\mathbf{x}_1) = \tag{A19a}$$

$$\left[A(\mathbf{x}) \delta_{ij} \delta_{mn} + N(\mathbf{x}) (\delta_{im} \delta_{jn} + \delta_{in} \delta_{jm}) \right] \frac{\partial G_{k;m}^{\alpha M}(\mathbf{x}_1;\mathbf{x})}{\partial x_n} + Q(\mathbf{x}) \frac{\partial G_{k;m}^{\alpha F}(\mathbf{x}_1;\mathbf{x})}{\partial x_m}$$

The corresponding fluid stress at $\mathbf{x}$ is:

$$s_{;k}^{GF\alpha}(\mathbf{x};\mathbf{x}_1) = Q(\mathbf{x}) \frac{\partial G_{k;m}^{\alpha M}(\mathbf{x}_1;\mathbf{x})}{\partial x_m} + R(\mathbf{x}) \frac{\partial G_{k;m}^{\alpha F}(\mathbf{x}_1;\mathbf{x})}{\partial x_m} \tag{A19b}$$

In all of the above relations for the stress-strain relations, the gradient of the Green tensor is with respect to **x**.

With the above expressions for the partial stresses at the surface ∂V_F, the following representation theorem is obtained for the displacement fields at **x**:

$$u_k^{\alpha}(\mathbf{x}) = \tag{A20}$$

$$\int_{V_S} G_{k;i}^{\alpha S}(\mathbf{x};\mathbf{x}')f_i^S(\mathbf{x}')dv + \int_{V_P}\left[G_{k;i}^{\alpha M}(\mathbf{x};\mathbf{x}')f_i(\mathbf{x}') + G_{k;i}^{\alpha F}(\mathbf{x};\mathbf{x}')F_i(\mathbf{x}')\right]dv'$$

$$+\int_{\partial V_F}\left[G_{k;i}^{\alpha M}(\mathbf{x};\mathbf{x}')\sigma_{ij}(\mathbf{x}') - \left\{C_{ijmn}^{M}(\mathbf{x}')\frac{\partial G_{k;m}^{\alpha M}(\mathbf{x};\mathbf{x}')}{\partial x_n'} + Q(\mathbf{x}')\frac{\partial G_{k;m}^{\alpha F}(\mathbf{x};\mathbf{x}')}{\partial x_m'}\right\}u_i(\mathbf{x}')\right]n_j^F da$$

$$+\int_{\partial V_F}\left[G_{k;j}^{\partial F}(\mathbf{x};\mathbf{x}')s(\mathbf{x}') - \left\{Q(\mathbf{x}')\frac{\partial G_{k;m}^{\alpha M}(\mathbf{x};\mathbf{x}')}{\partial x_m'} + R(\mathbf{x}')\frac{\partial G_{k;m}^{\alpha F}(\mathbf{x};\mathbf{x}')}{\partial x_m'}\right\}U_j(\mathbf{x}')\right]n_j^F da$$

The stiffness tensor for the porous matrix is:

$$C_{ijmn}^{M}(\mathbf{x}) = A(\mathbf{x})\delta_{ij}\delta_{mn} + N(\mathbf{x})\left[\delta_{im}\delta_{jn} + \delta_{in}\delta_{jm}\right] \tag{A21}$$

These representations give the displacement responses of the porous matrix, the fluid, and the solid, for an arbitrary distribution of body forces over their respective regions, and tractions and displacements over the inclusion bounded by ∂V_F embedded in the porous region.

A4 Moment Tensor Source Representation

A popular approach used for representing failures in a material is to develop a set of equivalent body force couples representing the effects of a displacement discontinuity due to failure of the material over some particular region bounded by the surface ∂V_F. (Aki and Richards, 1980) A rigorous representation requires determination of Green's functions which satisfy the condition of zero traction (Neumann) on ∂V_F if the stress tractions are to be prescribed alone, or the condition of zero displacement if the displacement is to be prescribed alone (Dirichlet). Exact computation of these Green's functions is perhaps impossible or impractical for all but the simplest of geometries, as noted by Archambeau and Minster (1976), who provide a detailed analysis of time dependent source

boundaries.

For a shear dislocation, involving no volumetric expansion, or dilatation, the stress across the inclusion is assumed continuous with the result that the surface integral term involving the stress is identically zero. Extending the approach to the case of a dilatational source is questionable, because the Green function may be varying across the width of the inclusion, with the result that the integral involving stress may no longer be set to zero. Only the response due to a given body force distribution over the volume V_F, or, equivalently, compatible traction and displacement distributions over the surface ∂V_F, may be determined. In general, both displacements and tractions may not be specified independently if the only source present is contained in the region ∂V_F.

For a source entirely contained within ∂V_F and caused by changes in the constitutive properties contained within ∂V_F, eg. fracturing, the force distribution will have zero resultant force and zero torque, giving a symmetric moment representation for the source. Suppose that the surface integral is deleted and the volume integral extended over the region V_F, that the sources are entirely contained within the volume V_F, and that the Green's functions and their gradients vary slowly over the volume. Expanding the Green's functions to first order relative to their values at some point within or near the inclusion, using Taylor's theorem:

$$G_{i;j}(\mathbf{x},\mathbf{x}') = G_{i;j}(\mathbf{x},\mathbf{x}_0) + \frac{\partial G_{i;j}(\mathbf{x},\mathbf{x}')}{\partial x_k'}(x_k' - x_{0k}) + \cdots$$

The representation integral for the displacement $\mathbf{u}^\alpha$, where $\alpha = M$, F, or S, according to whether the displacement of the porous matrix, fluid, or solid regions is being calculated, respectively, is thus approximated as follows:

$$u_k^\alpha(\mathbf{x}) = \tag{A22}$$

$$G_{k;i}^{\alpha M}(\mathbf{x};\mathbf{x}_0)\int_{\partial V_F} f_i(\mathbf{x}')da' + \frac{\partial G_{k;i}^{\alpha M}}{\partial x_{0j}}(\mathbf{x};\mathbf{x}_0)\int_{\partial V_F} f_i(\mathbf{x}')(x_j' - x_{0j})da'$$

$$+ G_{k;i}^{\alpha F}(\mathbf{x};\mathbf{x}_0)\int_{V_F} F_i(\mathbf{x}')dv' + \frac{\partial G_{k;i}^{\alpha F}}{\partial x_{0j}}(\mathbf{x};\mathbf{x}_0)\int_{V_F} F_i(\mathbf{x}')(x_j' - x_{0j})dv'$$

Assuming that the force distribution has zero resultant and zero moment, these integrals reduce to:

$$u_k^\alpha(\mathbf{x}) = \frac{\partial G_{k;i}^{\alpha M}}{\partial x_{0j}}(\mathbf{x};\mathbf{x}_0)M_{ij}^M(\mathbf{x}_0) + \frac{\partial G_{k;i}^{\alpha F}}{\partial x_{0j}}(\mathbf{x};\mathbf{x}_0)M_{ij}^F(\mathbf{x}^0) \tag{A23}$$

where

$$M_{ij}^{M}(\mathbf{x}_0)=\frac{1}{2}\int_{V_F}(f_i(\mathbf{x}')(x_j'-x_{0j})+f_j(\mathbf{x}')(x_i'-x_{0i}))dv' \tag{A24a}$$

$$M_{ij}^{F}(\mathbf{x}_0)=\frac{1}{2}\int_{V_F}(F_i(\mathbf{x}')(x_j'-x_{0j})+F_j(\mathbf{x}')(x_i'-x_{0i}))dv' \tag{A24b}$$

The symmetric moment tensors, M_{ij}^{α}, represent the force distributions within the inclusion, V_F, and are the fundamental source functions for the acoustic emission problem.

Alternatively, the surface integral over ∂V_F can be retained and the volume integrals restricted from the volume V_F. Assuming that there are no body forces acting, Equation (A20) can again be approximated by a Taylor expansion of the Green functions about some point near or within V_F. Assuming that the resultant traction and moment acting on the inclusion surface is zero, Equation (A23) is obtained again with the following expressions for the symmetric moment tensors:

$$M_{ij}^{M}(\mathbf{x}_0)=\frac{1}{2}\int_{\partial V_F}(t_i(\mathbf{x}')(x_j'-x_{0j})+t_j(\mathbf{x}')(x_i'-x_{0i}))da' \tag{A25a}$$

$$-\int_{\partial V_F}(C_{mnij}^{M}(\mathbf{x}_0)u_m(\mathbf{x}')n_n(\mathbf{x}')+\delta_{ij}Q(\mathbf{x}_0)U_m(\mathbf{x})n_n(\mathbf{x}))da'$$

$$M_{ij}^{F}(\mathbf{x}_0)=\frac{1}{2}\int_{\partial V_F}(T_i(\mathbf{x}')(x_j'-x_{0j})+T_j(\mathbf{x}')(x_i'-x_{0i}))da' \tag{A25b}$$

$$-\delta_{ij}\int_{\partial V_F}(Q(\mathbf{x}_0)u_m(\mathbf{x}')n_m(\mathbf{x}')+R(\mathbf{x}_0)U_m(\mathbf{x}')n_m(\mathbf{x}'))da'$$

where the traction acting on the matrix is given by t_i and that acting on the fluid by T_i.

The moment tensors are independent of the choice of $\mathbf{x}_{0i}$, a consequence of the assumption of zero resultant for the surface tractions, to the extent that the moduli are constant with respect to position. The moduli appearing in Equation A25a,b are those for the unfractured material.

A5 Moment Representation Based on Scattering Theory

The scattering theory of Gubernatis, et al, (1977), provides an alternative derivation of the moment tensor source representation for inclusions with finite volume and reduced but possibly finite moduli.

The result of the scattering theory approach is that for inclusions with appreciable mass, an inertial term is retained, which goes to zero for zero inclusion volume. The derivation is briefly outlined below:

The reduced moduli and density for the source region are defined as:

$$C_{ijkl}' = C_{ijkl} + \delta C_{ijkl} \tag{A26a}$$

$$Q' = Q + \delta Q \tag{A26b}$$

$$R' = R + \delta R \tag{A26c}$$

$$\rho\tilde{}_{\alpha\beta}' = \rho\tilde{}_{\alpha\beta} + \delta\rho\tilde{}_{\alpha\beta} \tag{A27}$$

The moduli and their "defects" may vary with position. Also, the "defects" δC_{ijkl}, δQ, δR, and $\delta\rho\tilde{}_{\alpha\beta}$ may vary with time or frequency. The development here is in the spectral domain. Require that the actual displacement and stress fields satisfy the equation of motion within the inclusion with the reduced moduli and densities. Further, require that the Green functions and Green stresses satisfy the equation of motion over the source region with the un-altered moduli and densities, as though the inclusion were not present. Expressing the surface tractions in terms of stresses, using the divergence theorem, the equations of motion for the actual displacements and stresses and for the Green's functions and Green stresses, and using the symmetry of the C_{ijkl} and the associated defect, obtain:

$$u_k^{\gamma}(\mathbf{x}) = -\omega^2 \int_V \sum_{\alpha\beta} \delta\rho\tilde{}_{\alpha\beta} u_i^{\beta}(\mathbf{x}') G_{i;m}^{\gamma\beta}(\mathbf{x}',\mathbf{x}) dv' \tag{A28}$$

$$+ \int_V G_{i;j,k}^{\gamma M}(\mathbf{x}'|\mathbf{x}) \left[\delta C_{ijmn}(\mathbf{x}') u_{m,n}(\mathbf{x}') + \delta_{ij} \delta Q(\mathbf{x}') U_{m,m}(\mathbf{x}') \right] dv'$$

$$+ \int_V G_{i;j,k}^{\gamma F}(\mathbf{x}'|\mathbf{x}) \left[\delta Q(\mathbf{x}') u_{m,m}(\mathbf{x}') + \delta R(\mathbf{x}') U_{m,m}(\mathbf{x}') \right] dv'$$

Here, α, β, or γ = M or F for the matrix or fluid constituent, respectively, or S for the solid region. The representation is analogous to the representation derived by Gubernatis, et al (1977), for scattering by a flaw within an elastic solid, and, according to Gubernatis, et al, is exact. Gubernatis, et al, arrives at the volume integral representation by an equivalent body force distribution resulting from a wave incident on the flaw. The approach used here is more direct than but equivalent to Gubernatis' approach. Because the representation is exact, it forms a convenient starting point for discussion of the nature of the moment tensor source.

The Green tensor appearing in the volume integral involving the accelerations can be approximated by a Taylor's series about some point within or close to the inclusion. Further, the gradients of the Green tensors in the volume integrals involving the displacement gradients can be considered constant over the inclusion and brought out from under the integrals. The result is:

$$u_m^{\gamma}(\mathbf{x}) = -\omega^2 \sum_{\alpha\beta} G_{i;m}^{\alpha\gamma}(\mathbf{x}_0|\mathbf{x}) \int_V \delta\rho^{-}{}_{\alpha\beta}(\mathbf{x}') u_i^{\beta}(\mathbf{x}') \tag{A29}$$

$$- \omega^2 \sum_{\alpha\beta} G_{i;j;m}^{\alpha\gamma}(\mathbf{x}_0|\mathbf{x}) \int_V \delta\rho^{-}{}_{\alpha\beta}(\mathbf{x}') u_i^{\beta}(\mathbf{x}')(x_j' - x_{0j}) dv'$$

$$+ G_{i;j;m}^{M\gamma}(\mathbf{x}_0|\mathbf{x}) \int_V \left[\delta C_{ijkl}(\mathbf{x}') u_{i,j}(\mathbf{x}') + \delta_{ij} \delta Q(\mathbf{x}') U_{k,k}(\mathbf{x}') \right] dv'$$

$$+ G_{i;i;m}^{F\gamma}(\mathbf{x}_0|\mathbf{x}) \int_V \left[\delta Q(\mathbf{x}') u_{k,k}(\mathbf{x}') + \delta R(\mathbf{x}') U_{k,k}(\mathbf{x}') \right] dv'$$

The gradients of the Green's functions are with respect to source region coordinate. Reciprocity relations between the fundamental solutions have not yet been incorporated. The first term can be set to zero in the absence of external sources because the rate of change of linear momentum must be zero. The second term involving the accelerations and the gradient of the Green tensors involves the time rate of change of angular momentum given by the antisymmetric part of the integral and a symmetric moment. The angular part is set to zero in the absence of external torques, leaving the symmetric part. Thus, the representation for the displacement field is again given in terms of the gradients of the Green's tensors contracted with moment tensors. In this case, the moment tensors are:

$$M_{ij}^{M}(\mathbf{x}_0) = -\omega^2 \sum_{\beta=1}^{2} \int_V \delta\rho^{-}{}_{1\beta}(\mathbf{x}') u_i^{\beta}(\mathbf{x}')(x_j' - x_{0j}) dv' \tag{A30a}$$

$$+ \int_V \left[\delta C_{ijkl}(\mathbf{x}') u_{k,l}(\mathbf{x}') + \delta Q(\mathbf{x}') U_{k,k}(\mathbf{x}') \right] dv'$$

$$M_{ij}^{F}(\mathbf{x}_0) = -\omega^2 \sum_{\beta=1}^{2} \int_V \delta\rho^{-}{}_{2\beta}(\mathbf{x}') u_i^{\beta}(\mathbf{x}')(x_j' - x_{0j}) dv' \tag{A30b}$$

$$+ \delta_{ij} \int_V \left[\delta Q(\mathbf{x}') u_{k,k}(\mathbf{x}') + \delta R(\mathbf{x}') U_{k,k}(\mathbf{x}') \right] dv'$$

If the moduli defects are constant over the inclusion, they can be removed from under the integrals, and the divergence theorem can the be applied to the displacement gradients to obtain surface integrals of the displacement field over the surface of the inclusion:

$$M_{ij}^{M}(\mathbf{x}_0) = -\omega^2 \sum_{\beta=1}^{2} \delta\rho^{-}{}_{1\beta}(\mathbf{x}_0) \int_V u_i^{\beta}(\mathbf{x}')(x_j' - x_{0j})dv' \tag{A31a}$$

$$+ \delta C_{ijkl}(\mathbf{x}_0) \int_{\partial V_F} u_k(\mathbf{x}') n_l(\mathbf{x}') da' + \delta_{ij} \delta Q(\mathbf{x}') \int_{\partial V_F} U_k(\mathbf{x}') n_k(\mathbf{x}') da'$$

$$M_{ij}^{F}(\mathbf{x}^0) = -\omega^2 \sum_{\beta=1}^{2} \delta\rho^{-}{}_{2\beta}(\mathbf{x}_0) \int_V u_i^{\beta}(\mathbf{x}')(x_j' - x_{0j})dv' \tag{A31a}$$

$$+ \delta_{ij} \delta Q(\mathbf{x}_0) \int_{\partial V} u_k(\mathbf{x}') n_k(\mathbf{x}') da' + \delta_{ij} \delta R(\mathbf{x}_0) \int_{\partial V} U_k(\mathbf{x}') n_k(\mathbf{x}') da'$$

The volume integral of the symmetric moment of momentum includes the radius of the inclusion. Moreover, the term becomes negligible at sufficiently low frequencies. If the inclusion has no volume, the integral involving the accelerations is identically zero, giving an expression for the moment tensor involving only a surface integral of the displacements and the unit normal over ∂V_F. If, further, the defects in the moduli are set to the negatives of the unaltered material, representing complete failure, the result is analogous to that given by Aki and Richards for the seismic moment of a point displacement discontinuity in an elastic material.

The conventional seismic moment for shear dislocation sources is normally derived by assuming continuity of tractions across the fracture surface (Aki and Richards, 1980). The above expressions for the moments in a porous material include an additional term when there is dilatation associated with the failure, and reduce to an expression analogous to the seismic moment used for fault dislocations if the inclusion volume is zero. In the limit of a point source, the volume term goes to zero faster than the surface integral, leaving the surface integral of the displacement as the primary source term.

An exact representation of the response to arbitrary source boundary stresses can be obtained with a Green's function exhibiting zero stress on the source boundary. With this selection of the Green's function, the tractions can be specified over the surface, so that the effect of a stress drop can be computed directly without knowledge of the displacements. Development of such a Green tensor entails solving the boundary value problem for both the inclusion and the boundaries between the porous and solid regions. The needed Green functions satisfying a condition of zero stress on the inclusion

surface can be approximated in principal by solving a scattering problem, for which the solutions are expressed as a superposition of the incident regular Green function existing in the absence of the inclusion, and a scattered Green function. Solving the scattering problem is difficult, though there is a great deal of prior research upon which to draw. A static analysis for the inclusion may provide a good approximation.

A6 Representation Theorem for Point Displacement Discontinuities

For source dimensions much smaller than the wavelength of interest, the source can be approximated as a point dislocation, for which the inertial forces represented by the volume integral of the accelerations are negligible. Alternatively, the procedures of Aki and Richards can be used to specialize to the case of a point dislocation at $\mathbf{x}_0$ in the absence of body forces, assuming that the Green's functions and stresses are continuous across the dislocation. For either of these approaches, the surface integrals appearing in the expressions for the seismic moments, involving the displacement of the surface of a penny shaped crack, can be approximated as:

$$\int_{\partial V_F} u_i(\mathbf{x}) n_j^F(\mathbf{x}) da = -\left[u_i^+(\mathbf{x}_0) - u_i^-(\mathbf{x}_0)\right] \nu_j^F(\mathbf{x}_0) A_F = -[u_i]\nu_j A_F \tag{A32a}$$

$$\int_{\partial V_F} u_i(\mathbf{x}) n_i^F(\mathbf{x}) da = -\Delta_M(\mathbf{x}_0) \tag{A32b}$$

$$\int_{\partial V_F} U_i(\mathbf{x}) n_i^F(\mathbf{x}) da = -\Delta_F(\mathbf{x}_0) \tag{A32c}$$

where Δ_M and Δ_F are the volumetric expansions of the matrix material and fluid materials, respectively, and ν_i is the unit normal to the fracture surface, pointing away from the inclusion in the "positive" direction, given by

$$\nu_i = -n_i^{F+} \tag{A33}$$

The moment tensor M_{mn}^M and an the isotropic fluid moment tensor $\delta_{mn} M^F$ become:

$$M_{mn}^M(\mathbf{x}_0) = C_{ijmn}^M(\mathbf{x}_0)[u_i]\nu_j A^{F+} + Q(\mathbf{x}_0)\Delta_F \delta_{mn} \tag{A34a}$$

$$M^F(\mathbf{x}_0) = Q(\mathbf{x}_0)\Delta_M(\mathbf{x}_0) + R(\mathbf{x}_0)\Delta_F(\mathbf{x}_0) \tag{A34b}$$

With these definitions, and using reciprocity of the Green tensors, the displacement fields are as

follows:

Porous matrix displacements:

$$u_k(\mathbf{x}) = M^M_{mn}(\mathbf{x}_0)\frac{\partial G^{MM}_{k;m}(\mathbf{x}|\mathbf{x}_0)}{\partial x_{0n}} + M^F(\mathbf{x}_0)\frac{\partial G^{MF}_{k;m}(\mathbf{x}|\mathbf{x}_0)}{\partial x_{0m}} \tag{A35a}$$

Fluid displacements:

$$U_k(\mathbf{x}) = M^M_{mn}(\mathbf{x}_0)\frac{\partial G^{FM}_{k;m}(\mathbf{x}|\mathbf{x}_0)}{\partial x_{0n}} + M^F(\mathbf{x}_0)\frac{\partial G^{FF}_{k;m}(\mathbf{x}|\mathbf{x}_0)}{\partial x_{0m}} \tag{A35b}$$

Solid displacements:

$$u^S_k(\mathbf{x}) = M^M_{mn}(\mathbf{x}_0)\frac{\partial G^{SM}_{k;m}(\mathbf{x}|\mathbf{x}_0)}{\partial x_{0n}} + M^F(\mathbf{x}_0)\frac{\partial G^{SF}_{k;m}(\mathbf{x}|\mathbf{x}_0)}{\partial x_{0m}} \tag{A35c}$$

Fluid partial pressure is of interest, rather than the fluid displacement field, because fluid pressure is most easily measured within the fractured zone. To develop a representation theorem for the the fluid partial pressure, use the constitutive relation for the fluid pressure and substitute expressions for the displacement fields:

$$s(\mathbf{x}) = Q(\mathbf{x})u_{k,k}(\mathbf{x}) + R(\mathbf{x})U_{k,k}(\mathbf{x}) \tag{A36}$$

$$= Q(\mathbf{x})\frac{\partial}{\partial x_k}\left\{M^M_{mn}(\mathbf{x}_0)\frac{\partial G^{MM}_{k;m}(\mathbf{x}|\mathbf{x}_0)}{\partial x_{0n}} + M^F(\mathbf{x}_0)\frac{\partial G^{MF}_{k;m}(\mathbf{x}|\mathbf{x}_0)}{\partial x_{0m}}\right\}$$

$$+ R(\mathbf{x}_2)\frac{\partial}{\partial x_k}\left\{M^M_{mn}(\mathbf{x}_0)\frac{\partial G^{FM}_{k;m}(\mathbf{x}|\mathbf{x}_0)}{\partial x_{0n}} + M^F(\mathbf{x}_0)\frac{\partial G^{FF}_{k;m}(\mathbf{x}|\mathbf{x}_0)}{\partial x_{0m}}\right\}$$

Interchanging the order of differentiation:

$$s(\mathbf{x}) = \tag{A37}$$

$$M^M_{mn}(\mathbf{x}_0)\frac{\partial}{\partial x_{0n}}\left\{Q(\mathbf{x})\frac{\partial G^{MM}_{k;m}(\mathbf{x}|\mathbf{x}_0)}{\partial x_k} + R(\mathbf{x})\frac{\partial G^{FM}_{k;m}(\mathbf{x}|\mathbf{x}_0)}{\partial x_k}\right\}$$

$$+ M^F(\mathbf{x}_0)\frac{\partial}{\partial x_{0m}}\left\{Q(\mathbf{x})\frac{\partial G^{MF}_{k;m}(\mathbf{x}|\mathbf{x}_0)}{\partial x_k} + R(\mathbf{x})\frac{\partial G^{FF}_{k;m}(\mathbf{x}|\mathbf{x}_0)}{\partial x_k}\right\}$$

Because the displacement Green's functions also satisfy the constitutive relations, the above expression for the fluid partial stress can be expressed as the contraction of a moment tensor M^M_{mn} and a

fluid source term M^F with the gradients of the Green's functions for partial stresses for matrix and fluid point loads:

$$s(\mathbf{x}) = M^M_{mn}(\mathbf{x}_0)\frac{\partial s^{GFM}_{;m}(\mathbf{x}|\mathbf{x}_0)}{\partial x_{0n}} + M^F(\mathbf{x}_0)\frac{\partial s^{GFF}_{;m}(\mathbf{x}|\mathbf{x}_0)}{\partial x_{0m}} \tag{A38}$$

A7 Fracture vs. Fluid Dilatation

A relationship between the fracture dilatation, Δ_M, and the fluid volume supply, Δ_F is needed to complete the development. As a fracture event occurs in the porous matrix, the fluid should be carried with the porous matrix, thus producing a cavity in the fluid phase with initial volume equal to the fracture volume. The cavity will subsequently collapse over a time period determined by the dynamics of the system. Unfortunately, a relation between the fracture's dilatation and cavitation of the fluid is not available.

One approach is to assume that the fluid cavitation is nil; that is, the fluid relaxes immediately to fill the inclusion, thus preserving the continuity of fluid displacement at the point **x**. This is essentially the approach taken by Chouet (1985) in modeling the dynamics of a discreet fluid driven crack, and is attractive because it provides a natural coupling between the fluid response and porous matrix dilatation. This case can be called "cavitation-free".

Cross-hole pulse testing of a fractured zone can be modeled by setting the fracture displacement discontinuity to zero, and using an appropriate fluid volume supply. Matrix dislocations due to borehole expansion or contraction in response to fluid pressure changes are thus ignored, possibly leading to significant error. The problem is analogous to the case of fracturing of the porous matrix, where the fluid supply is set to zero. The fluid volume supply can be negative, as for implosion of a diaphragm source. Conversely, the fluid volume supply can be positive, such as for pressure testing of the fracture zone.

Specification of a porous matrix dilatation with zero fluid displacement discontinuity will give a non-trivial isotropic moment for the fluid as well as the matrix. Specification of a fluid volume supply without matrix dilatation will produce a non-trivial isotropic moment for the porous matrix as well as for the fluid. That is, simply injecting fluid into the mixture will, through the Biot coupling parameter, Q, produce a moment for the structure. The responses for each of these cases will therefore

consist of a superposition of responses to each of these moments.

The contribution of the fluid volume supply to the seismic moment for the porous matrix appears on a similar footing with the matrix dilatation, through the parameter Q. The result is a finite static displacement of the porous matrix or solid region for a net fluid supply. From a physical standpoint, the static displacement resulting from a net fluid supply should be zero, due to relaxation of the matrix and fluid displacement fields. The isotropic fluid moment resulting from fluid injection, involving the parameter, R, must therefore produce a static displacement which just cancels the static displacement caused by the matrix moment.

There are certain interesting relationships between the moment source representations and displacement discontinuities. If the trace of the moment acting on the porous matrix during fluid injection is set to zero, then:

$$M_{ii}^{M} = (3A + 2N)\Delta_M + 3Q\,\Delta_F = 0 \tag{A39}$$

There exists a slight volume change of the matrix at the source:

$$\Delta_M = -\frac{3Q}{3A + 2N}\Delta_F \tag{A40}$$

If Q is small, the adjustment to Δ_M is much less than Δ_F.

The isotropic fluid moment becomes:

$$M_F = \left[R - \frac{Q^2}{A + \frac{2}{3}N}\right]\Delta_F \tag{A41}$$

For moments applied to the porous matrix, requiring the fluid isotropic moment to be zero gives:

$$M^F = 0 \tag{A42}$$

$$\Delta_F = -\frac{Q}{R}\Delta_M \tag{A43}$$

For low porosity fractured rock, $\frac{Q}{R} \gg 1$, so that the compensation to Δ_F is much larger than Δ_M.

The general porous matrix moment for zero fluid isotropic moment is:

$$M_{ij}^{M} = \left[\left[A - \frac{Q^2}{R}\right]\delta_{ij}\delta_{kl} + N(\delta_{ik}\delta_{jl} + \delta_{il}\delta_{jk})\right][u_k]n_l \tag{A44}$$

$$M_{ii}^{M} = \left[3A + 2N - \frac{3Q^2}{R}\right]\Delta_M \tag{A45a}$$

$$M_{ii}^{M} = \frac{B}{3}\Delta_M \tag{A45b}$$

In Equation A45b, the modulus, B, is simply the bulk modulus of the dry (drained) porous matrix, and is always greater than zero for a physically realizable material.

Equation A45b provides an interesting interpretation of this type of matrix failure. Requiring the fluid moment to be zero produces a finite negative fluid supply which results in a moment associated with the porous matrix computed as though the material were drained. That is, fluid is allowed to flow through the surface of and into the inclusion during the event, consistent with a requirement of zero pore pressure, or, equivalently, zero partial fluid stress, at the inclusion boundary. This can be conjectured as a physically plausible condition during (long term) expansion of a crack. However, requiring the fluid moment to be zero implies that the fluid volume supply is dependent on the matrix source dilatation, and not on the existing static partial fluid stress, or pore pressure. In the presence of finite porepressure, induced during a hydraulic fracturing, a failure of the porous matrix resulting from crack expansion would result in zero pore-pressure in the crack, a substantial positive going change of fluid partial stress. The rate of fluid back flow would depend on the magnitude of the fluid partial stress jump over the inclusion surface, dependent on the preexisting pore pressure; not simply on the matrix dilatation. During this process, the fluid moment would not necessarily be zero, because of the fluid stress jump at the boundary of the inclusion. After sufficient time, however, fluid will fill the inclusion, fluid inflow will cease, and the fluid partial stress over the surface will return to that existing prior to failure, producing zero long-term fluid partial traction over the surface. A similar interpretation exists for the condition of zero porous matrix moment and finite fluid volume supply. Requiring that the static (long term) porous matrix moment be zero during supply of fluid from the inclusion requires that there be some small retraction of the porous matrix inclusion boundary, proportional to the amount of fluid supplied.

Appendix B: Displacement-Stress Representation for Porous Materials

The displacement-stress representation discussed by Aki and Richards (1982) for propagation of waves in vertically heterogeneous elastic solids is extended to saturated vertically heterogeneous isotropic porous materials, using Biot's (1956) equations of motion. First, the constitutive equations for the porous material are inverted and then combined with the equations of motion. The displacements and stresses are then expanded in cylindrical harmonics to decompose the problem into two sets of linear, first order, differential equations: one set of six for PSV waves and a second set of two for SH waves. These two sets of equations can be integrated obtain propagator matrices which represent a state of stress and displacement at one position with a state of stress and displacement at a second position.

Other workers have recently developed methods for solving the equations of motion for vertically heterogeneous porous materials. Berryman, et al, (1983), evidently use matrix methods to solve the equations of motion for waves passing through vertically heterogeneous porous solids. (This reference was not obtained for review.) Yamamoto (1983), developed a displacement-stress representation for vertically heterogeneous regions, specifically sea beds, limiting its use to constant porosity. Yamamoto represents the motion of the fluid relative to the porous matrix and the total stress, rather than the absolute fluid displacement and partial fluid stress, as fundamental quantities. Yamamoto's approach, using Biot's representation of 1962, is particularly convenient for expressing boundary conditions between porous and solid regions. The approach used in this thesis employs the symmetric form originally posed by Biot in 1956, where the matrix and fluid displacements and partial stresses are placed on equal footing. The reason for this approach is that errors in the analysis are more easily identified by inspection of symmetries in the equations. Either approach is appropriate.

B1 Fundamental Equations

Biot's equations of motion for a fluid saturated isotropic porous material (1956) are:

$$-\omega^2\rho_{11}(\mathbf{x})\mathbf{u}-\omega^2\rho_{12}(\mathbf{x})\mathbf{U}= \qquad \text{(B1a)}$$

$$\nabla\cdot\sigma(\mathbf{x},\omega)+i\,\omega b\,(\mathbf{x},\omega)\left[\mathbf{U}-\mathbf{u}\right]+\mathbf{f}(\mathbf{x},\omega)$$

$$-\omega^2\rho_{21}(\mathbf{x})\mathbf{u}-\omega^2\rho_{22}(\mathbf{x})\mathbf{U}= \qquad \text{(B1b)}$$
$$\nabla s(\mathbf{x},\omega)-i\,\omega b(\mathbf{x},\omega)\left[\mathbf{U}-\mathbf{u}\right]+\mathbf{F}(\mathbf{x},\omega)$$

where:

$\mathbf{u}$ = matrix displacement field

$\mathbf{U}$ = fluid displacement field

$\sigma(\mathbf{x},\omega)$ = matrix stress tensor

$s(\mathbf{x},\omega)$ = fluid isotropic stress

$\rho_{ij}(\mathbf{x})$ = density parameters

$b(\mathbf{x},\omega)$ = Biot friction coefficient

$\mathbf{f}(\mathbf{x},\omega)$ = matrix body force per unit volume

$\mathbf{F}(\mathbf{x},\omega)$ = fluid body force per unit volume

$\mathbf{x}$ = position coordinate vector

ω = radian frequency

$i=\sqrt{-1}$

The following relations exist between the various densities: (Biot, 1956):

$$\rho_{11}+\rho_{12}=\rho_1 \qquad \text{(B2a)}$$

$$\rho_{21}+\rho_{22}=\rho_2 \qquad \text{(B2b)}$$

$$\rho_1+\rho_2=\rho \qquad \text{(B2c)}$$

$$\rho_{21}=\rho_{12} \qquad \text{(B2d)}$$

where the combined mass density of the aggregate material is ρ, and ρ_1 and ρ_2 are the respective masses of the porous matrix and fluid constituents.

The matrix force, **f**, and fluid force, **F**, act on the their respective constituents independently. Examples of static loads acting on the matrix and fluid constituents are the gravitational forces $\rho_1 g$ and $\rho_2 g$, respectively, where "g" is the gravitational acceleration.

Implicit in the above equations of motion is the Fourier transform with respect to time with the following convention:

$$\hat{f}(\omega) = \int f(t) e^{-i\omega t} dt \tag{B3}$$

Time derivatives are transformed as follows:

$$\frac{\partial}{\partial t} \rightarrow i\omega$$

This convention is consistent with the development used by Biot (1956). The alternate sign convention is used by Aki and Richards (1980), but in order to conform with the literature regarding wave propagation in porous materials, the above convention is used.

The inverse Fourier transform is

$$f(t) = \frac{1}{2\pi} \int \hat{f}(\omega) e^{+i\omega t} d\omega \tag{B4}$$

In cylindrical coordinates, the equations of motion for the porous region in physical components are:

$$\frac{1}{r}\frac{\partial}{\partial r}\sigma_{rr} + \frac{1}{r}\frac{\partial}{\partial \theta}\sigma_{r\theta} - \frac{\sigma_{\theta\theta}}{r} + \frac{\partial}{\partial z}\sigma_{rz} = -\omega^2 \tilde{\rho}_{11} u_r - \omega^2 \tilde{\rho}_{12} U_r - f_r \tag{B5a}$$

$$\frac{1}{r^2}\frac{\partial}{\partial r} r^2 \sigma_{r\theta} + \frac{1}{r}\frac{\partial}{\partial \theta}\sigma_{\theta\theta} + \frac{\partial}{\partial z}\sigma_{\theta z} = -\omega^2 \tilde{\rho}_{11} u_\theta - \omega^2 \tilde{\rho}_{12} U_\theta - f_\theta \tag{B5b}$$

$$\frac{1}{r}\frac{\partial}{\partial r} r\sigma_{rz} + \frac{1}{r}\frac{\partial}{\partial \theta}\sigma_{\theta z} + \frac{\partial}{\partial z}\sigma_{zz} = -\omega^2 \tilde{\rho}_{11} u_z - \tilde{\rho}_{12} U_z - f_z \tag{B5c}$$

$$\frac{\partial}{\partial r} s = -\omega^2 \tilde{\rho}_{12} u_r - \omega^2 \tilde{\rho}_{22} U_r - F_r \tag{B5d}$$

$$\frac{1}{r}\frac{\partial}{\partial \theta} s = -\omega^2 \tilde{\rho}_{12} u_\theta - \omega^2 \tilde{\rho}_{22} U_\theta - F_\theta \tag{B5e}$$

$$\frac{\partial}{\partial z} s = -\omega^2 \tilde{\rho}_{12} u_z - \omega^2 \tilde{\rho}_{22} U_z - F_z \tag{B5f}$$

The fluid-matrix friction is incorporated into the visco-dynamic densities $\tilde{\rho}_{ij}$ defined as:

$$\tilde{\rho}_{mn} = \rho_{mn} + (-1)^{m+n} \frac{b}{i\omega} \tag{B6}$$

The constitutive relations between stress and strain are given by:

$$\sigma_{rr}(\mathbf{x},\omega) = A(\mathbf{x}) e(\mathbf{x},\omega) + 2N(\mathbf{x}) e_{rr}(\mathbf{x},\omega) + Q(\mathbf{x}) \varepsilon(\mathbf{x},\omega) \tag{B7a}$$

$$\sigma_{\theta\theta}(\mathbf{x},\omega) = A(\mathbf{x}) e(\mathbf{x},\omega) + 2N(\mathbf{x}) e_{\theta\theta}(\mathbf{x},\omega) + Q(\mathbf{x}) \varepsilon(\mathbf{x},\omega) \tag{B7b}$$

$$\sigma_{zz}(\mathbf{x},\omega) = A(\mathbf{x}) e(\mathbf{x},\omega) + 2N(\mathbf{x}) e_{zz}(\mathbf{x},\omega) + Q(\mathbf{x}) \varepsilon(\mathbf{x},\omega) \tag{B7c}$$

$$\sigma_{r\theta}(\mathbf{x},\omega) = 2N(\mathbf{x}) e_{r\theta}(\mathbf{x},\omega) \tag{B7d}$$

$$\sigma_{rz}(\mathbf{x},\omega) = 2N(\mathbf{x}) e_{rz}(\mathbf{x},\omega) \tag{B7e}$$

$$\sigma_{\theta z}(\mathbf{x},\omega) = 2N(\mathbf{x}) e_{\theta z}(\mathbf{x},\omega) \tag{B7f}$$

$$s(\mathbf{x},\omega) = Q(\mathbf{x}) e(\mathbf{x},\omega) + R(\mathbf{x}) \varepsilon(\mathbf{x},\omega) \tag{B7g}$$

where:

$$e(\mathbf{x},\omega) = e_{rr}(\mathbf{x},\omega) + e_{\theta\theta}(\mathbf{x},\omega) + e_{zz}(\mathbf{x},\omega) \tag{B8a}$$

$$\varepsilon(\mathbf{x},\omega) = \frac{\partial}{\partial r} U_r + \frac{1}{r} \frac{\partial}{\partial \theta} U_\theta + \frac{U_r}{r} + \frac{\partial}{\partial z} U_z \tag{B8b}$$

The $e(\mathbf{x},\omega)$ and $\varepsilon(\mathbf{x},\omega)$ are the porous matrix and fluid volumetric strains, respectively.

The porous matrix strains are related to the matrix displacements by (Fung, Y.C., 1965):

$$e_{rr} = \frac{\partial}{\partial r} u_r \tag{B9a}$$

$$e_{\theta\theta} = \frac{1}{r} \frac{\partial}{\partial \theta} u_\theta + \frac{u_r}{r}$$

$$e_{zz} = \frac{\partial}{\partial z} u_z \tag{B9c}$$

$$e_{r\theta} = \frac{1}{2} \left[\frac{1}{r} \frac{\partial}{\partial \theta} u_r + r \frac{\partial}{\partial r} \frac{u_\theta}{r} \right] \tag{B9d}$$

$$e_{rz} = \frac{1}{2} \left[\frac{\partial}{\partial z} u_r + \frac{\partial}{\partial r} u_z \right] \tag{B9e}$$

$$e_{\theta z} = \frac{1}{2}\left[\frac{\partial}{\partial z}u_\theta + \frac{1}{r}\frac{\partial}{\partial \theta}u_z\right] \tag{B9f}$$

The inverse stress-strain relations are obtained by methods similar to those used for inverting the constitutive relations for elastic materials. That is, the constitutive relations are first decomposed into isotropic and deviatoric forms which are then inverted, giving:

$$e_{rr} = \frac{1}{2N}\sigma_{rr} + \frac{1}{2N}\frac{Q^2 - AR}{R(3A+2N) - 3Q^2}\sigma - \frac{Q}{R(3A+2N) - 3Q^2}s \tag{B10a}$$

$$e_{\theta\theta} = \frac{1}{2N}\sigma_{\theta\theta} + \frac{1}{2N}\frac{Q^2 - AR}{R(3A+2N) - 3Q^2}\sigma - \frac{Q}{R(3A+2N) - 3Q^2}s \tag{B10b}$$

$$e_{zz} = \frac{1}{2N}\sigma_{zz} + \frac{1}{2N}\frac{Q^2 - AR}{R(3A+2N) - 3Q^2}\sigma - \frac{Q}{R(3A+2N) - 3Q^2}s \tag{B10c}$$

$$e_{r\theta} = \frac{1}{2N}\sigma_{r\theta} \tag{B10d}$$

$$e_{rz} = \frac{1}{2N}\sigma_{rz} \tag{B10e}$$

$$e_{\theta z} = \frac{1}{2N}\sigma_{\theta z} \tag{B10f}$$

$$\varepsilon = -\frac{Q}{R(3A+2N) - 3Q^2}\sigma + 3A + \frac{2N}{R(3A+2N) - 3Q^2}s \tag{B10g}$$

where

$$\sigma = \sigma_{\alpha\alpha} = \sigma_{rr} + \sigma_{\theta\theta} + \sigma_{zz} \tag{B11}$$

The inverted stress-strain relations, Equations B10a through B10g, and the equations of motion, equations B5a through B5f, comprise thirteen first-order differential equations. Eight of these involve first order differentials with respect to the vertical coordinate z. The remaining five are eliminated by substitution. After moderately lengthy manipulations, the resulting reduced set of equations are:

$$\frac{\partial}{\partial z}u_r = -\frac{\partial}{\partial z}u_z + \frac{1}{N}\sigma_{rz} \tag{B12a}$$

$$\frac{\partial}{\partial z}u_\theta = -\frac{1}{r}\frac{\partial}{\partial \theta}u_z + \frac{1}{N}\sigma_{\theta z} \tag{B12b}$$

$$\frac{\partial}{\partial z}u_z = \frac{Q^2 - AR}{R(A+2N) - Q^2}(e_{rr} + e_{\theta\theta}) + \frac{R}{R(A+2N) - Q^2}\sigma_{zz} - \frac{Q}{R(A+2N) - Q^2}s \tag{B12c}$$

$$\frac{\partial}{\partial z}U_z = -\left[\frac{2NQ}{R(A+2N) - Q^2} - \frac{\rho_{12}}{\rho_{22}}\right](e_{rr} + e_{\theta\theta}) + \frac{1}{\omega^2\rho_{22}}\left[\frac{1}{r}\frac{\partial}{\partial r}r\frac{\partial}{\partial r}s + \frac{1}{r^2}\frac{\partial^2}{\partial \theta^2}s\right] \tag{B12d}$$

$$-\frac{Q}{R(A+2N) - Q^2}\sigma_{zz} + \frac{A+2N}{R(A+2N) - Q^2}s + \frac{1}{\omega^2\rho_{22}}\left[\frac{1}{r}\frac{\partial}{\partial r}F_r + \frac{1}{r}\frac{\partial}{\partial \theta}F_\theta\right]$$

$$\frac{\partial}{\partial z}\sigma_{rz} = -4N\frac{R(A+N) - Q^2}{R(A+2N) - Q^2}\frac{\partial}{\partial r}(e_{rr} + e_{\theta\theta}) + \frac{Q^2 - AR}{R(A+2N) - Q^2}\frac{1}{r}\frac{\partial}{\partial \theta}\sigma_{zz} \tag{B12e}$$

$$-\frac{2NQ}{R(A+2N) - Q^2}\frac{\partial}{\partial r}s + 2N\left[\frac{1}{r}\frac{\partial}{\partial r}re_{\theta\theta} - \frac{e_{rr}}{r} - \frac{1}{r}\frac{\partial}{\partial \theta}e_{r\theta}\right]$$

$$-\frac{\omega^2}{\rho_{22}}(\rho_{11}\rho_{22} - \rho_{12}^2)u_r + \frac{\rho_{12}}{\rho_{22}}F_r - f_r$$

$$\frac{\partial}{\partial z}\sigma_{\theta z} = -4N\frac{R(A+N) - Q^2}{R(A+2N) - Q^2}\frac{1}{r}\frac{\partial}{\partial \theta}(e_{rr} + e_{\theta\theta}) + \frac{Q^2 - AR}{R(A+2N) - Q^2}\frac{1}{r}\frac{\partial}{\partial \theta}\sigma_{zz} \tag{B12f}$$

$$-\frac{2NQ}{R(A+2N) - Q^2}\frac{1}{r}\frac{\partial}{\partial \theta}s + 2N\left[\frac{1}{r}\frac{\partial}{\partial \theta}e_{rr} - \frac{1}{r^2}\frac{\partial}{\partial r}r^2e_{r\theta}\right]$$

$$-\frac{\omega^2}{\rho_{22}}(\rho_{11}\rho_{22} - \rho_{12}^2)u_\theta + \frac{\rho_{12}}{\rho_{22}}F_\theta - f_\theta$$

$$\frac{\partial}{\partial z}\sigma_{zz} = -\frac{1}{r}\frac{\partial}{\partial r}r\sigma_{rz} - \frac{1}{r}\frac{\partial}{\partial \theta}\sigma_{\theta z} - \omega^2\rho_{11}u_z - \omega^2\rho_{12}U_z - f_z \tag{B12g}$$

$$\frac{\partial}{\partial z}s = -\omega^2\bar{\rho}_{12}u_z - \omega^2\bar{\rho}_{22}U_z - F_z \tag{B12h}$$

These are eight first-order differential equations involving only those field variables which must satisfy boundary conditions along the horizontal interfaces, perpendicular to the z - axis. These variables include the horizontal components of matrix displacement, u_r and u_θ either directly or through their derivatives represented by the strains e_{rr}, $e_{r\theta}$, and $e_{\theta\theta}$.

B2 Expansion in Orthogonal Vector Functions

Because of heterogeneity in the z- coordinate only, the traction vectors acting at z on a horizontal plane perpendicular to the z- axis, and the displacement vectors at z are expanded in orthogonal vector cylindrical harmonics. The vector fields are then decomposed into their component fields, and substituted directly into the above reduced set of equations. The procedure is discussed in detail by Aki and Richards (1980) and is equivalent to Hankel transformation, Fourier decomposition with respect to the azimuthal angle, and decomposition of the wave fields into PSV and SH components. What is different, though, is the incorporation of fluid stress and displacement into the displacement-stress representation. and specification of fluid load terms.

The matrix displacement vector $\mathbf{u}(\mathbf{x},\omega)$ and traction vector $\mathbf{T}(\mathbf{x},\omega)$ acting against the plane perpendicular to the z-axis, the fluid traction $\mathbf{S}(\mathbf{x},\omega)$ acting against a plane perpendicular to the z-axis, and the fluid displacement vector normal to the layering, $U_z\hat{\mathbf{z}}$, are represented by:

$$\mathbf{u} = \frac{1}{4\pi}\sum_{m=-\infty}^{m=+\infty}\int_0^\infty \left[l_1(z)\mathbf{T}_k^m + r_1(z)\mathbf{S}_k^m + r_2(z)\mathbf{R}_k^m\right]kdk \tag{B13a}$$

$$U_z\hat{\mathbf{z}} = \frac{1}{4\pi}\sum_{m=-\infty}^{m=+\infty}\int_0^\infty s_1\mathbf{R}_k^m kdk \tag{B13b}$$

$$\mathbf{T} = \frac{1}{4\pi}\sum_{m=-\infty}^{m=+\infty}\int_0^\infty \left[l_2\mathbf{T}_k^m + r_3\mathbf{S}_k^m + r_4\mathbf{R}_k^m\right]kdk \tag{B13c}$$

$$\mathbf{S} = \frac{1}{4\pi} \sum_{m=-\infty}^{m=+\infty} \int_0^\infty s_2 \mathbf{R}_k^m k dk \tag{B13d}$$

where

$$\mathbf{S} = s(\mathbf{x},\omega)\hat{\mathbf{z}} \tag{B14}$$

and $s(\mathbf{x},\omega)$ is the fluid's (isotropic) stress.

The vectors $\mathbf{T}_k^m$, $\mathbf{S}_k^m$, and $\mathbf{R}_k^m$, are cylindrical harmonics, defined by:

$$\mathbf{T}_k^m = \frac{1}{kr}\frac{\partial}{\partial\theta} Y_k^m \hat{\mathbf{r}} - \frac{1}{k}\frac{\partial}{\partial r} Y_k^m \hat{\boldsymbol{\theta}} \tag{B15a}$$

$$\mathbf{S}_k^m = \frac{1}{k}\frac{\partial}{\partial r} Y_k^m \hat{\mathbf{r}} + \frac{1}{kr}\frac{\partial}{\partial\theta} Y_k^m \hat{\boldsymbol{\theta}} \tag{B15b}$$

$$\mathbf{R}_k^m = -Y_k^m \hat{\mathbf{z}} \tag{B15c}$$

where Y_k^m is the scalar cylindrical harmonic

$$Y_k^m = J_m(kr)e^{im\theta} \tag{B16}$$

$\mathbf{T}_k^m$ is associated with shear horizontal motion (SH), and $\mathbf{S}_k^m$ and $\mathbf{R}_k^m$ with vertically and longitudinally polarized shear and compressional waves (PSV).

The fluid partial traction vector, $\mathbf{S}=s\hat{\mathbf{z}}$, is represented by a cylindrical vector harmonic, $s_2\mathbf{R}_k^m$, and includes the fluid's scalar isotropic stress. A second feature is that only the z - component of fluid displacement is represented. The transverse component of fluid displacement and fluid shear stresses are not included in the representation, because they are not required to satisfy boundary conditions at $z = +/-h$. If a constitutive relation were given for fluid shear, then transverse displacements and fluid tractions due to fluid shear would be included in the same manner as are the matrix displacements and tractions. The fluid viscosity is manifested in the friction term $b(\mathbf{x},\omega)$, which gives rise to a resistance

of fluid motion relative to the matrix.

The vector harmonics satisfy the following orthogonality relations (Aki and Richards, 1080, pg. 308):

$$\int_{-\pi}^{+\pi}\int_{0}^{\infty}\mathbf{T}_k^m\cdot\mathbf{T}_{k'}^{m'*}\,r\,dr\,d\theta=\frac{2\pi\delta_{mm'}\delta(k-k')}{\sqrt{kk'}} \tag{B17a}$$

$$\int_{-\pi}^{+\pi}\int_{0}^{\infty}\mathbf{S}_k^m\cdot\mathbf{S}_{k'}^{m'*}\,r\,dr\,d\theta=\frac{2\pi\delta_{mm'}\delta(k-k')}{\sqrt{kk'}} \tag{B17b}$$

$$\int_{-\pi}^{+\pi}\int_{0}^{\infty}\mathbf{R}_k^m\cdot\mathbf{R}_{k'}^{m'*}\,r\,dr\,d\theta=\frac{2\pi\delta_{mm'}\delta(k-k')}{\sqrt{kk'}} \tag{B17c}$$

$$\int_{-\pi}^{+\pi}\int_{0}^{\infty}Y_k^m Y_{k'}^{m'*}\,r\,dr\,d\theta=\frac{2\pi\delta_{mm'}\delta(k-k')}{\sqrt{kk'}} \tag{B18}$$

and all other combinations of the vector harmonics are zero.

With these definitions, the physical components of displacement and stress become:

$$u_r=\frac{1}{4\pi}\sum_{m=-\infty}^{m=+\infty}\int_0^{\infty}\left[l_1\frac{1}{kr}\frac{\partial}{\partial\theta}Y_k^m+r_1\frac{1}{k}\frac{\partial}{\partial r}Y_k^m\right]kdk \tag{B19a}$$

$$u_\theta=\frac{1}{4\pi}\sum_{m=-\infty}^{m=+\infty}\int_0^{\infty}\left[-l_1\frac{1}{k}\frac{\partial}{\partial r}Y_k^m+r_1\frac{1}{kr}\frac{\partial}{\partial\theta}Y_k^m\right]kdk \tag{B19b}$$

$$u_z=-\frac{1}{4\pi}\sum_{m=-\infty}^{m=+\infty}\int_0^{\infty}r_2Y_k^m\,kdk \tag{B19c}$$

$$U_z=-\frac{1}{4\pi}\sum_{m=-\infty}^{m=+\infty}\int_0^{\infty}s_1Y_k^m\,kdk \tag{B19d}$$

$$\sigma_{rz} = \frac{1}{4\pi} \sum_{m=-\infty}^{m=+\infty} \int_0^\infty \left[l_2 \frac{1}{kr} \frac{\partial}{\partial \theta} Y_k^m + r_3 \frac{1}{k} \frac{\partial}{\partial r} Y_k^m \right] kdk \tag{B19e}$$

$$\sigma_{\theta z} = \frac{1}{4\pi} \sum_{m=-\infty}^{m=+\infty} \int_0^\infty \left[-l_2 \frac{1}{k} \frac{\partial}{\partial r} Y_k^m + r_3 \frac{1}{kr} \frac{\partial}{\partial \theta} Y_k^m \right] kdk \tag{B19f}$$

$$\sigma_{zz} = -\frac{1}{4\pi} \sum_{m=-\infty}^{m=+\infty} \int_0^\infty r_4 Y_k^m kdk \tag{B19g}$$

$$s = -\frac{1}{4\pi} \sum_{m=-\infty}^{m=+\infty} \int_0^\infty s_2 Y_k^m kdk \tag{B19h}$$

Substituting the relations for displacements, the following expressions are obtained for the strains in terms of the cylindrical harmonics, Y_k^m:

$$e_{rr} + e_{\theta\theta} = -\frac{1}{4\pi} \sum_{m=-\infty}^{m=+\infty} \int_0^\infty r_1 Y_k^m k^2 dk \tag{B20a}$$

$$e_{rr} - e_{\theta\theta} = \frac{1}{4\pi} \sum_{m=-\infty}^{m=+\infty} \int_0^\infty \left[l_1 \frac{2}{k} \frac{\partial}{\partial \theta} \left(\frac{1}{r} \frac{\partial}{\partial r} Y_k^m - \frac{Y_k^m}{r} \right) \right. \tag{B20b}$$
$$\left. + r_1 \frac{1}{k} \left(\frac{\partial^2}{\partial r^2} Y_k^m - \frac{1}{r} \frac{\partial}{\partial r} Y_k^m - \frac{1}{r^2} \frac{\partial^2}{\partial \theta^2} Y_k^m \right) \right] kdk$$

$$e_{r\theta} = -\frac{1}{4\pi} \sum_{m=-\infty}^{m=+\infty} \int_0^\infty \left[l_1 \frac{1}{2k} \left(\frac{\partial^2}{\partial r^2} Y_k^m - \frac{1}{r} \frac{\partial}{\partial r} Y_k^m - \frac{1}{r^2} \frac{\partial^2}{\partial \theta^2} Y_k^m \right) \right. \tag{B20c}$$
$$\left. - r_1 \frac{1}{k} \frac{\partial}{\partial \theta} \left(\frac{1}{r} \frac{\partial}{\partial r} Y_k^m - \frac{Y_k^m}{r^2} \right) \right] kdk$$

The time transformed loads are similarly expanded in cylinder harmonics. For body forces applied to the porous matrix:

$$\mathbf{f}(r,\theta,z,\omega)=\frac{-1}{4\pi}\sum_{m=-\infty}^{m=+\infty}\int_0^\infty[f_T(z)\mathbf{T}_k^m(r,\theta)+f_S(z)\mathbf{S}_k^m(r,\theta)+f_R(z)\mathbf{R}_k^m(r,\theta)]kdk \tag{B21a}$$

For body forces applied to the fluid:

$$\mathbf{F}(r,\theta,z,\omega)=\frac{-1}{4\pi}\sum_{m=-\infty}^{m=+\infty}\int_0^\infty[F_T(z)\mathbf{T}_k^m(r,\theta)+F_S(z)\mathbf{S}_k^m(r,\theta)+F_R(z)\mathbf{R}_k^m(r,\theta)]kdk \tag{B21b}$$

The negative sign is included to remain consistent with the development of Aki and Richards (1980, pg. 308) point load representation.

The expressions for strains and displacements are substituted into the set of 8 first order differential equations for the displacements u_r, u_θ, u_z, and U_z, and stresses σ_{rz}, $\sigma_{\theta z}$, σ_{zz}, and s. Then, after carrying out very lengthy and and detailed algebraic computations, and comparing linearly independent terms, or, equivalently, using the orthogonality relation for Y_k^m and considerable manipulation, a set of first order ordinary differential equations are obtained for the displacement-stress vector components. To perform these operations, the following identity is useful:

$$\frac{1}{r}\frac{\partial}{\partial r}r\frac{\partial}{\partial r}Y_k^m+\frac{1}{r^2}\frac{\partial^2}{\partial\theta^2}Y_k^m=-k^2Y_k^m \tag{B22}$$

The results are:

$$\frac{\partial}{\partial z}l_1=\frac{1}{N}l_2 \tag{B23a}$$

$$\frac{\partial}{\partial z}l_2=[Nk^2-\frac{\omega^2}{\tilde{\sigma}_{22}}(\tilde{\sigma}_{11}\tilde{\rho}_{22}-\tilde{\sigma}_{12}^2)]l_1+\left[f_T-\frac{\tilde{\rho}_{12}}{\tilde{\rho}_{22}}F_T\right] \tag{B23b}$$

$$\frac{\partial}{\partial z} r_1 = k r_2 + \frac{r_3}{N} \tag{B24a}$$

$$\frac{\partial}{\partial z} r_2 = -\frac{(RA - Q^{2)})}{R(A+2N) - Q^2} k r_1 + \frac{R}{R(A+2N) - Q^2} r_4 - \frac{Q}{R(A+2N) - Q^2} s_2 \tag{B24b}$$

$$\frac{\partial}{\partial z} r_3 = \left[4Nk^2 \frac{R(A+N) - Q^2}{R(A+2N) - Q^2} - \frac{\omega^2}{\sigma^{-}_{22}} (\sigma^{-}_{11}\sigma^{-}_{22} - \sigma^{-}_{12}{}^2) \right] r_1 - \frac{Q^2 - AR}{R(A+2N) - Q^2} k r_4 \tag{B24c}$$

$$+ \left[\frac{2NQ}{R(A+2N) - Q^2} - \frac{\sigma^{-}_{12}}{\sigma^{-}_{22}} \right] k s_2 + \left[f_S - \frac{\sigma^{-}_{12}}{\sigma^{-}_{22}} F_S \right]$$

$$\frac{\partial}{\partial z} r_4 = -\omega^2 \sigma^{-}_{11} r_2 - r_3 k - \omega^2 \sigma^{-}_{12} s_1 + f_R \tag{B24d}$$

$$\frac{\partial}{\partial z} s_1 = \left[\frac{\sigma^{-}_{12}}{\sigma^{-}_{22}} - \frac{2NQ}{R(A+2N) - Q^2} \right] k r_1 - \frac{Q}{R(A+2N) - Q^2} r_4 \tag{B24e}$$

$$+ \left[\frac{A+2N}{R(A+2N) - Q^2} - \frac{k^2}{\omega^2 \sigma^{-}_{22}} \right] s_2 - \frac{k}{\omega^2 \sigma^{-}_{22}} F_S$$

$$\frac{\partial}{\partial z} s_2 = -\omega^2 \sigma^{-}_{12} r_2 - \omega^2 \sigma^{-}_{22} s_1 + F_R \tag{B24f}$$

Again, the body force terms have reversed sign relative to the corresponding equations in cylindrical polar coordinates.

The equations of motion and constitutive equations for the porous region are thus decomposed into two sets of coupled first order ordinary differential equations in z. Equations B23a and B23b correspond to the SH problem, and Equations B24a through B24f to the PSV problem. If Q ,and σ^{-}_{12} are set to zero, the displacement-stress formulas given by Aki and Richards (1980, pg. 269) for SH and PSV waves in vertically heterogeneous solid elastic media are obtained. The above equations are identical to those which may be obtained for the two-dimensional case, discussed by Aki and Richards in some detail for solid regions.

The inhomogeneous terms in expressions for the shear stress gradients are, in the case of r_3, $f_S - \frac{\tilde{\rho}_{12}}{\tilde{\rho}_{22}} F_S$, with a similar term for the SH case. An additional term, $-\frac{k}{\omega^2 \tilde{\rho}_{22}} F_S$, is included in the equation for the derivative of s_1, a displacement gradient. In this way, transverse fluid body forces are included in the displacement-stress representation, without the need for additional horizontal displacement-stress components for the fluid displacement and shear stress. Had fluid shear stresses been incorporated, requiring a constitutive relation for fluid shear and continuity of horizontal fluid displacements at various boundaries, the fluid body force terms would have appeared in the same way as the body force terms for the porous matrix.

The body force term, $-\frac{k}{\omega^2 \tilde{\rho}_{22}} F_S$, is substantially larger than $-\frac{\tilde{\rho}_{12}}{\tilde{\rho}_{22}} F_S$, at low frequencies. At zero frequency, the ratio, $-\frac{\tilde{\rho}_{12}}{\tilde{\rho}_{22}}$, approaches unity for finite viscosity. Without viscosity, the ratio would be zero in the absence of mass-coupling, and constant with mass coupling. The term, $-\frac{k}{\omega^2 \tilde{\rho}_{22}}$, diverges for finite k as the frequency goes to zero, a consequence of the inability of the fluid to support shear with finite displacement. For finite frequency, though, the representation is evidently complete, so that solutions may be developed for oscillatory fluid body force distributions.

B3 Matrix Representation

The PSV and SH displacement-stress problems are represented in matrix form as:

$$\frac{\partial}{\partial z} \mathbf{v}^{PSV}(z) = \mathbf{A}^{PSV}(z) \mathbf{v}^{PSV}(z) + \mathbf{q}^{PSV}(z) \tag{B25a}$$

$$\frac{\partial}{\partial z} \mathbf{v}^{SH}(z) = \mathbf{A}^{SH}(z) \mathbf{v}^{SH}(z) + \mathbf{q}^{SH}(z) \tag{B25b}$$

The displacement-stress vector $\mathbf{v}^{PSV}$ for the PSV problem is:

$$\mathbf{v}^{PSV}(z)=\begin{Bmatrix} r_1 \\ r_2 \\ r_3 \\ r_4 \\ s_1 \\ s_2 \end{Bmatrix} \tag{B26}$$

The inhomogeneous term $\mathbf{q}^{PSV}$ will be important when computing the response to point sources applied to either the matrix or to the fluid. The inhomogeneous term, or force term, is given by:

$$\mathbf{q}^{PSV}(z)=\begin{Bmatrix} 0 \\ 0 \\ +f_S - \dfrac{\sigma_{12}}{\sigma_{22}} F_S \\ +f_R \\ -\dfrac{k}{\omega^2 \sigma_{22}} F_S \\ +F_R \end{Bmatrix} \tag{B27}$$

The matrix A^{PSV} is given by:

$$\mathbf{A}^{PSV}(z) = \tag{B28}$$

$$\begin{bmatrix}
0 & k & \frac{1}{N} & 0 & 0 & 0 \\
-\frac{(RA-Q^{2)})}{K^2}k & 0 & 0 & \frac{R}{K^2} & 0 & \frac{-Q}{K^2} \\
4Nk^2\frac{R(A+N)-Q^2}{K^2} - \frac{\omega^2}{\tilde{\rho}_{22}}\tilde{\rho}^2 & 0 & 0 & \frac{(RA-Q^2)}{K^2}k & 0 & \left[\frac{2NQ}{K^2} - \frac{\tilde{\rho}_{12}}{\tilde{\rho}_{22}}\right]k \\
0 & -\omega^2\tilde{\rho}_{11} & -k & 0 & -\omega^2\tilde{\rho}_{12} & 0 \\
\left[\frac{\tilde{\rho}_{12}}{\tilde{\rho}_{22}} - \frac{2NQ}{K^2}\right]k & 0 & 0 & -\frac{Q}{K^2} & 0 & \left[\frac{A+2N}{K^2} - \frac{k^2}{\omega^2\tilde{\rho}_{22}}\right] \\
0 & -\omega^2\tilde{\rho}_{12} & 0 & 0 & -\omega^2\tilde{\rho}_{22} & 0
\end{bmatrix}$$

where

$$K^2 = R(A+2N) - Q^2 \tag{B30}$$

and

$$\tilde{\rho} = \tilde{\rho}_{11}\tilde{\rho}_{22} - \tilde{\rho}_{12}^2 \tag{B31}$$

For the SH problem:

$$\mathbf{v}^{SH}(z) = \begin{Bmatrix} l_1 \\ l_2 \end{Bmatrix} \tag{B32}$$

$$\mathbf{q}^{SH}(z) = \begin{Bmatrix} 0 \\ -\frac{\tilde{\rho}_{12}}{\tilde{\rho}_{22}}F_T + f_T \end{Bmatrix} \tag{B33}$$

The matrix $\mathbf{A}^{SH}(z)$ is:

$$\mathbf{A}^{SH}(z)=\begin{bmatrix} 0 & Nk^2-\dfrac{\omega^2}{\tilde{\rho}_{22}}\rho^{-2} \\ \dfrac{1}{N} & 0 \end{bmatrix} \tag{B34}$$

Again, the moduli N, A, R, and Q, and the visco-dynamic "densities" $\tilde{\rho}_{\alpha\beta}$ are functions of z and ω.

B4 Propagator Representation

The differential equations obtained above can be numerically integrated to yield propagator matrices for PSV and SH waves (Aki and Richards, 1980). The algebra and methods of computing propagators are described by Pipes and Hovanessian (1969).

The propagators are equivalent to transition matrices, or matrizants of the matrix, $\mathbf{A}(z)$, and determine the response at z_2 due to a state of displacement and stress at z_1, represented by the vector $\{ r_1, r_2, r_3, r_4, s_1, s_2 \}$ for PSV waves and by the vector $\{ l_1, l_2 \}$ for SH waves. The propagators are designated as $\mathbf{P}^{PSV}(z_2,z_1)$ and $\mathbf{P}^{SH}(z_2,z_1)$, and satisfy the relations:

$$\mathbf{P}(z_3,z_2)\mathbf{P}(z_2,z_1)=\mathbf{P}(z_3,z_1) \tag{B35a}$$

$$\mathbf{P}(z_2,z_1)\mathbf{P}(z_1,z_2)=\mathbf{P}(z_2,z_2)=\mathbf{I} \tag{B35b}$$

The propagators satisfy the differential equation for the displacement-stress components:

$$\frac{\partial}{\partial z}\mathbf{P}(z,z_0)=\mathbf{A}(z)\mathbf{P}(z,z_0) \tag{B36}$$

The displacement-stress vectors at z_2 relative to the displacement-stress vectors at z_1 are given by:

$$\mathbf{v}^{PSV}(z_2)=\mathbf{P}^{PSV}(z_2,z_1)\mathbf{v}^{PSV}(z_1)+\int_{z_1}^{z_2}\mathbf{P}^{PSV}(z',z_1)\mathbf{q}^{PSV}(z')dz' \tag{B37a}$$

$$\mathbf{v}^{SH}(z_2)=\mathbf{P}^{SH}(z_2,z_1)\mathbf{v}^{SH}(z_1)+\int_{z_1}^{z_2}\mathbf{P}^{SH}(z',z_1)\mathbf{q}^{SH}(z')dz' \tag{B37b}$$

The propagators are computed by numerically integrating equation 36 from z_1 to z_2, beginning with the identity matrix:

$$I = \mathbf{P}(z_1, z_1)$$

The propagators thus represent sets of linearly independent solutions which may be used to represent the complete solution within the porous layer, and the "solution" for the porous region is thus obtained by numerically solving an initial value problem. Aki and Richards provide detailed discussions of the properties of the propagators, and their special canonical forms for the case of homogeneous regions. In particular, the propagator may be diagonalized into up-going and down-going terms, with corresponding eigenvalues describing the velocity of propagation for each of the two coupled compressional waves and the shear wave.

The displacement-stress propagators form the fundamental solution for the porous layer. Their computation and use are described in detail in Chapter 3 and especially Chapter 4, regarding numerical solution of the boundary value problem.

Appendix C:
Center Plane Displacement and Fluid Partial Stress Responses

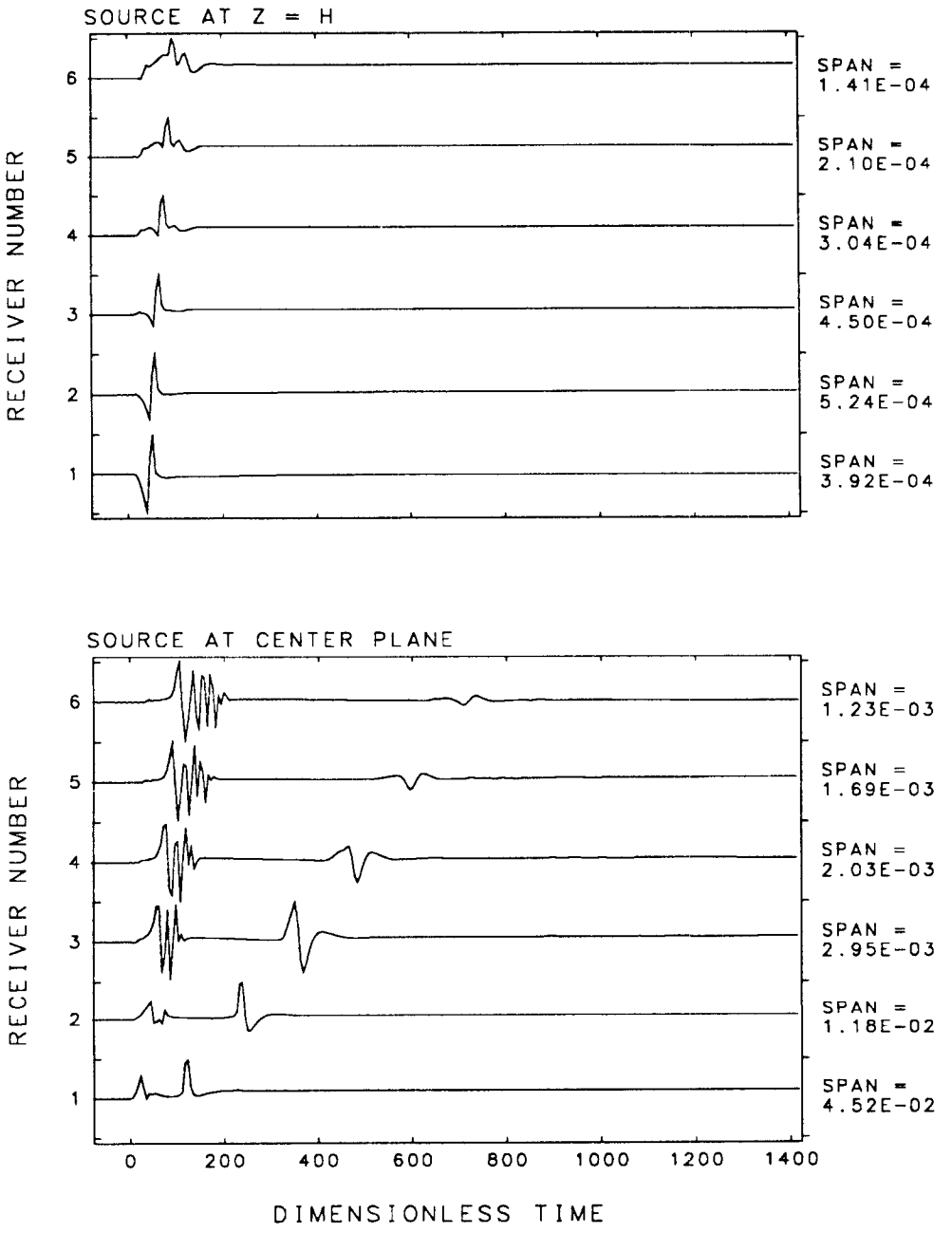

FIGURE C1.1 RADIAL DISPLACEMENT RESPONSE
AT CENTER PLANE DUE TO AN R - R MOMENT

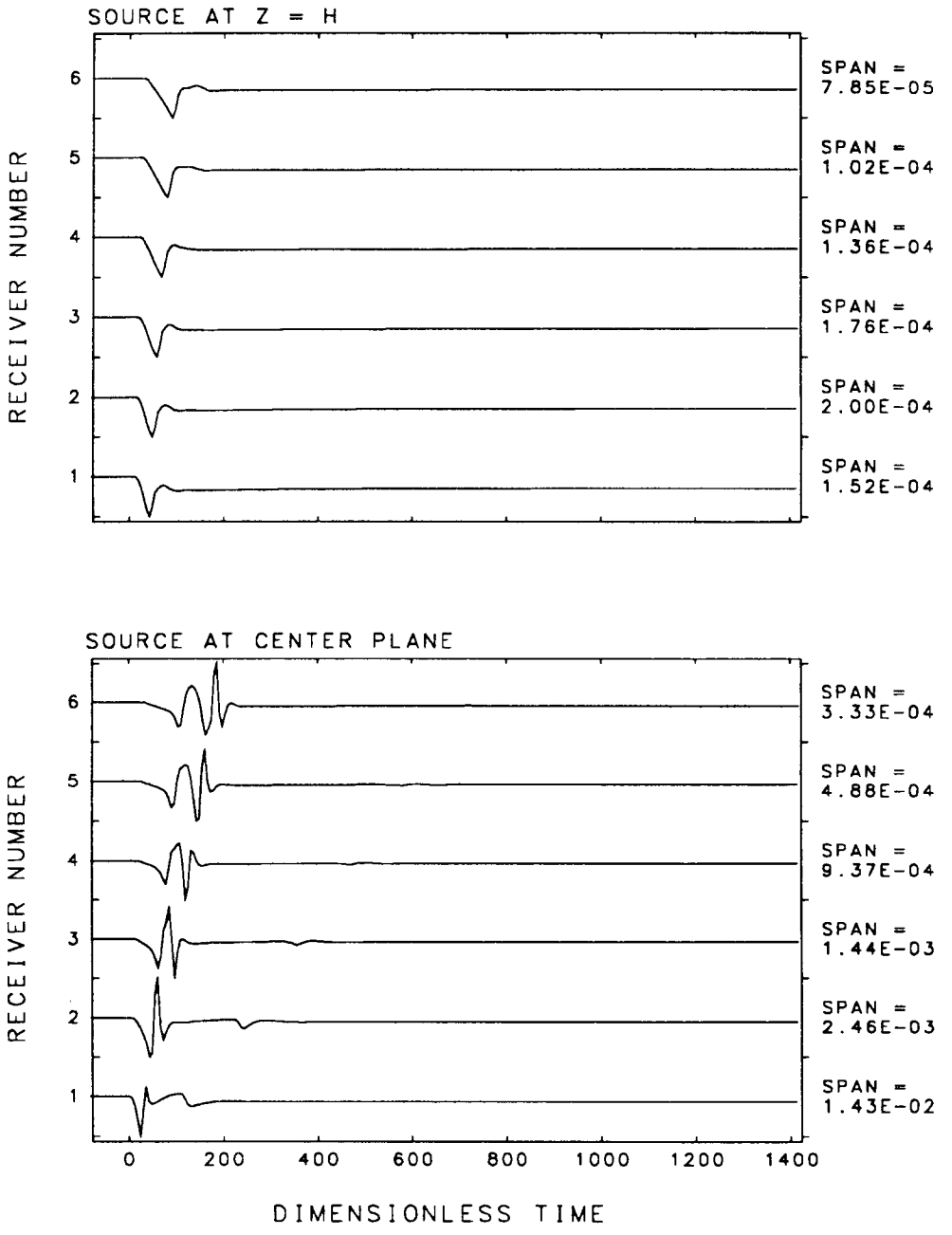

FIGURE C1.2 RADIAL DISPLACEMENT RESPONSE AT CENTER PLANE DUE TO A $\theta - \theta$ MOMENT

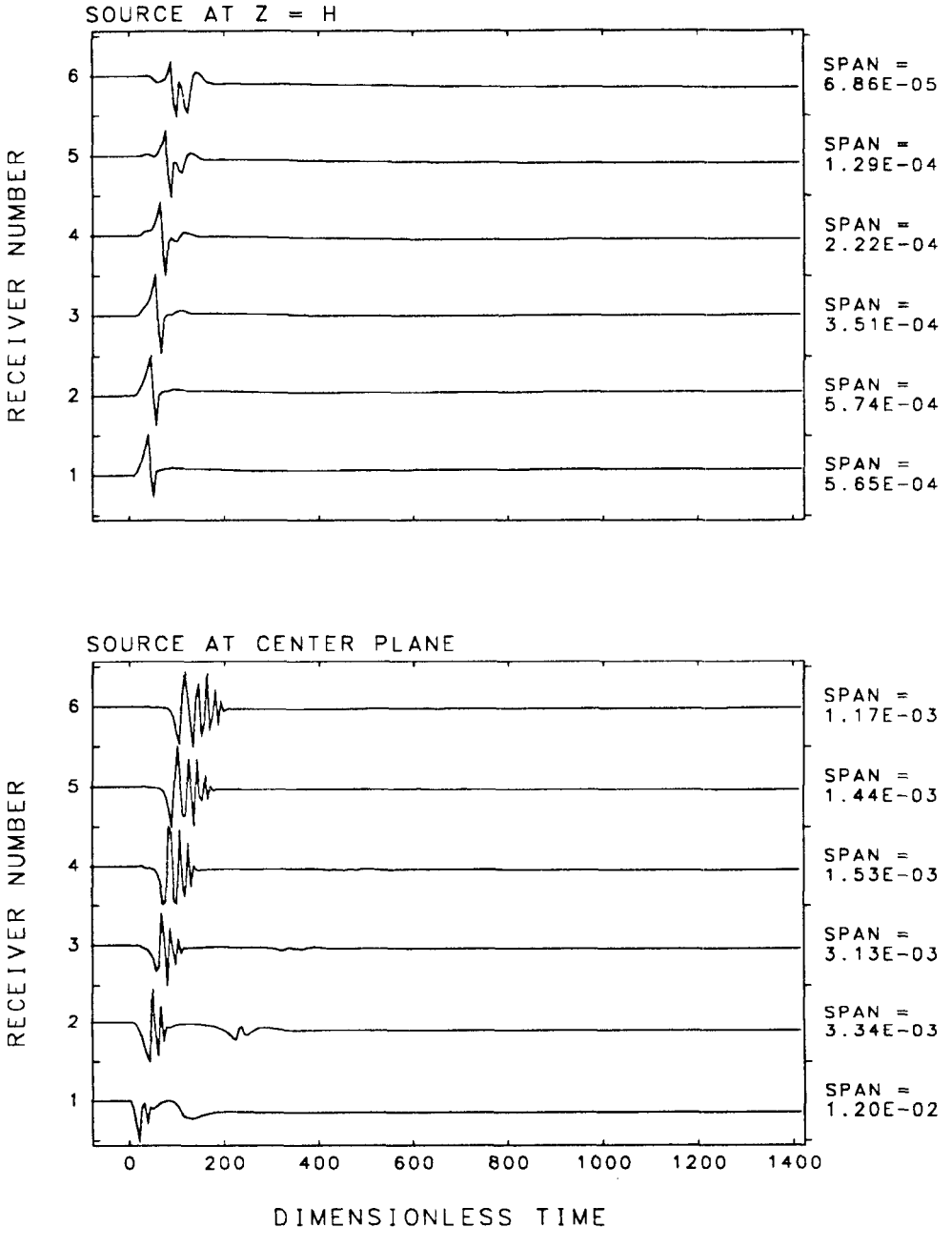

FIGURE C1.3 RADIAL DISPLACEMENT RESPONSE
AT CENTRAL PLANE DUE TO A Z - Z MOMENT

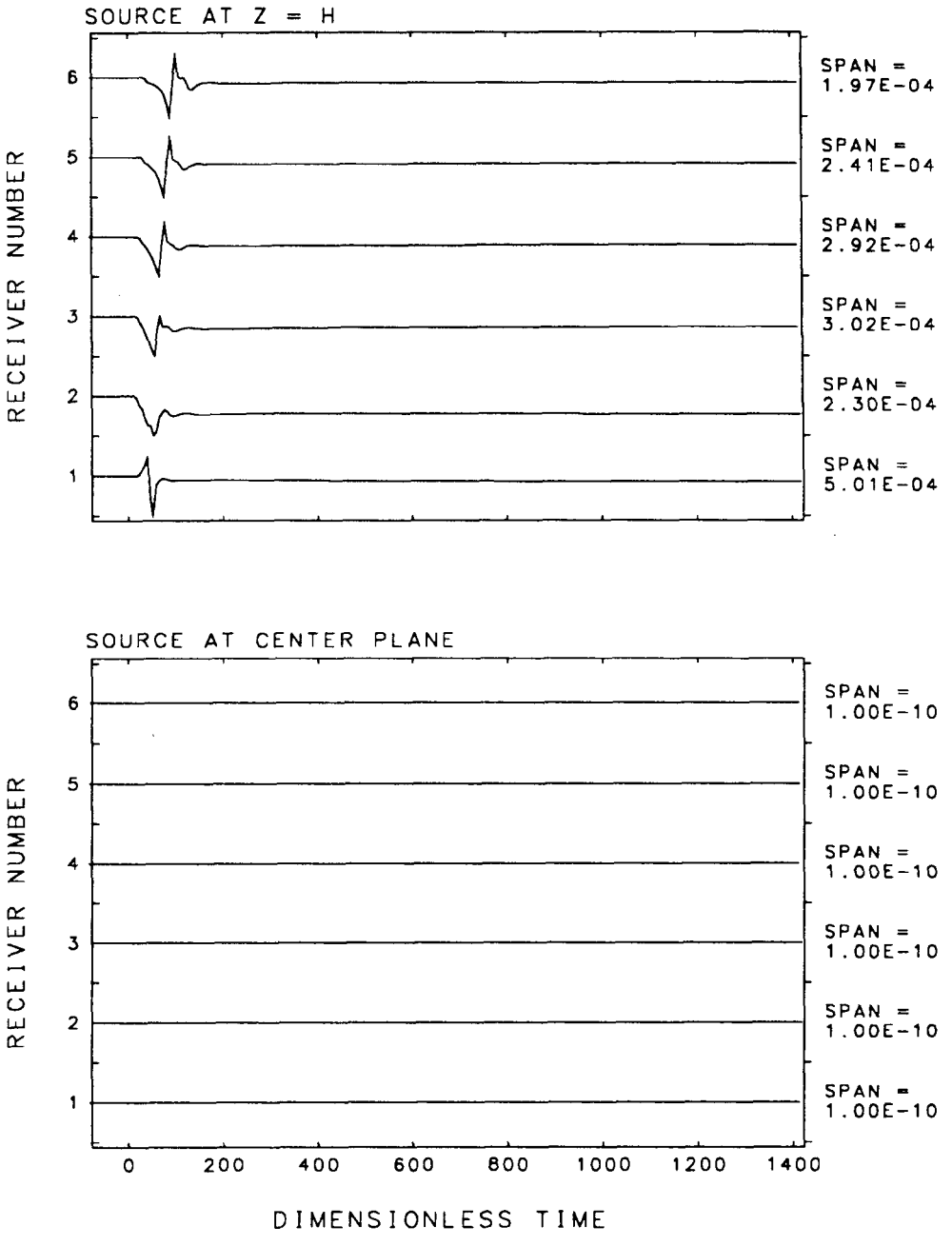

FIGURE C1.4 RADIAL DISPLACEMENT RESPONSE
AT CENTER PLANE DUE TO A SYMMETRIC R - Z MOMENT

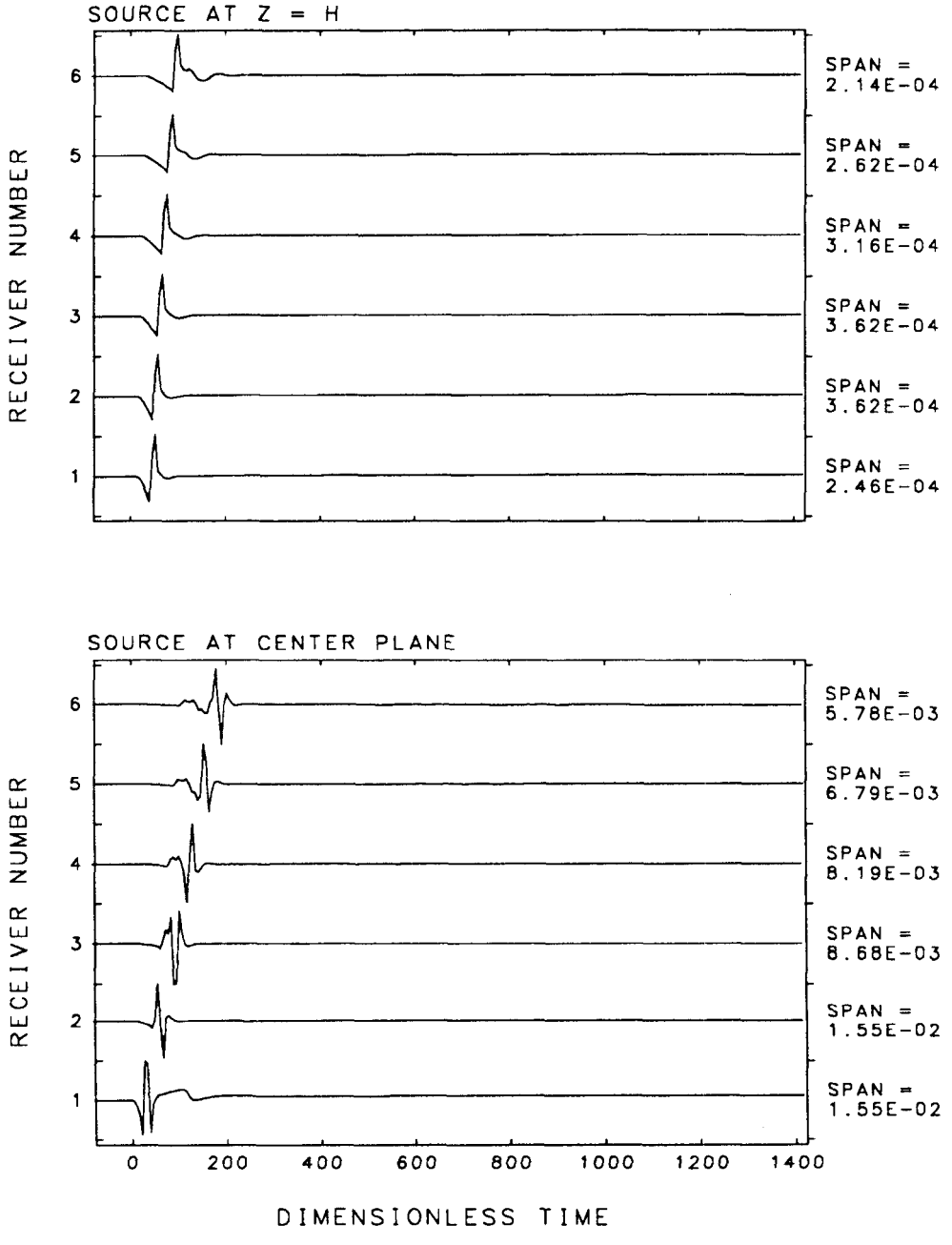

FIGURE C1.5 TRANSVERSE HORIZONTAL DISPLACEMENT RESPONSE AT CENTER PLANE DUE TO A SYMMETRIC R - θ MOMENT

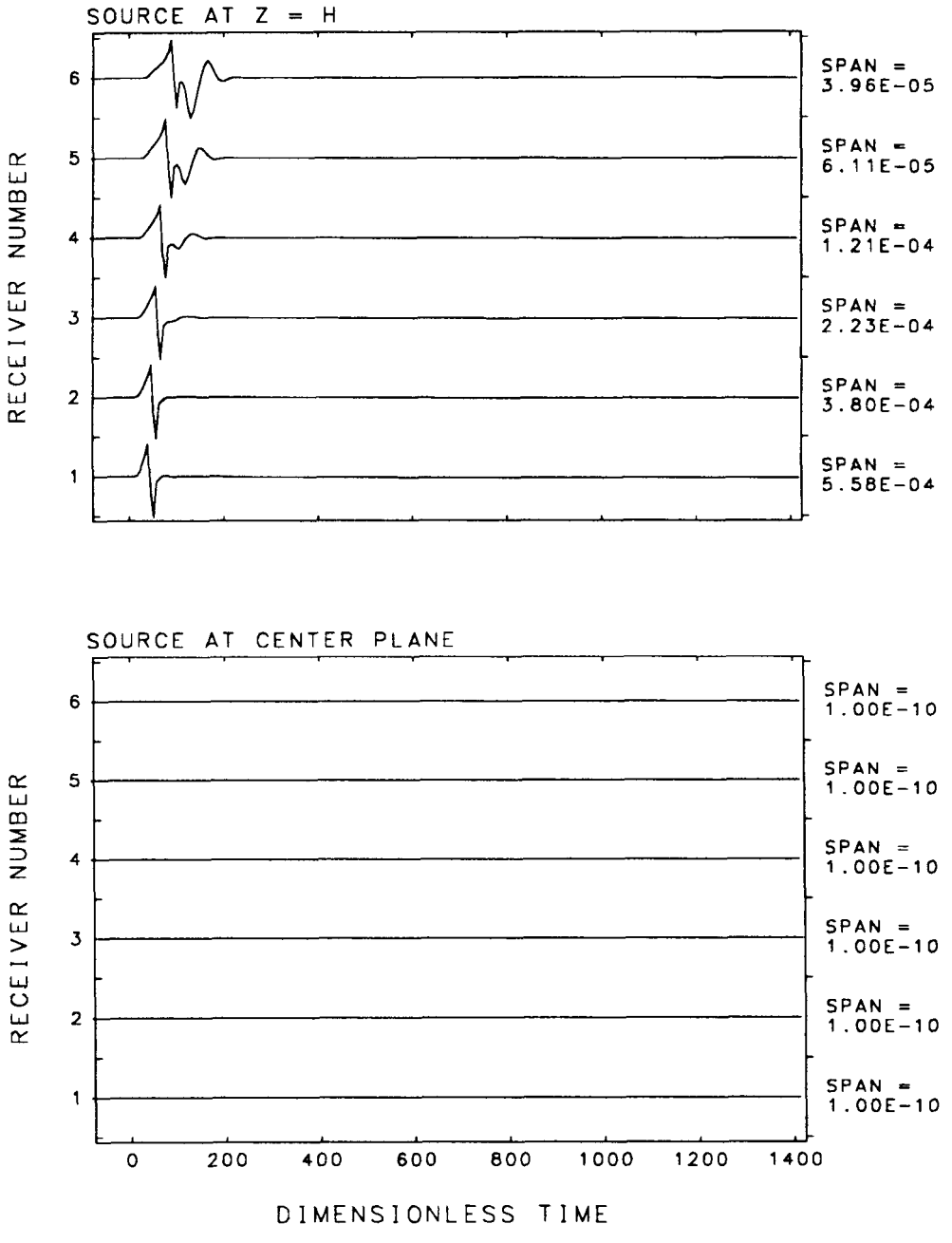

FIGURE C1.6 TRANSVERSE HORIZONTAL DISPLACEMENT RESPONSE AT CENTER PLANE FOR A SYMMETRIC $\theta - Z$ MOMENT

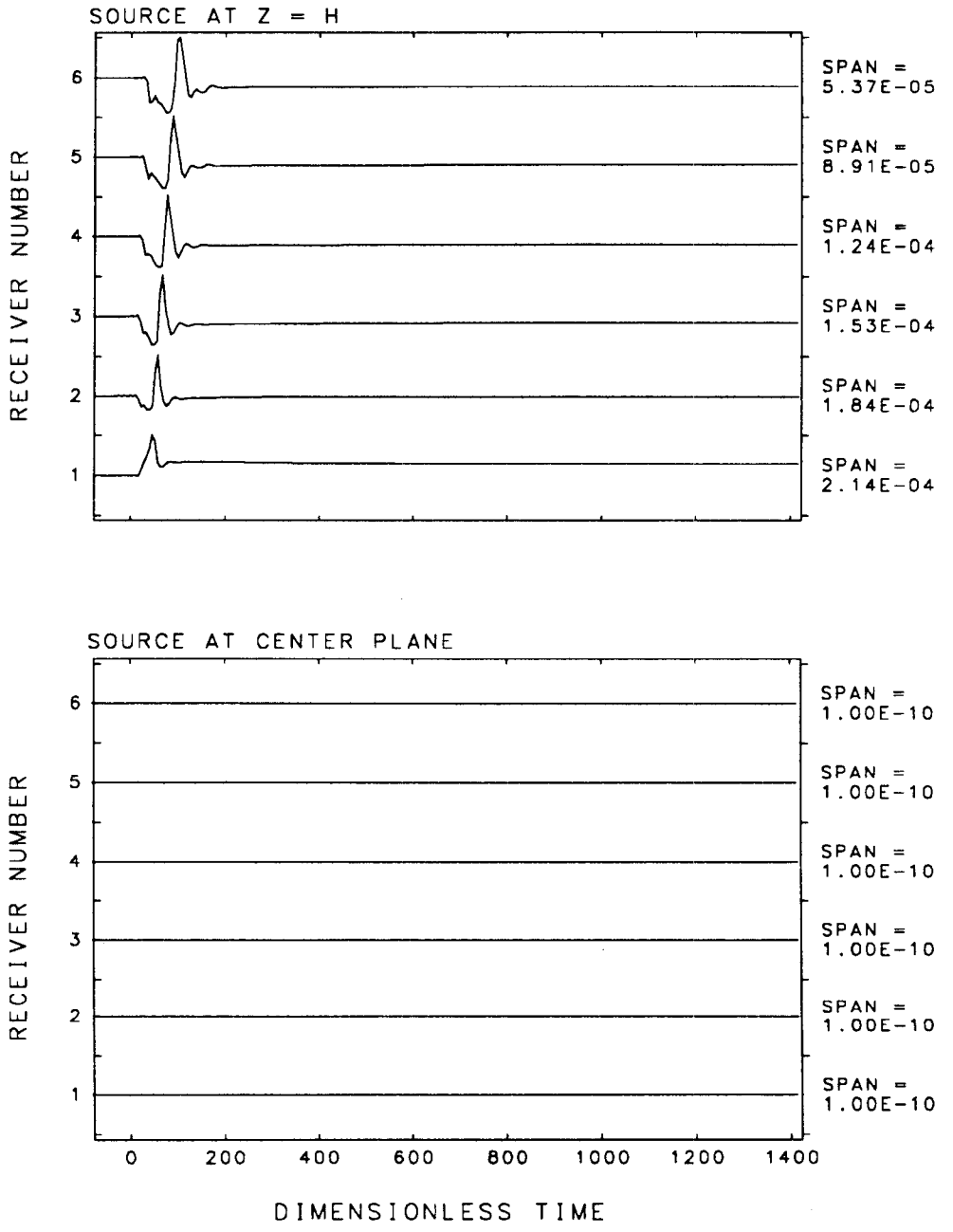

FIGURE C1.7 VERTICAL DISPLACEMENT RESPONSE AT CENTER PLANE FOR AN R - R MOMENT

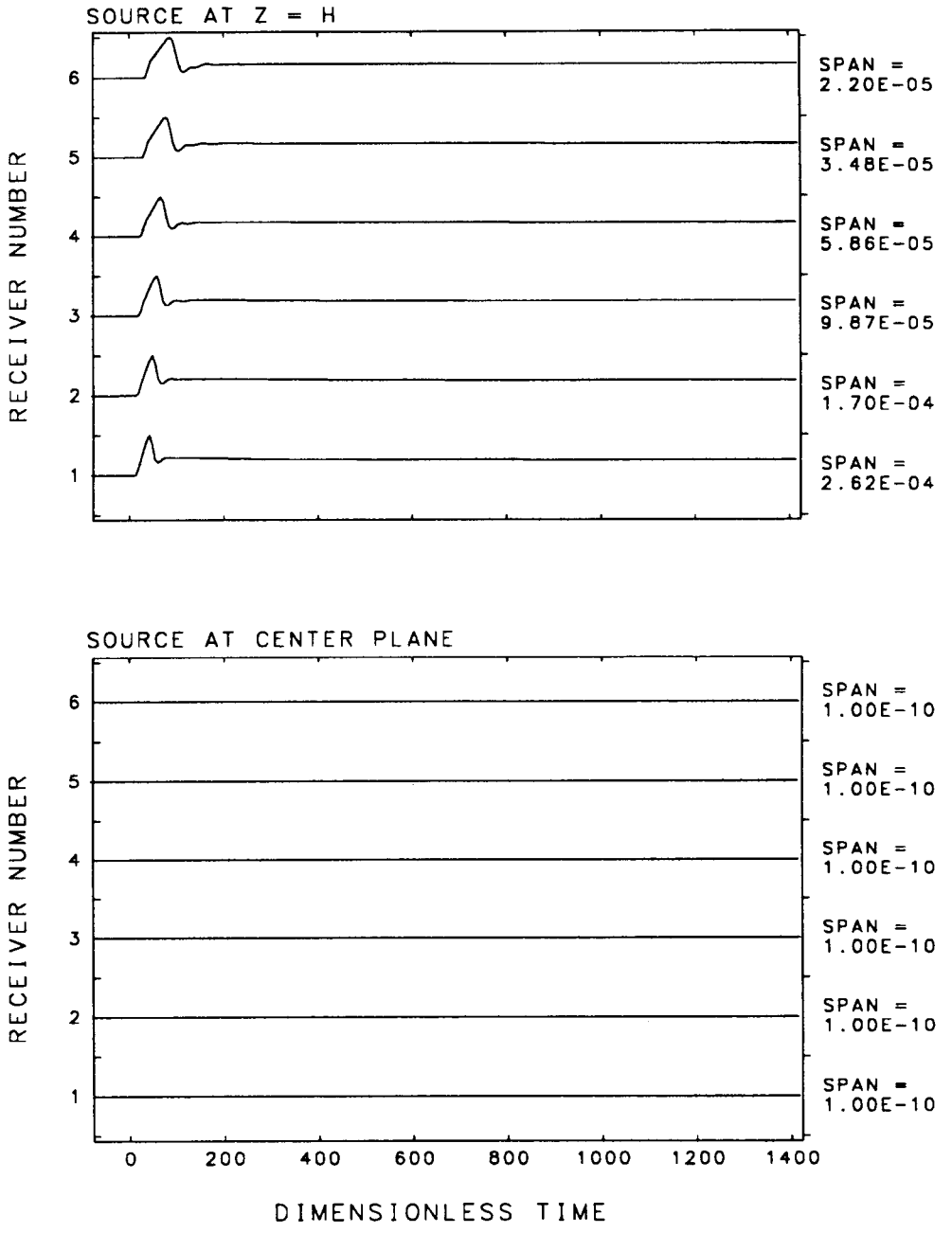

FIGURE C1.8 VERTICAL DISPLACEMENT RESPONSE AT CENTER PLANE FOR A $\theta - \theta$ MOMENT

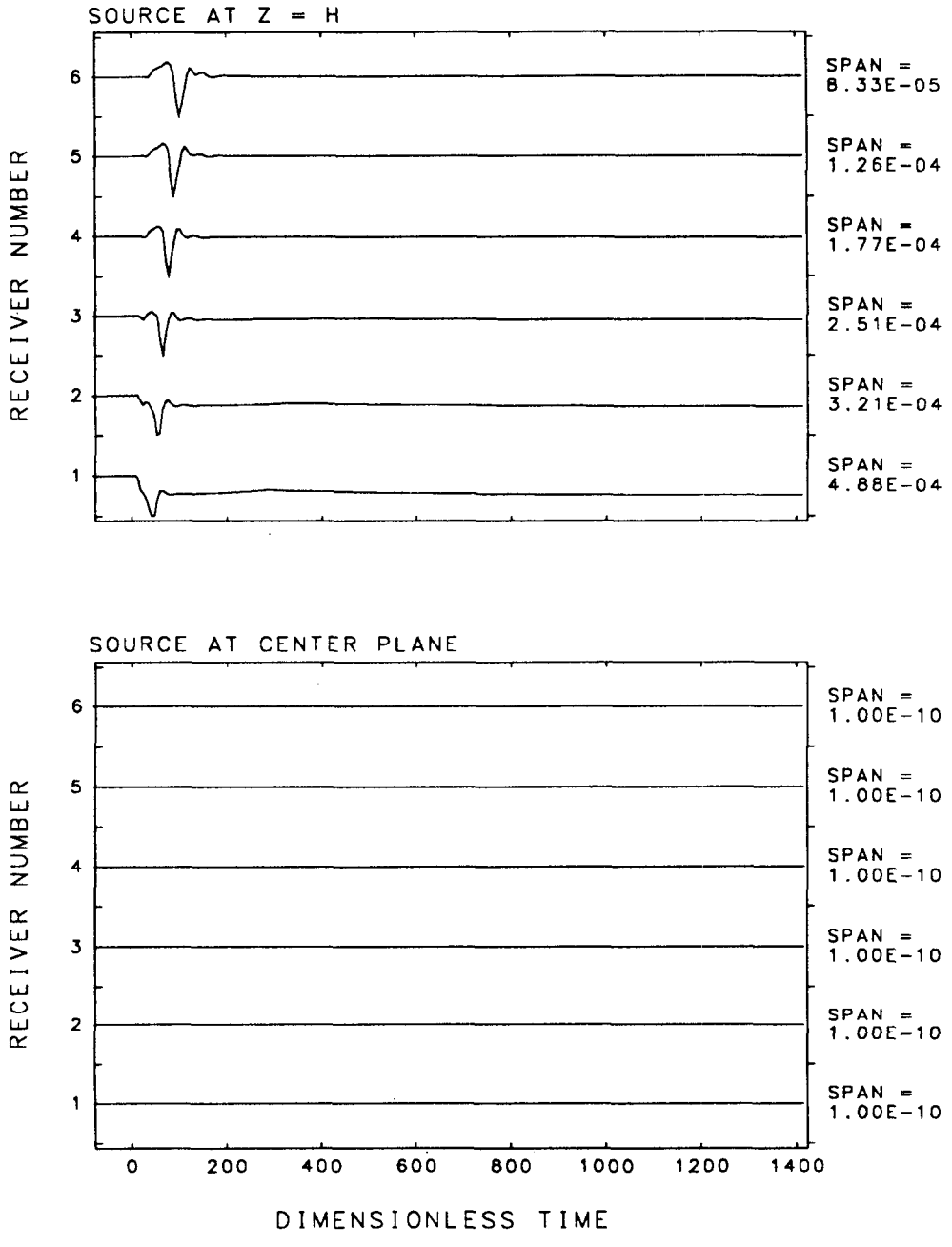

FIGURE C1.9 VERTICAL DISPLACEMENT RESPONSE AT CENTER PLANE DUE TO A Z - Z MOMENT

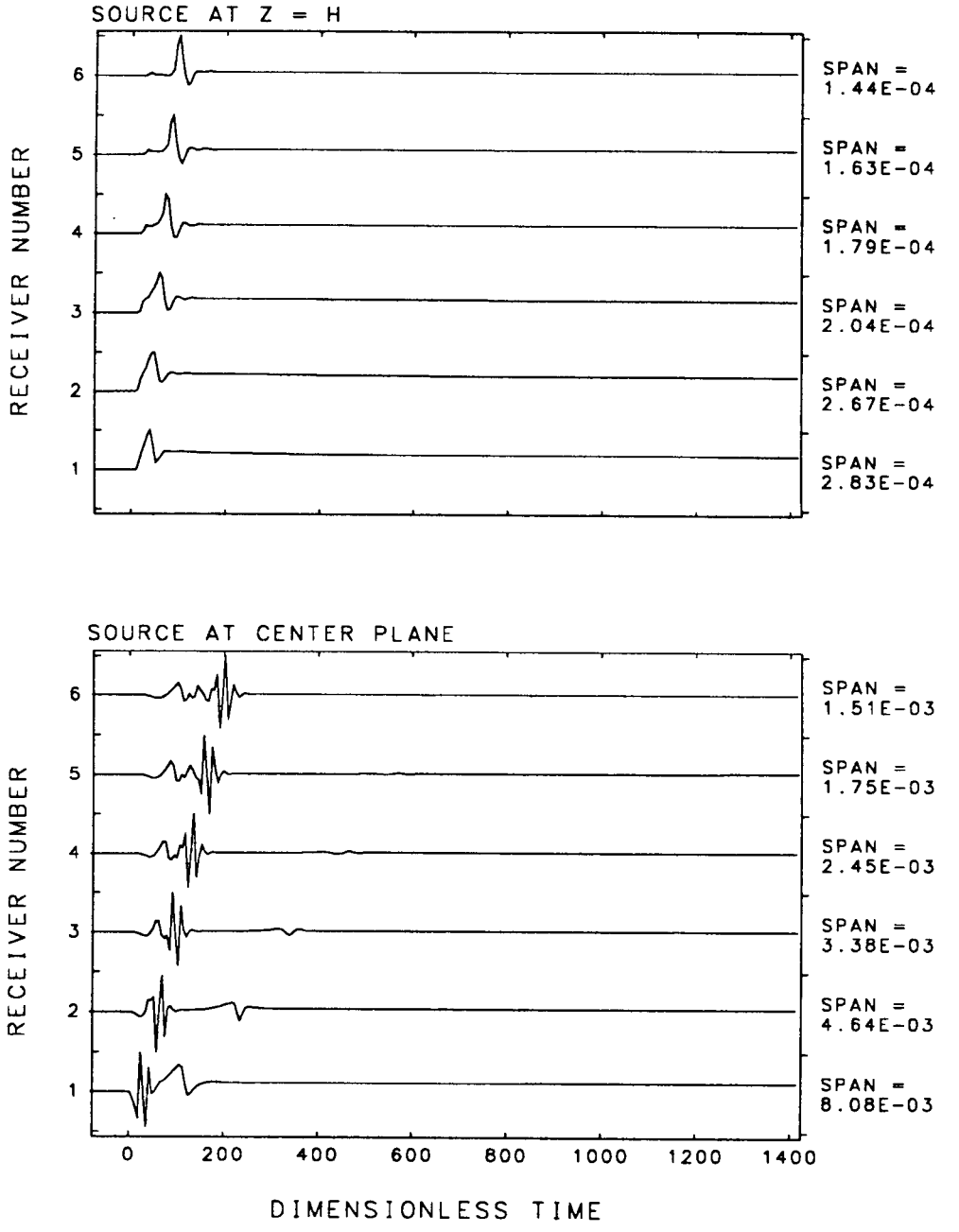

FIGURE C1.10 VERTICAL DISPLACEMENT RESPONSE
AT CENTER PLANE DUE TO A SYMMETRIC R-Z MOMENT

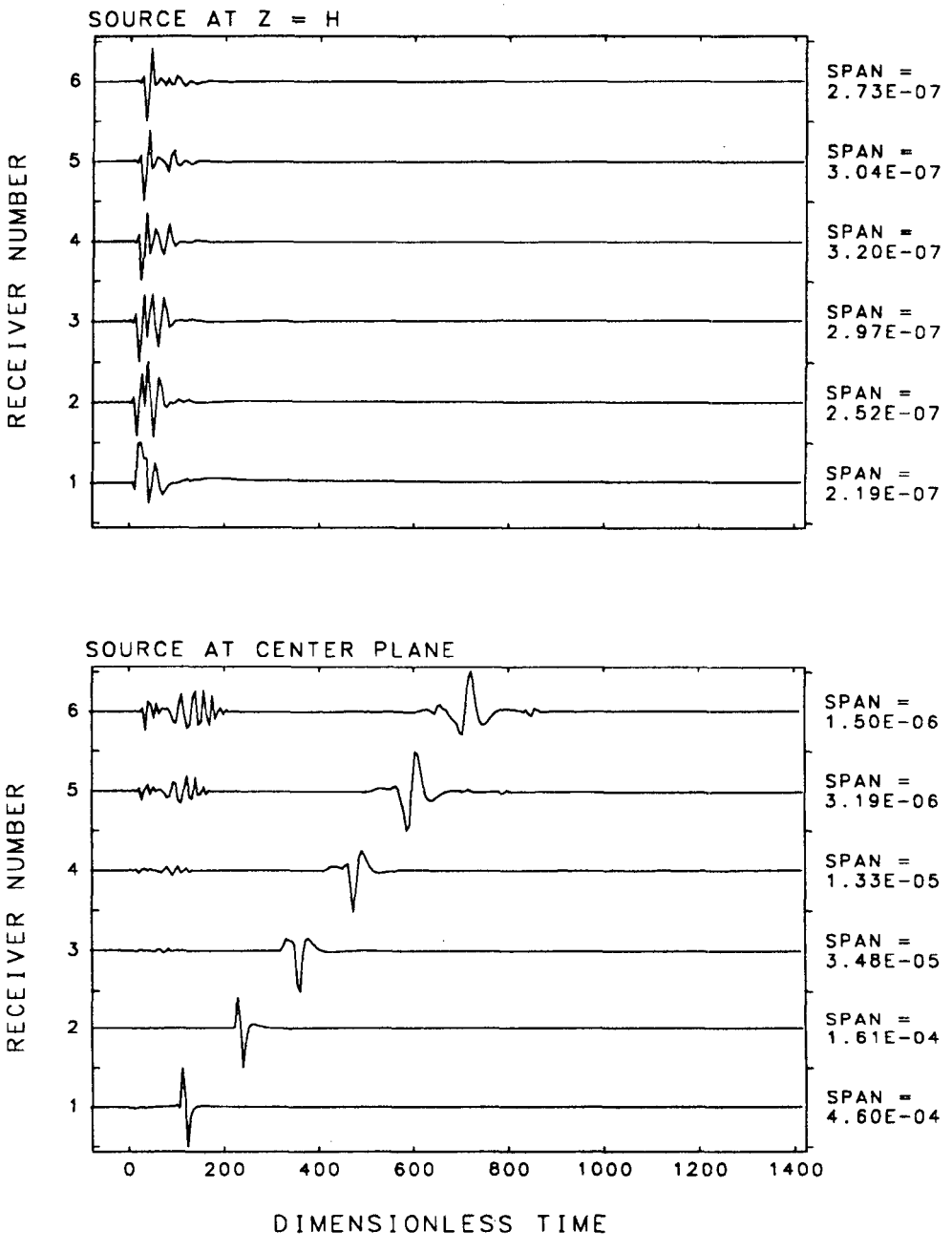

FIGURE C2.1 FLUID PARTIAL STRESS RESPONSE AT CENTER PLANE DUE TO AN R-R MOMENT

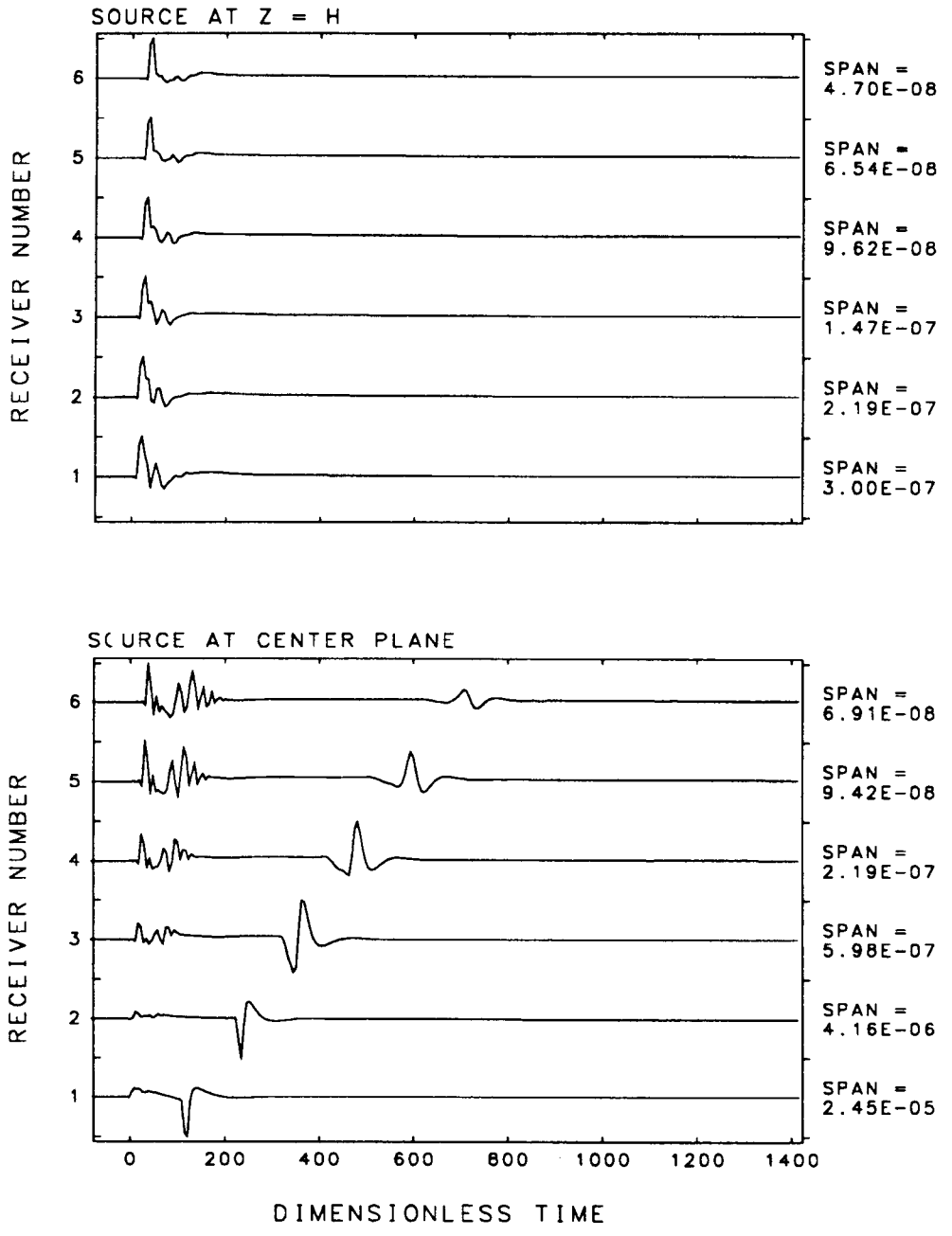

FIGURE C2.2 FLUID PARTIAL STRESS RESPONSE AT CENTER PLANE DUE TO A θ–θ MOMENT

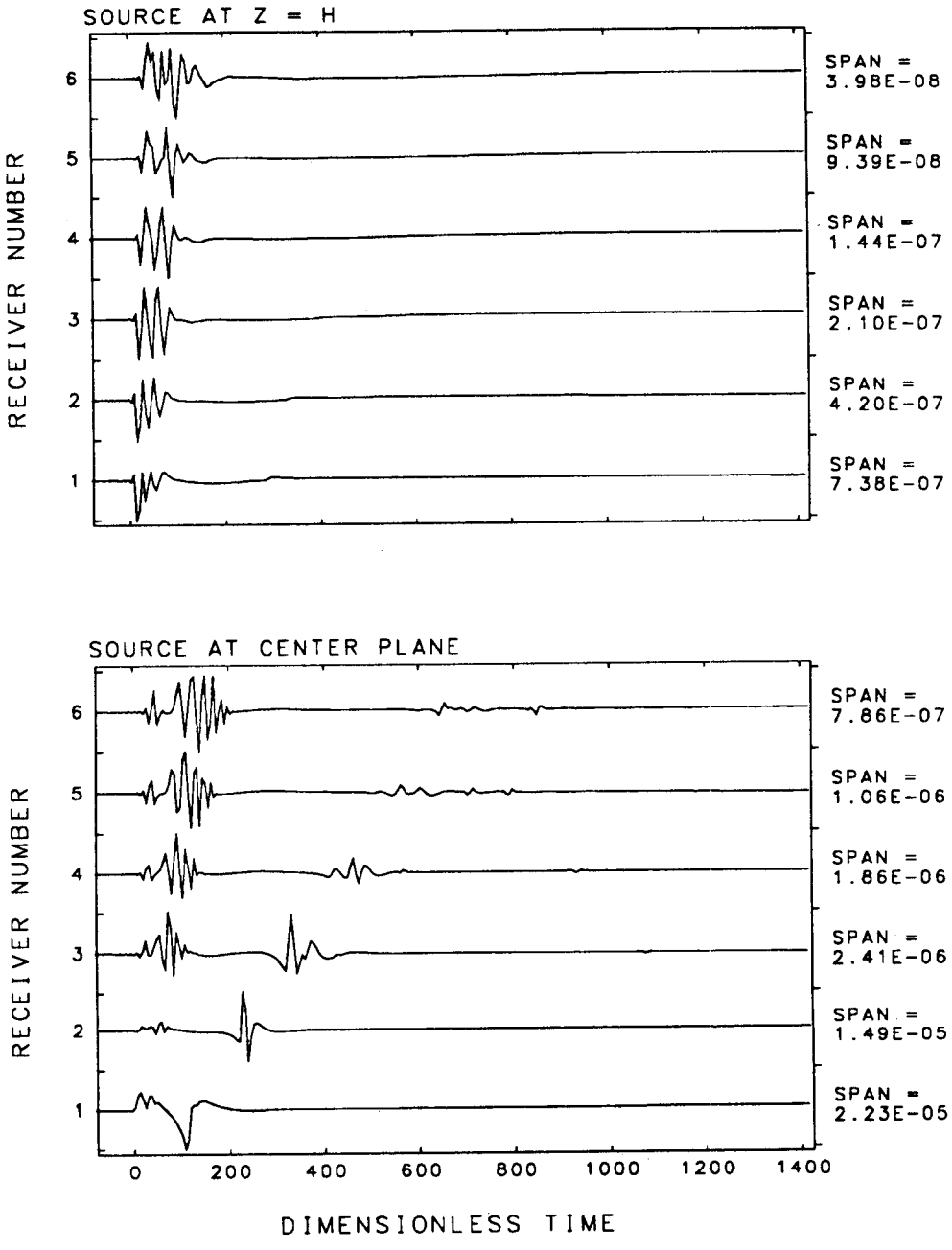

FIGURE C2.3 FLUID PARTIAL STRESS RESPONSE AT CENTER PLANE DUE TO A Z-Z MOMENT

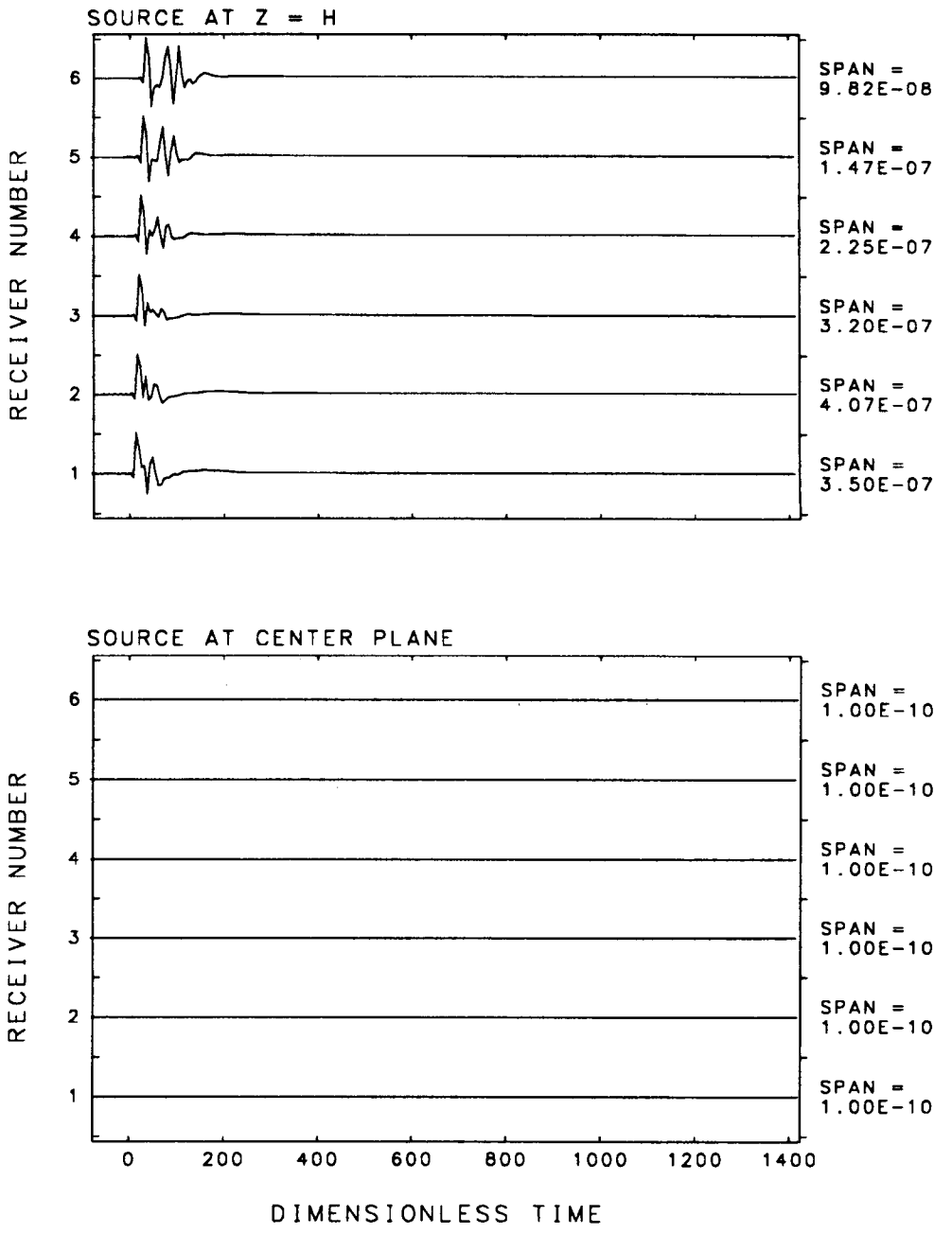

FIGURE C2.4 FLUID PARTIAL STRESS RESPONSE AT CENTER PLANE DUE TO A SYMMETRIC R-Z MOMENT

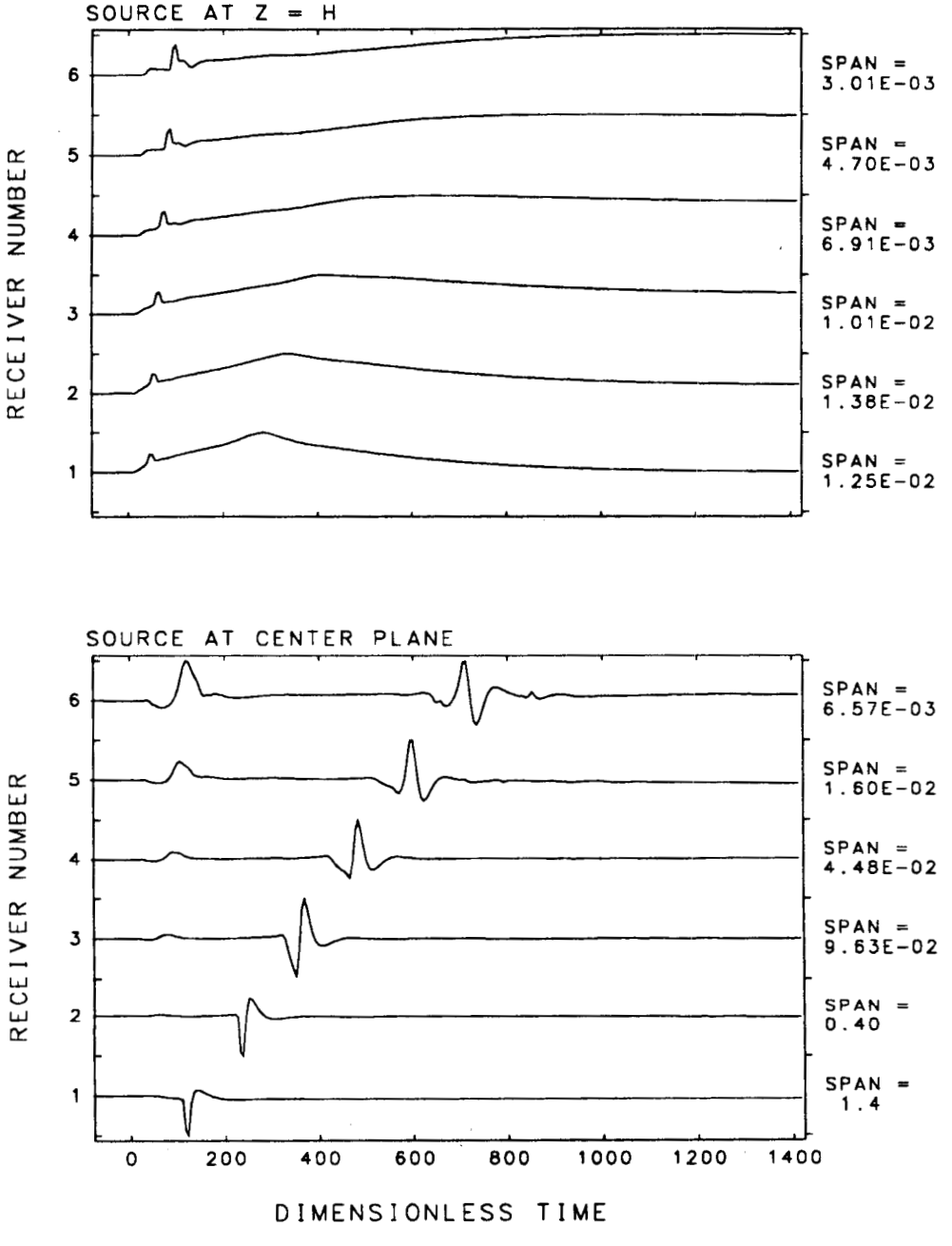

FIGURE C3.1 RADIAL DISPLACEMENT AT CENTER PLANE FOR AN ISOTROPIC FLUID MOMENT

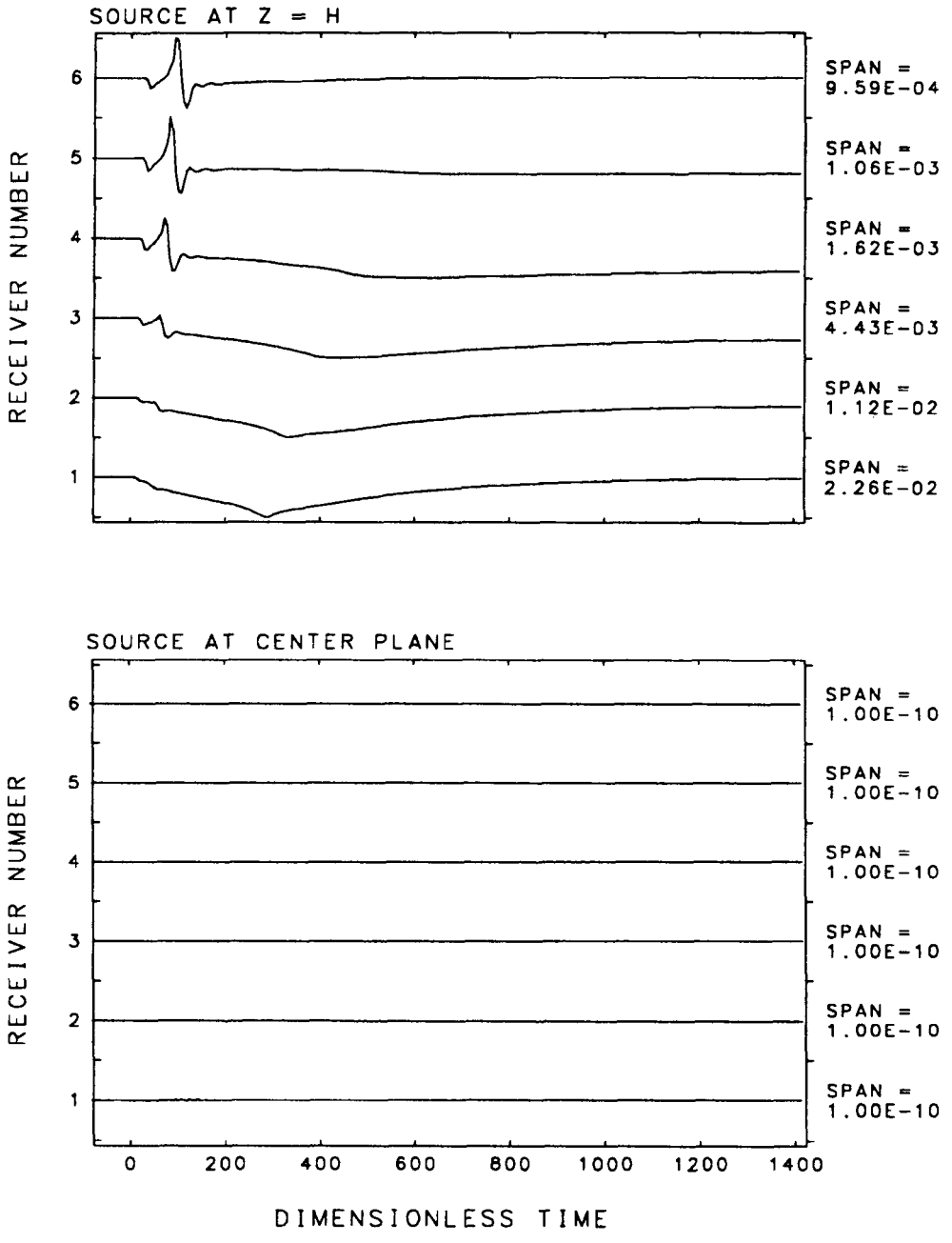

FIGURE C3.2 VERTICAL DISPLACEMENT RESPONSE AT CENTER PLANE FOR AN ISOTROPIC FLUID MOMENT

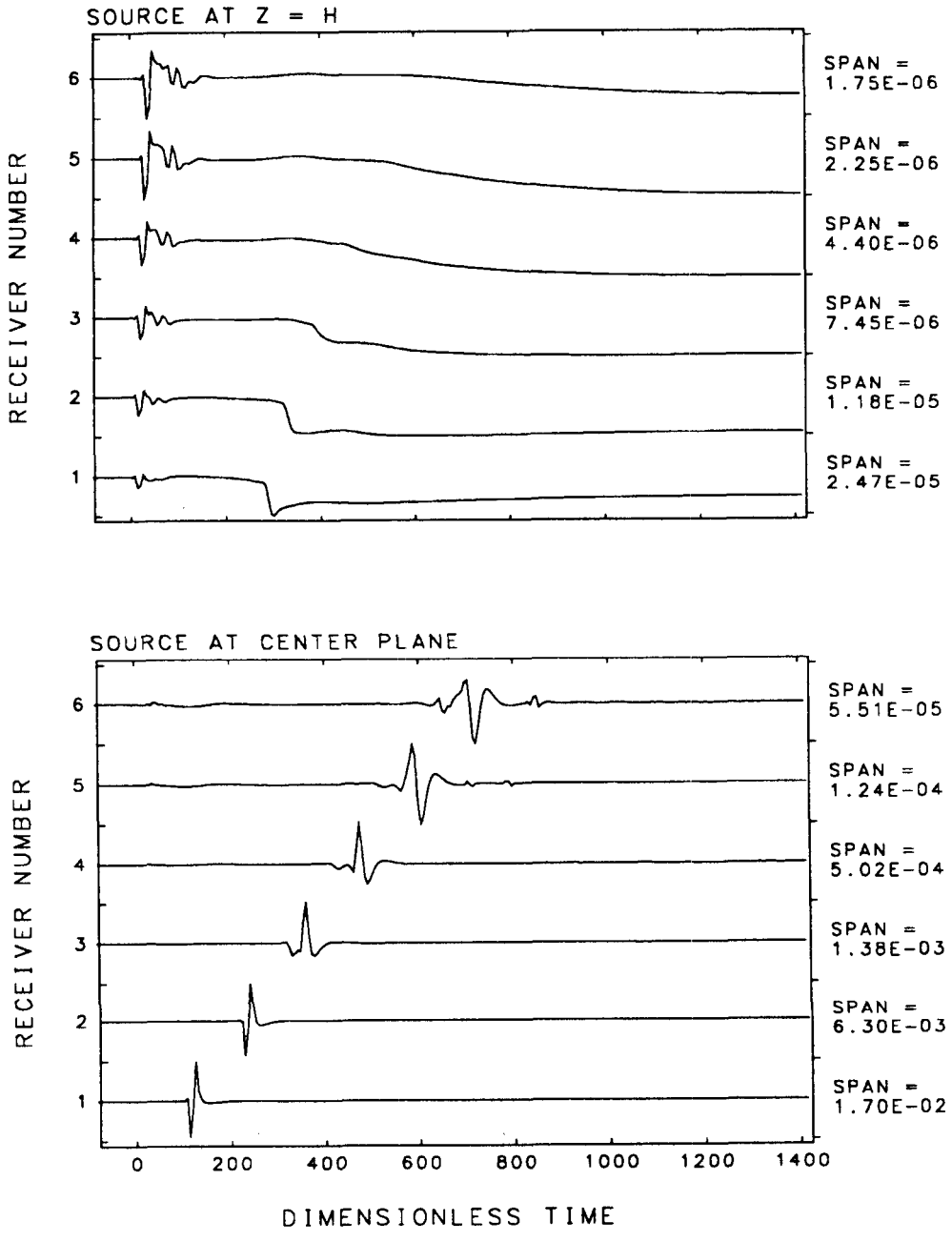

FIGURE C4 FLUID PARTIAL STRESS RESPONSE AT CENTER PLANE DUE TO AN ISOTROPIC FLUID MOMENT

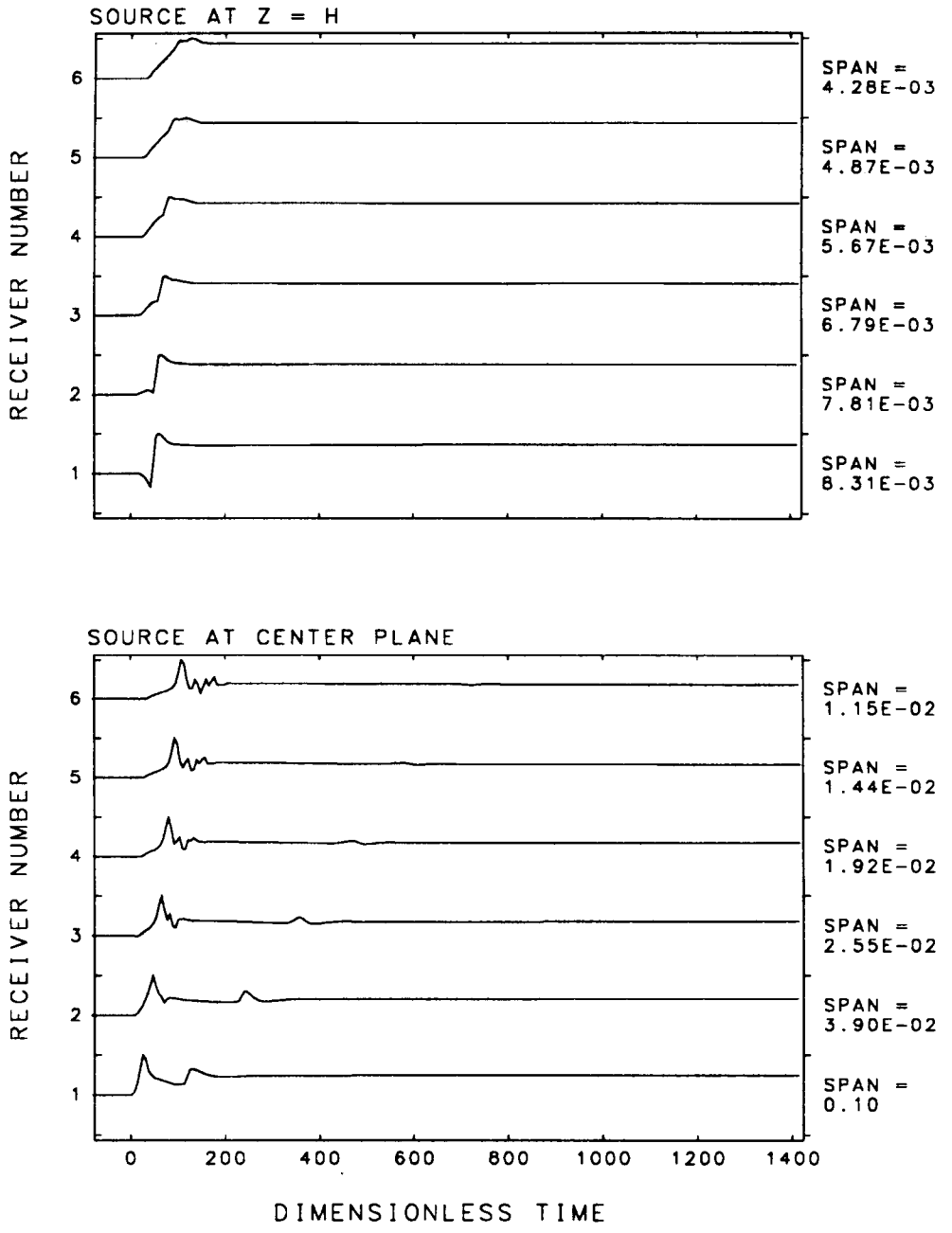

FIGURE C5.1 RADIAL DISPLACEMENT RESPONSE
AT CENTER PLANE FOR A RADIAL POINT LOAD

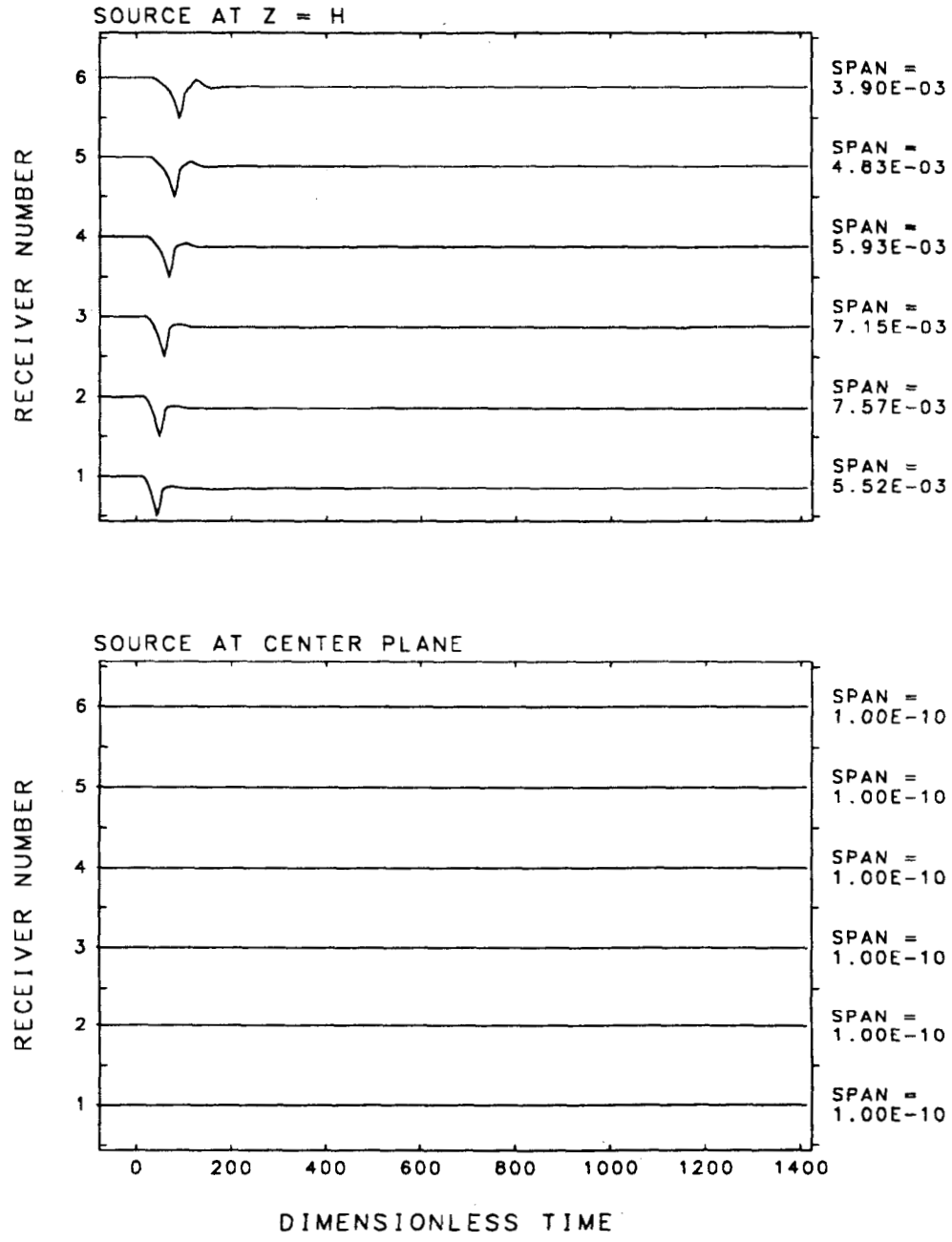

FIGURE C5.2 RADIAL DISPLACEMENT RESPONSE AT CENTER PLANE TO A VERTICAL POINT LOAD

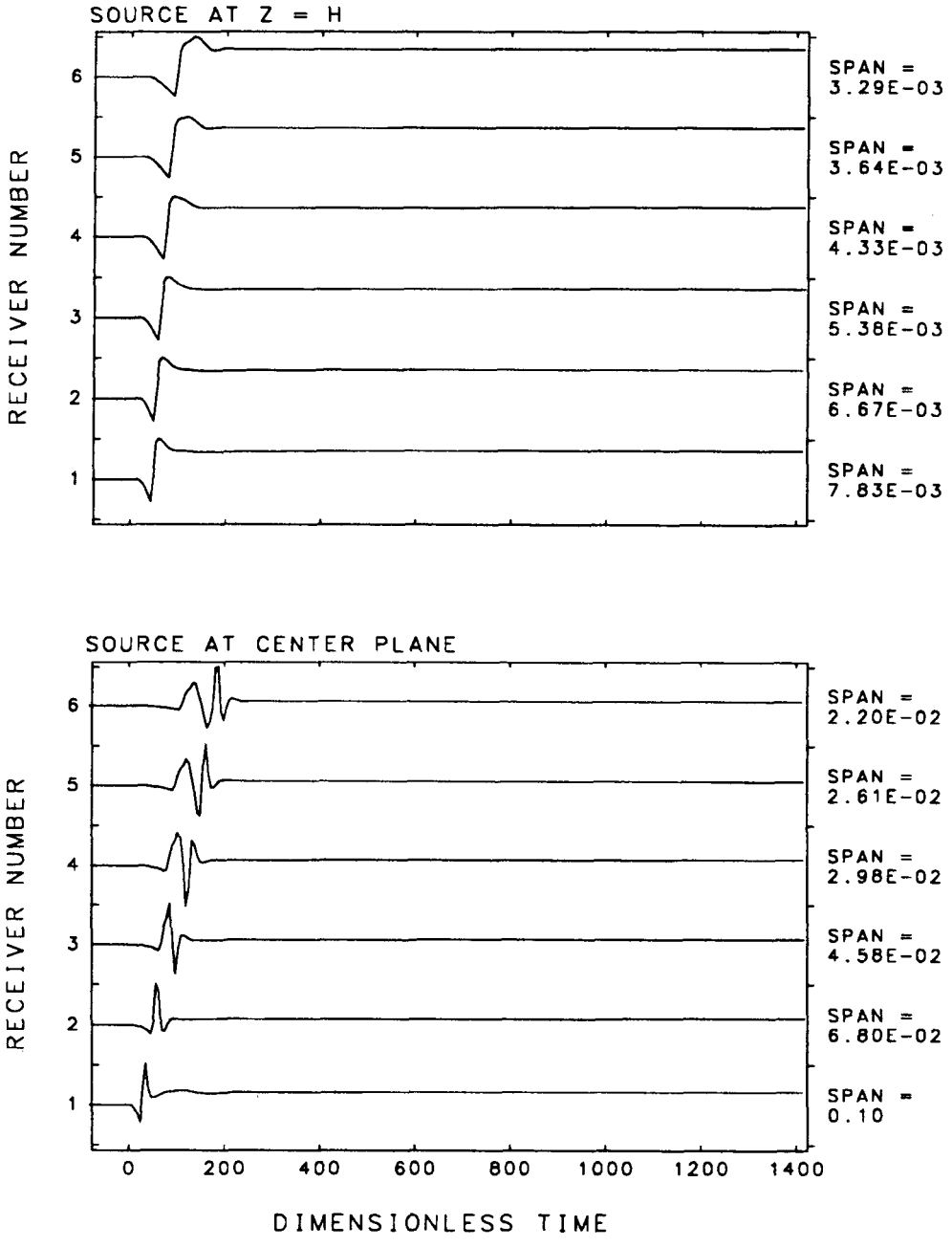

FIGURE C5.3 TRANSVERSE HORIZONTAL DISPLACEMENT RESPONSE AT CENTER PLANE TO A TRANSVERSE POINT LOAD

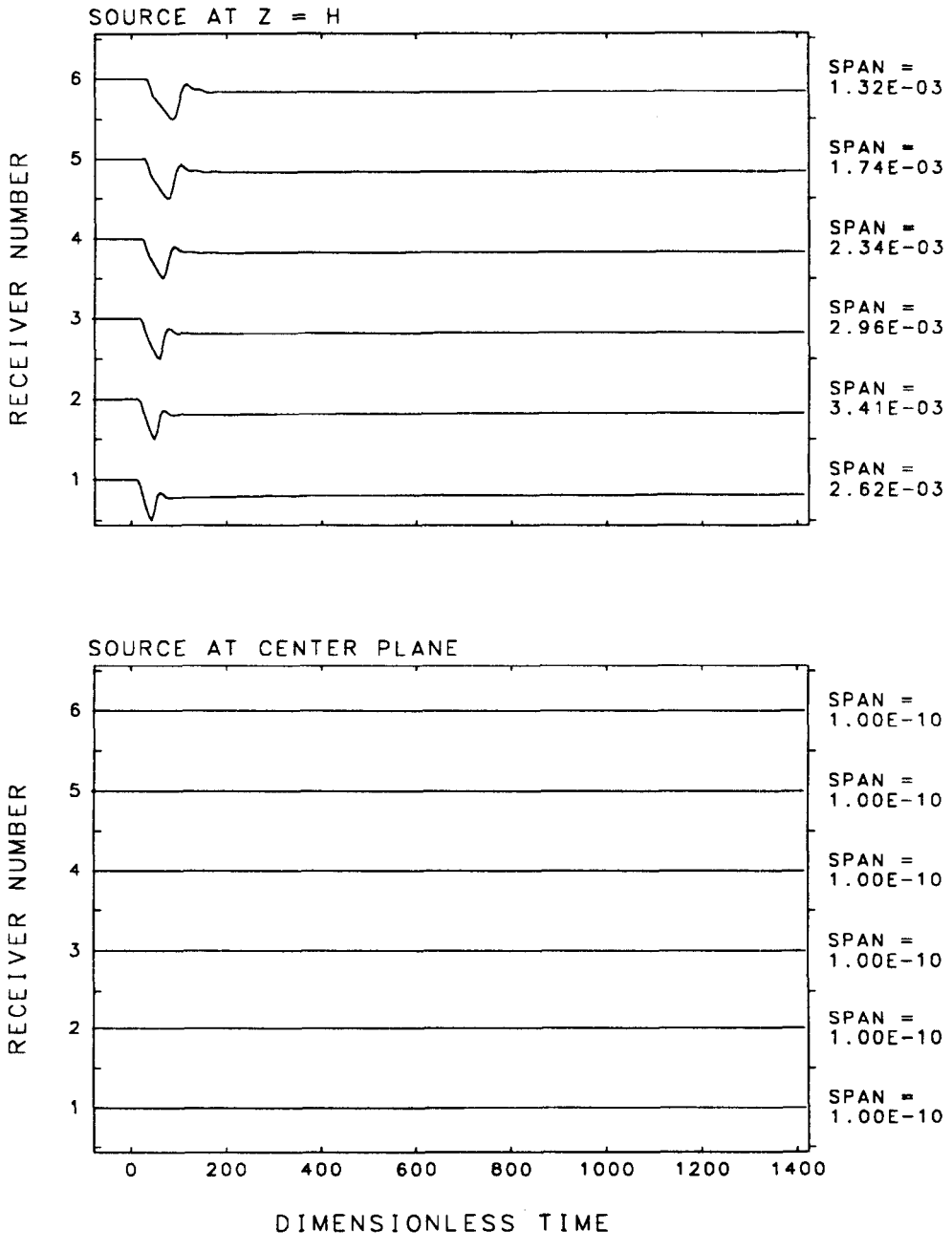

FIGURE C5.4 VERTICAL DISPLACEMENT RESPONSE AT CENTER PLANE TO A RADIAL POINT LOAD

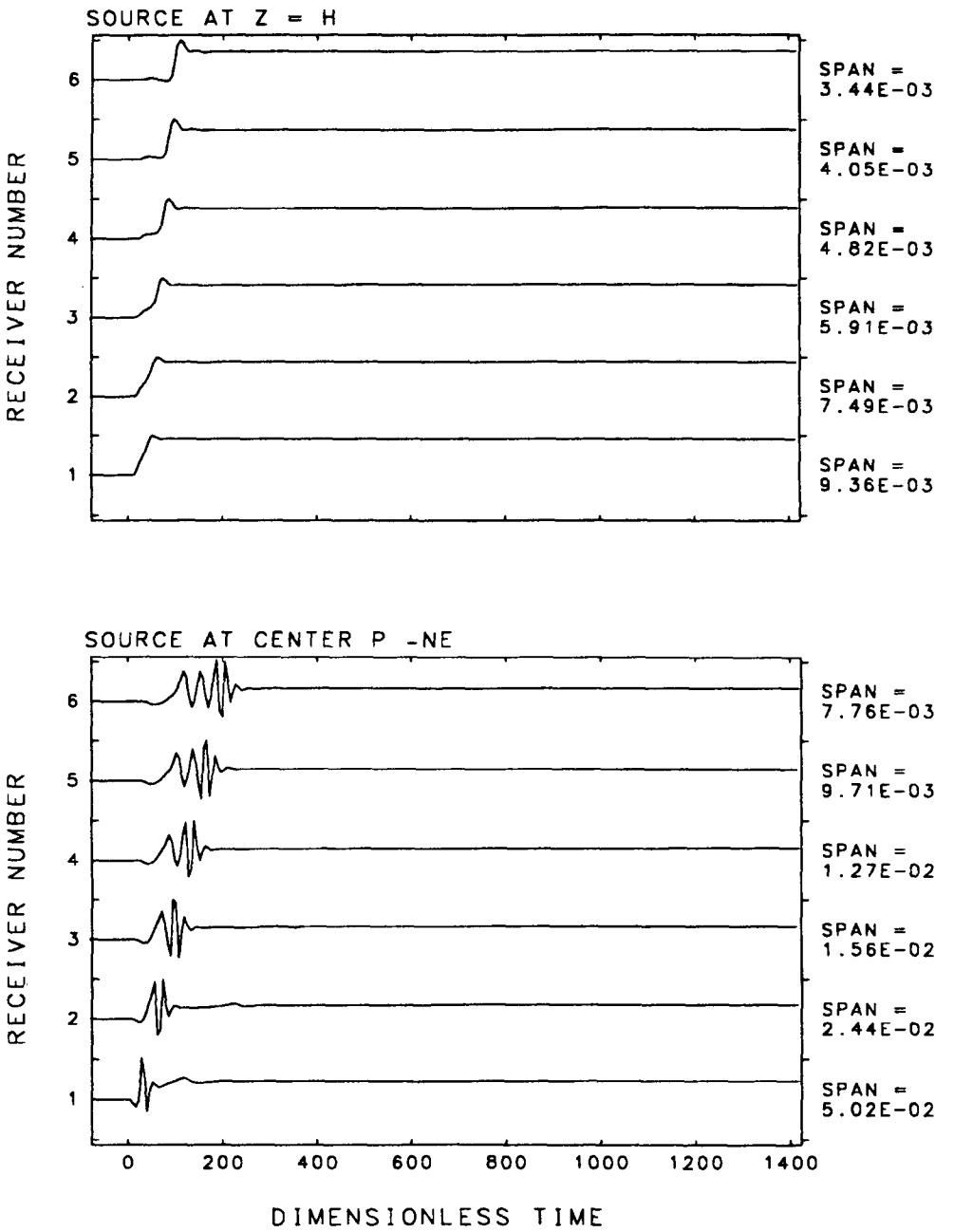

FIGURE C5.5 VERTICAL DISPLACEMENT RESPONSE AT CENTER PLANE TO A VERTICAL POINT LOAD

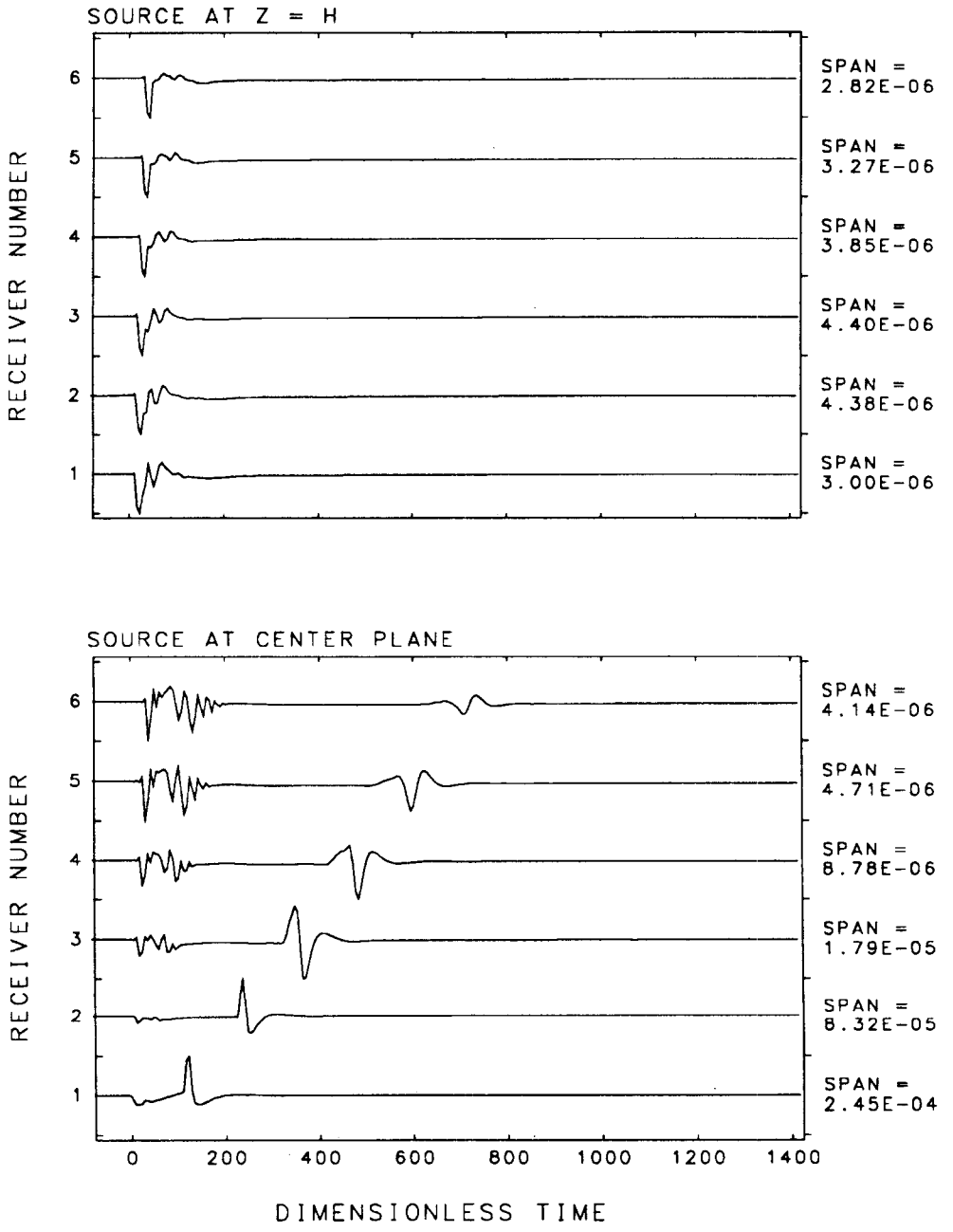

FIGURE C6.1 FLUID PARTIAL STRESS RESPONSE AT CENTER PLANE TO A RADIAL POINT LOAD

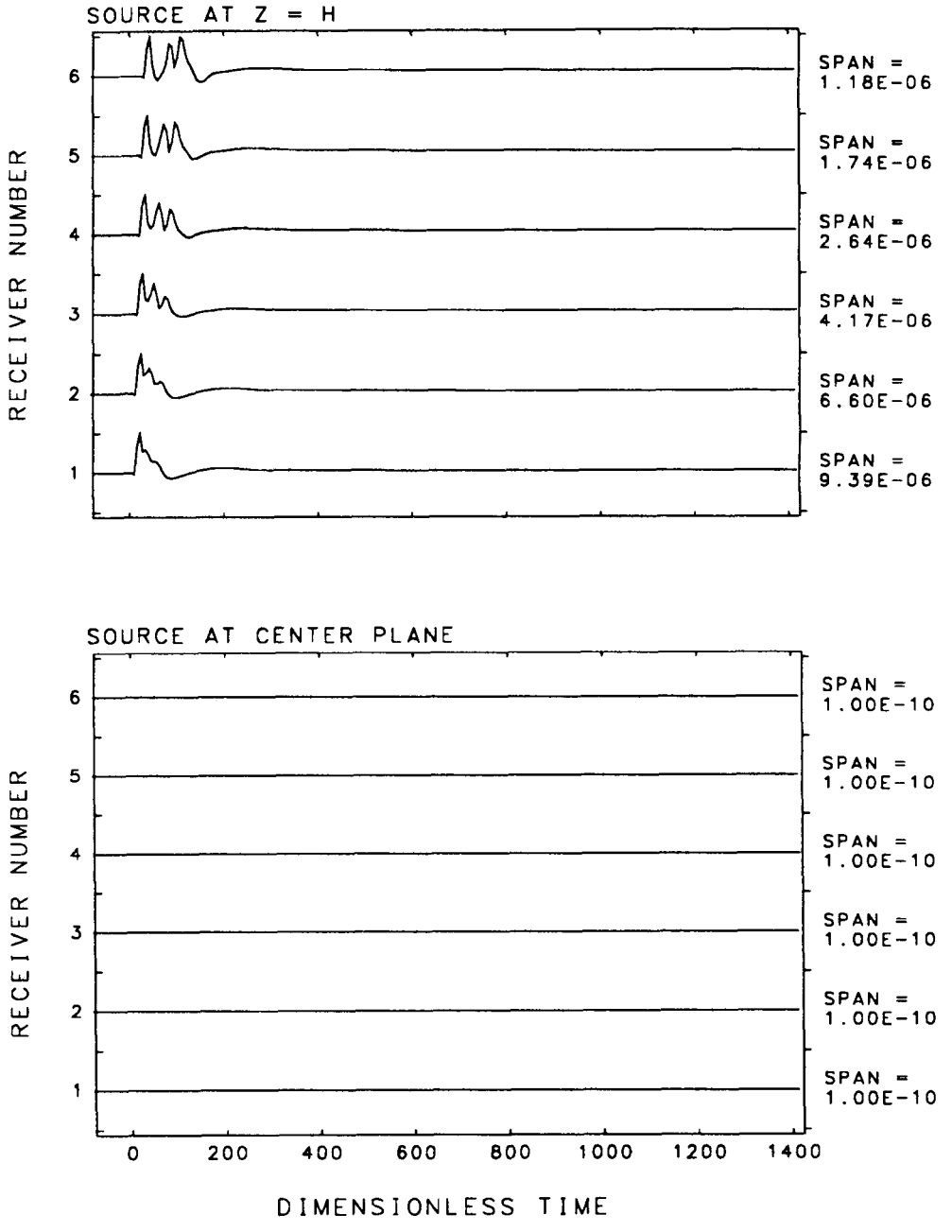

FIGURE C6.2 FLUID PARTIAL STRESS RESPONSE AT CENTER PLANE TO A VERTICAL POINT LOAD

Appendix D:
Solid Region Displacement Responses
Along a Vertical Line at Radial Offset 10

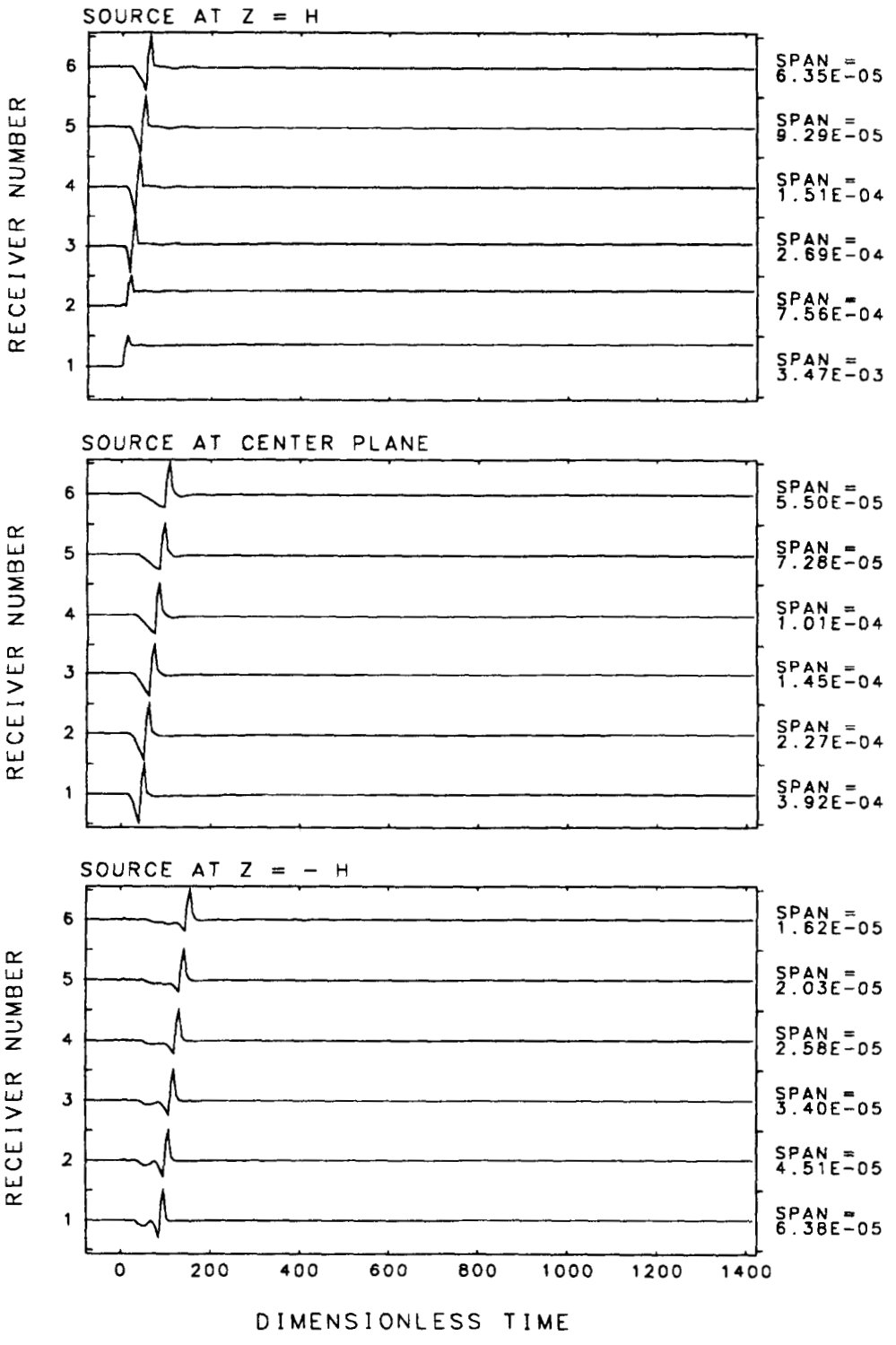

FIGURE D1.1 RADIAL DISPLACEMENT RESPONSE OF SOLID REGION FOR A UNIT R-R MOMENT

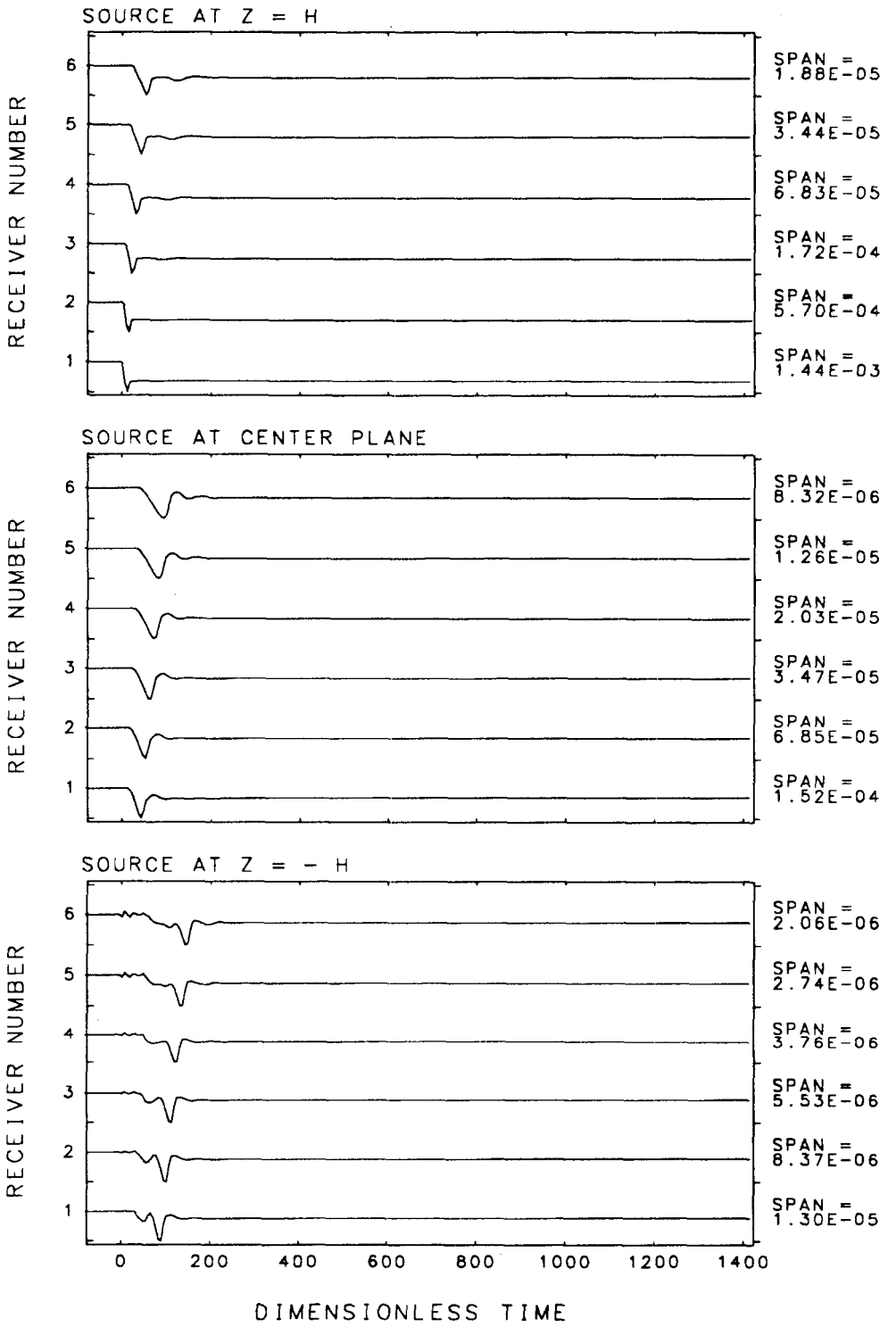

FIGURE D1.2 RADIAL DISPLACMENT RESPONSE OF SOLID REGION FOR A UNIT θ–θ MOMENT

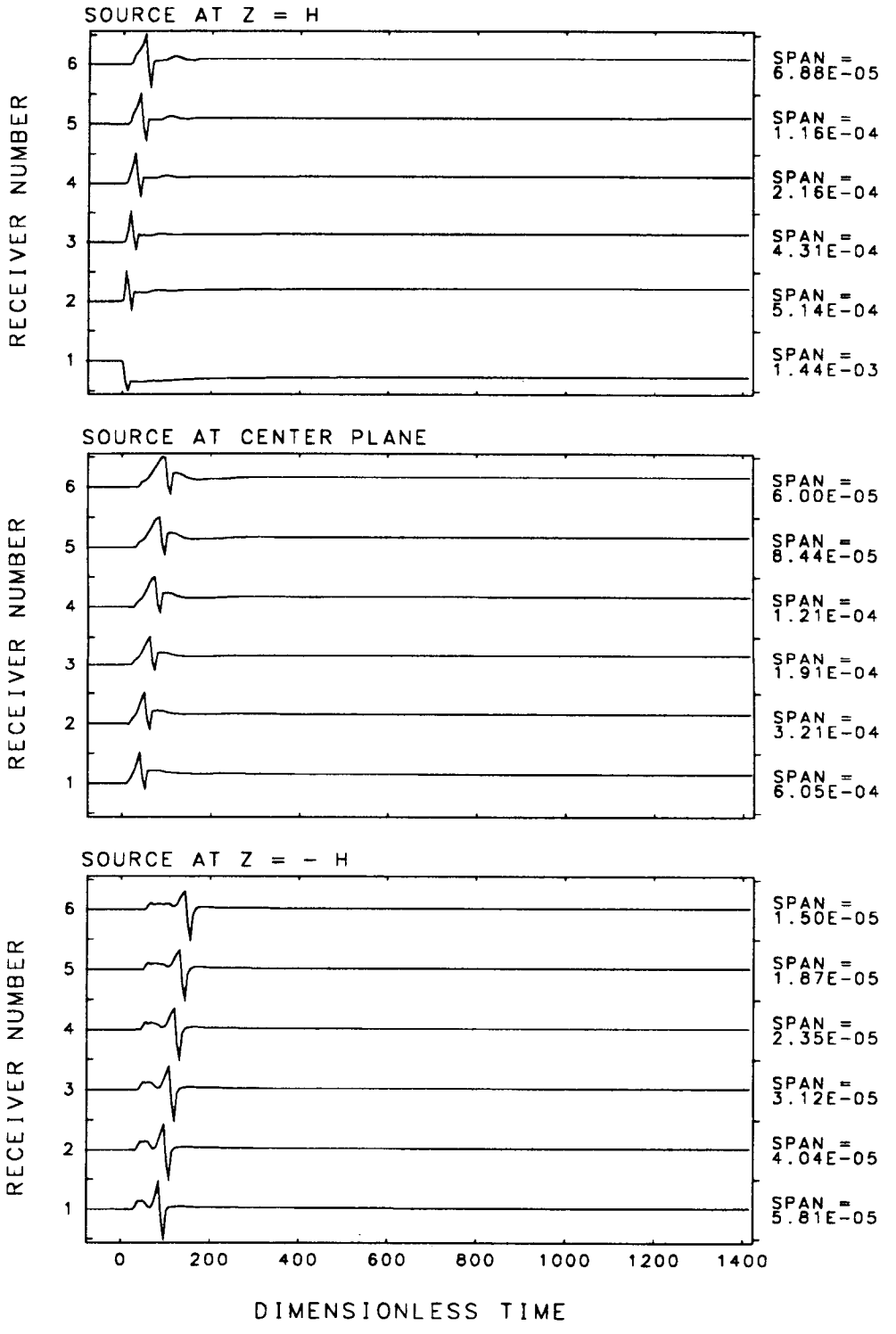

FIGURE D1.3 RADIAL DISPLACEMENT RESPONSE OF SOLID REGION FOR A UNIT Z-Z MOMENT

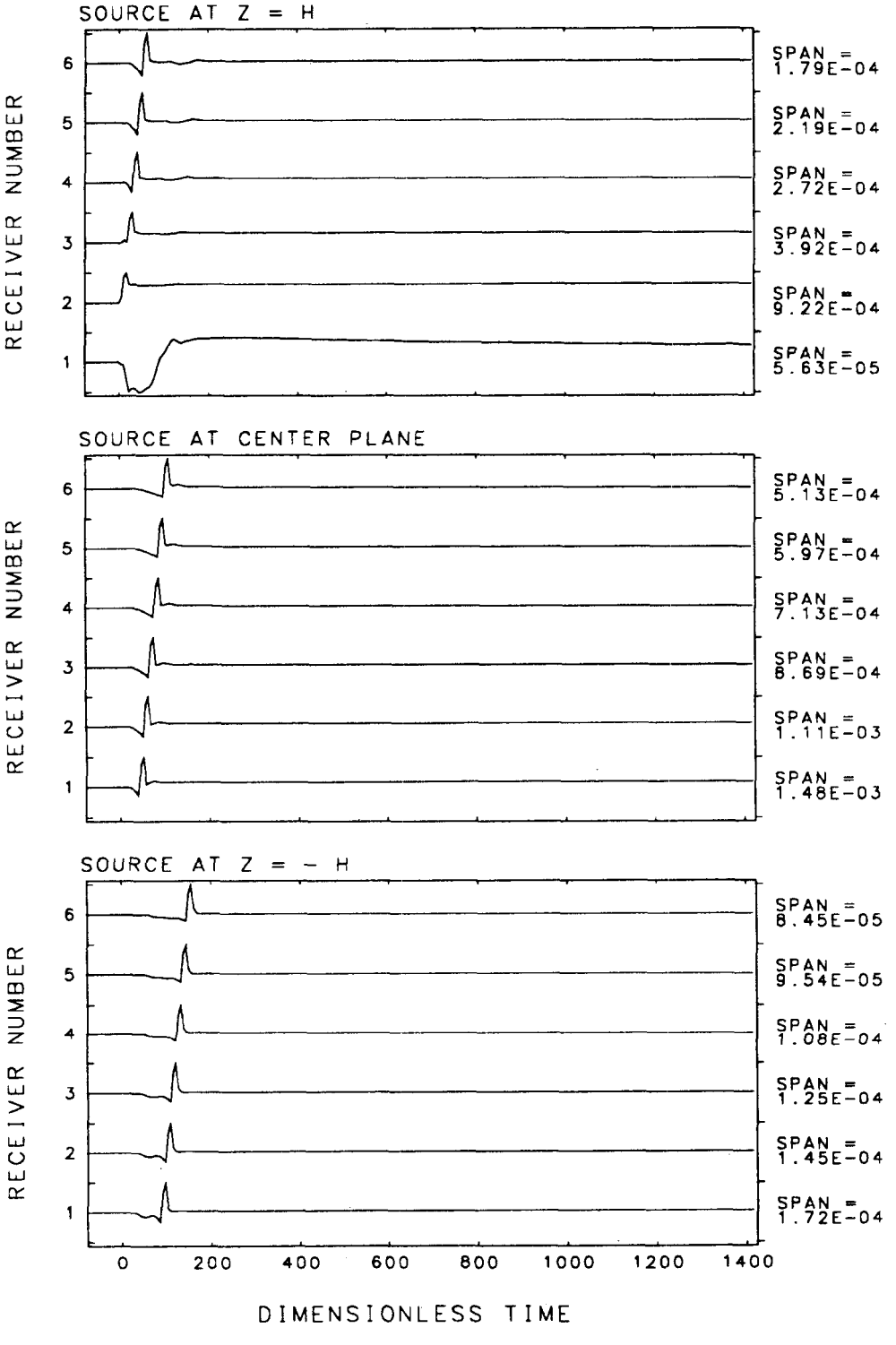

FIGURE D1.4 RADIAL DISPLACEMENT RESPONSE OF SOLID REGION FOR A UNIT SYMMETRIC R-Z MOMENT

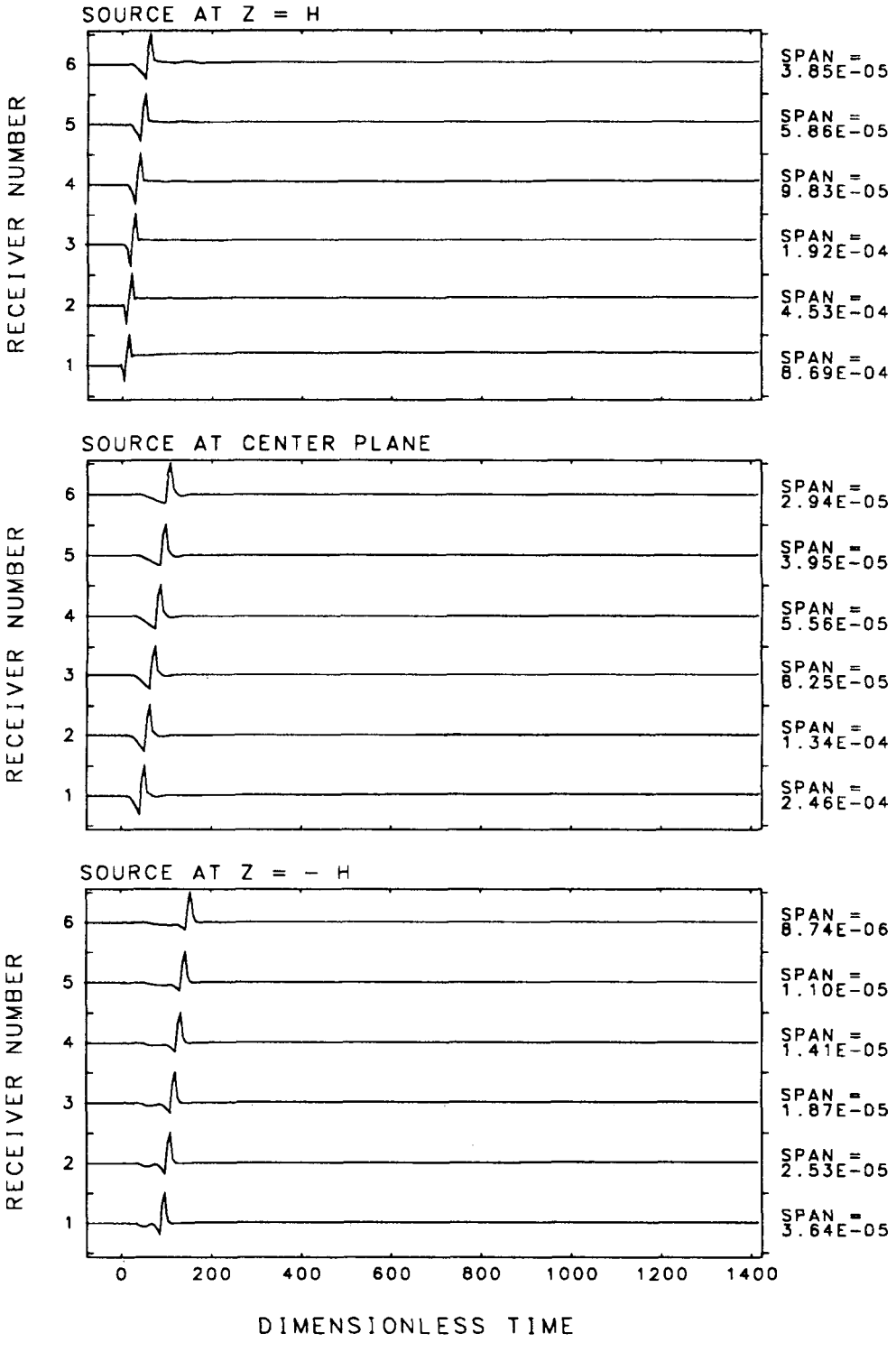

FIGURE D1.5 TRANSVERSE HORIZONTAL DISPLACEMENT RESPONSE OF SOLID REGION TO A UNIT SYMMETRIC R-θ MOMENT

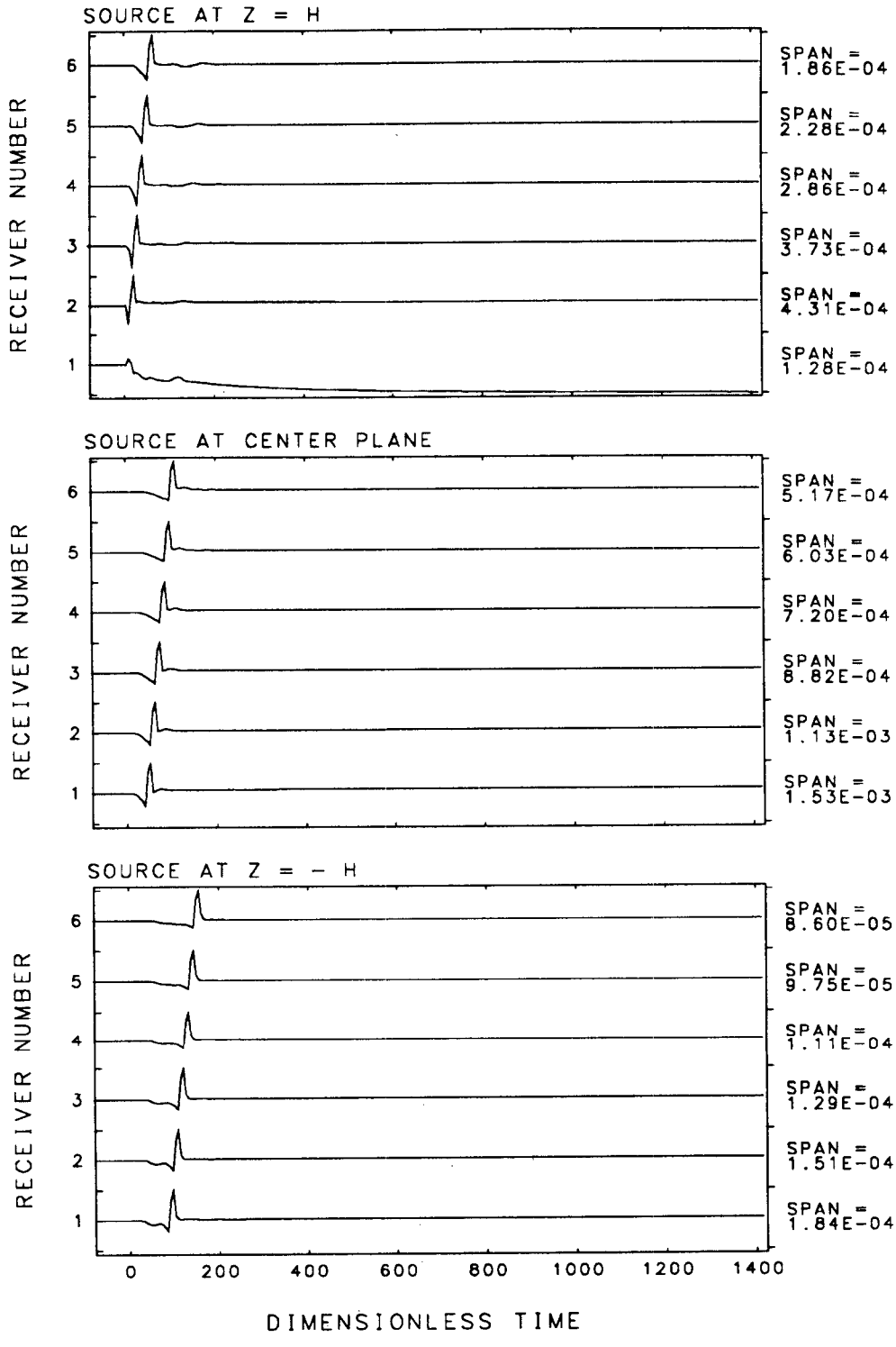

FIGURE D1.6 TRANSVERSE HORIZONTAL DISPLACEMENT RESPONSE OF SOLID REGION TO A UNIT SYMMETRIC θ-Z MOMENT

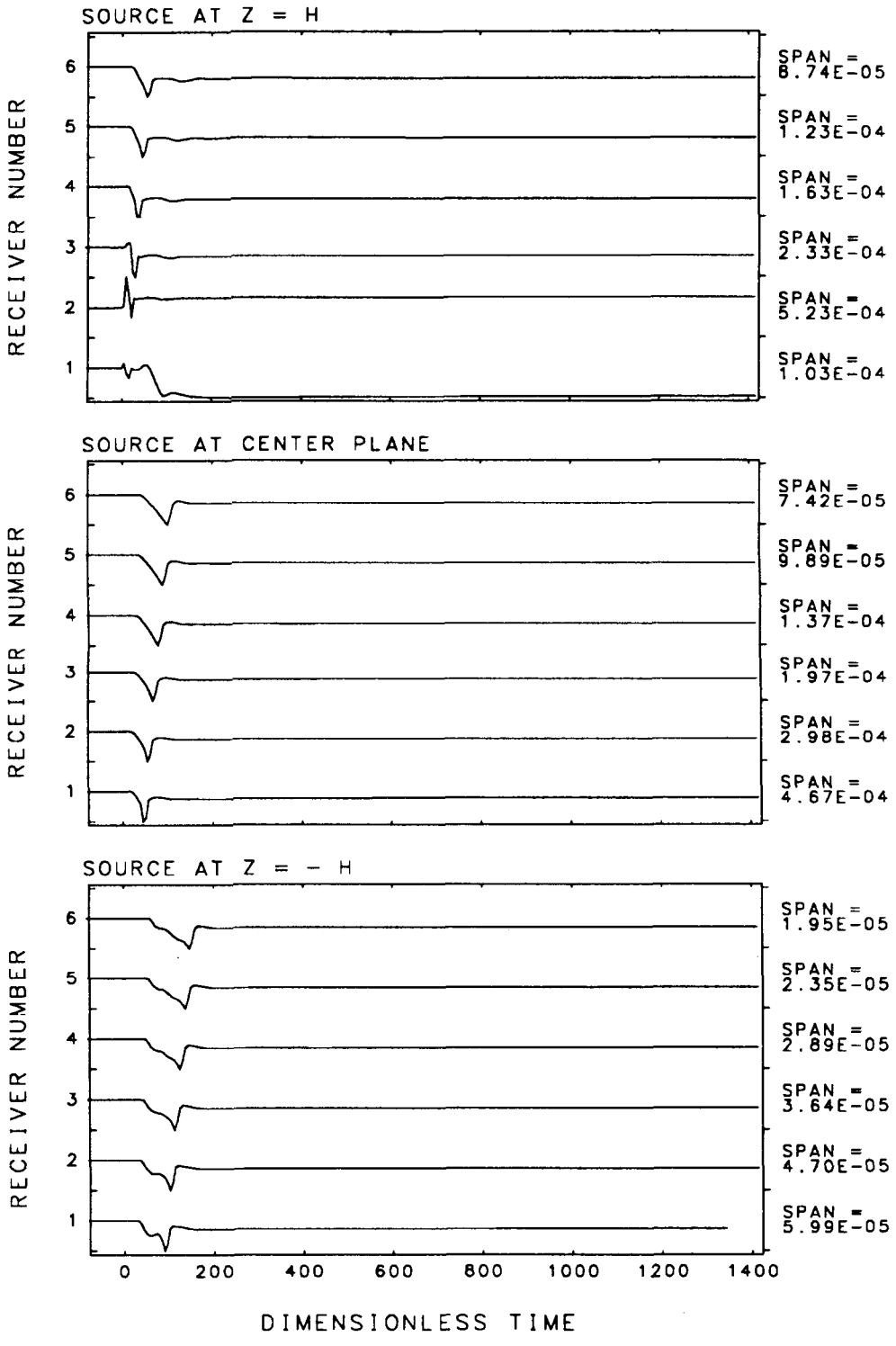

FIGURE D1.7 VERTICAL DISPLACEMENT RESPONSE OF SOLID REGION TO A UNIT R-R MOMENT

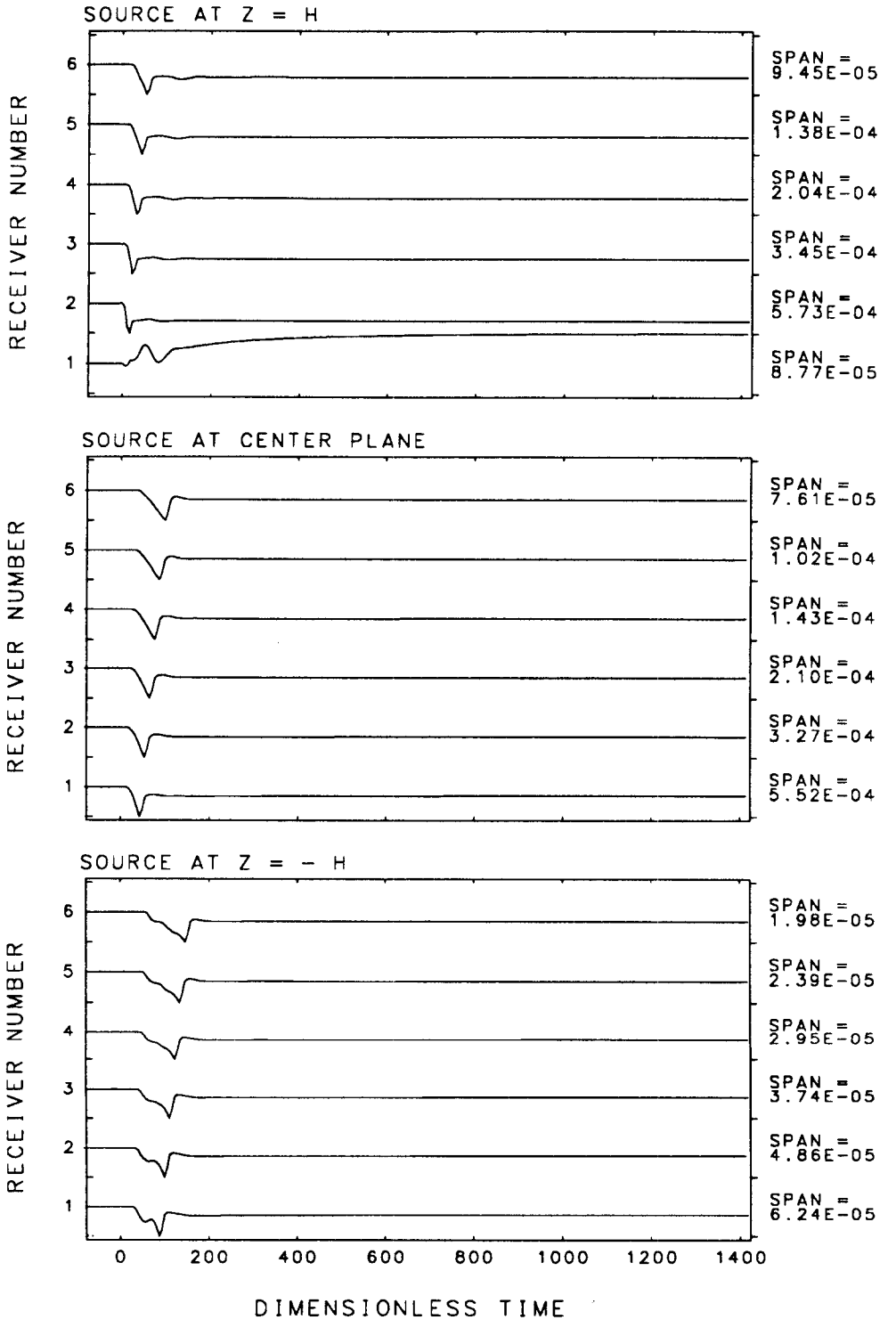

FIGURE D1.8 VERTICAL DISPLACEMENT RESPONSE OF SOLID REGION TO A UNIT θ–θ MOMENT

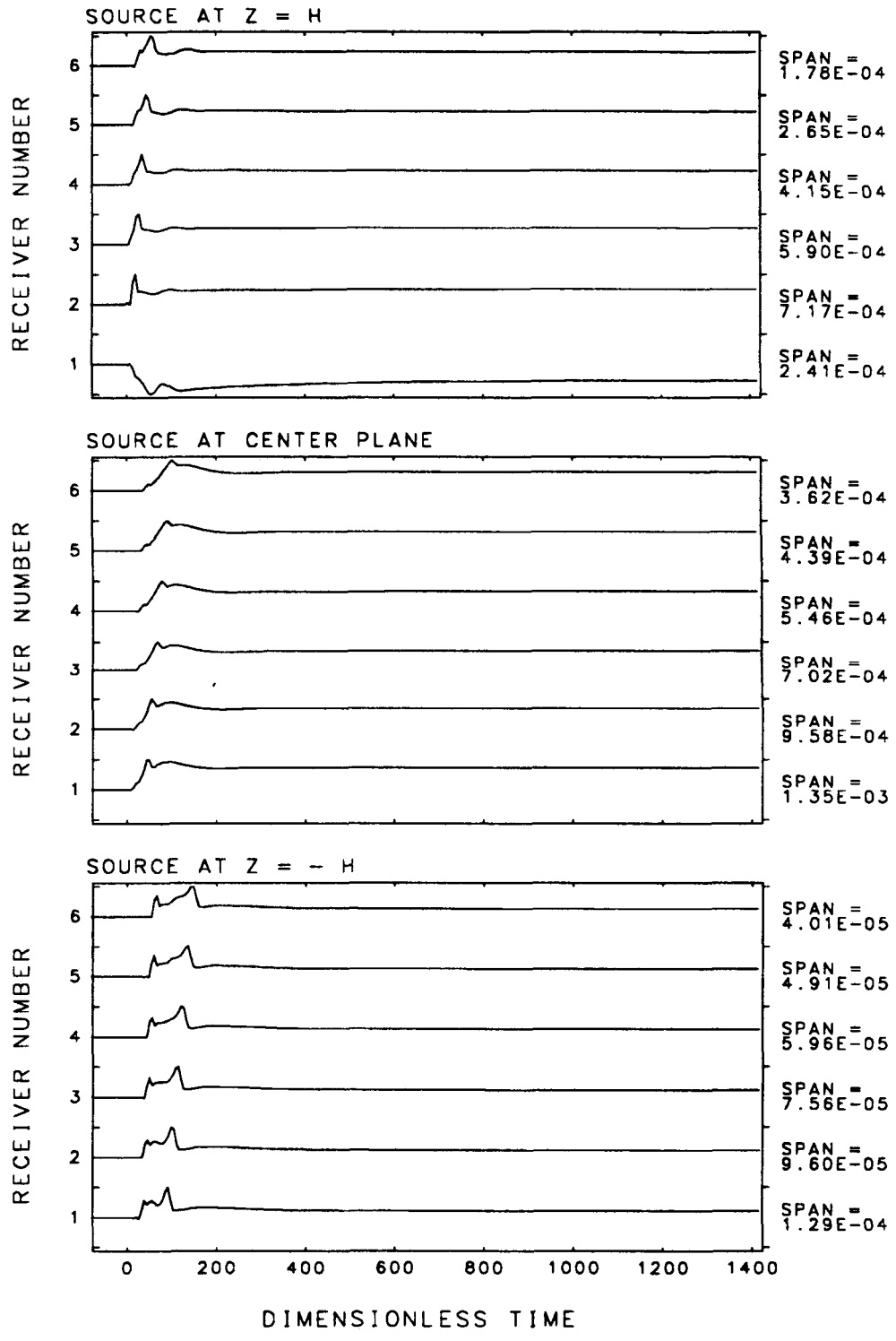

FIGURE D1.9 VERTICAL DISPLACEMENT RESPONSE OF SOLID REGION FOR A UNIT Z-Z MOMENT

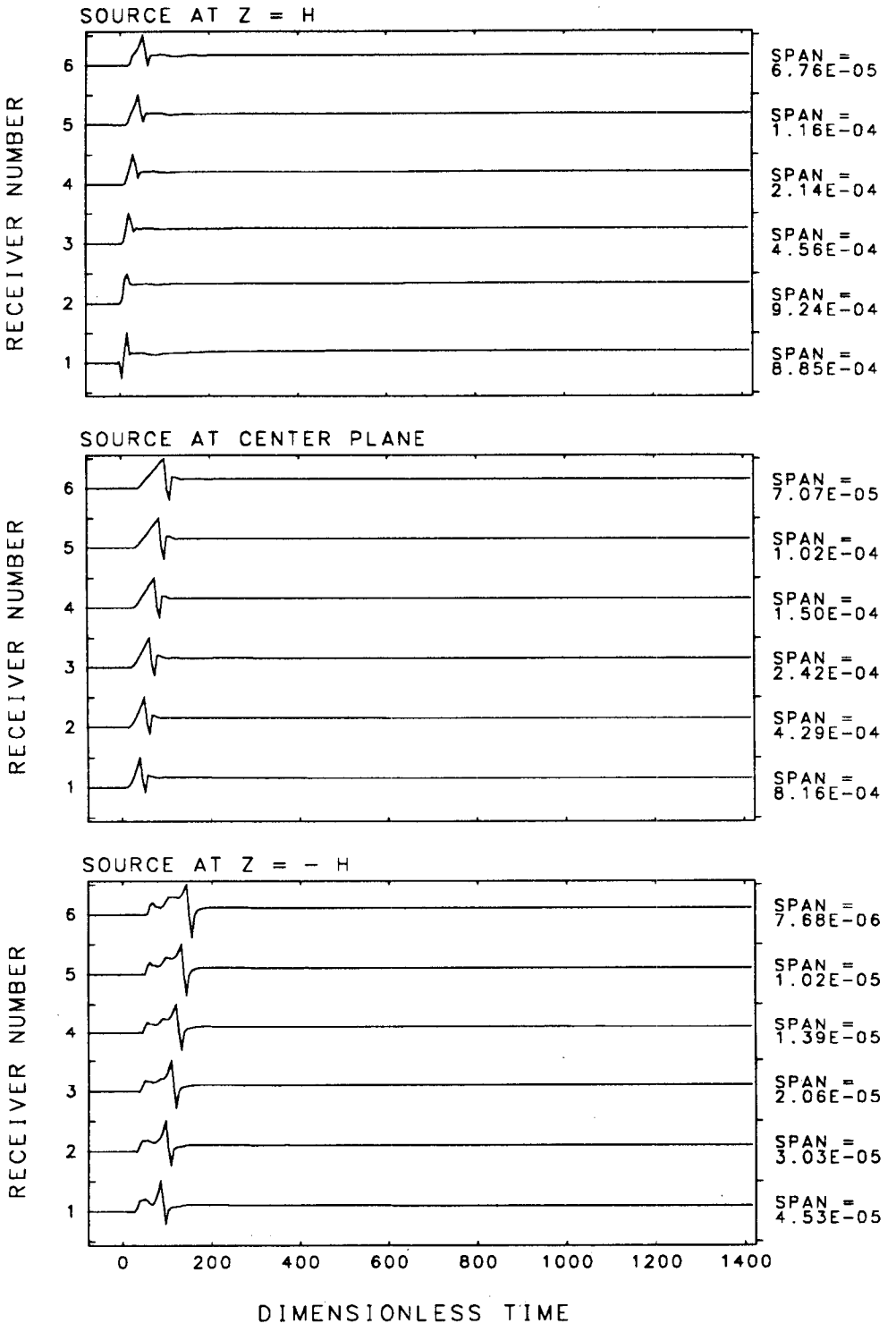

FIGURE D1.10 VERTICAL DISPLACEMENT RESPONSE OF SOLID REGION TO A UNIT SYMMETRIC Z-R MOMENT

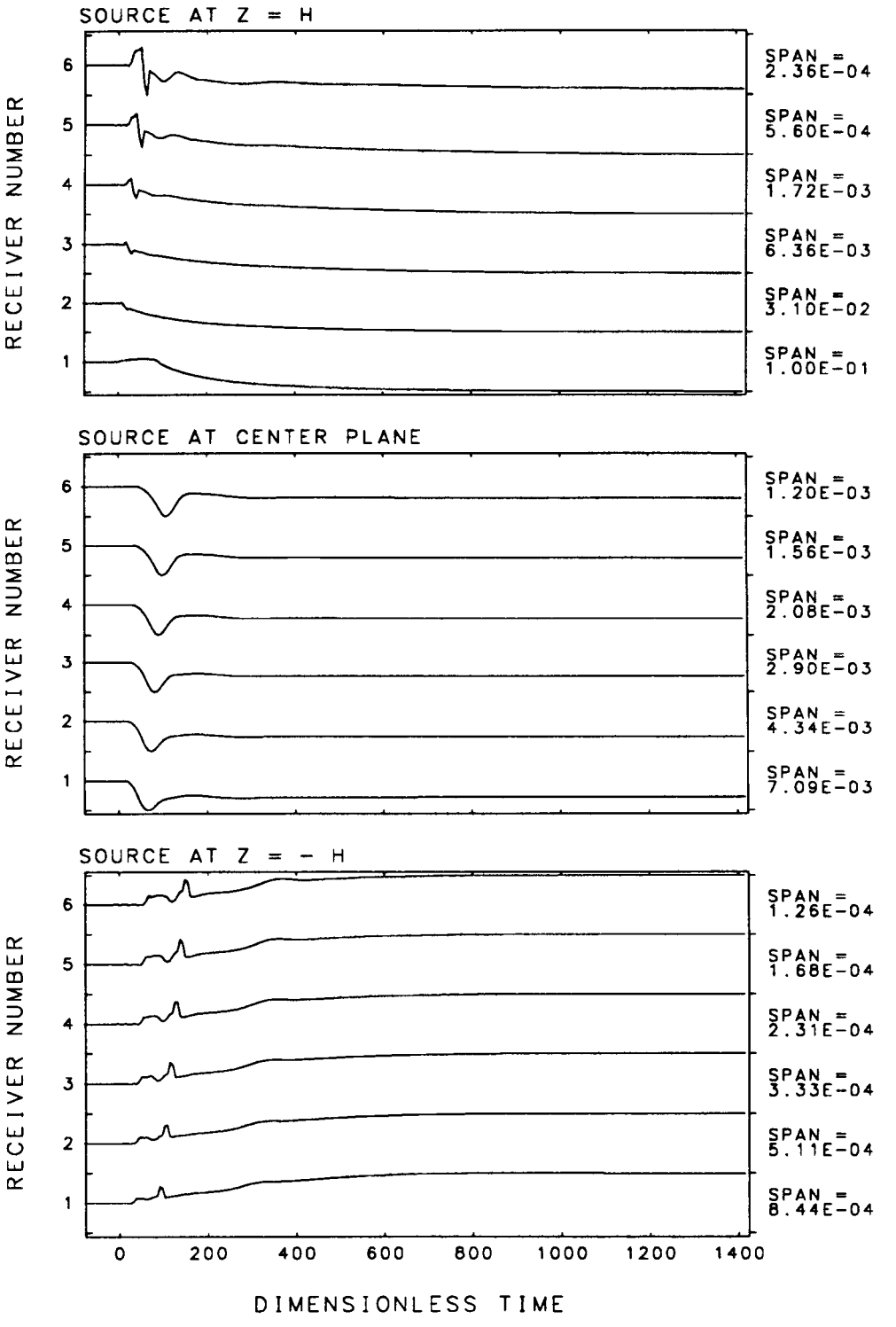

FIGURE D2.1 RADIAL DISPLACEMENT RESPONSE OF SOLID REGION TO A UNIT ISOTROPIC FLUID MOMENT

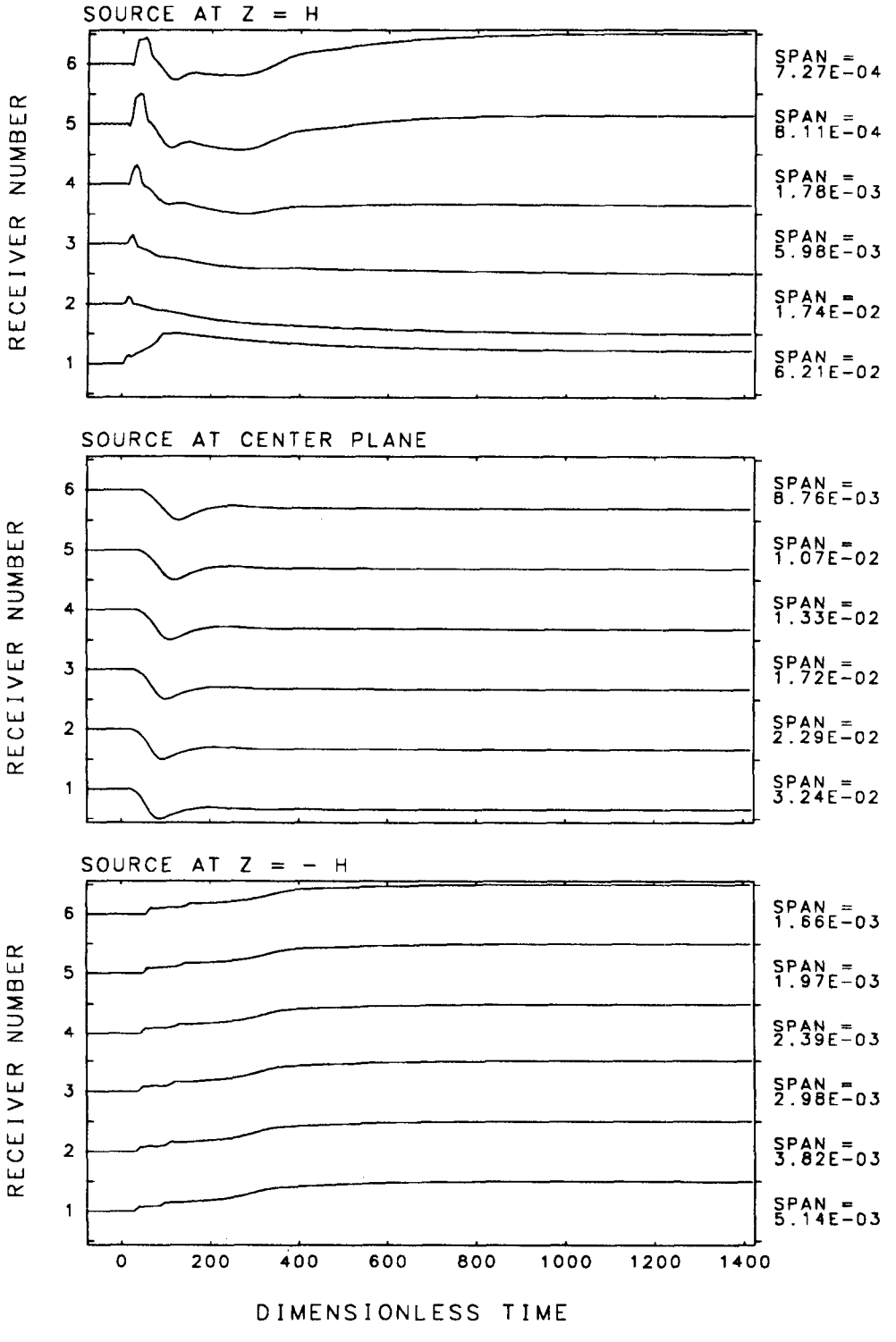

FIGURE D2.2 VERTICAL DISPLACEMENT RESPONSE OF SOLID REGION TO A UNIT ISOTROPIC FLUID MOMENT

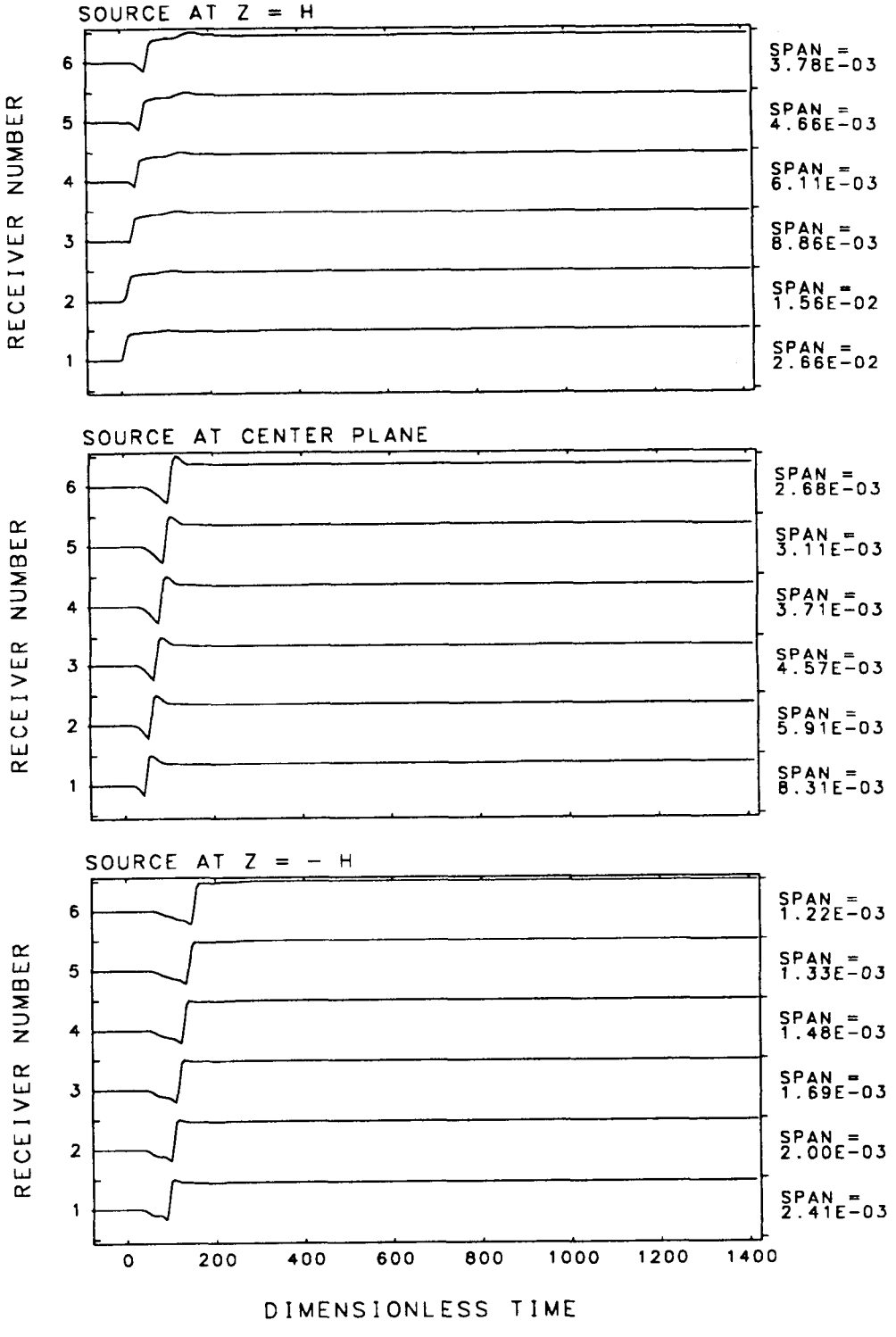

FIGURE D3.1 RADIAL DISPLACEMENT RESPONSE OF SOLID REGION FOR A RADIAL POINT UNIT LOAD

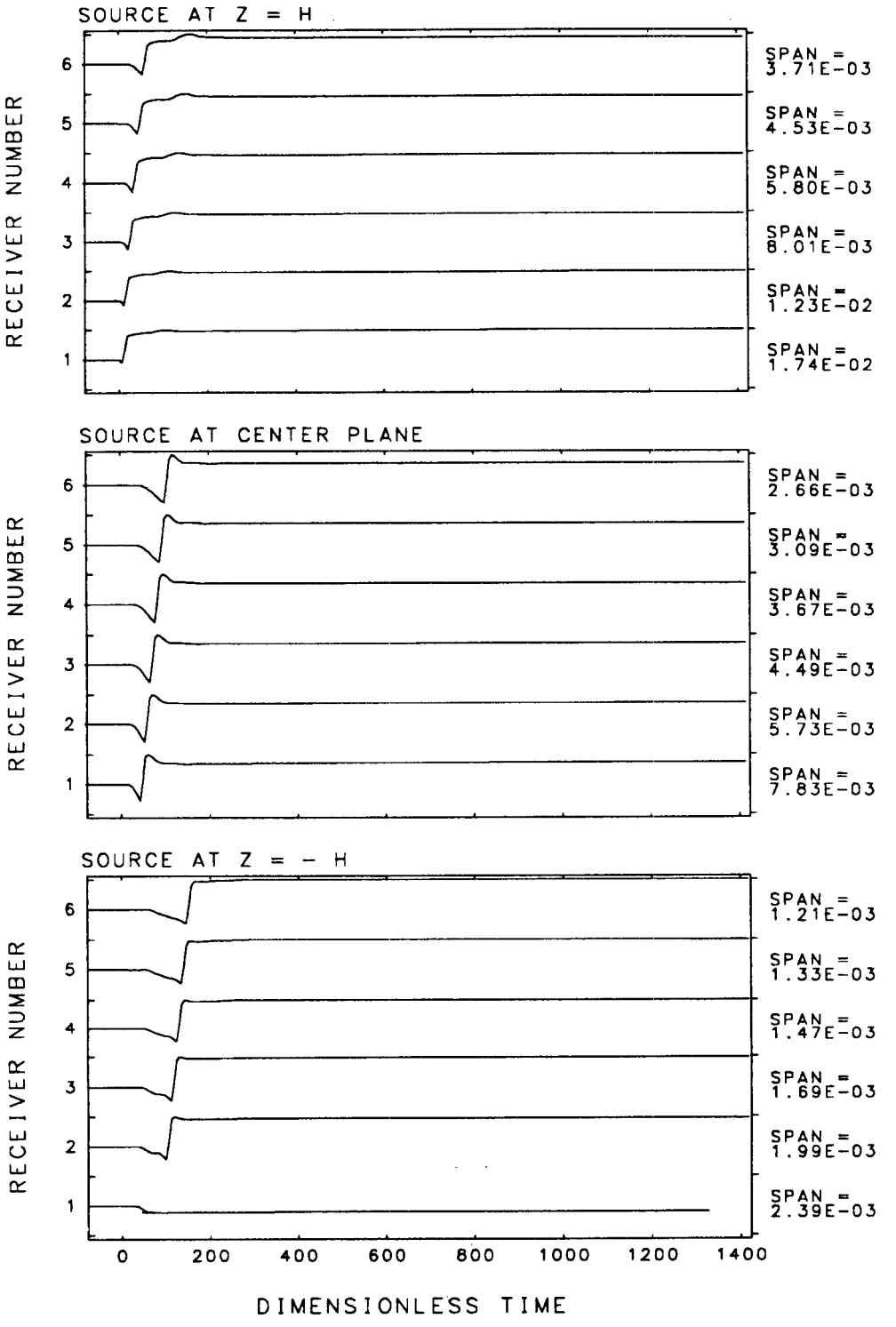

FIGURE D3.2 TRANSVERSE HORIZONTAL DISLPLACEMENT RESPONSE FOR A TRANSVERSE HORIZONTAL POINT UNIT LOAD

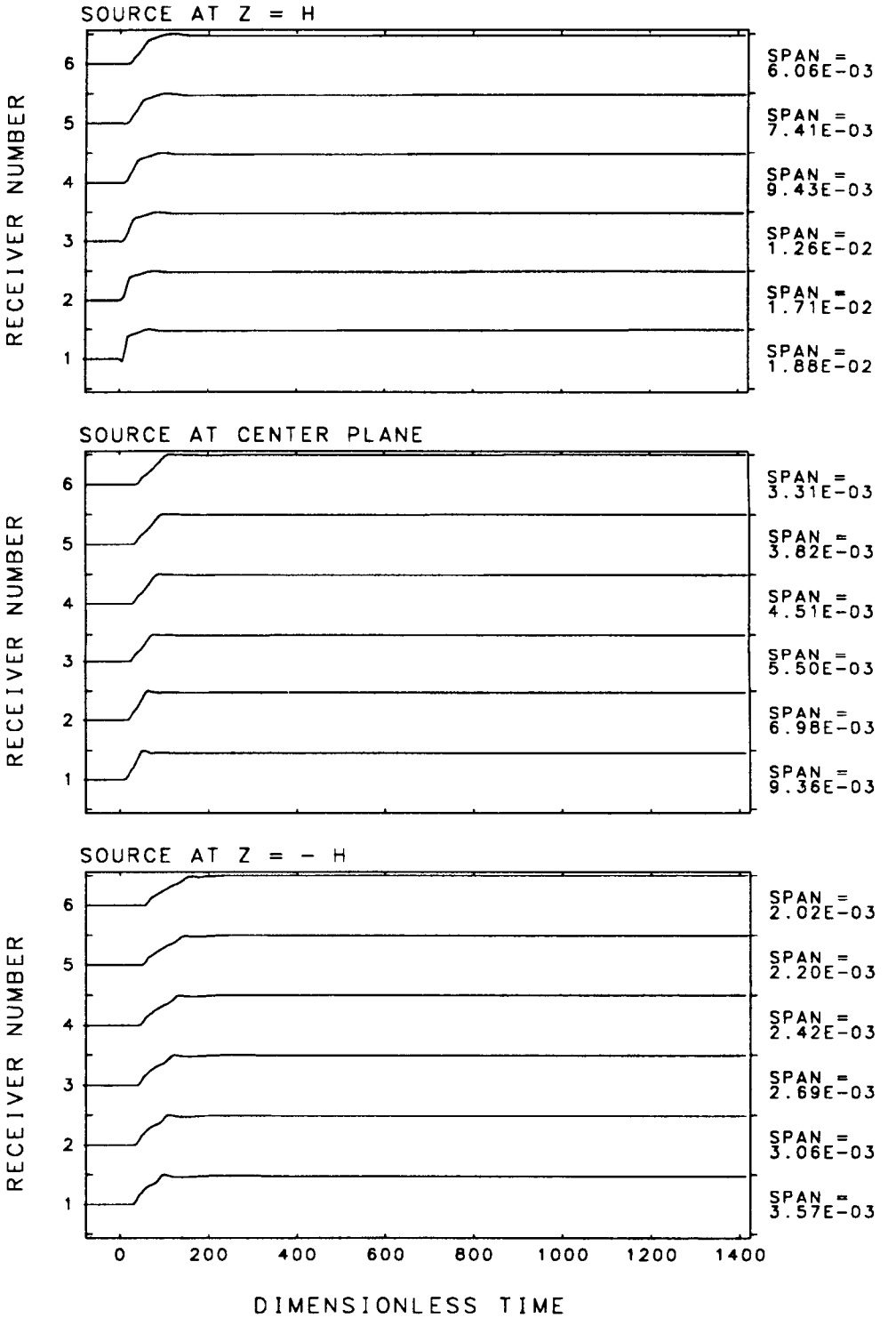

FIGURE D3.3 VERTICAL DISPLACEMENT RESPONSE OF SOLID REGION FOR A VERTICAL POINT UNIT LOAD

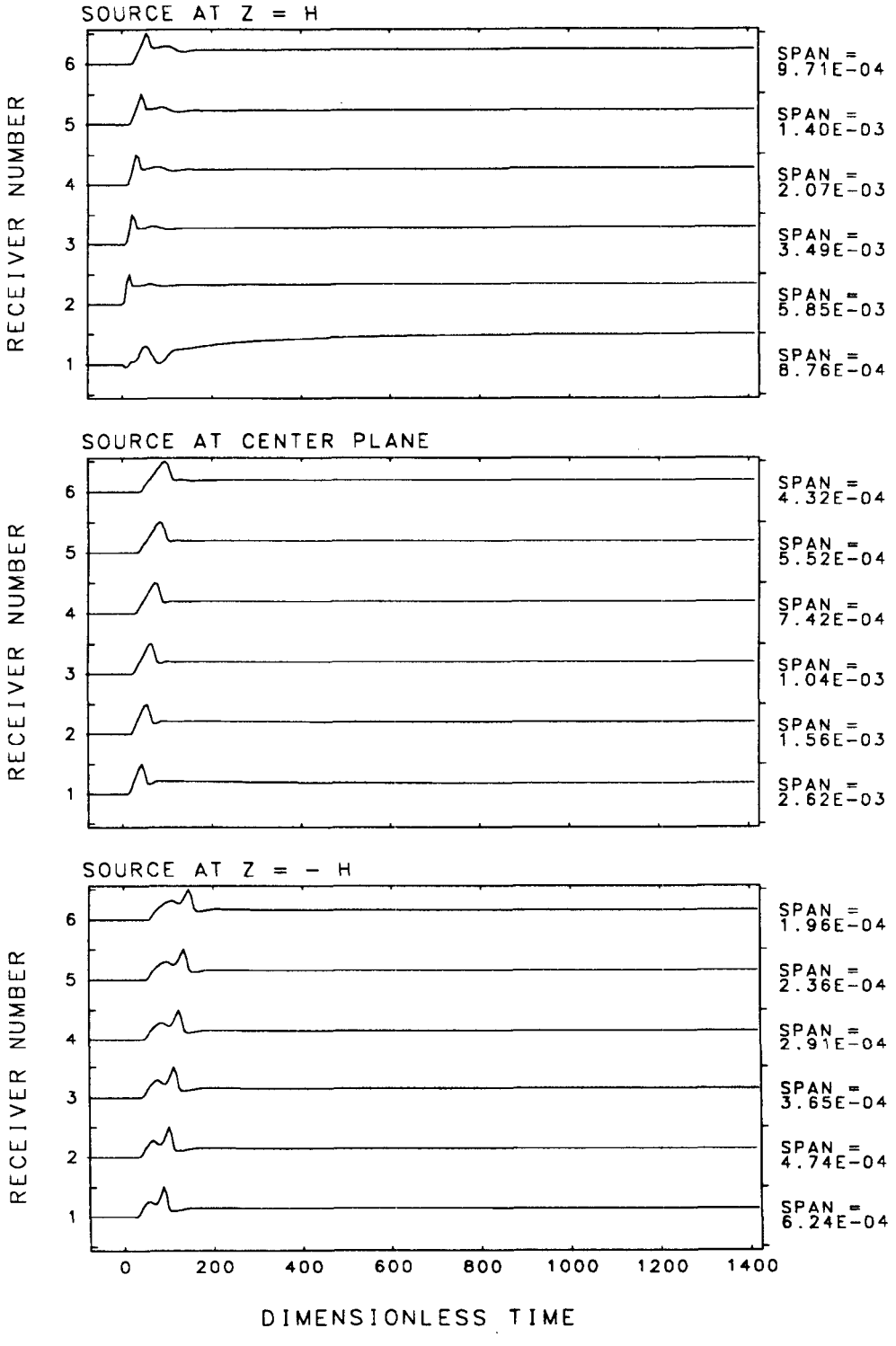

FIGURE D3.4 RADIAL DISPLACEMENT RESPONSE OF SOLID REGION FOR A VERTICAL POINT UNIT LOAD

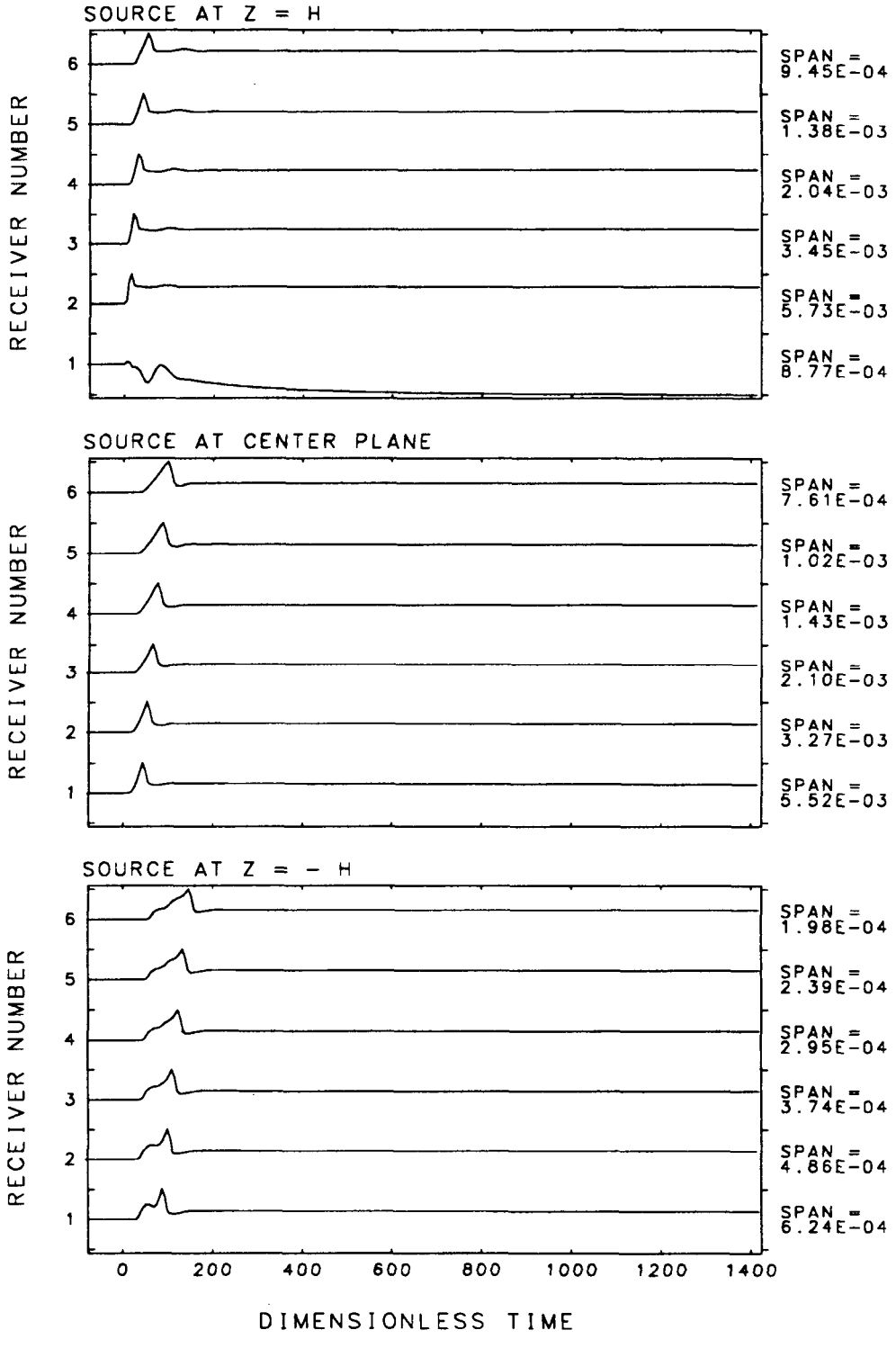

FIGURE D3.5 VERTICAL DISPLACEMENT RESPONSE OF THE SOLID REGION FOR A RADIAL POINT UNIT LOAD

Appendix E:
Upper Boundary Displacement Responses

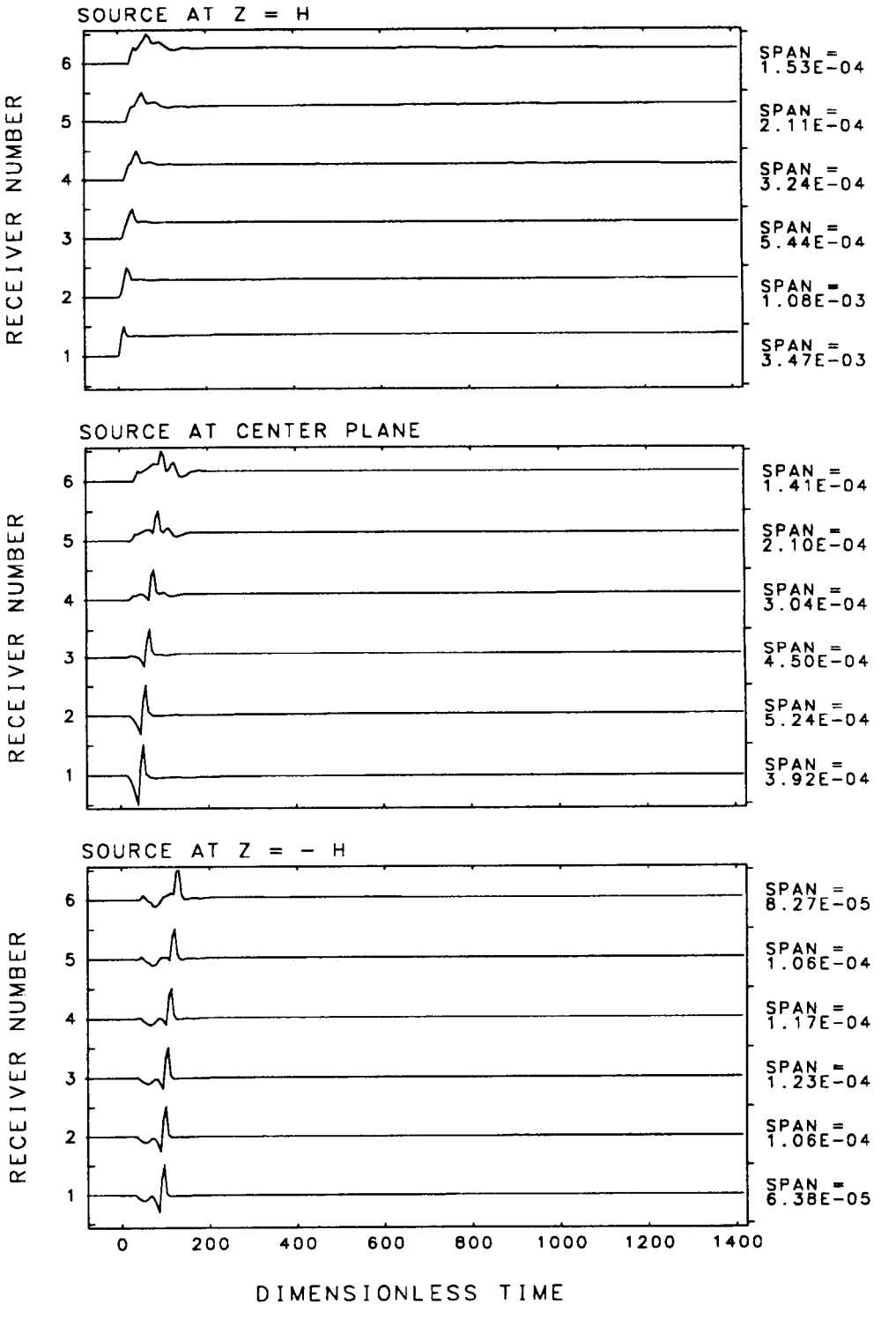

FIGURE E1.1 RADIAL DISPLACEMENT RESPONSE AT UPPER BOUNDARY TO A UNIT R-R MOMENT

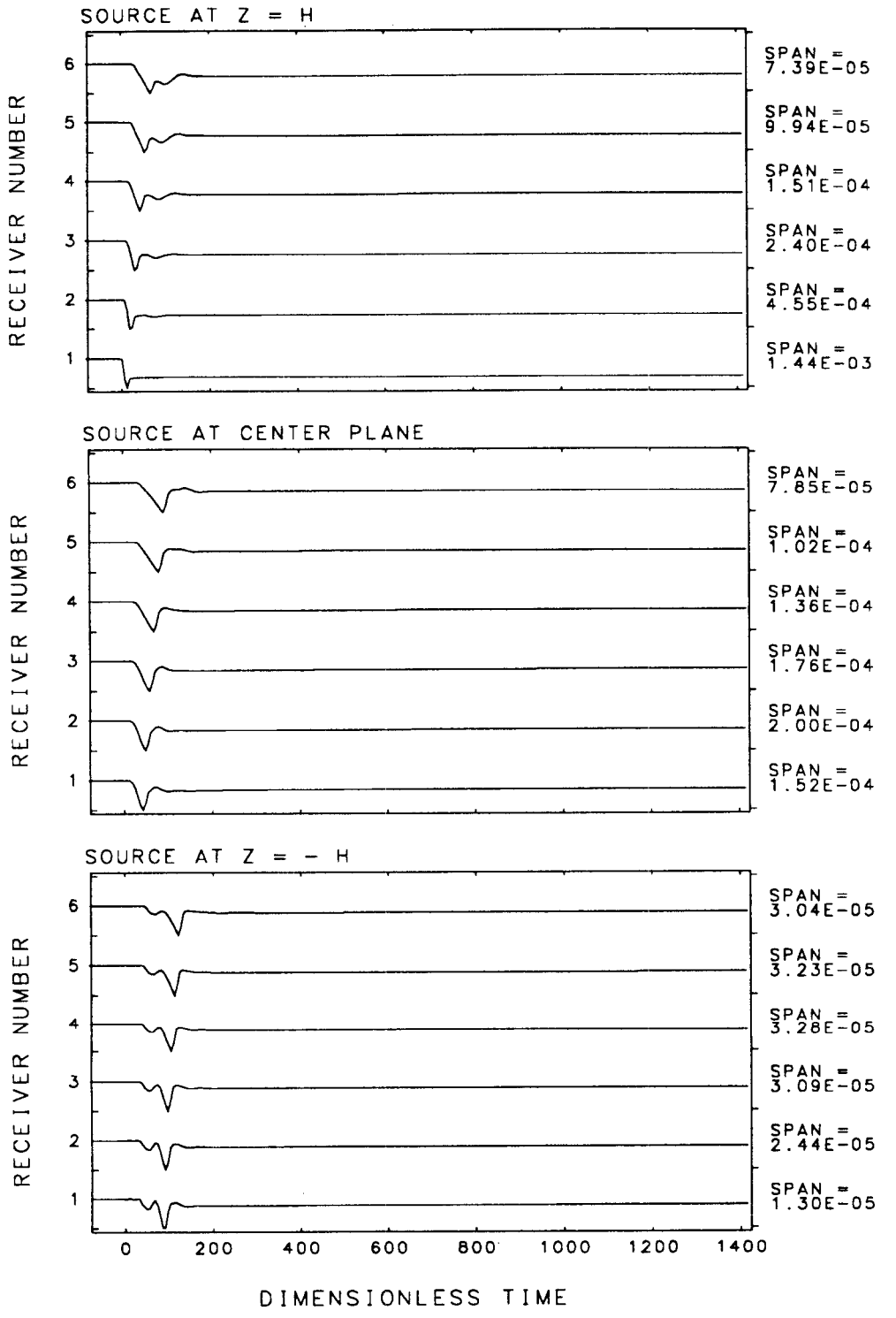

FIGURE E1.2 RADIAL DISPLACEMENT RESPONSE AT UPPER BOUNDARY TO A UNIT θ–θ MOMENT

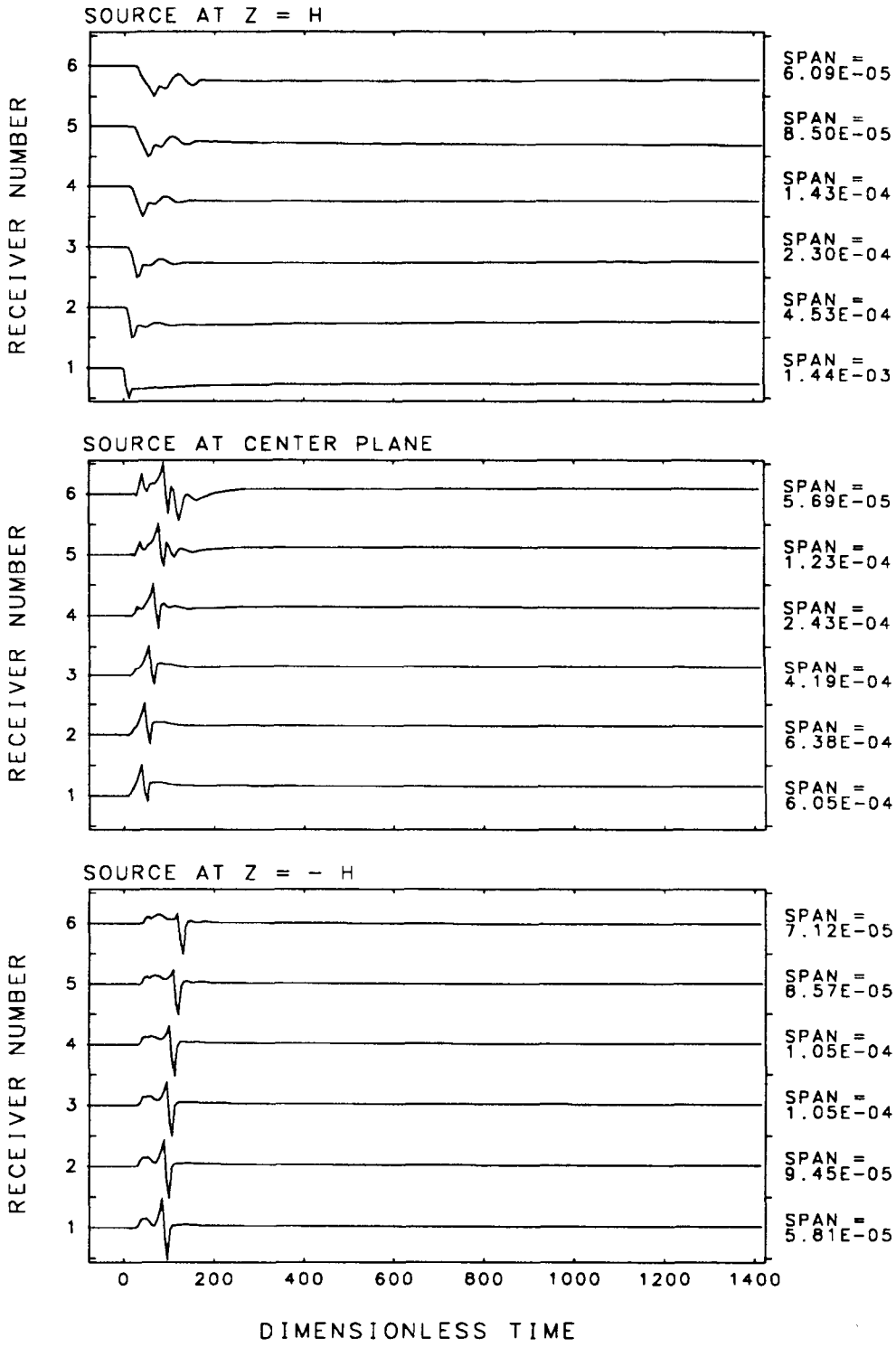

FIGURE E1.3 RADIAL DISPLACEMENT RESPONSE AT UPPER BOUNDARY TO A UNIT Z-Z MOMENT

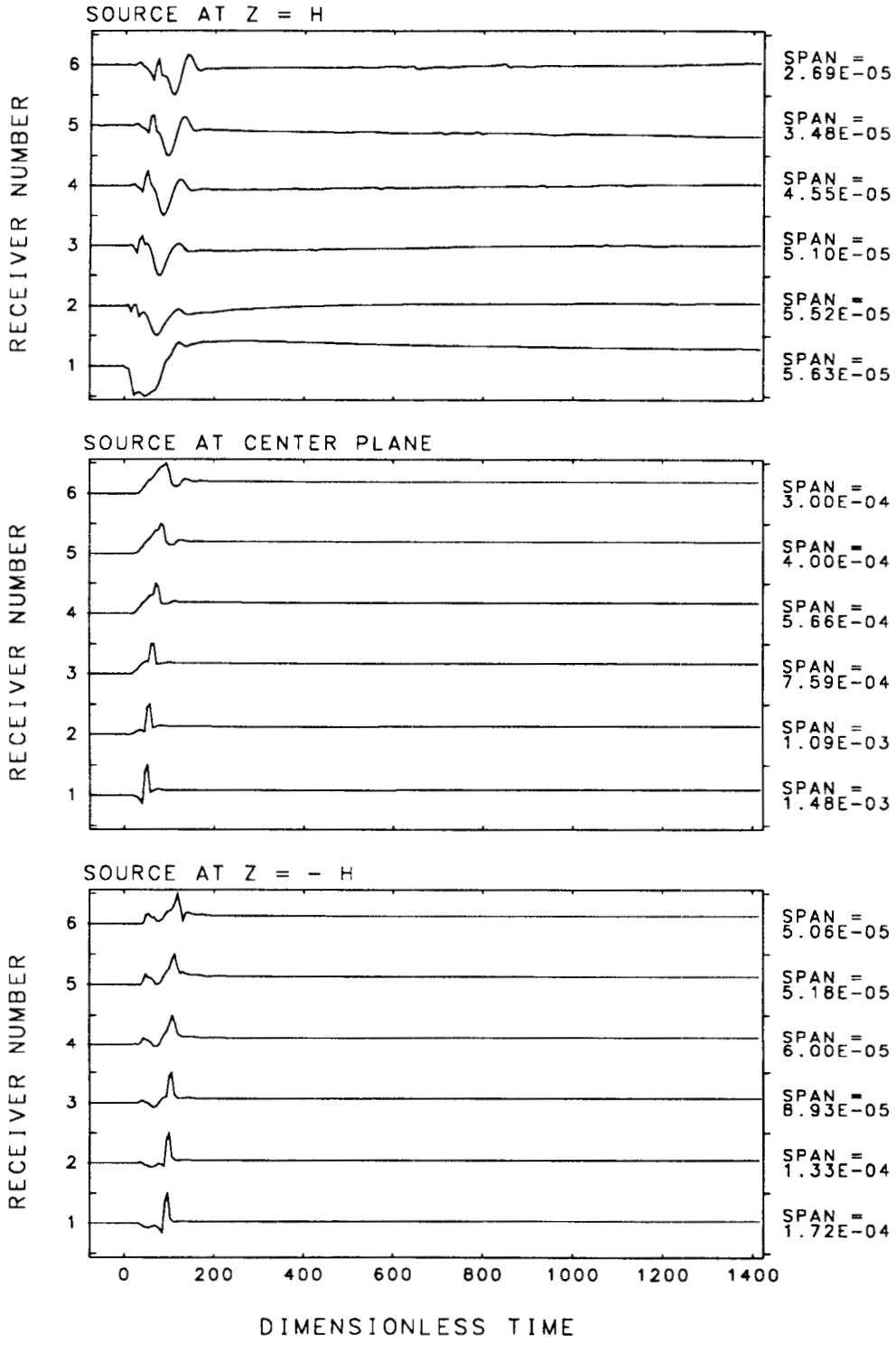

FIGURE E1.4 RADIAL DISPLACEMENT RESPONSE AT UPPER BOUNDARY TO A UNIT SYMMETRIC R-Z MOMENT

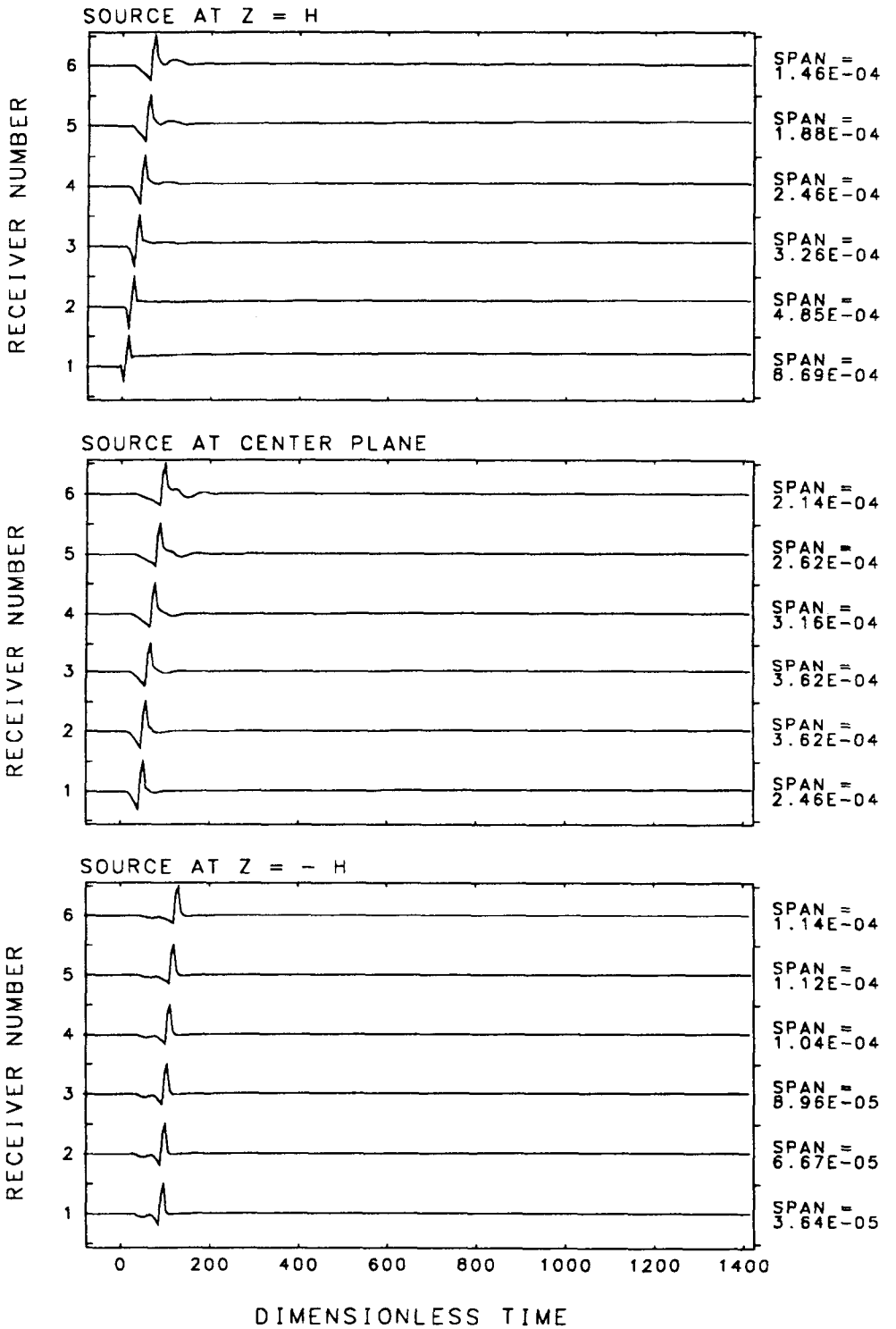

FIGURE E1.5 TRANSVERSE HORIZONTAL DISPLACEMENT RESPONSE AT UPPER BOUNDARY TO A UNIT SYMMETRIC R-θ MOMENT

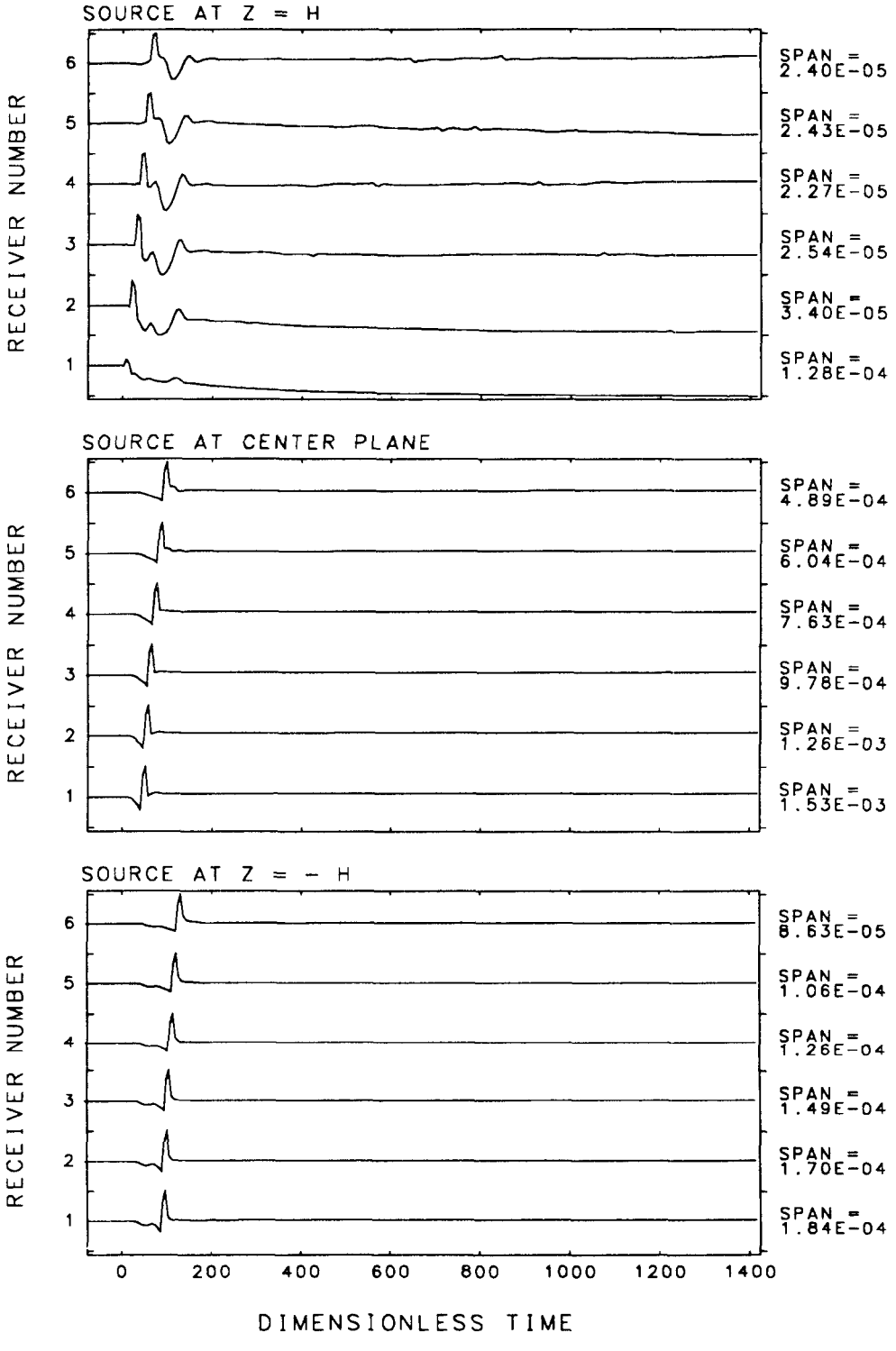

FIGURE E1.6 TRANSVERSE HORIZONTAL DISPLACEMENT RESPONSE AT UPPER BOUNDARY TO A UNIT SYMMETRIC θ-Z MOMENT

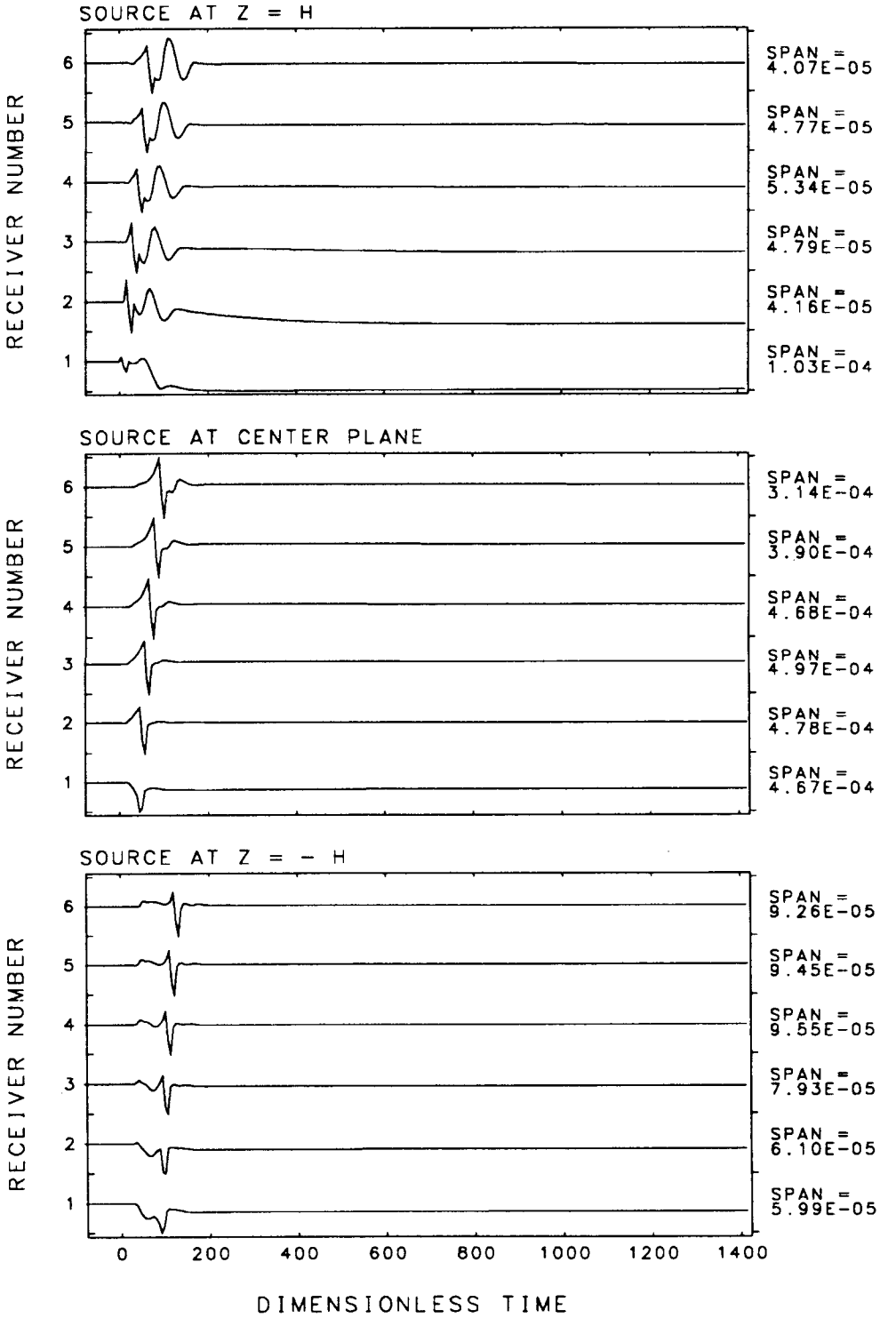

FIGURE E1.7 VERTICAL DISPLACEMENT RESPONSE AT UPPER BOUNDARY FOR A UNIT R-R MOMENT

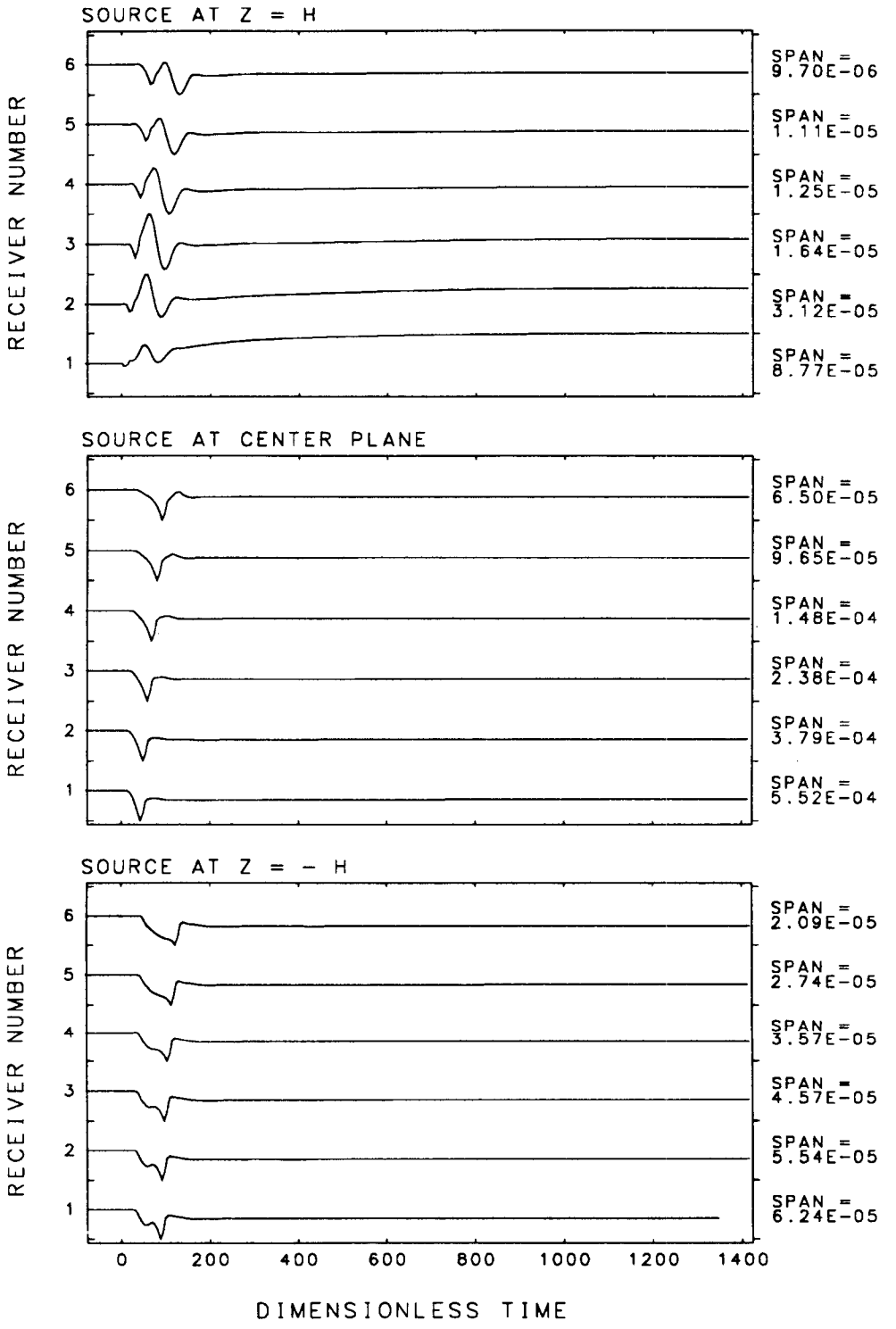

FIGURE E1.8 VERTICAL DISPLACEMENT RESPONSE AT UPPER BOUNDARY FOR A UNIT θ–θ MOMENT

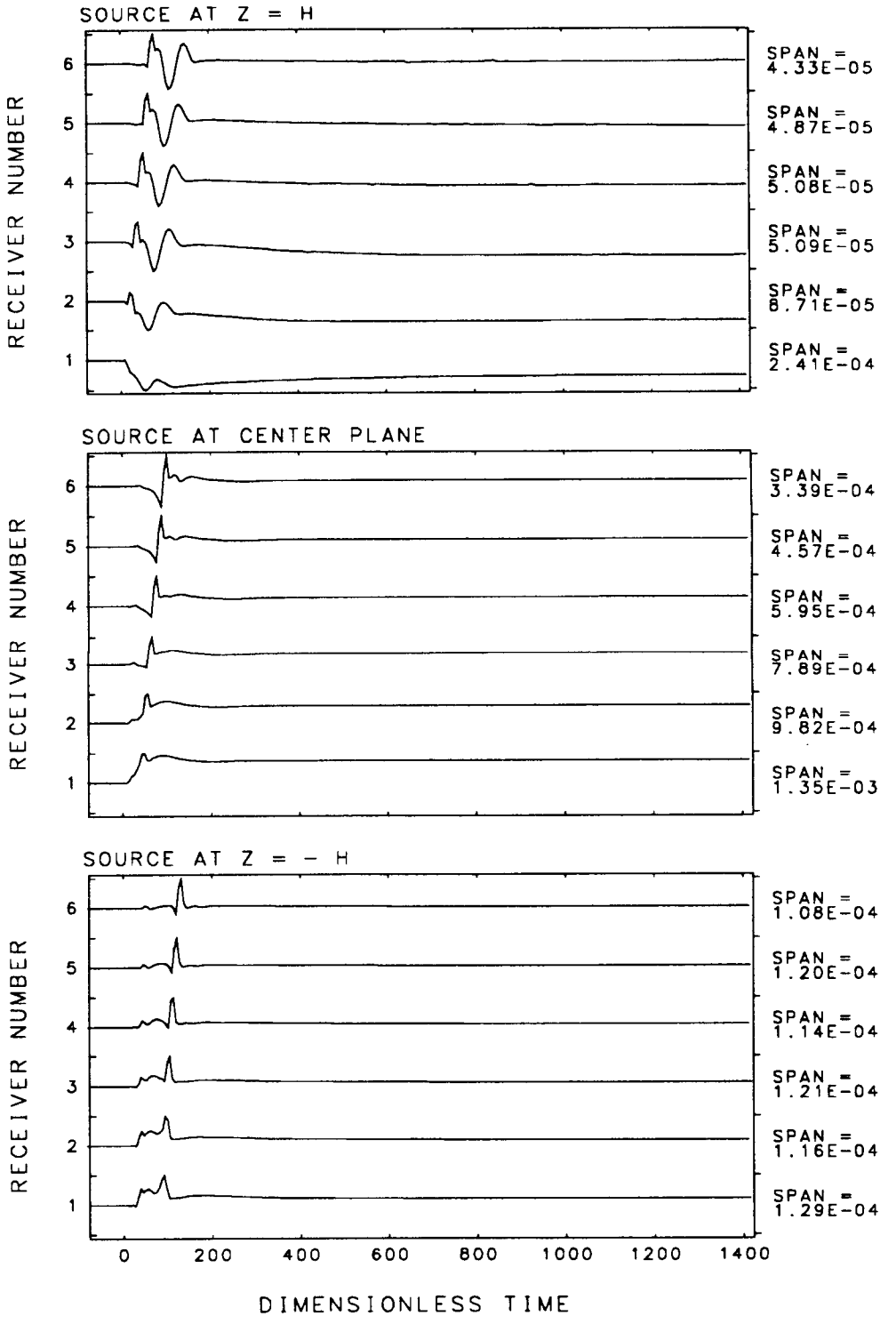

FIGURE E1.9 VERTICAL DISPLACEMENT RESPONSE AT THE UPPER BOUNDARY BOUNDARY TO A UNIT Z-Z MOMENT

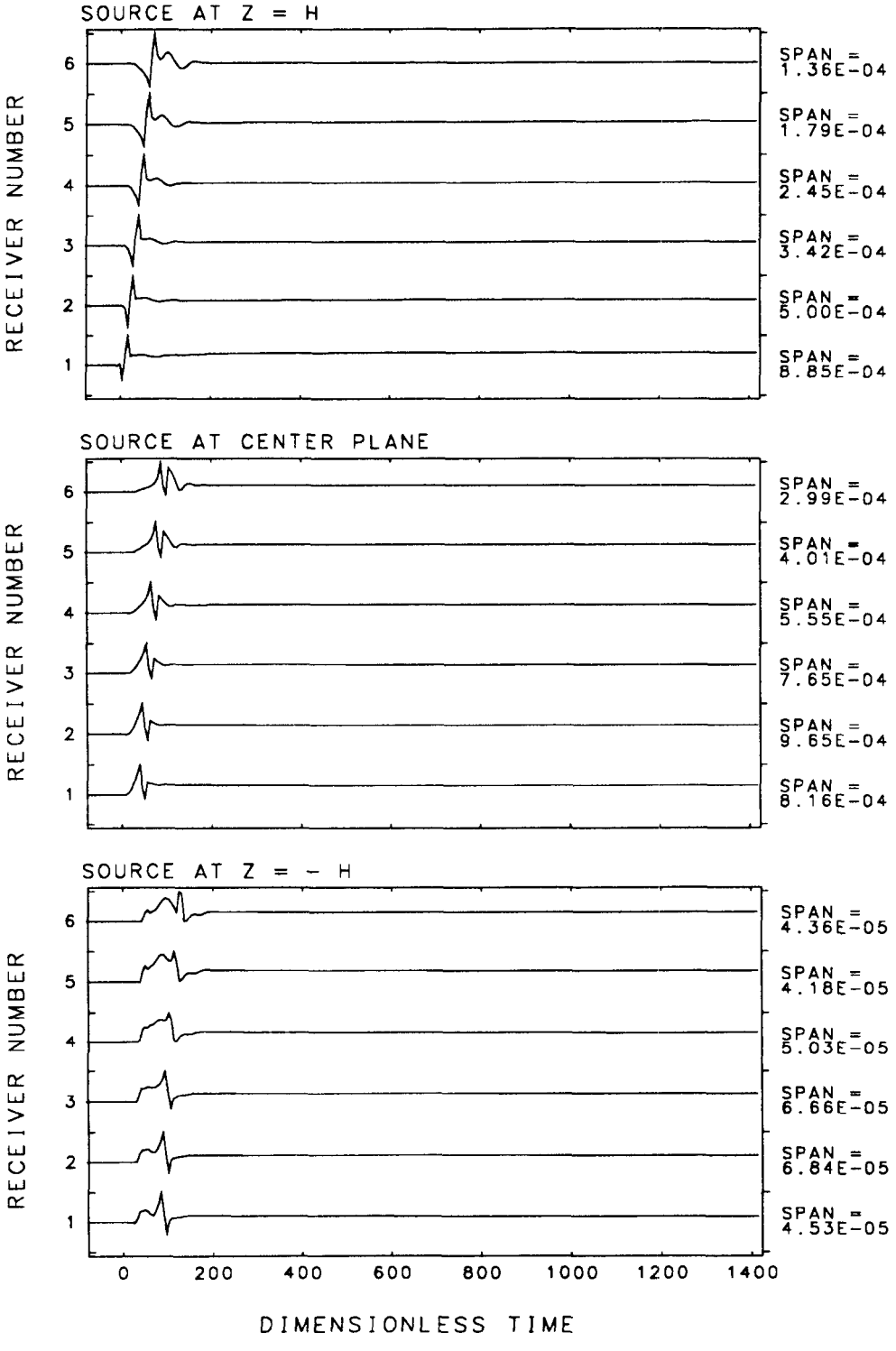

FIGURE E1.10 VERTICAL DISPLACEMENT RESPONSE AT THE UPPER BOUNDARY FOR A UNIT SYMETRIC Z-θ MOMENT

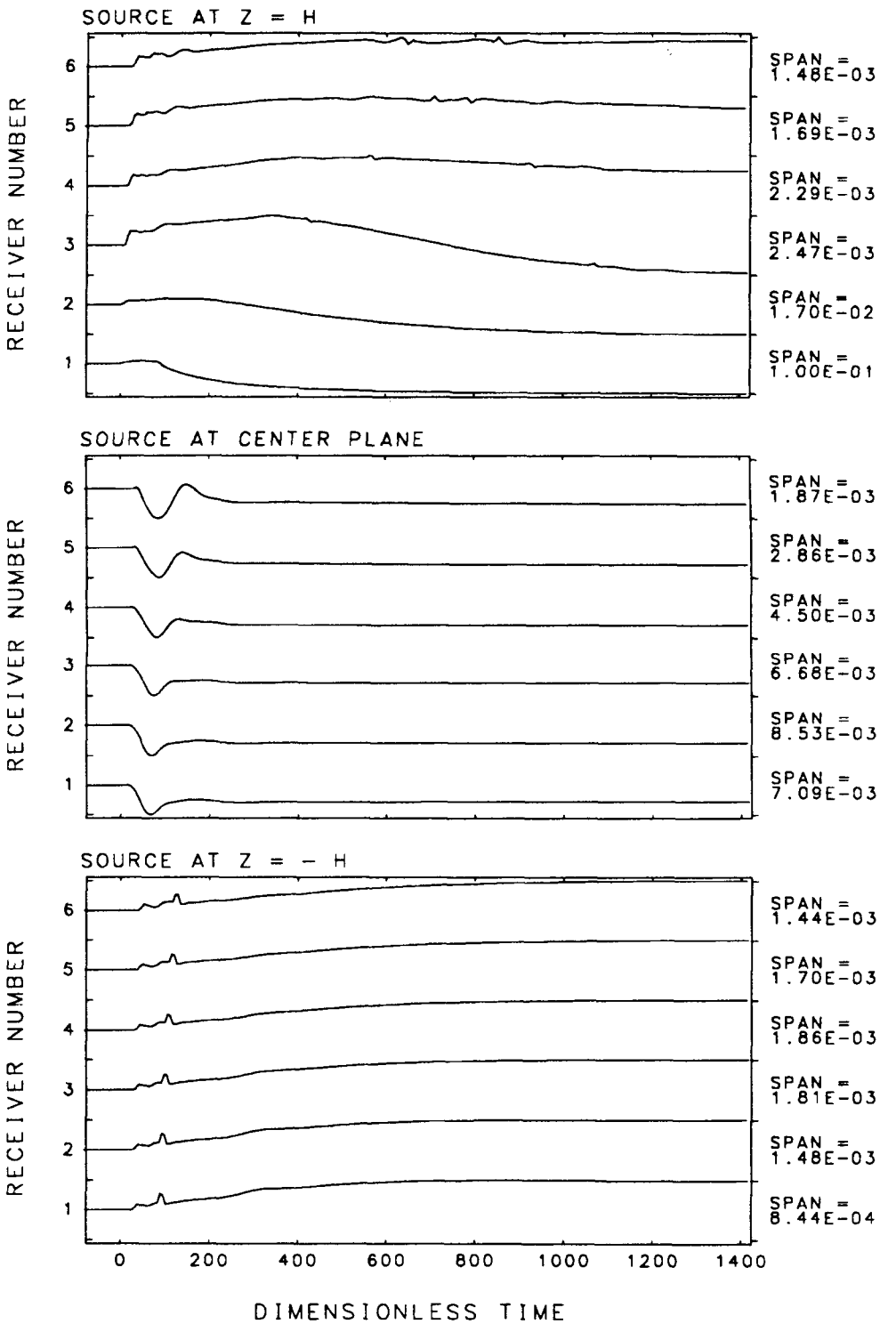

FIGURE E2.1 RADIAL DISPLACEMENT RESPONSE AT THE UPPER BOUNDARY TO A UNIT ISOTROPIC FLUID MOMENT

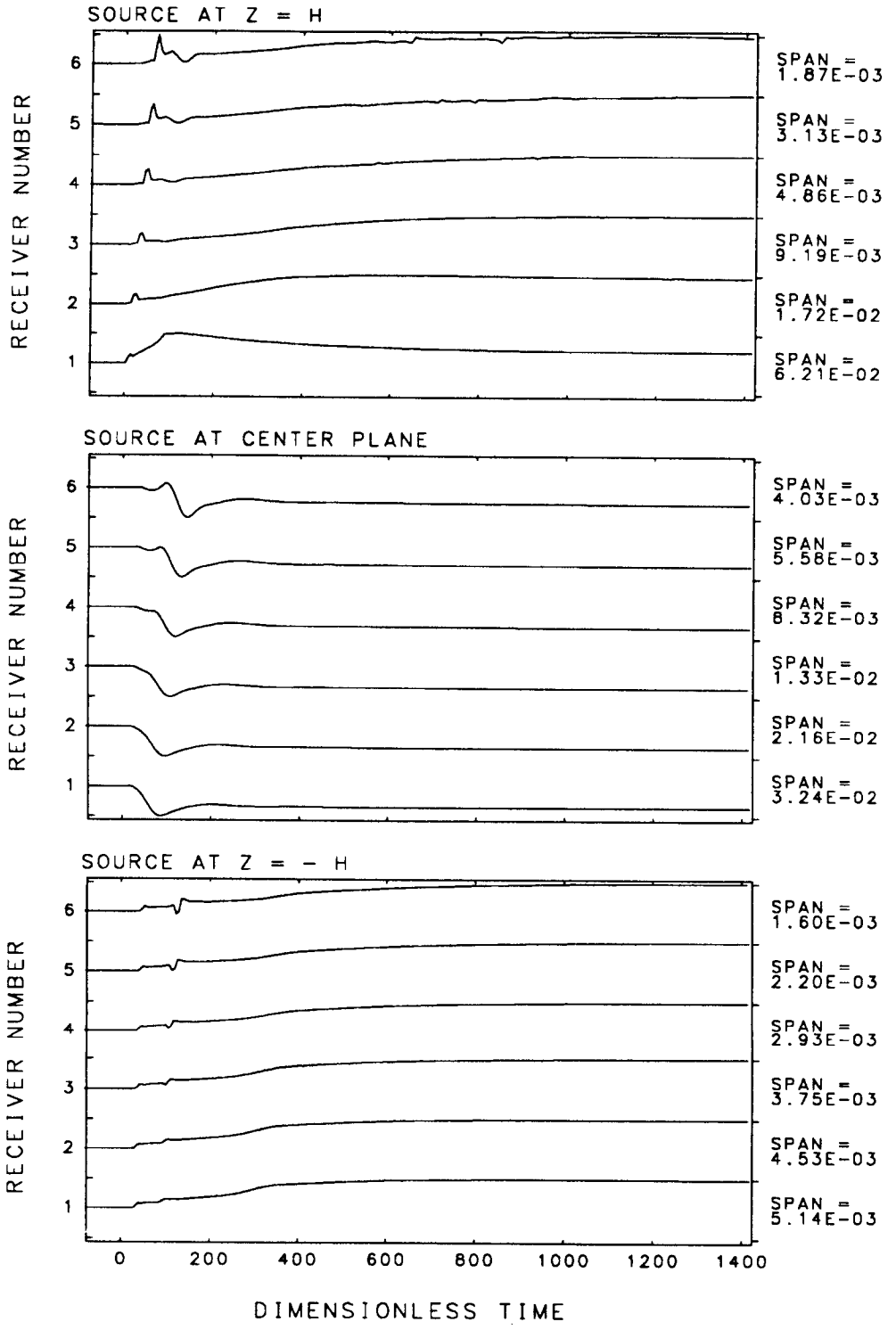

FIGURE E2.2 VERTICAL DISPLACEMENT RESPONSE AT THE UPPER BOUNDARY TO A UNIT ISOTROPIC FLUID MOMENT

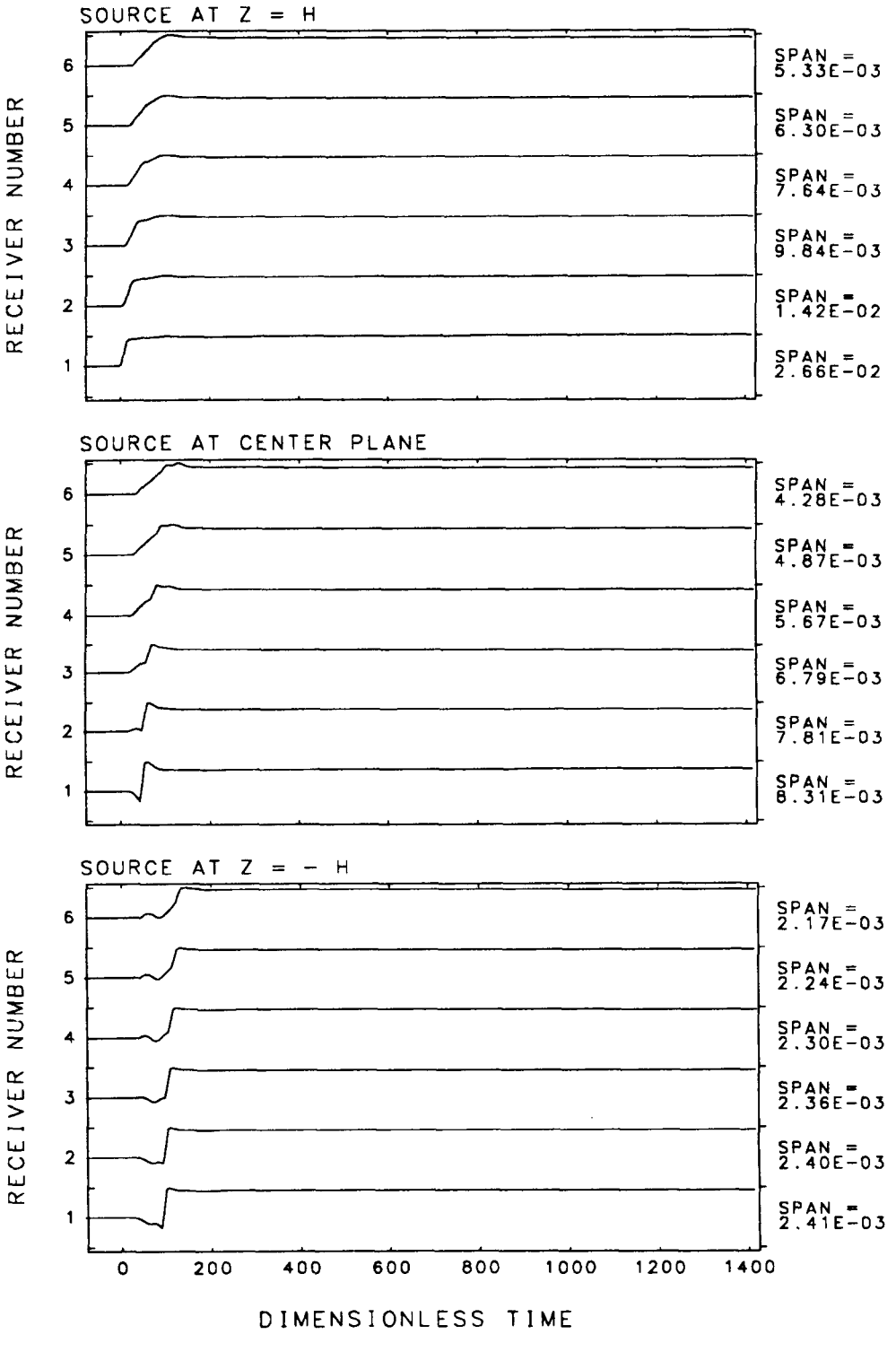

FIGURE E3.1 RADIAL DISPLACEMENT RESPONSE AT THE UPPER BOUNDARY TO A RADIAL POINT UNIT LOAD

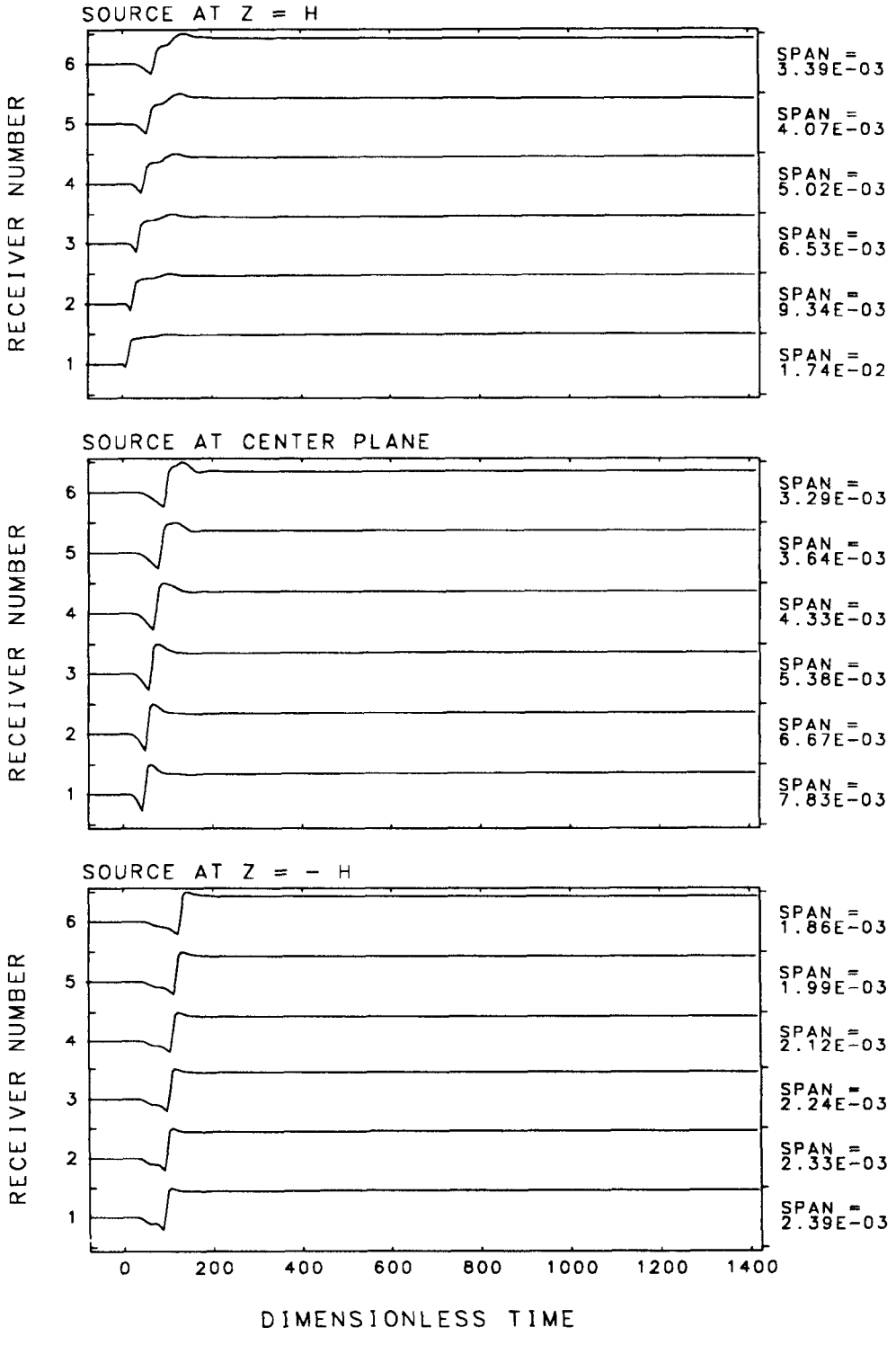

FIGURE E3.2 TRANSVERSE HORIZONTAL DISPLACEMENT RESPONSE AT THE UPPER BOUNDARY TO A TRANSVERSE HORIZONTAL POINT UNIT LOAD

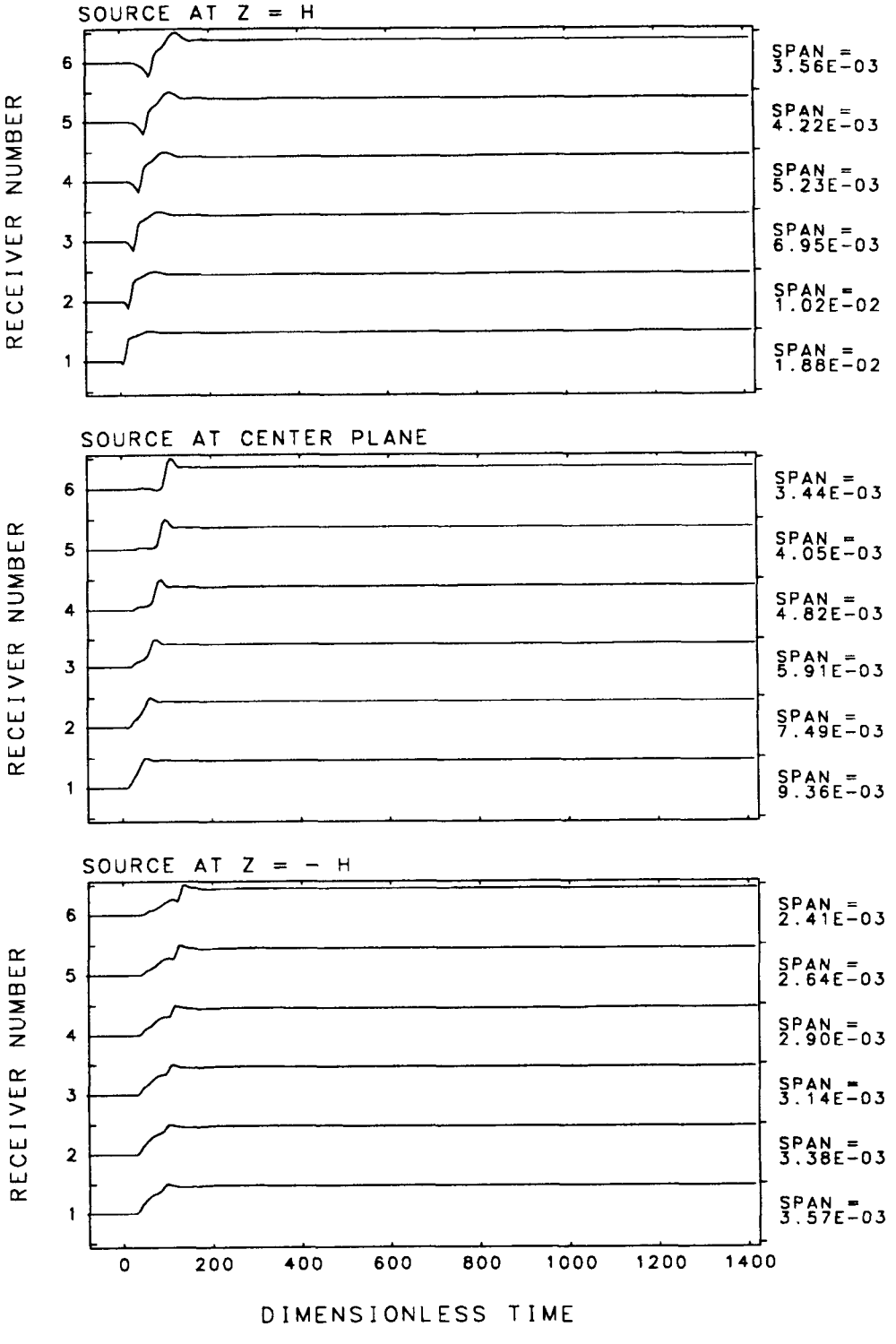

FIGURE E3.3 VERTICAL DISPLACEMENT RESPONSE AT THE UPPER BOUNDARY FOR A VERTICAL POINT UNIT LOAD

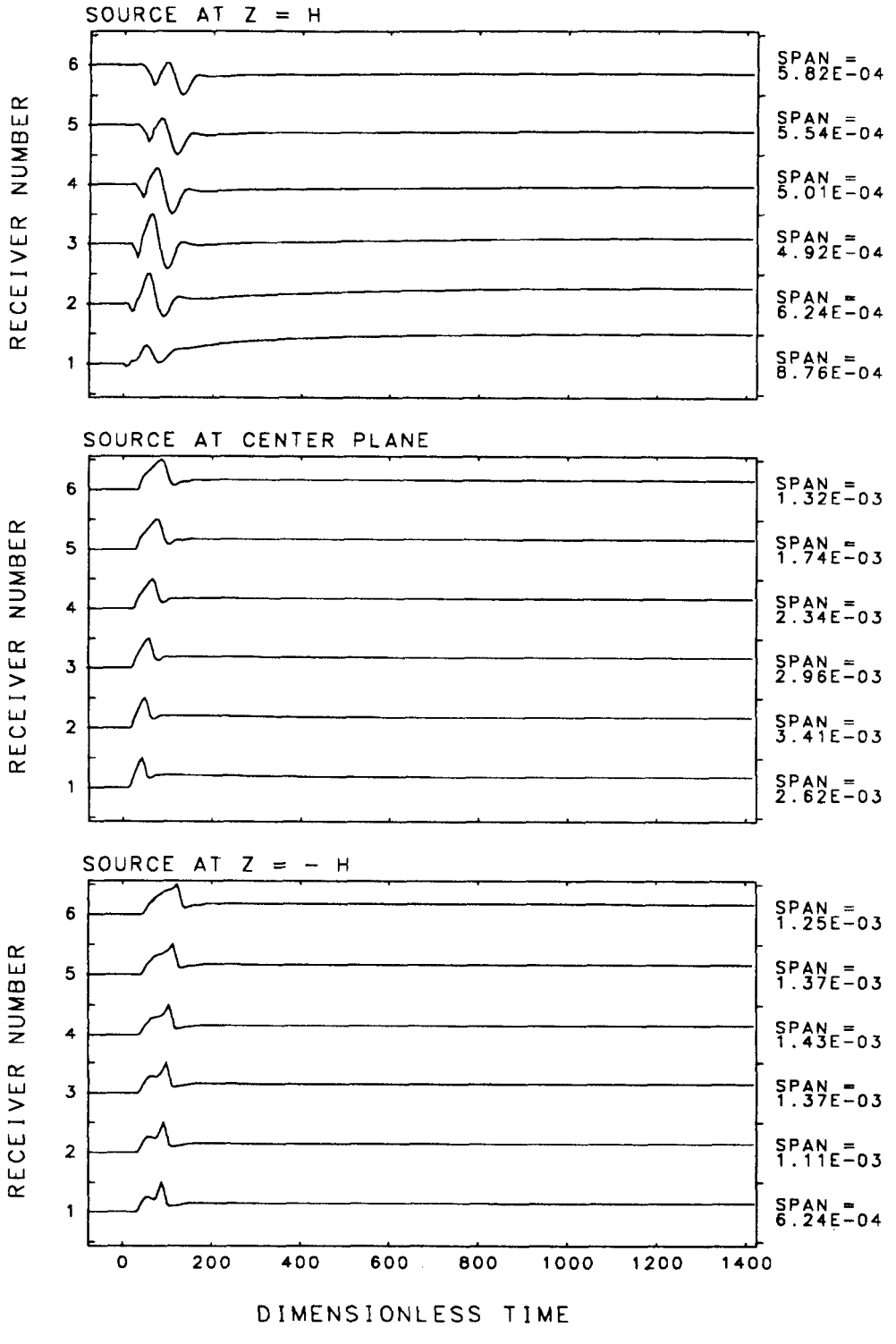

FIGURE E3.4 RADIAL DISPLACEMENT RESPONSE AT THE UPPER BOUNDARY FOR A VERICAL POINT UNIT LOAD

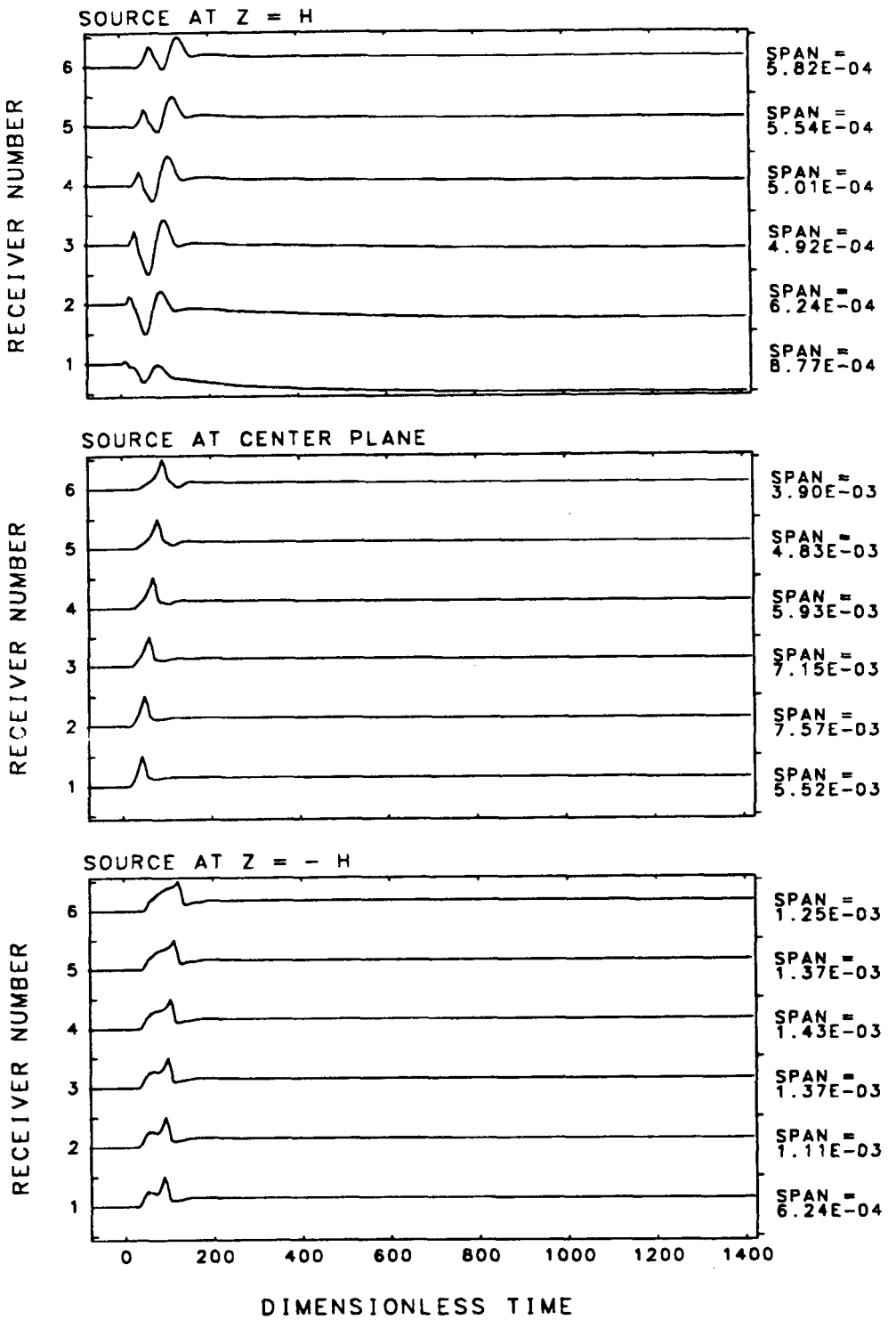

FIGURE E3.5 VERTICAL DISPLACEMENT RESPONSE AT THE UPPER BOUNDARY FOR A RADIAL POINT UNIT LOAD